Karlsruhe Institute of Technology

Synthesis of Highly Branched Polystyrene Model Systems with Superior Strain Hardening and their Influence on Foaming Properties

Zur Erlangung des akademischen Grades eines

DOKTORS DER NATURWISSENSCHAFTEN

(Dr. rer. nat.)

von der KIT-Fakultät für Chemie und Biowissenschaften
des Karlsruher Instituts für Technologie (KIT)

genehmigte

DISSERTATION

von

Dipl.-Chem. Lorenz Faust

aus Hatzenbühl

Dekan / Referent:	Prof. Dr. Manfred Wilhelm
Korreferent:	Prof. Dr. Patrick Théato
Tag der mündlichen Prüfung:	19. Juli 2021

Die vorliegende Arbeit wurde von Februar 2016 bis Juni 2021 unter der Betreuung von Herrn Prof. Dr. Manfred Wilhelm am Institut für Technisch Chemie und Polymerchemie (ITCP) des Karlsruher Institut für Technologie (KIT) - Universitätsbereich angefertigt.

Ich versichere hiermit wahrheitsgemäß, die Arbeit selbstständig verfasst, alle benutzten Hilfsmittel vollständig und genau angegeben, und alles kenntlich gemacht zu haben, was aus Arbeiten anderer unverändert oder mit Abänderungen entnommen wurde, sowie die Satzung des KIT zur Sicherung guter wissenschaftlicher Praxis in der jeweils gültigen Fassung beachtet zu haben.

Lorenz Faust

Karlsruhe, den 07. Juni 2021

...for my godmother "Tante Anne".

"Experimenters don't come in late – they never went home."

– Leon M. Lederman

Zusammenfassung

Die molekulare Struktur bestimmt maßgeblich die Verarbeitbarkeit eines Polymers in der Schmelze und die daraus resultierenden makroskopischen Eigenschaften des Endprodukts, die wiederum über seine Anwendung entscheiden. Viele dieser Anwendungen beruhen auf dünnen Film- und Faserstrukturen, von denen polymere Schäume mit ihrer porösen Zellmorphologie ein wichtiger Vertreter sind. Die Schmelzefestigkeit ist entscheidend für die Expandierbarkeit eines Schaums, da sie die Zellwände und Verstrebungen auf mikro- und nanoskaliger Ebene stabilisiert. Verzweigungen, insbesondere Langkettenverzweigungen sind eine Schlüsseleigenschaft eines Polymers um eine gute Schmelzefestigkeit in Dehnströmung zu erreichen. Es ist von großem Interesse, den Einfluss der Topologie eines Polymers auf das rheologische Verhalten zu verstehen und die Struktur-Eigenschafts-Beziehung vorherzusagen und letztendlich effizient zu nutzen.
Die hier vorgestellte Arbeit untersucht den Einfluss von mehrfach verzweigten Polymerarchitekturen auf die Schäumbarkeit, speziell auf die Volumenexpansion und korreliert die erzielten Schaumeigenschaften mit der Molekularstruktur mittels dem Fließverhalten aus der Scher- und Dehnrheologie. Um einen systematischen Ansatz zu ermöglichen, werden definierte Modellpolystyrole (PS) mit Kamm- und Dendrigraft-Topologie und einer variierenden Anzahl von Verzweigungen mittels anionischer Synthese hergestellt. Die Schmelzeeigenschaften werden in oszillatorischer Scherung und uniaxialer Dehnung rheologisch charakterisiert. Das Batch-Schäumen wird bei 180 und 500 bar unter Verwendung von Kohlendioxid (CO_2) als physikalisches Treibmittel durchgeführt. Die resultierenden Schäume werden hinsichtlich ihrer Volumenausdehnung, Zellgröße und Zelldichte analysiert. Es wird eine Reihe von Kamm-PS mit gut verzweigten, aber unterschiedlicher Anzahl von Langkettenverzweigungen synthetisiert, die von spärlich verzweigt bis hin zu flaschenbürstenartiger Strukturen reichen. Die Korrelation der rheologischen und der Schaumeigenschaften zeigt einen Bereich optimaler Verzweigungszahl, die in einen maximalen Volumenexpansionskoeffizient von 40 bei gleichzeitig maximalem Dehnverfestigungsfaktor (*strain hardening factor*) von SHF = 200 resultiert, wobei die Nullscherviskosität auch am niedrigsten ist.
Dendrigraft-PS werden aus einem langkettenverzweigten Kamm-PS synthetisiert, auf den eine Korona aus Kurzkettenverzweigungen aufgepfropft wird. Die sogenannte “branch-on-Branch” (bob)-Architektur weist molekulare Parameter auf, die eindeutig drei verschiedene Relaxationsmodi zeigen, die jeder Verzweigungsgeneration zugeordnet werden können und auf die hierarchische Kettendynamik hinweisen. In uniaxialer Dehnung wird ein enormer Dehnungsverfestigungfaktor bis zu SHF = 700 erreicht. Dabei zeigt sich die Dehnrate als ein wichtiges Kriterium dafür, ob eine hohe Dehnverfestigung zu einer verbesserten Schäum-

barkeit führt. Dies wird durch das Schäumen eines kurzkettenverzweigten Kamm-PS validiert, der sich durch eine Dehnverfestigung von SHF = 200 bei schnellen Dehnungsraten von $\dot{\varepsilon}_H = 3–10\,s^{-1}$ auszeichnet und im Vergleich zu Dendrigraft- und langkettenverzweigten Kamm-PS konstant höhere Volumenexpansionen liefert, insbesondere bei hohen Schäumungstemperaturen und schnellen Druckentlastungsraten.
Weiterhin werden bimodale Kamm-Lineare PS-Blends hergestellt, um das Zusammenspiel zwischen verzweigter und linearer Kettentopologie zu untersuchen. Die Schmelzrheologie gibt einen Einblick in Relaxationsdynamiken und deren Skalengesetze und zeigt das Potenzial von verzweigt-linearen Blends zur Einstellung und Optimierung der Schmelzeeigenschaften für Verarbeitungsprozesse in Dehnung oder Scherung.

Abstract

The molecular structure strongly governs a polymer's processability in the bulk melt state and the resulting macroscopic properties of the final product, that further decides about its application. Many of those applications rely on thin film and filament structures of which polymeric foams with their porous cell morphology are a major representative. Melt strength is crucial for the expandibility of a foam, as it stabilizes the cell walls and struts on micro- and nanoscale dimensions. Branching, in particular long chain branching (LCB), is known as one of the key features of a polymer to achieve good melt strength in elongational flow. It is of major interest to understand the effect of a polymer's topology on the rheological behavior and to predict and ultimately make efficient use of the structure-property relationship.

The here presented thesis investigates the influence of multiply branched polymer architectures on the foamability, specifically the volume expansion, and correlates the final foam properties to the molecular structure by means of shear and extensional rheology. To enable a systematic approach, defined, model branched homopolymer polystyrenes (PS) with a varying number of branches are synthesized using anionic polymerization. The melt properties are analyzed via small amplitude oscillatory shear (SAOS) and uniaxial extensional rheology. One-step batch foaming is performed at 180 and 500 bar using carbon dioxide (CO_2) as physical blowing agent. The resulting foams are analyzed by quantifiying the volume expansion, cell size and cell density.

A series of comb PS with well-entangled but varying number of LCB is synthesized, ranging from sparsely branched to bottlebrush-like structures. The correlation of the rheological and foaming properties reveals an optimum number of branching corresponding to a maximum volume expansion ratio (VER = 40) and simultaneously also a maximum strain hardening factor (SHF $\approx$ 200), while the zero-shear viscosity was found to be the lowest.

Dendrigraft PS are synthesized from a LCB comb PS core that is further grafted with a corona of short chain branches (SCB). The branch-on-branch (bob) architecture exhibits molecular parameters that uniquely show three distinct relaxation modes that can be assigned to each branch generation and correlate with the hierarchical chain dynamics. Tremendous strain hardening up to SHF $\approx$ 700 is achieved in extensional flow. The strain rate is found to be an important criteria whether a high SHF translates to improved foamability. This is validated by foaming a comb PS with barely entangled SCB, that excels in SHF $>$ 200 at fast extensional rates ($\dot{\varepsilon}_H$ = 3–10 s^{-1}), giving also consistently high VER, especially at high temperatures and fast depressurization rates.

Furthermore, bimodal comb-linear PS blends are prepared to study the interplay between

branched and linear chain topology. Melt rheological measurements give an insight into the polymer relaxation dynamics, the tube dilution and its scaling laws, as well as show the potential of branched-linear blends to tune and optimize the melt properties for polymer processing in shear or elongation.

Nomenclature

Abbreviations

Å	Ångström ($= 10^{-10}$ m)
Ac	Acetyl- (–CO-CH_3)
ATRP	Atom transfer radical polymerization
bb	Backbone
br	Branches
bob	Branch-on-branch
n-BuLi	*n*-Butyllithium
s-BuLi	*s*-Butyllithium
CCR	Convective constraint release
CFC	Chlorofluorocarbon
CLF	Contour length fluctuation
CMME	Chloromethyl methyl ether
CNT	Classical nucleation theory
CRP	Controlled radical polymerization
DB	Densely-grafted bottlebrush
DC	Densely-grafted comb
DE	Doi-Edwards (model)
DFS	Dynamic frequency sweep
DPE	1,1-Diphenylethylene
DSC	Differential scanning calorimetry
DSS	Dynamic strain sweep
DTD	Dynamic tube dilation/dilution; also DD: dynamic dilution
EVF	Extensional Viscosity Fixture
EPS	Expanded polystyrene
FC	Friedel-Crafts (acylation reaction)
FSR	Filament stretch rheometer
HCFC	Hydrochlorofluorocarbon
HFC	Hydrofluorocarbon
HER	Horizontal Extensional Rheometer
kDa	Kilodalton (1 kDa = 1 kg/mol)
LAOS	Large amplitude oscillatory shear
LB	Loosely-grafted bottlebrush
LC	Loosely-grafted comb
LDPE	Low density polyethylene
LCB	Long chain branches/branched/branching

LVE	Linear viscoelasticity, linear viscoelastic behavior
MALLS	Multi-angle laser light scattering
MAOS	Medium amplitude oscillatory shear
MeOH	Methanol
MSF	Molecular stress function (model)
Mt	Megaton, 1 million tons ($=10^9$ kg)
MTR	Münstedt Tensile Rheometer
MWD	Molecular weight distribution
NMP	Nitroxide-mediated radical polymerization
NMR	Nuclear magnetic resonance
Nu	Nucleophile, nucleophilic group
PB	Polybutadiene
PE	Polyethylene
PEOX	Polyethyloxazoline
PET	Polyethylene terephthalate
PI	Polyisoprene
PMMA	Polymethyl methacrylate
POM	Polyoxymethylene
PP	Polypropylene
PPF	Primitive path fluctuation
PS	Polystyrene
PS-Li	Polystyryl lithium (anionic PS chain with Li counterion)
PU	Polyurethane
PVC	Polyvinylchloride
RAFT	Reversible addition fragmentation chain transfer polymerization
RME	Rheometrics Melt Extensional rheometer
ROMP	Ring-opening metathesis polymerization
ROP	Ring-opening polymerization
SAOS	Small amplitude oscillatory shear
SBR	Styrene-butadiene rubber
SBS	Styrene-butadiene-styrene block copolymer, e.g. Kraton
sc	Supercritical
SEM	Scanning electron microscopy
SER	Sentmanat Extensional Rheometer
SCB	Short chain branches/branched/branching
SEC	Size exclusion chromatography
SHF	Strain hardening factor
SIS	Styrene-isoprene-styrene block copolymer
SLS	Static light scattering
THF	Tetrahydrofuran
TMEDA	*N,N,N',N'*-tetramethylethane-1,2-diamine
TTS	Time-temperature superposition
vGP	van Gurp-Palmen (plot), data plot of δ vs. $\lvert G^* \rvert$
VHC	Volatile hydrocarbon
VER	Volume Expansion ratio
WLF	Williams-Landell-Ferry (equation)

XPS	Extruded polystyrene
ZSV	Zero-shear viscosity

Physical Quantities

a	Tube diameter, deformed
a_0	Tube diameter in undeformed state
A	Area
a_T	Horizontal shift factor
b	Chain segment length
b_T	Vertical shift factor
c	Concentration (of sth.)
d	Diameter
d_cell	Cell size
De	Deborah number
$Đ$	Dispersity ($= M_\mathrm{w}/M_\mathrm{n}$)
f	MSF parameter
f^2_max	Maximum (steady-state) value of MSF parameter
F	Force
g_i	Relaxation strength
G	Shear modulus
G'	Storage modulus
G''	Loss modulus
G^0_N	Plateau modulus
$G^0_\mathrm{N,s}$	Diluted modulus
G^*	Complex modulus
$\lvert G^*\rvert$	Complex modulus, absolute value
$\lvert G^*\rvert_{\delta=\mathrm{min1}}$	Complex modulus at "local" 1$^\mathrm{st}$ minimum of the phase angle, δ, from the low towards high frequency region
$\lvert G^*\rvert_{\delta=\mathrm{min2}}$	Complex modulus at "global" 2$^\mathrm{nd}$ minimum of the phase angle, δ, in the high frequency region
k_B	Boltzmann constant ($= 1.38 \cdot 10^{-23}\,\mathrm{J\,K^{-1}}$)
m	Mass
M	Molecular weight
M_0	monomer molecular weight
M_c	Critical molecular weight
M_e	Entanglement molecular weight
M_n	Number average molecular weight
M_r	Reptation molecular weight
M_w	Weight average molecular weight
$M_\mathrm{w,bb}$	Weight average molecular weight of the backbone
$M_\mathrm{w,br}$	Weight average molecular weight of the branches
$M_\mathrm{w,lcb}$	Weight average molecular weight of the long chain branches
$M_\mathrm{w,scb}$	Weight average molecular weight of the short chain branches
n_bb	degree of polymerization of the backbone
n_br	degree of polymerization of the branches

N	Number (of sth.)
N_{ac}	Number of acetyl groups
N_{br}	Number of branches; used for the nomenclature of comb PS290 series (Chapter 5)
N_{cell}	Number of cells per unit volume, cell density
N_{lcb}	Number of LCB; used for the nomenclature of comb and bob PS310 series (Chapter 6)
N_{scb}	Number of SCB; used for the nomenclature of comb and bob PS310 series (Chapter 6)
O	Overlap parameter
O_{KN}	Kavassalis-Noolandi number ($\approx$ 10–20)
p	Pressure
p_{c}	Critical pressure (at critical point)
p_{max}	Maximum reactor pressure
P_{n}	Degree of polymerization
$\mathrm{p}K_{\mathrm{a}}$	Acid dissociation constant
R	Gas constant ($= 8.3144\,\mathrm{J\,K^{-1}\,mol^{-1}}$); Radius of sth. (specified when needed)
R_{b}	Bubble radius
R_{c}	Critical bubble nuclei radius
R_{g}	Radius of gyration
$S(\theta)$	Surface factor
t	Time
T	Temperature
T_{c}	Critical temperature (at critical point)
T_{g}	Glass transition temperature
T_{max}	Maximum reactor temperature
T_{ref}	Reference temperature
Tr	Trouton ration ($= \eta_{\mathrm{E}}^{+}/\eta_{\mathrm{S}}^{+} = 3$)
V	Volume
V_{e}	Elution volume
Wi	Weissenberg number
Z	Entanglement number
Z_{bb}	Backbone entanglement number
Z_{br}	Branch entanglement number
Z_{s}	Segmental entanglement number, number of entanglements between branch points
α	Dilution exponent
β	MSF parameter
γ	Surface tension
γ	Shear strain
γ_0	Deformation amplitude
$\dot{\gamma}$	Shear rate
δ	Phase angle
ε	Extensional strain

ε_{H}	Hencky strain
$\dot{\varepsilon}_{\mathrm{H}}$	Hencky strain rate
ζ	Friction
ζ_{a}	Arm/Branch friction
η	Viscosity
η_0	Zero-shear viscosity (ZSV)
η^*	Complex viscosity
$\lvert\eta^*\rvert$	Complex viscosity, absolute value
η^+_{DE}	Transient extensional viscosity (DE prediction)
$\eta^+_{\mathrm{DE,max}}$	Maximum transient extensional viscosity (DE prediction)
η^+_{E}	Transient extensional viscosity
$\eta^+_{\mathrm{E,max}}$	Maximum extensional viscosity (tensile stress growth coefficient)
η^+_{S}	Transient shear viscosity
π	pi (≈ 3.14)
ρ	Density
σ	Shear stress
σ_{ext}	Extensional stress, tensile stress
τ	Relaxation time
τ_{a}	Arm relaxation time
τ_{d}	Reptation relaxation time
τ_{e}	Entanglement relaxation time
τ_{R}	Rouse relaxation time
ϕ	Volume fraction
ϕ_{comb}	Volume fraction of comb
ϕ_{bb}	Volume fraction of backbone
ϕ_{br}	Volume fraction of branches
ϕ_{lin}	Volume fraction of linear chains
ϕ_{p}	Volume fraction of polymer
ω	Excitation angular frequency

Contents

1 Introduction

The success story of synthetic polymer foams concurs with the establishment of modern polymer science, that was fundamentally laid by the work of Hermann Staudinger about 100 years ago. Foaming as a complex process is majorly governed by the melt flow behavior, that originates from the macromolecular topology. The following section provides a brief introduction into the elucidation of the molecular structure-foam property relationship and highlights the challenges concerning its investigation. The motivation behind the research is presented as well as the the scientific approach that outlines the thesis topic.

Polymers undoubtfully belong among the most, if not the most versatile material groups and therefore are an indispensable part of a technologically developed world. From simple linear chains to structurally and chemically highly complex architectures, they offer almost infinite potential to shape our environment and tune material properties according to specific needs and purposes, that cannot be achieved with materials found in nature.
Even though naturally available and synthetic polymers always played a role in the human evolution and the rise of civilizations, with the use and modification of cellulose and natural rubber dating back to ancient times, polymer chemistry as an own scientific field only evolved in the 19th century.[1] However, major progress that sparked a new era were only made between the 1920th and 40th. One of the first driver was the understanding of the macromolecular physics of polymers that are not solely explainable by their chemical composition. The revolutionary concept of viewing polymers as chains of covalently linked molecules was steadily estabilshed in the scientific community.[2] The Second World War can be considered as another catalyst in polymer research. Increased material wear, scarcity due to limited access to natural polymer sources (e.g. natural rubber), and technological advancements fueled the development of synthetic alternatives.[1] New polymers and processing methods were discovered that further opened the field of application, and exceeded the use of metal or wood already within 30 years.[3,4]
Closely linked to this development, also the material sector of polymeric light-weight materials grew. Major milestones were the invention of thermoset foams with its biggest representative polyurethane (PU), and on the other hand the processing of thermoplastics, such as polystyrene (PS), into cellular materials.[4,5] From those early stages of foaming science, that were marked by the discovery of new, processable polymers into foams, a phase of technological development followed in the 1950s and 1970s. Processing methods like foam extrusion became more sophisticated, and the multitude of processing parameters

were controlled in order to tailor to the foamed product.[6] In consequence, innovative applications were found around the 1980s, and the quality and quantity of foams met criteria that made them suitable for further upening up new markets.[4]

Modern synthetic foams offer a broad spectrum of application that rely on one or more advantageous properties of the following: thermal insulation, shock absorption, compressibility, and light-weight construction while also providing mechanical stability.[4,6,7] Thus, contrary to the reputation of polymers as being environmentally problematic, their foams are indispensable and an integral part to save resources and energy.

The specific properties of polymer foams are dominated not only by the polymer type itself, but furthermore by the resulting cellular structure. Apart from the processing conditions, the foaming outcome is influenced by the macromolecular topology; an intrinsic property, that predetermines the melt flow in shear and elongation during foaming.[4,5,8] Melt strength is a necessary prerequisite in most processes, e.g. calendaring, deep drawing, fiber spinning or foaming in particular, that shape the polymer by elongation into uniform thin film or filament structures.[9,10]

Long chain branching (LCB) is especially known for providing melt strength in elongational flow.[9,11] Consequently, this material characteristic has been also found beneficial in foaming and is therefore exploited in the production of cellular materials from thermoplastics.[4,6,12] Higher melt stability reduces the cell wall rupture and coalescence of bubbles, resulting in higher cell densities and volume expansions. Therefore, the viscoelastic properties of polymers with LCB topologies are an important research topic, especially when it comes to foaming.[13–16]

The variation of the branching content modifies the rheological behavior of the melt and allows to investigate the impact of branching on the foam characteristics. The degree of branching usually originates from the following approaches:

a) Polymerization: The synthesis conditions ultimately decide about the chain growth mechanism of the monomer, that is based on the choice of initiators, (co)reagents and catalyst systems.[1] b) Post-polymerization modification: Reactive extrusion with free radical initiators or gamma-rays creates new covalent bonding sites.[2] c) Blending: Branched components can be mixed with linear ones.

Unfortunately, the majority of studies uses commercial grade polymers or branching methods that produce polydisperse, structurally ill-defined systems that are poorly characterizable. Thus, branching might be roughly quantified, but topological features like chain lengths and branching numbers, and their specific impact on foaming, especially in deformation during the bubble growth phase, remain unknown.

Several studies[13–19] previously compared the foamability of linear and LCB polypropylene (*i*-PP) and unanimously concluded that polymer melts of a higher branching content perform better with respect to a lower foam density, i.e. higher volume expansion ratio (VER), a more homogenous cell structure and smaller cell sizes. Simultaneously, the higher

[1] For example: Branched polyethylene (low density, LDPE) is produced radically, while linear PE (high density (HDPE) is catalytically polymerized. Divinyl compounds and "T"-reagents can introduce LCB in Polypropylene (PP) and polystyrene (PS) polymerization.

[2] Depending on the dose of radicals or irradiation, the chain structure can be modified from slightly branched to even crosslinked.

branched grades exhibit an increased strain hardening in elongational flow, indicating a higher melt strength that is important for bubble stability.

Gotsis et al.[20] modified linear PP into LCB PP by reactive extrusion with increasing amounts of peroxydicarbonates. While the processability of the extruded foams increased with radical reagent content, the induced strain hardening and foam properties suggested an optimum of branching beyond which the benefits of additional branching declined. However, this optimum could not be specified and correlations to molecular parameters are almost impossible to interpret if the molecular structure is basically unknown.

Using *i*-PP for the investigation of structure-property relationships reveals another disadvantage. Polymers of semi-crystalline nature, e.g. PE and *i*-PP, contribute another unknown parameter to this already multifactoral and complex topic, making it difficult to clearly separate between effects of branching and the presence of crystal morphologies or crystallization. Branching is known to disturb the chain conformation and promotes folding to finer crystallites, whereas larger spherulites are facilitated by linear chain conformations. Therefore, investigating the structure-property relationship of such melts of different degrees of branching – independently of their crystallinity – is nearly impossible. Especially when the foaming conditions are close to the melting points, both effects contribute to a great extent to the nucleation and bubble growth phases, and definite conclusions are difficult to draw.[21–25]

Just recently, Weingart et al.[26] compared the foam qualities of linear and branched extrusion processed *i*-PP, and found the linear PP performed significantly better in regard to low density, small cell sizes and a homogenous cell morphology[3]. In contrast to the scientific consensus of the origins of foamability, even though only the LCB PP indicated superior melt strength by its elongational performance, the linear one without any strain hardening superseded in every aspect of foam qualities. Those findings questioned "the legend of strain-hardening as a requirement for good foamability".[26] However, the authors explained the different result by a crystallization and gelation behavior that is more favorable for the linear *i*-PP when it comes to foam qualities in extrusion foaming.

Nevertheless, the presented findings emphasize the necessity to investigate the effects of topology alone on the basis of amorphous polymers, of which – up to date – only few studies can be found.

Liao et al.[27] generated LCB in commercial PS by reactive extrusion with peroxide and a multi-functional grafting agent.[4] Batch foaming with CO_2 and analysis of the cellular structure revealed a finer, more uniform cell morphology with smaller cell sizes and higher cell densities as compared to the foam made of linear PS. The improvements strongly correlated with the amount of grafting agent as well as the increase in strain hardening, even though the maximum strain hardening factor[5] was relatively small. They estimated the maximum number of branching points to about 1.6/1000 carbon atoms using rheological

[3] Linear *i*-PP foam had a density of $40\,\mathrm{kg/m^3}$ vs. $140\,\mathrm{kg/m^3}$ and an average cell diameter of 0.9 mm vs. 0.2mm, as compared to branched *i*-PP foam.

[4] GPPS with a molecular weight of $M_w \approx 200\,\mathrm{kg/mol}$ was used for reactive extrusion. The obtained LCB levels ranged from an average of 0.15 to 1.6 branching points per 1000 carbon atoms.[27]

[5] Those LCB PS samples showed a maximum strain hardening factor of SHF < 3 at $\dot{\varepsilon}_H = 1\,\mathrm{s^{-1}}$. For comparison, the SHF of LCB *i*-PP is rather found in the range of ∼5–50.

data and model predictions, but further structural information was not accessible due to the random grafting mechanism that assumingly resulted also in a mixture of three-arm star-like chains and unreacted linear PS.

1.1 Motivation

If the topology of a polymer influences the foaming outcome to a great extent – which is often demonstrated – there should be an optimized structure or a range of beneficial topological features that result in the best foamability for a set of given processing conditions (i.e. pressure, temperature, etc.). As the foaming process starts from the melt state of a polymer, the rheological properties can be considered as the mediator between the chain dynamics and the flow fields that occur during expansion until the cell structure solidifies. In that sense, rheology holds key information to elucidate the molecular structure-foam property relationship.
However, conclusions cannot be drawn if a crucial piece of the puzzle is missing, and that is information about topological parameters. The main issues arising in previous research to connect those parameters and their impact on the foaming behavior and final foam properties can be summarized as follows:

a) Structural heterogeneity: The use of commercial grade polymers with a high dispersity and the randomness of the grafting renders the characterization of the branching impossible. Structural information cannot be boiled down to a set of few, independently variable parameters like number, length and distance of branches.

b) Crystallinity: Branching and the formation of highly ordered islands of lamellae with the properties of physical crosslinking can have an interfering or overlapping effect on the chain dynamics in semi-crystalline polymer melts, especially when foaming temperatures are close to or approach the melting temperature. The variation in branching usually also changes the degree in crystallinity and both effects are hardly separable. This can affect both, the early nucleation, the bubble growth and the late cell stabilizing phase.

c) Impurities: Depending on the polymerization methods, commercial polymers often contain residual amounts of monomer, oligomeric low molecular weight fractions, catalysts, reagents, surfactants and processing agents[6]. Those impurities might change the nucleation mechanism or impair cell stabilization.

d) Not probing the limits with respect to the branching number/density: Branching in general is considered as beneficial for the resulting foam qualities. The existence of an optimum was suggested, but could not be specified. Adverse effects of branch crowding on the foamability are very likely, but sufficiently branched systems were not investigated so far.

[6] Common processing agents in commercial thermoplastic foam processing are fatty acid derivatives based on stearic acid, that act as permeability modifiers for physical blowing agents, decomposition modifiers for chemical blowing agents or surface modifiers to prevent bead agglomeration[5,8]

1.2 Research Objectives

The aim of this work is to contribute to the elucidation of the structure-property relationship, while simultaneously addressing the abovementioned challenges. The investigation of the influential parameters from the molecular level to the macroscopic level of the cellular structure includes:

- The synthesis of monodisperse model branched topologies on the basis of an amorphous polymer with means of polymerization methods that allows the best possible control towards well-defined structural parameters. Sufficient purification is a premise to exclude erroneous effects in the following investigations.
- The molecular characterization of the those stuctural features with regards to the respective chain lengths and number of branches.
- The full rheological characterization of the melt properties to understand the chain dynamics in shear and elongational flow fields that also occur in the stages of foaming, with particular interest on the bubble growth phase.
- The foaming of the model branched samples and the analysis of the microscopic and macroscopic foam properties.
- The correlation of the molecular structure with the foaming result, using the rheological fingerprint to determine influential parameters of the topology, and to propose a foaming mechanism based on the melt properties.

Since foaming is a multifactoral process that includes the intrinsic properties of the polymer melt, as well as the extrinsic conditions like pressure, temperature and depressurization rate, therefore, different outcomes can be achieved. For example, the focus of the investigation can be the optimization towards certain foam properties like high volume expansions (i.e. low foam densities) or small cell sizes. Both goals might necessitate different experimental approaches.
The here presented thesis is aimed to specifically study the strain hardening behavior of branched polymer topologies on the basis of well-characterized structural compositions. The foaming properties are investigated with the objective to optimize molecular parameters and processing conditions that promote foam expandability, resulting in low-dense foams.

1.3 Outline

Figure 1.1 gives a graphical representation of the thesis's content:

The fundamentals of the employed approach to synthesize model branched topologies are explained in **Chapter 2**, and comprise the anionic polymerization and grafting-onto methods to have best possible structural control over molecular parameters.

Shear and elongational rheology are very sensitive to branching, and therefore powerful tools to study *offline* the melt behavior that influences the bubble formation and cell growth. The basic principles are presented in **Chapter 3**, followed by a brief description of the underlying chain dynamics.

An overview of the complex topic of foaming and their application is given in **Chapter 4**. The stages of the foaming process are outlined and common technical implementations are presented. Due to their general economic relevance, but also central part of this thesis, polystyrene foams are more discussed in detail, leading then over to the practical part of the work.

Chapter 5 starts with the synthesis and characterization of a series of model long chain branched PS with comb topology and a broad range of branch densities from sparsely grafted comb to bottlebrush-like structure. Shear and extensional rheology provide information to correlate the resulting foaming properties to the number of branches that was the only parameter systematically varied in the synthesis.

Thereafter, **Chapter 6** introduces the synthesis of a series of dendrigraft PS. Based on data of the previous chapter, a long chain branched comb PS with structural features that promised optimized foam expandability was synthesized as a core. Further "branch-on-branch" (bob) grafting resulted in a corona of short chain branches. This kind of novel structure was further rheologically investigated. Extensional rheology, and comparison with short chain branches comb PS in particular, gave more insight into the dynamics of the bubble growth and the requirements of good expandability.

Chapter 7 exploits the set of previously synthesized comb PS samples from Chapter 5 and further extends the rheological investigation towards comb-linear PS blends – a topic of which up to date not much can be found in current literature. Different aspects of shear and extensional rheology are highlighted and give a promising outlook to enhance the current knowledge and molecular theories about the interplay between branched and linear chains.

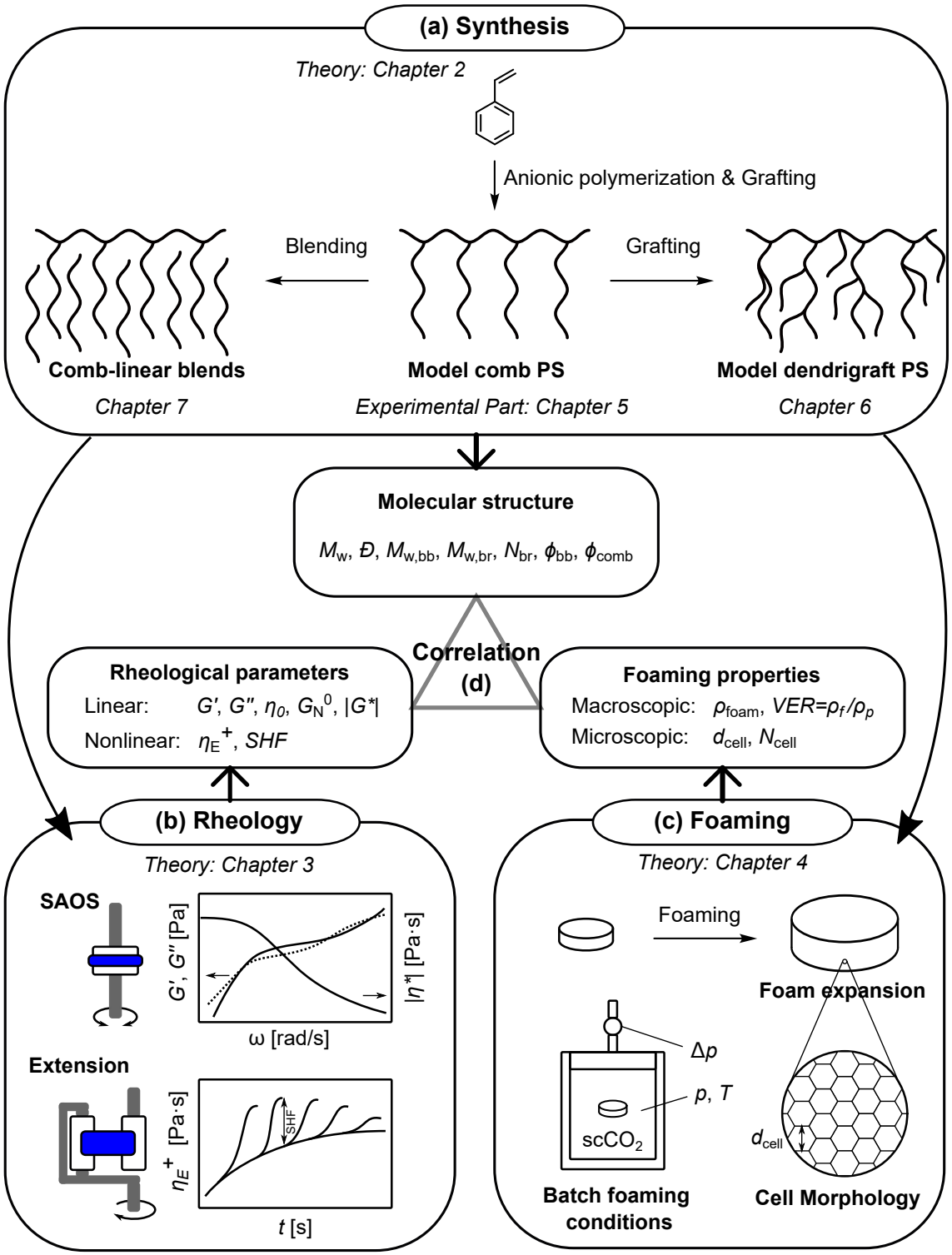

Figure 1.1: Schematic illustration of the outline of the thesis. **(a)** Synthesis and molecular characterization of model comb polystyrenes and model dendrigraft polystyrenes, as well as blending of comb PS with linear PS. **(b)** Rheological characterization in linear (SAOS) and nonlinear (extension) deformation. **(c)** Batch foaming with supercritical carbon dioxide ($scCO_2$) and investgation of the foam properties. **(d)** Correlation of molecular structure, rheological parameters and foaming properties.

2 Fundamentals of Model Branched Polymer Synthesis

The foundation of investigating polymeric structure-property relationships is the access to topological model systems. Defined molecular parameters enable to interpret the obtained measurement results and correlate the data to structural features. Depending on the polymer type and topology that is in the focus of interest, the appropriate synthetic methods have to be wisely chosen and to satisfy to be capable of molecular control and characterization.

The following chapter, therefore, is dedicated to introduce the synthetic foundation of the here presented thesis in three sections, each addressing a specific method, technique, or concept which were utilized in the scope of the conducted chemical work with specific focus on the here obtained model branched comb and dendrigraft polystyrene topologies.
Those are namely the anionic polymerization, the grafting-onto, and divergent synthesis.

2.1 Living Anionic Polymerization

The modern age of polymer science is considered to be founded by the work of Hermann Staudinger when in 1920 the first time it was proposed that polymers consist of long chains of repeating building blocks (monomer units) which are covalently bonded together, rather than being merely associated or aggregated molecules attracting each other by an unknown force.[2] This novel concept slowly gained wide acceptance in the scientific community. It was not only a prerequisite to understand the molecular nature and dynamic behavior of polymers, but also brought significant advances to polymer synthesis and polymerization mechanisms.[28]
Apart from his research field of coordinative polymerization and the development of catalysts for the synthesis of polyethylene (PE) and polypropylene (PP), Karl Ziegler[29] proposed an alkyl lithium initiated anionic polymerization mechanism for styrene and butadiene in the absence of chain transfer or termination.[28]
However, it was not until 1956 (3 years after Staudinger received the Nobel Prize in Chemistry for his advances in polymer science) when the technical requirements, i.e. the right choice and purity of monomer and solvents, for this challenging type of synthesis were met. Szwarc demonstrated the first anionic chain-growth polymerization by using an initiator system of sodium naphtalenide. In the presence of styrene, an electron transfer

occurred forming a styryl radical anion which subsequently dimerized to a dicarbanion and consumed the rest of styrene in a chain growth reaction.[30,31]

In the following years also alkyl lithium initiators were developed and more monomers suitable to undergo anionic polymerization were found. The utilization of 1,3-dienes and especially the discovery of *cis*-1,4-polyisoprene (PI) with its properties interesting for rubber industry sparked commercial interest in anionic polymerization methods despite the challenging aspects of the technical implementation for bulk production. However, this cost-intensive process also limits the use of anionically synthesized polymers to a niche market[7] where specific, high-performance properties cannot be achieved or substituted by materials that are produced in a more cost-efficient polymerization process like radical or coordinative polymerization. Compared to those methods, anionic polymerization enables the synthesis of polymers with defined chain length, high molar mass ($M_n > 1\,000\,\mathrm{kDa}$) and narrow molecular weight distribution (with dispersities, $Đ < 1.1$). Furthermore, one of the unique applications of living polymerization techniques is the controlled synthesis of sequential block copolymers.[35]

The propagating species is an anion as active center, see **Figure 2.1**, and the polymerization is characterized by the absence of termination or chain transfer reactions. When all monomer is consumed, the chain ends maintain their reactivity and are able to continue the polymerization when new monomer is added. Thus, the anionic polymerization belongs to the group of "living" polymerization methods. However, the presence of impurities (e.g. traces of humidity, oxygen, or carbon dioxide) or the addition of terminating agents (e.g. protic methanol, MeOH) leads to a deactivated chain. Therefore, achieving a high molecular weight and low dispersity demands a high purity of monomers, solvents, and initiators. The application of Schlenk techniques with high vacuum and inert gas system, as well as the distillation of all reagents is the foundation of synthetic work in the chemical laboratory.[36]

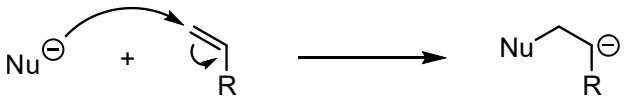

Figure 2.1: The polymerization is initiated by a nucleophilic (Nu) addition to the double bond of the monomer. The negative charge is transferred to the chain end which keeps the nucleophilic character and is able to propagate the reaction.

2.1.1 Monomers

The restriction in the choice of monomers results from the high basicity of the chain propagating anion. Substituents that are protic or with high relative protic activity – which can be evaluated by the pK_a value – are an exclusion criteria for monomers.[37] Another disqualifying criteria are functional groups with strong electrophilic properties like halogens

[7] For 2009, an annual, woldwide commercial production of 3 million tons (Mt) is reported for anionic polymerization (mostly PB, PI, SBR, SBS and SIS), compared to a total polymer volume of 230 Mt.[32] For 2018 a total polymer production volume of >350 Mt is reported,[33] compared to 0.7 Mt of anionically synthesized thermoplastic multiblock copolymers and about 1 Mt of anionically synthesized elastomers. Oxyanionic polymers make up another several Mt per year.[34]

or carbonyls. For these reasons, the direct polymerization of acrylic acid[8] and vinyl halides is impossible. The synthesis of poly acrylates can only be conducted at low temperatures to decreases the reactivity towards a nucleophilic attack at the carbonyl group.[38]
The capability of a vinyl monomer to undergo anionic polymerization is governed by its stabilization of the forming carbanion by substituents (–R) withdrawing electron density from the active center. The more pronounced the -I/-M effect in vinylic compounds (H_2C=CHR), the more reactive and faster the chain propagation is happening. Therefore, double bonds, aromatic rings, ester, and cyano groups are suitable substituents as they stabilize the negative charge, see **Figure 2.2**.[36]

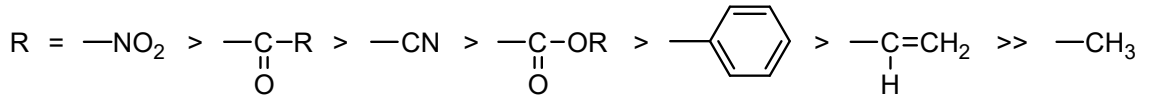

Figure 2.2: Influence of substituents (–R) on the reactivity of vinylic monomers in order of decreasing carbanion stabilization, i.e. decreasing -I/-M effect.[39]

Furthermore, ring-opening polymerizations of heterocyclic structures are possible. Common examples are epoxides (e.g. ethylene oxide, propylene oxide), cyclic esters (lactones) and amides (lactams), see **Figure 2.3**. Chain growth polymerization of carbonyl compounds, i.e. the synthesis of polyacetals is also conducted anionically and is utilized for the production of polyoxymethylene (POM).

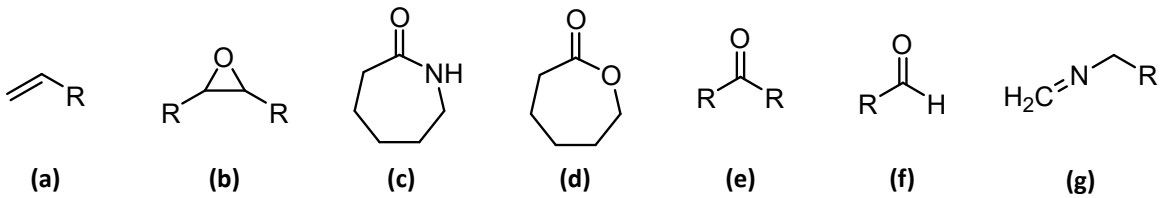

Figure 2.3: Examples of monomer functionalities that are able to undergo anionic polymerization: **(a)** vinylic monomers: diene, styrene, acrylonitrile, alkyl acrylates; **(b)** epoxides; **(c)** lactams (e.g. ε-caprolactame); **(d)** lactons (e.g. ε-caprolacton); **(e)** ketones; **(f)** aldehydes; **(g)** isocyanides.[40]

2.1.2 Initiation

The anionic polymerization is initiated by bases and Lewis bases, including organometallics like alkyl lithium or Grignard compounds, but also alkali metal amides and alkoxides. The initiation mechanism depends on the type of initiator system. The most common example is the direct addition of a strong nucleophilic Lewis base such as (*n*-, *s*- or *t*-)butyl lithium to the C=C double bond, as shown in **Figure 2.4**. Those are commercially used and work well with economically important monomers like styrene, 1,3-butadiene and isoprene, as at the example of styrene and *s*-butyl lithium.[41]

[8] The synthesis of acrylic acid via anionic polymerization is still indirectly possible via the *t*-butyl ester and subsequent saponification.

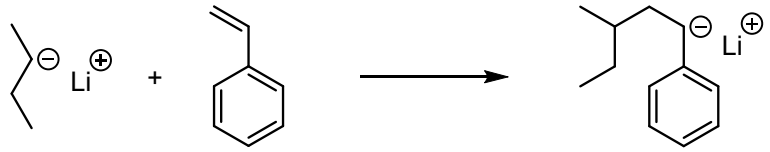

Figure 2.4: Initiation reaction via alkali metal organyl on the example of *s*-butyl lithium and styrene. Depending on the anion concentration and the solvent, a light yellow to deep orange or even red-orange color is characteristic for the presence of living PS in the solution and is an indicator of a successful initiation.

One of the prerequisites of the anionic polymerization in terms of low dispersity is a fast and quantitative initiation starting the chain growth. Only then the kinetic conditions (as discussed in more detail in **Section 2.1.6**) are fulfilled to successfully achieve a narrow molecular weight distribution. This requires the strength of the initiator to be chosen according to the electronegative nature of the substituent (–R): The higher the electronegativity, the more pronounced is the electron withdrawing effect from the double bond and the easier it is for a base to attack the positively polarized β-carbon atom of the double bond. Vice versa, a weak -I/-M effect of the substituent, like induced by the phenyl ring of styrene, requires strong bases like lithium organyls or potassium amides to be able to add to the monomer double bond.[42]
On the other hand, styrene has a high electron affinity that makes it very susceptible for electron transfer reactions so it can be easily initiated by aryl alkali metal compounds.[41] This method, originally found and utilized by Szwarc[30], enables bifunctional chain growth, see **Figure 2.5**, and therefore enhanced the topological spectrum of achievable polymer architectures, for example towards ring polymers or highly symmetric block copolymers.[43]

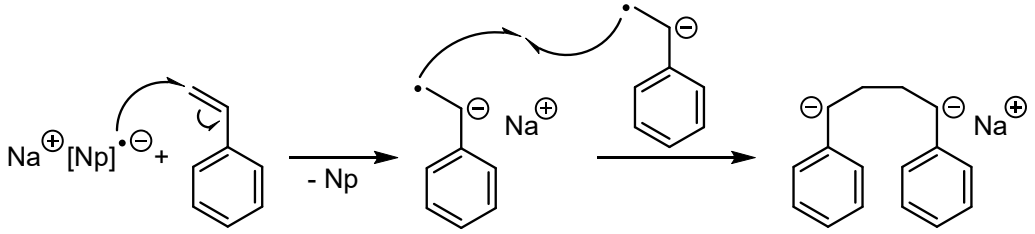

Figure 2.5: Initiation reaction via electron transfer from sodium naphthalenide (NaNp) to styrene. Radical anions are formed which immediately dimerize to dianions. Upon initiation, the dark green color of NaNp turns into the characteristic orange-reddish color range indicating living PS anions.

Ring-opening polymerizations require less strong bases. Grignard- and alkoxide-based initiators for epoxide polymerization or alkali metal hydroxides and alcoholates for the polymerization of lactams (e.g. ε-caprolactam) are sufficient.

2.1.3 Propagation

After initiation, the chain continues to grow by addition of further monomers to the chain end, as shown in **Figure 2.6**. Ideally, all chains grow at the same rate, and the degree of polymerization increases linearly with conversion. Compared to radical polymerization, termination through recombination is not possible due to the electrostatic repulsion of the negatively charged chain ends.

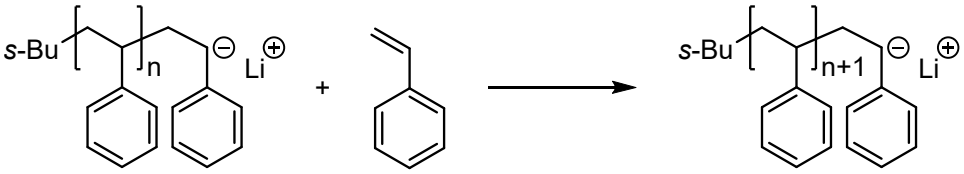

Figure 2.6: Chain propagation via monomer addition on the example of styrene polymerization. The speed of monomer consumption not only depends on the concentration of the reactive species but is majorly governed by the influence of the solvent, see **Section 2.1.5**.[39]

In the ideal case, also no side reactions like proton abstraction occur, and therefore the concentration of the active centers equals the initiator concentration from the beginning, $[I]_0$. So the degree of polymerization, $P_\mathrm{n}(t)$, at each time, t, can be easily estimated by the amount of monomer consumed, $([M]_0 - [M]_t)$, using **Equation 2.1**.[44]

$$P_\mathrm{n}(t) = \frac{[M]_0 - [M]_t}{[I]_0} \tag{2.1}$$

If the polymerization time is sufficiently long and full conversion is achieved ($[M]_t \to 0$), Equation 2.1 can be simplified to **Equation 2.2**.
Consequently, the degree of polymerization can be predicted by the initial concentration of reagents allowing the precise synthesis of polymers with specific average molecular weight.[45]

$$P_\mathrm{n} = \frac{[M]_0}{[I]_0} \tag{2.2}$$

When all monomer molecules are consumed, the propagation stops, and the chains keep their active centers. The living anions can be terminated or the polymerization can be continued at any time by adding further monomers. If a different monomer type is added to the reaction mixture, block copolymers with specific block orders can be achieved.

2.1.4 Termination and Side Reactions

Termination of the chain ends occurs by deactivation of the anions which can be done intentionally by simply adding proton donating agents like methanol, as shown in **Figure 2.7**.

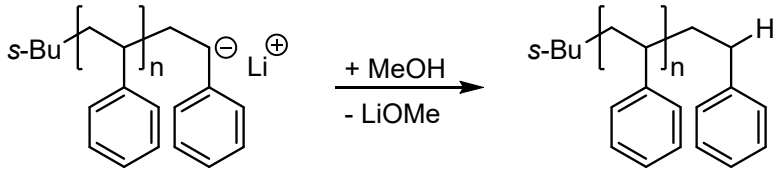

Figure 2.7: Termination of living PS anions via proton transfer. Typically, degassed methanol (MeOH) is added, which is miscible in all organic solvents that are used in anionic synthesis. Lithium methoxide (LiOMe) will immediately decompose to LiOH and MeOH when in contact with traces of water.

However, terminations are also caused by residual moisture on glassware, air humidity, oxygen, or carbon dioxide as shown in **Figure 2.8**. Like methanol, water will lead to a proton transfer, deactivating the chains, see **Figure 2.8b**).

The reaction with carbon dioxide will result in a carboxylic endgroup. When dry, gaseous carbon dioxide is introduced to the living polymeric organolithium solution, the chain ends can be even functionalized deliberately, as shown in **Figure 2.8b**.[46] More generally, end-capping provides a versatile way of forming macromonomers which can be used in subsequent coupling or polymerization reactions to build various topologies, as addressed in **Section 2.2**.

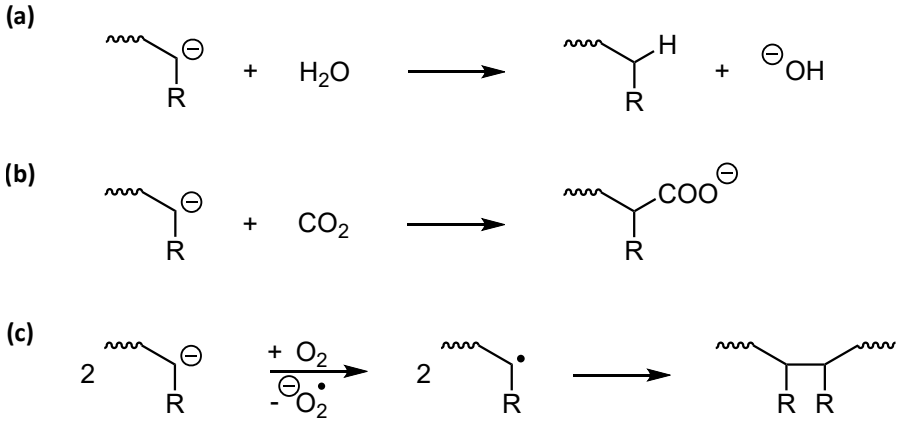

Figure 2.8: Termination reactions with **(a)** water via proton transfer, **(b)** carbon dioxide via nucleophilic addition, and **(c)** oxygen via dimerization of chain-end radicals as the major termination pathway.[47]

Oxygen leads to several side reactions due to the radical nature of the termination mechanism. As a result, simple chain deactivation but also chain recombination will occur as major termination pathways, see **Figure 2.8c**.[48] The chain coupling will increase the chain length and is most often noticed in the SEC chromatogram as a peak shoulder having exact the double average molecular weight. Therefore, even after the polymerization is finished, prior to quenching the reaction, every terminating or telomerization agent (e.g. methanol, carbon dioxide, etc.) has to be deoxygenated (degassed) to avoid broadening the molecular weight distribution.

2.1.5 Solvent Influence

Like the monomers, also all solvents have to be aprotic and inert against nucleophilic agents. Apart from its role as diluent for heat control and solvating agent for reactants, the solvent properties play an important role in the reaction kinetics.
The anionic base with the metal counterion act as ion pairs and the strength of interaction mainly depends on the type and size of counterion. Small ionic radii like lithium facilitate close proximity to the anionic active center, thus favor partial covalent bond character. Cations with bigger radii like potassium are more separated and therefore the bond tends to have the nature of loose or free ion pairs.

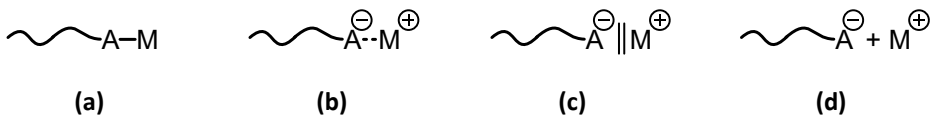

Figure 2.9: Range of ion pair interaction between polymer anions (A) and metal (M) counterions: **(a)** covalent, **(b)** tight contact, **(c)** solvent-separated/loose, and **(d)** highly solvated/free.

The polarity of the solvent interacts with the ion pairs and has a major impact on the aggregation and association of the contact ion pair. The spectrum of interactions between those ion pairs is exemplarily shown in **Figure 2.9**. Reactions in nonpolar hydrocarbon solutions (e.g. cyclohexane, toluene, benzene) shift the equilibrium more towards aggregate formation and the charge separation is energetically disfavored due to a low dielectric constant. In contrast to that, polar solvents like tetrahydrofuran (THF), can break up the aggregates and form solvated ion pairs, highly increasing the reactivity of the "naked" anion as it's easier for the monomer to insert. Consequently, the initiation and propagation rate is increased. One possibility to increase the propagation rate in the presence of nonpolar solvents is the use of solvating Lewis bases like tertiary amines, glycol, or crown ethers or cryptands, shown in **Figure 2.10**, which strip away the counterion.[41]

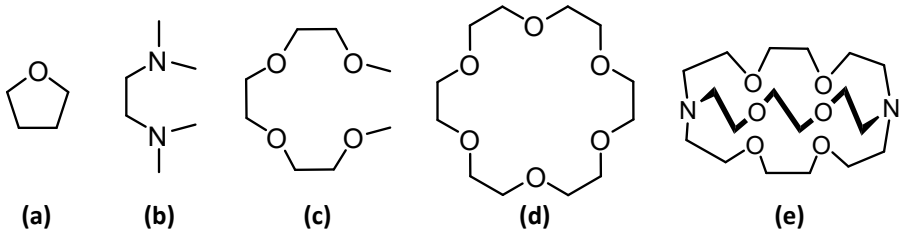

Figure 2.10: Examples of common solvents: **(a)** THF; and solvating agents: **(b)** *N,N,N',N'*-tetramethylethane-1,2-diamine (TMEDA), **(c)** triethylene glycol dimethyl ether (triglyme), **(d)** 18-crown-6, and **(e)** [2.2.2]-cryptand, with good ability to dissociate counterions and form solvent-separated ion pairs to increase the reactivity of the propagating species.

2.1.6 Kinetics and Molecular Weight Distribution

Ideal anionic polymerization kinetics are based on the following fundamental assumptions. Any polymerization mechanism that meets these conditions can be considered as "living":[39,44]

1. The initiation step is much faster than the chain propagation ($k_i \gg k_p$). The initiator is immediately and stoichiometrically consumed. All chains start at the same time.

2. All chains propagate under the same conditions. For the individual chain, the propagation rate is independent of the molecular weight. Therefore, the chains are kinetically identical.

3. The number of growing chains remains constant throughout the polymerization. There is no chain transfer or termination reaction. The active centers remain at the chain end.

4. The chain propagation proceeds until the monomer is fully consumed or the polymerization is intentionally quenched.

If all initiated chains have statistically the same propagation probability within the same time, it can be proven that the probability function $P(n)$ to find a polymer molecule with chain length n can be expressed as a Poisson distribution according to **Equation 2.3**, with the kinetic chain length ν or the number average degree of polymerization P_n (since $\nu = P_\mathrm{n} - 1 \approx P_\mathrm{n}$ for high P_n), as the expectation value which is determined by the monomer-initiator ratio (see Eq. 2.2).[44,45]

$$P(n) = \frac{(P_\mathrm{n} - 1)^{n-1} \cdot \exp(1 - P_\mathrm{n})}{(n-1)!} \tag{2.3}$$

Therefore, the molecular weight distribution of the living anionic polymerization is extraordinarily narrow and the dispersity converges to $Đ \to 1$ for high degrees of polymerization, shown in **Equation 2.4**.[49]

$$Đ = \frac{M_\mathrm{w}}{M_\mathrm{n}} = 1 + \frac{P_\mathrm{n}}{(P_\mathrm{n}+1)^2} \approx 1 + \frac{1}{P_\mathrm{n}} \qquad \text{for high} \quad P_\mathrm{n} \tag{2.4}$$

Experimental dispersity values measured via size exclusion chromatography (SEC) are mostly in the range of $Đ = 1.01$–1.10 and therefore higher than theoretically predicted. It should be noted that – apart from possible improper handling and insufficiently clean polymerization conditions – the SEC method suffers from a not insignificant band broadening to even resolve this narrow distribution. However, Lee et al.[50] could show via temperature-gradient interaction chromatography (TGIC) on anionically synthesized PS, that for high degrees of polymerization low dispersities of $Đ < 1.01$ close to the true expectation value are possible, whereas SEC overestimated dispersity values due to the band broadening effect. They also concluded that any additional broadening came from nonideal factors in the initial polymerization stage.

Furthermore, due to the reactivity of the anions, even the presence of traces of impurities, involuntarily introduced by diffusion through sealings, insufficient purification of reagents, or improper preparation and handling of Schlenk flasks, but also chain transfer as well as uneven stirring or temperature effects might contribute to the molecular weight broadening under real polymerization conditions.

2.2 Synthetic Strategies for Model Comb Polymers

Comb polymers are macromolecular topologies at which several (three or more) linear side chains, also called branches, are covalently attached at various trifunctional[9] branch points to a polymer backbone. Typically, all side chains are identical in length, that means the branches have the same degree of polymerization with low dispersity. In their most simple architecture, backbone and branches consist of the same type of monomer and are referred to as comb homopolymer. In contrast, graft copolymers are made of backbone and branches having different chemical composition.

[9] In case of quadrifunctional branch points, the topology is usually referred to as “barbwire”.

Comb polymers can be defined by three structural parameters: the molecular weight of the backbone, $M_{w,bb}$, and branches, $M_{w,br}$, as well as the number of branches, N_{br}, that further determines the distance between branch points.[36,51]
In an ideal comb macromolecule, the branch points are equidistantly spaced along the backbone with the same segment molecular weight, $M_{w,s}$, between branches. However, up to date few examples of such "exact" combs with regularly spaced branches have been achieved by different synthetic approaches.[52–64] Controlling the branch position is still the most challenging parameter. The biggest disadvantage of these methods is the high synthetic effort, involving the stepwise iterative integration of each junction point, the requirement of perfect stoichiometry or isolation of byproducts.[36,65] As a result, the synthesis of exact combs with more than ca. 10 sidearms is practically not feasible.
Therefore, for studying the rheological properties of model comb polymer architectures across the full range of grafting densities from sparsely to densely branched or even bottlebrush-like structures, the synthetic approach relies on conventional grafting methods. These methods result in an average number of side chains, N_{br}, randomly attached and therefore statistically distributed along the backbone.

In general, three main strategies for the synthesis of comb-shaped molecular structures exist, called grafting-through, grafting-from, and grafting-onto method.[36,37] All of these grafting methods can be utilized in combination with a wide variety of other living (e.g. ionic, RAFT, ATRP, NMP, ROP) or non-living (e.g. ROMP) polymerization techniques and coupling mechanisms (e.g. addition, substitution, cycloaddition, etc.) to exploit their synthetic strengths and to nearly infinitely expand the spectrum of sophisticated structural and chemically functionalized compositions with unique properties.[66,67]
The following sections will illustrate the basic concepts of those methods with specific focus on living anionic polymerization to achieve the synthesis of high molecular weight homopolymer comb PS.

2.2.1 Grafting-Through

The grafting-through method (also called macromonomer method) makes use of the possibility to copolymerize monomers with different side groups but same vinylic moieties (H_2C=CH–) that can undergo anionic polymerization. If the monomer's side group consists of a polymer chain, it is called macromonomer and can be incorporated during chain growth of the backbone structure like a regular monomer compound,[36] see **Figure 2.11**.

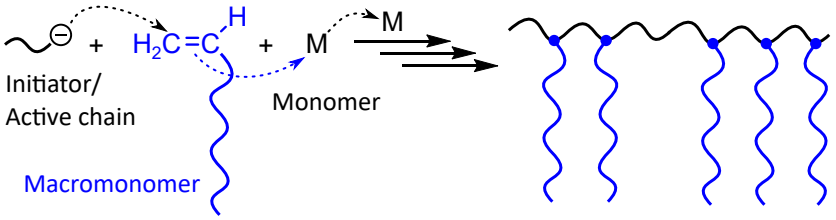

Figure 2.11: Grafting-through method. Macromonomers are copolymerized in a matrix of monomers. Due to the living character, the branches can be incorporated in one reaction or stepwise.

The branching density of the final comb polymer depends on the ratio of macromonomer and monomer. However, using this method successfully for an even or random distribution of side chains along the main chain requires a thorough understanding of the copolymerization parameters of all monomeric reactants. This is especially important when it comes to anionic polymerization which is highly affected by charge effects and their solvating environment as compared to radical mechanisms. Mismatched copolymerization parameters and to some extent steric hindrance effects of the macromonomer precursors might result in a gradient of branch point spacing. Therefore, the introduction of controlled radical polymerization (CRP) methods – which on the flipside do not allow very high molecular weights – is advantageous over ionic mechanisms in the case of grafting-through.[67] To gain more control over side chain location in anionic polymerization processes, the synthesis can be conducted by sequential macro-/monomer addition or DPE end functionalization to inhibit macromonomer homopolymerization, which however on the downside increases the synthetic effort.[66] On the other hand, the macromonomer method does not require fractionation as all reagents should have been incorporated into the final comb polymer already upon termination. One major disadvantage of the grafting-through method is that the characterization turns out to be challenging as only one parameter, the macromonomer length with $M_{w,br}$ is certainly known.

2.2.2 Grafting-From

In the grafting-from method, active anionic centers are introduced along with a precursor polymer backbone. These centers serve as initiators, each of them able to start a chain propagation. The branches then grow *in situ* outwards in the presence of monomers,[36] see **Figure 2.12**.

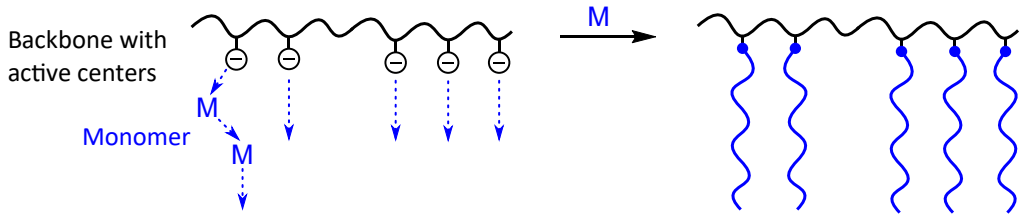

Figure 2.12: Grafting-from method. The backbone is functionalized with active centers and the branches are formed in *in situ* growing outwards during chain propagation with the monomer.

Formation of carbanionic centers that react with vinyl monomers requires C-H bond functionalization via organometallic compounds.[62] Metalation agents, e.g. *s*-BuLi, in combination with a strong, chelating base, e.g. TMEDA, are able to deprotonate allylic, benzylic and aromatic protons of the backbone.[68–70] Side chain growth by ring opening polymerization, e.g. of epoxy monomers, can be initiated by less strong nucleophiles. Backbone alcohol, phenol or amide protons are acidic enough to be removed by bases like potassium *tert*-butoxide or lithium diisopropylamide.[36,66,71–73]

The grafting-from method comes with several major disadvantages making it the least reliable approach for model branched polymer synthesis. As the side chains are initiated *in situ* and cannot be analyzed separately in terms of molecular weight or dispersity, the

exact branch length is unknown and can only be back-calculated indirectly by the total molecular weight of the final comb polymer, but missing the distribution information of the branches. Moreover, as the side chain polymerization often initiates slowly, the molecular weight distribution of the branches is expected to be broader than compared with other grafting techniques. In principle, the grafting can result in few long chain branches (LCB) or many short chain branches (SCB), hardly distinguishable with common characterization methods like SEC or NMR, making important structural information like grafting yield, branch length and branch molecular weight distribution basically not accessible, let alone planning for specific topological features nearly impossible.[67]

2.2.3 Grafting-Onto

The grafting-onto method, exemplarily shown in **Figure 2.13**, makes use of the nucleophilic behavior of the living polyanions to undergo addition or substitution reaction. The backbone precursor can be post-polymerization functionalized with haloalkyl[74–80], carbonyl[81–84], chlorosilyl[85–91] or epoxy[92–94] groups, that offer suitable electrophilic sites for the grafting reaction with readily polymerized living side chains.[36,66]

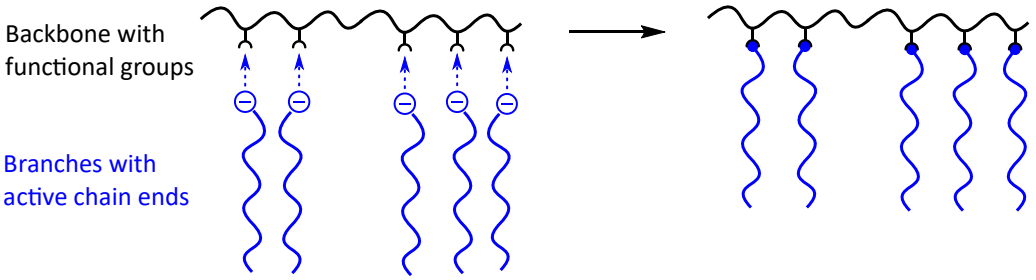

Figure 2.13: Grafting-onto method. The polymerized branches with living chain ends attach to the functionalized backbone in a nucleophilic addition or substitution reaction.

The main advantage of the grafting-onto method is the synthesis of the main chain and branches in separate reactions allowing the independent characterization of the molecular weight and dispersity of each chain component. Therefore, structural parameters like the branch and backbone lengths can be well-controlled. The average branching density, as the only unknown structural information, can be indirectly accessed either by back-calculation from the total molecular weight, or the analysis of the changes of functional groups before and after the reaction.[36,67]

With increasing grafting density the steric barriers for additional side chains increase, lowering the reaction rate or grafting yield of the final branched polymer. Therefore, usually an excess of living side chains is used to partially compensate this effect bringing the side benefit that the grafting-onto reaction is less sensitive against residual impurities in solvent or backbone polymer. However, after termination of the reaction the residual unreacted side chains have to be removed from the raw product by fractionation which adds further purification steps before obtaining the final polymer. Nonetheless, due to the fully characterizable structure of comb and dendrigraft polymers (see the following **Section 2.3**) by means of the grafting-onto approach, this method arguably offers the most reliable

method to synthesize defined model branched systems and study their structure-property relationship.

2.3 Synthetic Concepts towards Dendrigraft Polymers

Since the early pioneering work of Vögtle, Tomalia and Frechét, polymers with cascade-branched structure have evolved from academic interest to sought-after materials for modern application utilizing their unique properties originated from their spatial architecture in combination with their versatile functionality.[95]

2.3.1 The Dendritic Polymer Family

Dendrigraft polymers, as well as dendrimers and hyperbranched polymers, belong to the family of dendritic polymer architectures[10], as exemplarily illustrated in **Figure 2.14**. They are characterized by a multilevel cascade-branched structure, synthesized "under more or less strictly controlled polymerization conditions".[99,100]

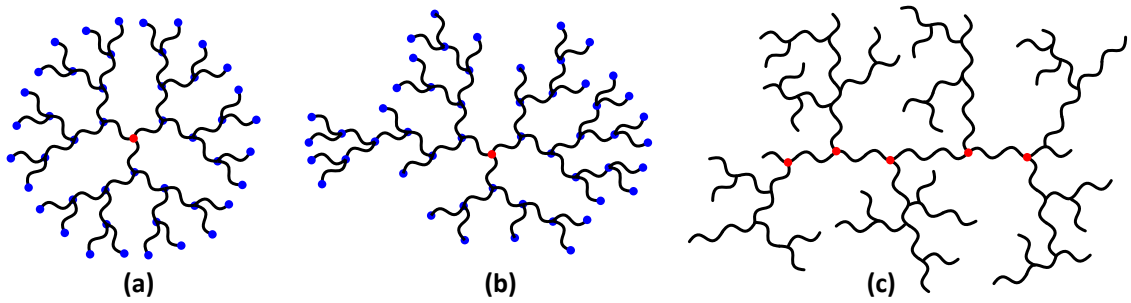

Figure 2.14: Dendritic polymer architectures: **(a)** dendrimer, **(b)** hyperbranched polymer, and **(c)** dendrigraft polymer; adapted from Teertstra et al.[99] Whereas for dendrimers and hyperbranched polymers the branching extends from one focal point (●), and the branch point distances and functionalities are well-defined on a monomeric scale (●), dendrigrafts possess several focal points along a polymeric backbone chain with more random branch point spacing.

From the here presented three categories, dendrimers, **Figure 2.14a**, have the highest structural control, attained by using defined small molecule AB_n-type monomers as building blocks stepwisely assembled in many controlled reaction cycles. Therefore, the molecular weight of each grafting level is exactly predictable and not only extremely narrow molecular weight distributions ($Đ < 1.01$) can be achieved, but also the framework with regular branching and end group number as well as branch point distance is considered as monodisperse.[97,99]

The macromolecular properties of dendrimers, as well as dendrigraft and hyperbranched polymers, are roughly summarized in **Table 2.1**, that lists the major tendencies and basic structural differences.

[10] The here mentioned architectures represent basic structural principles of the dendritic family. However, the list is not exhaustive and the architectural concepts comprise partial and hybrid structures.[96] For a more extensive overview and detailed explanation will be referred to further literature.[97,98]

Table 2.1: Major tendencies of structural characteristics of the dendritic polymer family (see Figure 2.14), summarized in a simplified manner.[98,99].

	Dendrimer	Dendrigraft	Hyperbranched
Branch units	monomeric [a]	polymeric	monomeric
Framework	monodisperse	polydisperse	polydisperse
Synthetic control	strict	semi	statistical
Dispersity, $Đ$	1.00 – 1.05	1.1 – 1.5	>2 [b]
Entangling ability	no	substancial	little to no

[a] Dendrimer-like topologies with polymeric units have also been reported in literature.[101]

[b] Low conversions: $Đ \approx 2$ (Flory distribution); high conversions: $Đ \to \infty$ (increased structural flaws)

Hyperbranched polymers, **Figure 2.14b**, are on the other end of the dendritic spectrum. Their synthesis is less complex and often performed as self-condensation in a one-pot reaction. Even though AB_n-type monomers are used for dendrimer synthesis, the random step-growth process leads to many structural flaws, especially with increasing conversions. The result is a polydisperse framework in terms of branching structure, but also with regard to the molecular weight distribution that exceeds the Flory distribution ($Đ \geq 2$) at higher levels of conversion.[98,99,102,103]

Dendrigraft polymers, **Figure 2.14c**, exhibit semi-structural control and therefore can be considered as intermediate between dendrimers and hyperbranched polymers, where the framework itself is polydisperse, i.e. the branch points are statistically distributed. However, the polymer still has a relatively narrow MWD ($Đ \leq 1.5$) despite the fairly random branching order.

A main feature that distinguishes dendrigrafts from dendrimers or hyperbranched polymers is the size of the branching segments. Whereas the latter are synthesized from relatively small multifunctional molecules and grow exponentially in molecular weight with each additional branching level, dendrigraft polymers are composed of polymeric side arms as building blocks. The extended branch segment lengths allow for a high branching multiplicity, i.e. number of higher-level chains per precursor branch, while simultaneously the branching density can be low enough to strongly entangle with other dendrigraft molecules. Due to their macromolecular build-up, very high molecular weights reaching 10^8 g/mol can be achieved in only 2–4 grafting steps.[99]

In contrast, even with low branching multiplicity for dendrimers (about 2–3) and hyperbranched polymers (about 1–2), the tight spaces of branch segments on monomeric level and fast-growing number of space-occupying branch ends will rapidly converge to a spherical or ellipsoidal superstructure, resulting in little to no room for entanglement interaction.[9] As a consequence, dendrimers and other highly densely branched topologies are in principle not employed where melt or mechanical strength is a key property, but rather where their low viscosity, end group functionalization, and almost endless possibility for chemical modification are in the focus of interest for large-scale applications, e.g. processing agents, coatings and biomedical technology.[103]

2.3.2 Synthetic Methods towards Multilevel Branching

For the synthesis of such topologies with cascade-branched structure, two different main strategies have evolved, called "divergent" or "convergent" approach, that describes the way to build the branching levels from inside outwards or from outside inwards, respectively, as schematically shown in **Figure 2.15**.

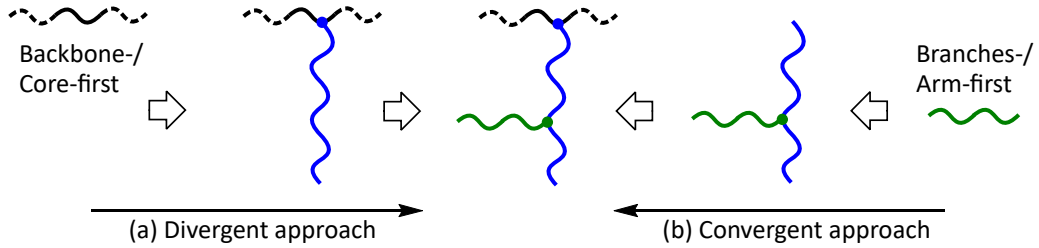

Figure 2.15: Simplified representation of strategies for the controlled synthesis of dendritic, multilevel branched polymers using successive grafting reactions: **(a)** Divergent or "core-first" approach, starting with the inner layer and building the branches outwards. **(b)** Convergent or "arm-first" approach starting with the outermost layer of branches and grafting inwards.

Either of those strategies can be combined with the grafting-onto, -through or -from method, with the latter suffering from significant disadvantages due to sterical hindrance, as already discussed in **Section 2.2.2**.
Apart from that, also other approaches and hybrid strategies have been realized, like the "double-stage convergent" or "double-exponential" growth as a strategic combination of divergent and convergent growth in one synthetic route.[97]

As the focus of this thesis is the utilization of entanglement properties of dendritic structures, the synthetic concepts of divergent and convergent synthesis are discussed with specific emphasis on dendrigraft polymers.

2.3.2.1 Divergent Approach

The first two syntheses of dendrigraft-type polymers were reported almost simultaneously in 1991 and followed a divergent grafting-onto strategy, both with the same principle: A linear backbone served as core and the functionalization with reactive groups and subsequent coupling with living chains yielded in a comb-like topology. The functionalization and grafting were successively repeated leading to higher-generation branched structure.[100]
The preparation method, reported by Tomalia et al.[104] involved the cationic polymerization and grafting of polyethyloxazoline (PEOX) onto a linear polyethylenimine substrate. After deacylation of the amide group, the grafting cycle was repeated yielding in multilevel branched Comb-burst® polyethylenimines.
A different approach was published in the same year by Gauthier et al.[77] who applied living anionic polymerization techniques to graft 1,1-diphenylethylene (DPE) endcapped polystyryllithium onto randomly chloromethylated polystyrene precursors. Successive cycles of functionalization and grafting resulted in higher generations of arborescent homopolymer polystyrenes.

Later modification of this method replaced the chloromethylation step with its hazardous and expensive reagents, i.e. chloromethyl methyl ether and carbon tetrachloride, by a Friedel-Crafts acylation with acetyl chloride in nitrobenzene. This changed the reaction mechanism in the grafting step from a nucleophilic substitution of chlorine to an addition reaction to the carbonyl group of acetylated PS phenyl rings. Endcapping of the living polystyryllithium with isoprene or 2-vinylpyridine attenuated the basic character of the anions and increased the yield from ca. 60% to over 90% by reducing the competing proton abstraction and enolate formation at the neighboring α-carbon atom. The work of Li and Gauthier[81] has successfully introduced this combination of Friedel-Crafts acetylation and anionic polymerization techniques as a straight forward method to synthesize relatively well defined dendrigraft-type homopolymer polystyrenes.

For this reason, the chemical work of this thesis resorts back to the abovementioned synthetic route and extends this abovementioned grafting-onto technique, previously introduced to the workgroup of Prof. Manfred Wilhelm by the work methods of Kempf[105] and Riazi[106], to synthesize a novel series of comb PS from sparsely to densely branched, bottlebrush-like structures, as well as branch-on-branch (bob) PS with dendrigraft-type architecture.

2.3.2.2 Convergent Approach

The first convergent synthesis for dendrigrafts was achieved by Knauss et al.[107] who developed a one-pot grafting-through strategy. Living polystyryllithium was coupled to both sides of a bifunctional vinylbenzy chloride (*p*-chloromethyl styrene) monomer. Whereas one of the living chains underwent nucleophilic substitution to the chloromethyl group, the other chain added to the vinylic moiety and could continue propagation when more styrene monomer was added. This self-condensation process where parts of the living chains were intentionally terminated with less than stoichometric amount of coupling agent and ending up as branches on the second living chain could be repeated to result in dendron-like fragments. The polystyrene spacer introduced by the addition of styrene before the next iteration reduced the branching density from a star-like framework to a wider dendron-like branch structure. However, this method was found to be very limited in molecular weights of maximum 10^5 g/mol due to steric inhibition. Moreover, except of the molecular weight and dispersities of the initiator chain and the final dendrigraft polymer, the characterization of structural parameters is nearly impossible in this on-pot method.

As already mentioned, a common problem accompanying the synthesis of dendritic structures is the rapidly increasing sterical difficulties with higher generations, which especially can turn out an issue when it comes to the convergent approach if focal points of several bulky dendrons have to be connected.

3 Fundamentals of Rheology

This chapter gives an introduction into the rheological concepts, experimental implications and data interpretation. Subdivided into four sections, first, the fundamentals of shear rheology and its governing equations are explained. Small amplitude oscillatory shear (SAOS) is introduced for rheological polymer characterization in nonlinear deformation. Thereafter, the underlying molecular dynamics are highlighted. Nonlinear extensional rheology as an important method to characterize polymer melts in elongational deformation gives the transition to the theories behind polymer foaming.

Rheology is the scientific field studying the flow of matter and the deformation of materials under applied forces.[9,11] Between ideal solids which are purely elastic and follow Hooke's law, and ideal fluids which are purely viscous following Newton's law, there is a continuous spectrum of material properties having an elastic as well as a viscous part, so-called viscoelasticity. Materials considered as solids can show partially viscous flow behavior, whereas mainly viscous liquids can also have an elastic component. Most materials and especially polymers and their melts are classified within this range. Rheological experiments enable to correlate the macroscopic viscoelastic material response with the chain dynamics on a molecular level during deformation. The understanding of the influence of molecular structure (chemical composition, topology, etc.) on the deformation behavior is of fundamental interest to improve and optimize material properties.[108]
The following chapter focuses on the basics of shear and elongational rheology of polymer melts.

3.1 Shear Rheology

A simple two-plate shear experiment serves to illustrate the basics of rheology. A material (e.g. polymer melt) is placed between two parallel plates having an area, A, in a distance, h, as schematically shown in **Figure 3.1**.

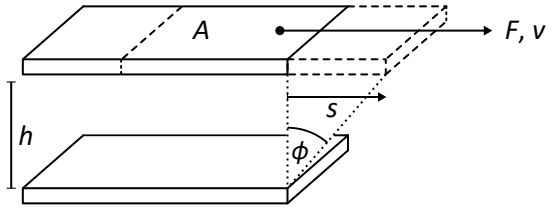

Figure 3.1: Illustration of a shear experiment via two-plate model. A material is placed between the plates and sheared by moving the upper plate with a constant force, F, and velocity, v.[109,110]

When the upper plate is then moved with a constant force, F, over a distance, s, the resulting shear stress, σ, is given by the applied shear force, normalized to A, **Equation 3.1**.

$$\sigma = \frac{F}{A} \tag{3.1}$$

The shear strain, γ, is the deformation of s normalized to h, see **Equation 3.2**). Ideally, at each plate distance the material experiences the same strain.

$$\gamma = \frac{s}{h} \tag{3.2}$$

As the velocity, v, of each "slice" of the sheared sample depends on the distance from the plate, therefore the shear rate, $\dot{\gamma}$, is introduced, which is the velocity normalized to the distance, expressed by **Equation 3.3**.[108]

$$\dot{\gamma} = \frac{1}{h} \cdot \frac{\mathrm{d}s}{\mathrm{d}t} = \frac{\mathrm{d}\gamma}{\mathrm{d}t} = \frac{v}{h} \tag{3.3}$$

3.1.1 Phenomenological Models

The plate-plate shear experiment above was described in linear direction of motion. However, the methods most commonly used to characterize the flow behavior of polymers in the melt state are conducted in rotational rheometers, either in simple or in oscillatory shear. The advantages to study the relaxation behavior with dynamic-mechanical oscillatory instrumentation comes with the data acquisition being easier, faster and more accurate in the frequency domain than in the time domain.[9] Therefore the following section describing the phenomenological models (Hookean and Newtonean behavior) of strain-stress response relates to shear experiments under oscillatory (sinusoidal) deformation.

3.1.1.1 Ideal Elastic Behavior - Hooke Model

Ideal elastic deformation can be described by Hooke's law using a one-dimensional spring model, see **Figure 3.2a**. The force, F, acting on the material is proportional to its deformation, x, with the constant of proportionality, k, describing the stiffness of the spring, i.e. material.[9,108]

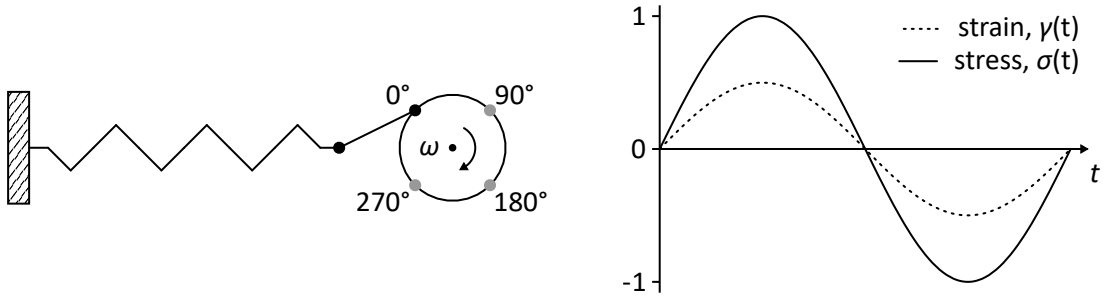

(a) Hookean spring model. **(b)** Ideal elastic behavior.

Figure 3.2: Hookean spring model for ideal elastic solids. **(a)** An oscillatory excitation strain, $\gamma(t)$, with constant angular frequency, ω, is applied to the material. **(b)** the stress response, $\sigma(t)$, is proportional and in phase, $\delta = 0°$, with the sinusoidal deformation.[110]

Analogous to Hooke's law, in a shear experiment, the stress response, σ, is proportional to the shear deformation, γ. In this case, the shear modulus, G, describes the proportionality and is a material constant.

$$\sigma = G \cdot \gamma \tag{3.4}$$

In oscillatory shear, the time-dependent deformation, $\gamma(t)$, of the material is sinusoidal, with the excitation frequency, ω_1, and the strain amplitude, γ_0, as the maximum deformation.

$$\gamma(t) = \gamma_0 \cdot \sin(\omega_1 t) \tag{3.5}$$

Inserting **Equation 3.5** into **Equation 3.4** results in the shear stress for the oscillatory case.

$$\sigma(t) = G \cdot \gamma_0 \cdot \sin(\omega_1 t) \tag{3.6}$$

In the linear regime, $G = \sigma(t)/\gamma(t) = const.$, so $\sigma(t)$ and $\gamma(t)$ are sinusoidal as well as in phase, $\delta = 0°$, as shown in **Figure 3.2b**.

3.1.1.2 Ideal Viscous Behavior - Newton Model

Ideal viscous behavior can be described by a damper plate which is immersed in a Newtonian fluid, called dashpot model, dissipating energy by converting viscous friction into heat, see **Figure 3.3a**.

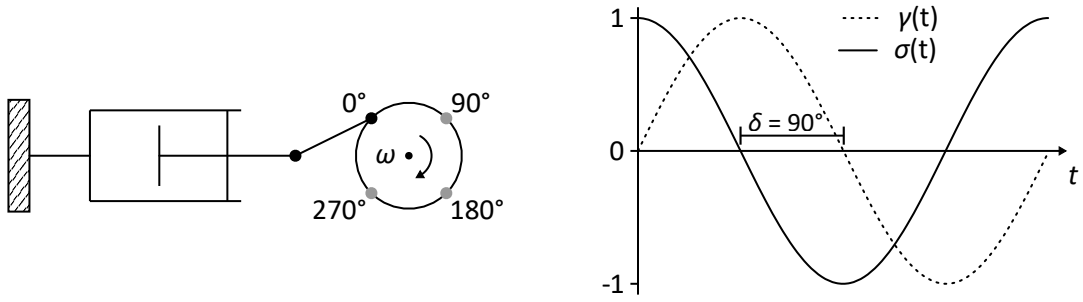

(a) Newtonean dashpot model. **(b)** Ideal viscous behavior.

Figure 3.3: Newtonean dashpot model for ideal viscous fluids. **(a)** A piston moves back and forth by an oscillatory excitation. **(b)** The measured stress, $\sigma(t)$, is out of phase with the applied strain, $\gamma(t)$, shifted by a phase angle of $\delta = 90°$.[110]

In the linear case, the force, F, is proportional to the piston velocity, v. Applied to the case of shear, the shear stress, σ, is then proportional to the shear rate, $\dot{\gamma}$ with the (temperature dependent) viscosity, η, as specific for the material.

$$\sigma = \eta \cdot \dot{\gamma} \tag{3.7}$$

The first derivative of the time-dependent deformation, γ, from Equation 3.5 gives the shear rate, $\dot{\gamma}$, in oscillatory motion.

$$\dot{\gamma}(t) = \frac{\mathrm{d}\gamma}{\mathrm{d}t} = \gamma_0 \cdot \omega_1 \cdot \cos(\omega_1 t) \tag{3.8}$$

Inserting **Equation 3.8** into Newton's law from **Equation 3.7** results in the time-dependent shear stress, $\sigma(t)$. In sinusoidal deformation, $\sigma(t)$ has a 90° phase shift relative to the deformation, γ, i.e. relative to ideally elastic materials, see **Figure 3.3b**.

$$\sigma(t) = \eta \cdot \gamma \cdot \omega_1 \cdot \cos(\omega_1 t + \delta) \tag{3.9}$$

$$= \eta \cdot \gamma \cdot \omega_1 \cdot \sin(\omega_1 t + 90°) \tag{3.10}$$

3.1.1.3 Viscoelasticity

Ideal elastic (Hookean) or viscous (Newtonean) behavior is only observed for few materials and in limited range of shear conditions. The majority of materials at deformation exhibit elastic and viscous response at the same time. Such simultaneous behavior is called viscoelasticity[11] and can be modelled in its simplest cases by a combination of a linear Hookean spring and a Newtonian dashpot in parallel (Kelvin-Voigt model) or in serial (Maxwell model) arrangement, as illustrated in **Figure 3.4**.[9,108]

[11] Sometimes the term "elastoviscous" is found to specifically address elastic properties under short duration stress in a liquid or molten state and to differentiate from a rubbery "viscoelastic" solid whose relaxation is dampened by viscous flow. The distinction is not always clear, therefore mostly the superordinate term "viscoelasticity" is used.[111]

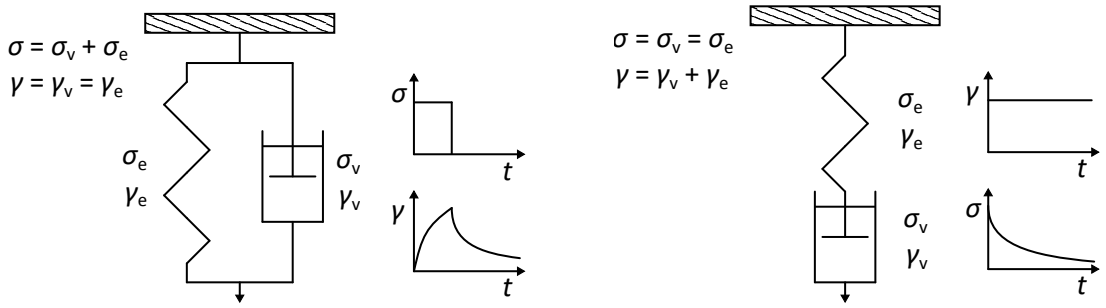

(a) Kelvin-Voigt model: creep-recovery. **(b)** Maxwell model: stress-relaxation.

Figure 3.4: Combinations of spring and dashpot with viscoelastic response: **(a)** Kelvin-Voigt model for elastic solids with viscous part. **(b)** Maxwell model for viscous fluids with elastic part (sometimes referred to as elastoviscous). Subindices "e" for elastic and "v" for viscous component.[9]

3.1.1.4 Kelvin-Voigt Model

An elastic solid with low viscous part is simply approximated by a Kelvin-Voigt Model in which spring and dashpot are aligned parallel, illustrate in **Figure 3.4a**. After displacement in tension or shear, the total relaxation of the system reaching its initial position is governed by the spring, however the dashpot induces a time-delayed component due to energy dissipation via viscous friction.
Parallel connection of spring and dashpot results in the same deformation (**Equation 3.11**) and shear rate (**Equation 3.12**).

$$\gamma = \gamma_\mathrm{e} = \gamma_\mathrm{v} \tag{3.11}$$

$$\dot{\gamma} = \dot{\gamma}_\mathrm{e} = \dot{\gamma}_\mathrm{v} \tag{3.12}$$

In this model, the total stress, σ, of the deformation is splitted into an elastic stress component, σ_e, and a viscous stress component, σ_v. Using Hooke's law (Equation 3.4) and Newton's law (Equation 3.7), the total stress of the system results in a differential **Equation 3.13**.

$$\sigma = \sigma_\mathrm{e} + \sigma_\mathrm{v} = G \cdot \gamma_\mathrm{e} + \eta \cdot \dot{\gamma}_\mathrm{v} = G \cdot \gamma + \eta \cdot \dot{\gamma} \tag{3.13}$$

3.1.1.5 Maxwell Model

Completely viscous fluids dissipate energy when undergoing deformation, so in a typical dashpot model no retraction force is exerted. However, some liquids exhibit also an elastic part. A common example for such a behavior is a polymer melt. Owing to its macromolecular nature, the coil-like structure and physical entanglements can be seen as temporary springs which elastically resist initial deformation. After a strain is applied, the resulting stress will resolve over time due to material relaxation caused by motion of the polymer chains; see also **Section 3.3** for chain dynamics of polymer melts.

This behavior is best described by the Maxwell model with a spring and dashpot in series, see **Figure 3.4b** where each component experiences the same stress, as expressed in **Equation 3.14**.

$$\sigma = \sigma_{\mathrm{e}} = \sigma_{\mathrm{v}} \tag{3.14}$$

The total strain, γ, and strain rate, $\dot{\gamma}$, are the sum of each part of elastic and viscous strains (**Equation 3.15**), respectively strain rates (**Equation 3.16**).

$$\gamma = \gamma_{\mathrm{e}} + \gamma_{\mathrm{v}} \tag{3.15}$$

$$\dot{\gamma} = \dot{\gamma}_{\mathrm{e}} + \dot{\gamma}_{\mathrm{v}} \tag{3.16}$$

Applying Hooke's law (Equation 3.4) for the elastic and Newton's law (Equation 3.7) for the viscous part to Equation 3.16 results in Maxwell's differential **Equation 3.17**.

$$\dot{\gamma} = \frac{\dot{\sigma}_{\mathrm{e}}}{G} + \frac{\sigma_{\mathrm{v}}}{\eta} = \frac{\dot{\sigma}}{G} + \frac{\sigma}{\eta} \tag{3.17}$$

In oscillatory shear, Equation 3.3 can be applied to Equation 3.17, to result the time-dependent shear rate $\dot{\gamma}(t)$, see **Equation 3.18**.

$$\dot{\gamma}(t) = \frac{\dot{\sigma}}{G} + \frac{\sigma}{\eta} = \gamma_0 \cdot \omega_1 \cdot \cos(\omega_1 t) \tag{3.18}$$

The Kelvin-Voigt model and the Maxwell model represent the simplest viscoelastic models, with the former best applying to (reversible) strain creep, whereas the latter is better for predicting stress relaxation, respectively, see graphical representations in Figure 3.4.[112]
In addition to both fundamental models, Kelvin-Voigt and Maxwell, there are also more sophisticated combinatorial setups, e.g. three-element models which are composed of a Kelvin-Voigt or Maxwell element with additional spring or dashpot (Zener or Standard linear solid model), or Kelvin-Voigt and Maxwell combined with each other (Burgers model) which will not be discussed here but referred to literature.[113]
In contrast to ideal viscoelastic behavior, the response of real materials is often insufficiently described by only one Maxwell or Kelvin-Voigt element. The more complex viscoelastic response of e.g. polymers can be taken into account by extending the Maxwell model and adding further elements in parallel. The result is a generalized, multi-mode Maxwell model, mathematically represented by a sum of exponentials to fit experimental data.[9]
The practical implementation is further explained in **Section 3.2.1**.

3.2 Small Amplitude Oscillatory Shear (SAOS)

Small amplitude oscillatory shear (SAOS) is the technique most often employed in investigating the flow behavior of polymer melts and determining the linear viscoelastic characteristics. In the linear mechanical regime, the deformation is very small and the chains remain nearly in Gaussian configuration. The mechanical response under these conditions can be described with models of linear mathematical equations, that means a linear relationship between strain and stress.
The generated master curve (obtained by TTS; see following **Section 3.2.2**) displays the polymers flow behavior in the plateau and terminal zones which are of special interest because of their sensitivity to molecular structure and branching in particular, which makes SAOS suitable to study structure-property relationships.[9]

The mathematical solution to the differential **Equation 3.18** of the rheological Maxwell model in oscillatory case is leading to the linear viscoelastic constitutive **Equation 3.19** with the relaxation time, $\tau = \eta/G$.

$$\sigma(t) = \gamma_0 \cdot \left[G \cdot \frac{(\omega_1\tau)^2}{1+(\omega_1\tau)^2} \cdot \sin(\omega_1 t) + G \cdot \frac{\omega_1\tau}{1+(\omega_1\tau)^2} \cdot \cos(\omega_1 t) \right] \tag{3.19}$$

$$= \gamma_0 \cdot \left[G' \cdot \sin(\omega_1 t) + G'' \cdot \cos(\omega_1 t) \right] \tag{3.20}$$

G' is called storage modulus and describes the reversibly stored deformation energy related to the elastic contribution, whereas G'' is called loss modulus and refers to the dissipated energy caused by viscous deformation.
The trigonometric form of **Equation 3.20** enables to conveniantly express the moduli as complex numbers with G' and G'' being the real and imaginary components of the complex modulus, G^*.[9]

$$G^*(\omega) = G'(\omega) + i\,G''(\omega) \tag{3.21}$$

The absolute value of the complex modulus, $|G^*|$, is simply the application of the Pythagorean theorem on **Equation 3.21**, resulting in **Equation 3.22**.

$$|G^*| = \sqrt{G'^2 + G''^2} \tag{3.22}$$

The phase angle, δ, as the angle between storage and loss moduli in the complex plane can be used to define a dissipation factor, $\tan\delta$, as the ratio of the two moduli, G'' and G', representing the ratio of viscous to elastic effects, as expressed in **Equation 3.23**.

$$\tan\delta = \frac{G''}{G'} \tag{3.23}$$

For polymer melts with viscoelastic behavior, the disspation factor is between $\tan\delta = 0$ (ideal elastic) and $\tan\delta = \infty$ (ideal viscous), the loss angle therefore is in the range of

$0° < \delta < 90°$.

Two limiting cases can be considered for Equation 3.20: At high excitation frequencies, ω, or long relaxation times, τ, G' dominates and $\tan\delta \to 0$. The shear stress is not relieved fast enough by the polymer chains' dynamics and follows the deformation (shear strain) without phase shift, which results in a close to ideal elastic behavior. In the other case, by lowering the excitation frequencies or shortening the relaxation times of the polymer (e.g. increase the relaxation dynamics with temperature), the viscous behavior prevails and G'' has a higher contribution. In this range a proportionality of $G' \propto \omega^2$ and $G'' \propto \omega$ can be observed.

Another representation of dynamic data uses the relationship $G^* = i\omega\eta^*$ to display the complex viscosity vs. frequency via **Equation 3.24**.

$$|\eta^*| = \frac{|G^*|}{\omega} \tag{3.24}$$

At low shear rates, the viscosity is shear rate independent and appears as first Newtonian plateau. The limit is called zero-shear viscosity, η_0, and can be determined according to **Equation 3.25**, showing the Cox-Merz relation[114] between the shear rate dependent viscosity, $\eta(\dot{\gamma})$, and the frequency dependent complex viscosity, $\eta(\omega)$.

$$\eta_0 = \lim_{\dot{\gamma}\to 0} \eta(\dot{\gamma}) = \lim_{\omega\to 0} |\eta^*(\omega)| \tag{3.25}$$

For linear polymers, the zero-shear viscosity is strongly molecular weight dependent, following characteristic scaling laws, as further explained in **Section 3.2.3**. Moreover, branching has a strong effect on the plateau value and any deviation of the expected scaling law gives a hint about dominant relaxation dynamics which is one major focus of this thesis and therefore further discussed in **Section 5.3.1.3**.

3.2.1 Relaxation Spectrum and Multi-mode Maxwell Model

When it comes to polymeric liquids, one Maxwell element with its single exponential stress relaxation already can approximate the behavior of a polymeric liquid in good qualitative agreement.

However, the relaxation of polymer melts is governed by different molecular relaxation modes. The broad spectrum of real material response at different frequencies can be simulated with a (theoretically) infinite number of parallelly-connected Maxwell elements and with high accuracy.[9]

This so-called multi mode Maxwell model which applies for linear viscoelasticity can be mathematically expressed by **Equation 3.26** as a sum of N (discrete) exponential stress relaxations with each mode having a different relaxation strength, g_i.

$$G(t) = \sum_{i=1}^{N} g_i \exp(-t/\tau_i) \tag{3.26}$$

Using this principle and applying it to the linear viscoelastic (LVE) constitutive equations (Eq. 3.19 and 3.20), the parameter set of g_i and τ_i can be fitted to the oscillatory shear

data with linear or nonlinear regression methods, representing the dynamic moduli G' and G'' (**Equation 3.27**) as discrete relaxation spectrum.[115]

$$G'(\omega) = \sum_{i=1}^{N} \frac{g_i(\omega\tau_i)^2}{1+(\omega\tau_i)^2} \qquad \text{and} \qquad G''(\omega) = \sum_{i=1}^{N} \frac{g_i(\omega\tau_i)}{1+(\omega\tau_i)^2} \tag{3.27}$$

3.2.2 Time-Temperature Superposition (TTS)

Oscillatory shear measurements yield the frequency dependent storage (G') and loss moduli (G'') over a broad dynamic range which can be extended via the time-temperature superposition (TTS) principle.

To examine the melt flow properties of viscoelastic materials over a wide range of frequencies over which linear behavior can be determined, rheology makes use of the time-temperature superposition (TTS) principle, which enables data collection at frequencies far outside the mechanical limits of the instrument. The fundamental basis of the concept is that all relaxation modes have the same temperature dependency, so every motion on molecular and segemental level is slowed down or speeded up by the same factor when lowering or increasing the measurement temperature.

The basic procedure is that frequency sweeps are conducted in several temperature intervals and the obtained rheological data showing the curves at different temperatures can then be shifted with respect to a reference temperature, T_{ref}, resulting a single master curve for G' and G'' over an extended frequency spectrum.[9]

The mathematical time-temperature dependency is expressed via the Williams-Landell-Ferry (WLF) **Equation 3.28**, which is based on the assumption that above the glass transition temperature, T_{g}, the free volume increases linearly with temperature.[116]

$$\log a_{\mathrm{T}} = \frac{-C_1(T-T_{\mathrm{ref}})}{C_2+T-T_{\mathrm{ref}}} \tag{3.28}$$

The horizontal shift factor, a_{T}, is determined by the superpositioning of the data, whereas C_1 and C_2 are empirical parameters. When choosing the glass transition as the reference ($T_{\mathrm{ref}} = T_{\mathrm{g}}$), they become polymer-independent constants with $C_1 = 17.44$ and $C_2 = 51.6\,\mathrm{K}$ for a wide range of materials with similar dynamics, i.e. isoviscous behavior.

$$b_{\mathrm{T}} = \frac{T_0 \cdot \rho_0}{T \cdot \rho} \tag{3.29}$$

A vertical shift factor, b_{T}, compensates the stress magnitudes (e.g. dynamic moduli G' and G'') which are proportional to the product of density, ρ, and temperature, T, **Equation 3.29**. Since the changes in material density due to thermal expansion and contraction are in general very small for polymer melts, the vertical shift is close to unity. Several material and sample specific parameters like the entanglement molecular weight, M_{e}, the zero-shear viscosity, η_0, and characteristic relaxation times, τ, of molecular chain segment motions can be obtained.[9]

3.2.3 Molecular Weight Dependence of the Zero-Shear Viscosity

The molecular dynamics of unentangled polymer chains are governed by Rouse motions, which is in essence described as the idea of chain segments represented by beads with a center-of-mass and those spring-like attached to each other in a string to simulate the model chain, with the spring constant proportional to kT times the extension.[9]. Originally, the Rouse model was formulated for polymers in dilute solutions where the system's restoring entropic spring force relaxes deformation against the viscous resistance of the solvent matrix.[117]

Bueche applied this concept to unentangled melts, simply replacing the polymer concentration by the melt density. So, according to the Bueche-Rouse theory, Rouse motion occurs along the chain with the only interference by the matrix imposing molecular weight dependent friction. In this range, at low molecular weights, the zero-shear viscosity is proportional to M_w.[118] The different scaling regimes are compared in **Table 3.1**.

Table 3.1: Scaling laws for molecular weight dependence of the zero-shear viscosity and contributing relaxation modes for a polymer having a molecular weight of M_w.[9,119]

Proportionality [a]	Regime [b]	Dominant relaxation modes
$\eta_0 \propto M_\mathrm{w}$	$M_\mathrm{w} < M_\mathrm{c}$	Rouse motion
$\eta_0 \propto {M_\mathrm{w}}^{3.4}$	$M_\mathrm{c} < M_\mathrm{w} < M_\mathrm{r}$	Reptation, CLF, CCR
$\eta_0 \propto {M_\mathrm{w}}^{3}$	$M_\mathrm{r} < M_\mathrm{w}$	Reptation (only)

[a] For linear homopolymer melts

[b] Examples for PS: $M_\mathrm{e} \approx 15\,\mathrm{kg/mol}$[120,121]; $M_\mathrm{c} \approx 35\,\mathrm{kg/mol}$[122]; $M_\mathrm{r} \approx 15\,M_\mathrm{c} \approx 480\,\mathrm{kg/mol}$[123].

As the chain length increases, the polymers free motion is prone to be constraint by surrounding chains, which substantially takes effect at a threshold called critical molecular weight, M_c, above which the polymer intertwines with its matrix and forms a physical network of entanglements. In this region, where the viscosity as a function of molecular weight has a steeper power law with a scaling exponent of 3.4, the chain's relaxation is governed by a snake-like reptation mechanism, along with contour length fluctuation (CLF) and convective constraint release (CCR), see **Section 3.3**. The critical molecular weight depends on the type of polymer and typical values vary between 2–4 entanglement molecular weights M_e.[9]

For sufficiently long chains, the effects of CLF and CCR decrease as they primarily contribute to the total relaxation via chain end motions. Therefore, with increasing length the chain end contribution becomes neglectable compared to the inner segments of the chain. As this happens only gradually, the transition to pure reptation is not very sharp and the scaling slightly changes from 3.4 to an exponent of 3.[123,124]

3.2.4 Plateau Modulus and Entanglement Molecular Weight

Entanglements, created by the random intertwining of polymer strands change the relaxation dynamics to a reptation dominated mechanism and results in a dramatically slowed down relaxation. When a deformation of high enough strain rate is faster then the disentanglement

time of the polymer is applied, the physical entanglements act like temporary crosslinks and the response is a rubbery-elastic behavior with a constant value (plateau) in $G'(\omega)$ observed over a fairly wide frequency range (depending on the molecular weight). This rubber plateau region with its plateau modulus, G_N^0, is most pronounced for monodisperse polymers and extends to lower frequencies (longer relaxation times) with increasing molecular weight, as can be experimentally observed by the shift of the crosspoint where G' and G'' intersect. The inverse of this angular frequency, ω_d, is the longest or terminal relaxation time, τ_d, defining the transition to the terminal regime. The value of G_N^0 is relatively independent of temperature and molecular weight for well entangled polymers ($M_w \gg M_c$).[9,45,110]
In contrast to that, polydisperse systems contain a broad range of chain lengths, each relaxing at its own frequency and contributing to the overall relaxation time of the melt. Therefore the plateau does not appear as "flat" and the transition into the terminal regime happens with a rather gradual slope than being "sharp", as seen for monodisperse melts. The shapes of the moduli curves, especially $G'(\omega)$, therefore contain information about the molecular weight distribution.[119]

Similarly to the modulus of a rubber which is dependent on the density of the molecular network, the plateau modulus of an uncrosslinked polymer gives information about the density of the physical network, quantified by the entanglement molecular weight M_e which is defined as **Equation 3.30**,[9]

$$M_e = \frac{4}{5}\frac{\rho RT}{G_N^0} \tag{3.30}$$

whereby the prefactor (4/5) takes into account that one fifth of the initial stress is already relieved by fast Rouse modes re-equilibrating the tension along the chain.[125]
The higher M_e, the longer is the distance between entanglements, implying a polymeric network with low entanglement density. In that regard, M_e is also an indicator of molecular stiffness of the chains.[126] For example, the most simple vinylic polymer, linear polyethylene (HDPE), has a $M_e \approx 1\,\mathrm{kg/mol}$,[123] substituting a proton with a methyl group increases the $M_e \approx 7\,\mathrm{kg/mol}$ (for atactic and isotactic PP),[127] and even bulkier phenylic substituents further reduce the flexibility and increase the entanglement distance, e.g. PS with $M_e \approx 15\,\mathrm{kg/mol}$.[120] The corresponding plateau moduli, G_N^0, are approximately 2.6 MPa (HDPE), $5.2 \cdot 10^5\,\mathrm{Pa}$ (*a*-PP, *i*-PP), and $2 \cdot 10^5\,\mathrm{Pa}$ (PS), respectively.

3.3 Dynamics of Linear and Branched Polymers

The macroscopic stress response of a polymer sample is fundamentally governed on the microscopic scale by the dynamic motion of the polymer chains. Various concepts about the relaxation behavior of polymer systems have been developed to correlate the polymer dynamics to the results obtained in rheological measurements. This allows a better understanding of the relationship between the molecular structures and their contribution to the polymer properties. Vice versa, rheological results give a hint on the underlying relaxation behaviors.[9,126,128]

3.3.1 Tube Model

The tube model, one of the first descriptive concepts for polymer motion in dense melts, was proposed by Edwards[129]. With contributions by deGennes[130], Doi and Edwards[131,132] later refined this new important theory, serving as fundamental approach to explain and predict dynamic-mechanical measurements in entangled polymer systems from a macromolecular level. Instead of examining the motion of all polymer chains in the melt state, the problem is simplified to one single mobile chain, observed in a tube formed by surrounding polymer chains which are considered as static. Due to conformational constraints imposed by confining macromolecules (entanglements), the movement of the chain is restricted to a diffusion along the axis of the tube, see **Figure 3.5a**.[9]

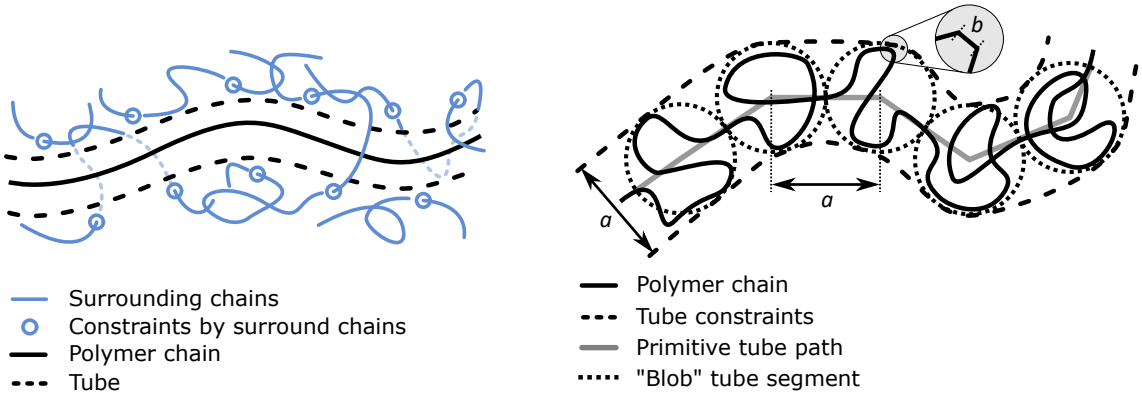

(a) Simple polymer tube model.

(b) Tube theory as blob model.

Figure 3.5: Tube models. **(a)** Entangled polymer chain in a matrix of surrounding polymer chains. **(b)** The meandering polymer inside the tube has conformational freedom and the constraints are only felt beyond the tube diameter, a, which is also the tube segment length, illustrated as "blobs" along the primitive path. The chain itself has a monomer-based segment length of b.

In a more detailed view on the tube theory, the chain has a certain degree of lateral freedom and the space occupied by the meandering polymer inside its channel-like tube can be illustrated by a string of impenetratable "blobs" with tube diameter, a, see **Figure 3.5b**.

The relative dimensions of the blob tube and chain parameters can be roughly summarized in **Equation 3.31**,[133]

$$b \ll a \ll \sqrt{\langle R^2_{\text{chain}} \rangle_0} = \sqrt{6}\, R_{\text{g}} \ll L_{\text{tube}} \ll L_{\text{chain}} \tag{3.31}$$

with $\langle R^2_{\text{chain}} \rangle_0$ as the root-mean-square end-to-end distance of the chain, as well as L_{tube} and L_{chain} as the contour lengths of the tube and the polymer, respectively.

The blob coil size a is equivalent to its average (root-mean-square) end-to-end distance, $\langle R^2_{\text{blob}} \rangle_0^{1/2}$, and scales proportional to the square roof of the number of monomers constituting the blob. If we assume that each blob contributes to one entanglement along the whole primitive tube path, then the number of monomers per entanglement N_{e} with statistical monomer-based segment length b, results in the tube diameter, a, see **Equation 3.32**.

$$a \equiv \sqrt{\langle R^2_{\text{blob}} \rangle_0} = b\sqrt{N_{\text{e}}} \tag{3.32}$$

The whole polymer chain itself is composed of a degree of polymerization of N monomers with mean square end-to-end distance, $\langle R^2_{\text{chain}}\rangle_0$, in the relationship $b = \sqrt{\langle R^2_{\text{chain}}\rangle_0 / N}$. If one blob is considered to be the distance between two constraints, therefore the entanglement molecular weight (via $N_\text{e} = M_\text{e}/M_0$) is directly related to the tube diameter.
Inserting Equation 3.30 in Equation 3.32 leads to **Equation 3.33**, that enables to determine the tube diameter with rheological methods like SAOS.[9]

$$a^2 = b^2 \frac{M_\text{e}}{M_0} = b^2 \frac{4}{5} \frac{\rho R T}{G^0_\text{N}} \frac{1}{M_0} \tag{3.33}$$

Bulky substituents along the polymer chain widen the tube diameter. In consequence, also the entanglement molecular weight, M_e, increases and the polymer is constraint by less entanglements per unit volume.

According to Kavassalis and Noolandi,[134] a simplified estimation when and how strong a chain starts "feeling" the presence of entanglements is based on the ratio of pervaded (spatially occupied) volume, V_pervaded, to the actual physical volume, V_physical, of the polymer chain per unit volume, called overlap parameter, O, estimated by **Equation 3.34**.

$$O \approx \frac{V_\text{pervaded}}{V_\text{physical}} \approx \frac{(b\, N^{1/2})^3}{b^3\, N} \tag{3.34}$$

If the overlap parameter exceeds a certain threshold (Kavassalis-Noolandi number) of the packing order of $O_\text{KN} \approx 10$–20, that means about 10 to 20 neighboring chain segments share the same unit volume, it is postulated that the number of molecules per chain segment constituting the unit volume is equal to one entanglement chain length N_e.[135] For short chains in bulk or long chains with high amounts of surrounding solvent, the number of neighbour segments is small an therefore no-to-little restricted motion occurs. If the chain reaches a size where $O \approx O_\text{KN}$, one blob with diameter a, equal to one entanglement is formed (see above). Further increasing the length of the chain will result in the string-like accumulation of blobs, i.e. entanglements, like shown in the previous Figure 3.5b. This approach to calculate N_e is fundamentally based on packing considerations with an average coodination number[12] of $\tilde{N} = 8.1$ polymer strands surrounding the chain who creates the entangled blob.[136,137]

3.3.2 Reptation

A polymer chain can move along its tube contour by a snake-like diffusive process, called reptation. In the direction of movement the chain will face new constrictions and re-entangle with surrounding chains, thus a new tube with random conformation is created.[130] The other chain end is dragged into the old tube, abandoning the former tube space which is immediately occupied by surrounding chains, **Figure 3.6**.

[12] The reported coordination numbers were found in the range of $\tilde{N} \approx 6.5 - 10$ and slightly vary with chemical species, e.g. $\tilde{N}_\text{PE} \approx 8$, $\tilde{N}_\text{PS} \approx 9$, $\tilde{N}_\text{PVAc} \approx 10$.[136]

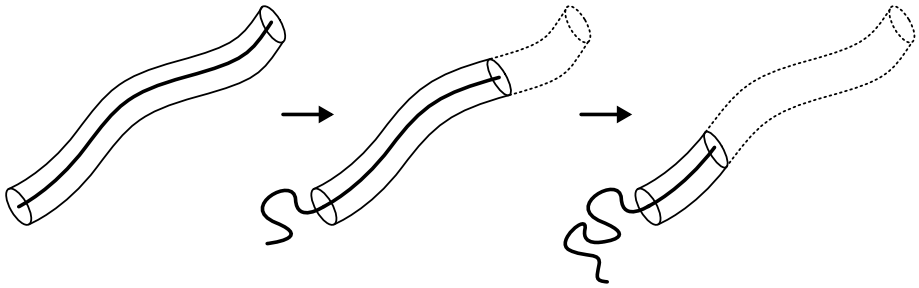

Figure 3.6: Reptation of a polymer chain out of its confining "tube" by a snake-like diffusion process. The escaping chain end adopts a new conformation and forms a new tube by the constraints of the surrounding polymer chains.

The reptation time, also called disengagement time, τ_d, that is the time required for the polymer to fully escape its old tube and adopt a new conformation, is given by **Equation 3.35**.[133]

$$\tau_\mathrm{d} = \frac{\zeta\, N^3\, b^4}{\pi^2\, k_\mathrm{B} T\, a^2} \tag{3.35}$$

With $D = k_\mathrm{B}T/N\zeta$ as the diffusion coefficient and ζ as the monomeric friction coefficient. With this equation (3.35), based on the entanglement equilibration time, τ_e, from Milner and McLeish[138], the pure reptation time (excluding other relaxation mechanisms) and also the zero-shear viscosity, η_0, is proportional to the third power of the degree of polymerization, N, or the molecular weight, M, respectively.

$$\tau_\mathrm{d} \propto \eta_0 \propto \frac{L_\mathrm{tube}^2}{D} \propto N^3 \propto M^3 \tag{3.36}$$

As can be seen from the scaling law of **Equation 3.36**, $\eta_0 \propto M^3$, the tube model for reptation already gives a very good prediction for experimentally observed behavior in polymer melt rheometry, in particular for very high molecular weights, where reptation is the dominant relaxation mode, as previously shown in Table 3.1, see Section 3.2.3.

In the regime of "medium" chain lengths, between the critical and the reptation molecular weight, $M_\mathrm{c} < M_\mathrm{w} < M_\mathrm{r}$, the expected scaling increases from 3 to about 3.4. Thus, additional relaxation processes have to be considered contributing to the dynamics in real polymer melts and allowing a quantitative description for the observed molecular weight dependencies.

For linear polymers, those additional relaxation modes are the contour length fluctuation (CLF) and the convective constraint release (CCR), which are discussed in the following **Section 3.3.3**. Their contribution accelerates the overall relaxation of the polymer chains and therefore allows for a higher M_w to have the same relaxation time then compared to reptation only. Furthermore, branched polymer topologies "profit" from these processes as the dynamics of CLF and CCR are mostly dictated by fast relaxing chain ends of which branched polymers occupy a higher volume fraction in the melt.

3.3.3 Contour Length Fluctuation (CLF)

Since the polymer is folded and the diameter of the chain is smaller then its tube diameter, the chain segments are continuously in Brownian motion and constantly change their orientation and degree of folding. Due to the randomness of this process, by chance the chain can shortly transition into a more folded state then usual. The increased wrinkling is pull the chain ends into the tube and shortly decrease the contour length of the primitive path. When the chain is unfolding again, the chain ends are pushed outwards and extend into a newly created tube segment with random orientation. In continuous motion of the polymer, the occupied tube fluctuates in length and the stress is thereby relaxed. This contour length fluctuation (CLF), also called primitive path fluctuation (PPF), is a fast relaxation mechanism for chain ends, see **Figure 3.7a**.
However, a highly folded conformation becomes increasingly entropically unfavorable for chain segments closer to the center, so the relaxation of the middle part of the polymer is dominated by reptation, rather than by a significantly slowed down CLF process.[9,130]

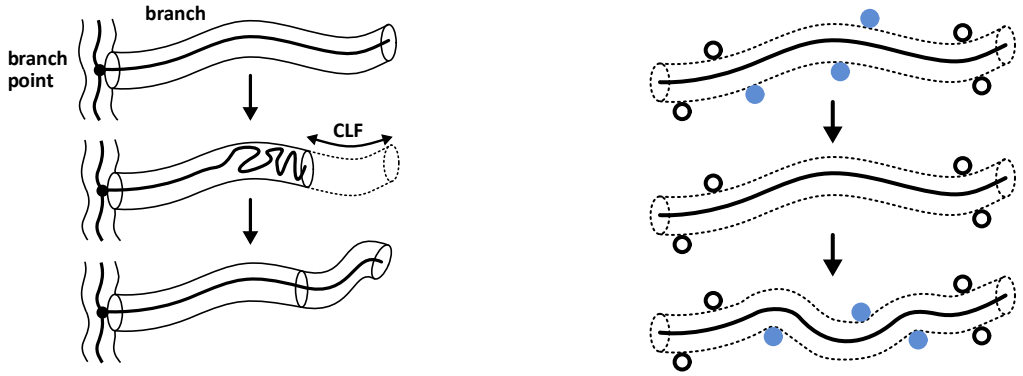

(a) Contour length fluctuation (CLF). **(b)** Convective constraint release (CCR).

Figure 3.7: Relaxation mechanisms with contribution of chain ends. **(a)** Chain ends retract and re-extend into new tube segment. This mode of relaxation applies also to the chain ends of linear polymers, however it is one of the most mechanisms allowing branched polymers to relax. **(b)** Orthogonal chain fluctuations (blue circles) lead to a frequent release in entanglements allowing the tube to occupy the free space and take a new conformation.

Nonetheless, for linear polymers the relaxation of the chain ends via CLF contributes to the overall relaxation process in a way that the outer part of the molecule relaxes at higher frequencies, thus shortening the effective tube length which facilitates reptation of the whole molecule. In consequence, the longest relaxation time, τ_d, and therefore the zero-shear viscosity, η_0, is diminished. Above the critical molecular weight, M_c, where the chain is entangled and starts to reptate, and below the reptation molecular weight, M_r, where due to chain length fast relaxation processes like CLF are neglectable and pure reptation is assumed, in this regime of intermediate chain lengths, $M_\mathrm{c} < M_\mathrm{w} < M_\mathrm{r}$, the experimentally observed scaling of $\tau_d \propto \eta_0 \propto M_w^\alpha \approx M_w^{3.4}$ can be fairly good explained quantitatively assuming reptation in combination with CLF relaxation mechanism. Values for the exponent that ranges from $\alpha = 3.3$ to 3.6 might be attributed to the actual M_w of the polymer chain within this regime, depending on the contribution of CLF relative to the reptation process.[138]

The explanation for the "3.4 power law" over the range $5 \ll M/M_e \ll 30$ (e.g. PS[123]) for the viscosity of entangled polymer melts is a major achievement of the tube theory in general. Moreover, the inclusion of the CLF also explains the broadening in the relaxation spectrum, taking into account that every tube increment has its own fluctuation relaxation time, thus leading to a flattened decrease of $G''(\omega)$ in the rubber region.[9,119,126]

When it comes to topologically branched polymer architectures (e.g. star-, comb-shaped), the CLF mechanism contributing to the total stress relaxation gains even more significance, because the branch ends which are structurally fixed via joints to a common backbone cannot reptate along each their side tubes. Reptation as a whole polymer molecule is still possible via dynamic dilution (see **Section 3.3.5**), making the CLF mechanism a necessary prerequisite and majorly governing the relaxation dynamics of branched chains.

3.3.4 Convective Constraint Release (CCR)

So far reptation motion and contour length fluctuation have been considered for a single polymer chain in a static matrix of surrounding polymer molecules. However, the chain in turn also imposes topological constraints on their neighbors and in a real polymer melt the surrounding chains are also moving, continuously creating and releasing entanglements around the chain and vice versa. The mutual release of constraints in fast flowing environments, called convective constraint release (CCR), accelerates the relaxation of the melt, see **Figure 3.7b**.[139] However, its effect is supposed to be rather small in monodisperse, linear polymers, whereas CCR has more influence on polydisperse linear or branched polymer topologies, because short chains or side chains can release constraints via faster relaxation mechanisms, e.g. diffusion or CLF respectively, than long and bulky chains via reptation.

A simplified theoretical description of the generally very complex CCR effect is based on the idea of double reptation, proposed by desCloizeaux[140], and shows reasonable accuracy for many cases. The basic idea behind the mathmatical approach of the double reptation is to view the crossing of two polymers (entanglements) as motionless stress point, which disappears if either one of those chains reptate entirely through it. If both chains reptate independently, what is a priori assumed, the chance that the entanglement point survives and the stress is unrelaxed at time t adds a time-dependent survival probability factor to the relaxation modulus.[9]

3.3.5 Dynamic Tube Dilation (DTD)

In polymer systems with different relaxation time scales, the faster relaxing polymer (or chain segment) can have a distinctive effect on the stress relaxation of the slower moving compound, as already mentioned at the example of CLF on reptation, see Section 3.3.3. In the case of polydisperse linear polymers, with the extreme example of a bidisperse blend, i.e. a binary blend of two monodisperse polymers with different molecular weights, the relaxation time of the high molecular weight component is significantly reduced by the presence of the low molecular weight component. Even though also the shorter chains impose constraints (entanglements) on the longer ones, due to a relative faster motion, the

constraints are released so frequently that the motion of the long chains is significantly less affected then compared with an environment of purely long chains.[138] Therefore, the short chains can be considered as solvents surrounding the higher molecular weight chains. Using the tube model, the lower hindrance in motion and the wider distance to neighboring long chains essentially dilates (enlarges) the tube diameter around the long chain. This concept is called dynamic (tube) dilation[141] or tube enlargement[142].
In the most general case, considering a polymer solution in small molecules, the plateau modulus, G_N^0, decreases with decreasing polymer concentration, ϕ_p, according to **Equation 3.37**, with α as the dilution exponent.[143,144]

$$G_N^0 \propto {\phi_p}^{1+\alpha} \quad \text{with} \quad 1 \leq \alpha \leq 4/3 \tag{3.37}$$

Since the tube diameter, a, is proportional to $a \propto 1/G_N^0$ (Equation 3.33), consequently, the tube diameter is also proportional to $a \propto {\phi_P}^{-1/2}$ (implied by Equation 3.37). If the solvent concentration, or respectively in bidisperse systems the volume fraction of short chain matrix increases, then the reptation time decreases with $\tau_d \propto a^{-2}$, see Equation 3.35. It is important to mention, that this dilation is dynamic, thus the tube enlargement only applies at much longer observation times (low excitation frequencies) than the reptation time of short chains. When the time is decreased comparable to or shorter than the reptation time of the low molecular weight matrix, the constraints are still fully intact and the long chain "feels" a tube diameter which is reduced to its original, non-dilated size.

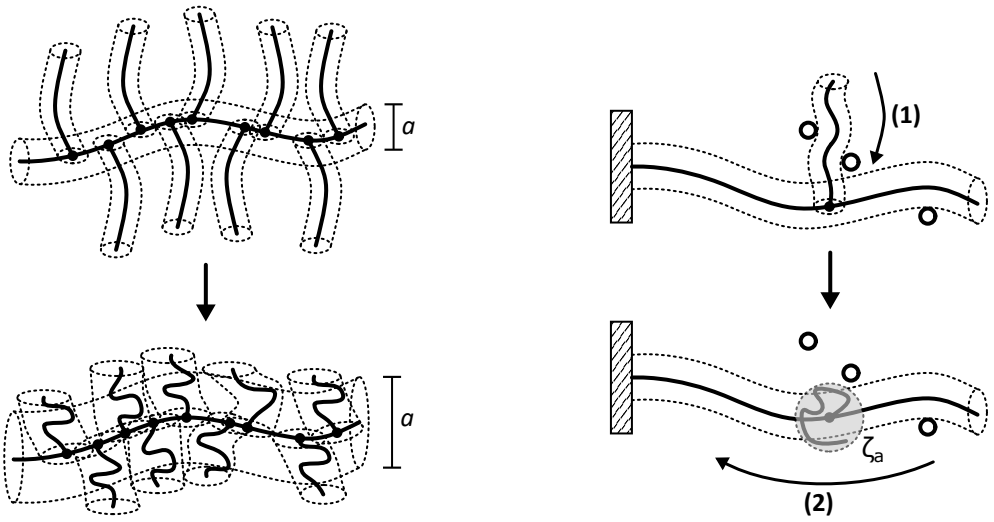

(a) Dynamic tube dilution (DTD). **(b)** Hierarchical relaxation.

Figure 3.8: Concepts describing the dynamical behavior of branched polymer chains with the tube model: **(a)** Dynamic tube dilution (DTD) by relatively fast relaxing chain ends of the branches (by CLF) increases the effective diameter of the tube, a, and decreases the ability of the backbone to entangle. The effective average entanglement molecular weight of the backbone, M_e, becomes larger. **(b)** Hierarchical relaxation of a branched chain where the constrained side arm has to collapse first (1) and becomes a drag point with friction ζ_a, before the inner segments of the chain can further relax (2).

Aside from linear polymers, the effect of dynamic tube dilation (DTD), also called dynamic dilution (DD), is also observed for branched polymers like stars[145] and combs[146]. Due

to the side chains on one end covalently connected to the backbone and the other end conformationally rather unrestricted, the outer segments relax exponentially faster then the inner branch or even backbone segments. Even though for a single side arm reptation is prohibited, the branches are still able to relax, e.g. via fast CLF, around the main chain and therefore dynamically dilute the backbone segments, which results in tube dilation, as schematically shown in **Figure 3.8a**.
From Equation 3.35 one could also conclude that the longest reptation time, τ_d, inverse proportional to a^2, will also be lower for branched polymers than compared with a linear polymer chain of same degree of polymerization, N. Experimentally, there is indeed found a decreased zero-shear viscosity, η_0, for branched polymers, in particular comb polymers, over a wide range of topological constitutions.[120] However, this effect depends on the specific structural parameters of the polymer, e.g. backbone and branch molecular weight, as well as branch number and density. However, for this discussion, the reader is referred to the results in Chapter 5, Section 5.3.1.6 which is addressing this issue in more detail.
It is important to keep in mind that on one hand molecular ends accelerate relaxation due to high mobility, on the other hand branching introduces covalent joints (chemical entanglements) which are sluggish and retard relaxation. Thus, depending on the balance of these effects – resulting from the actual molecular parameters – a linear or branched topology might show a longer relaxation time compared to its equivalently weighing counterpart.

3.3.6 Hierarchical Relaxation

In branched polymers the motion of the inner segments close to the branch points depends on the motion of the chain ends and their ability to relax. Due to different relaxation times with faster mechanisms like CLF at the peripherial chain ends and slower mechanisms like center of mass diffusion (reptation), a (multiply) branched molecule relaxes hierarchically from its extremities inwards.[147,148]

If we consider a branched polymer distorted by a step strain and stress is built across the molecule, the stress release initially starts by relaxation of the motionally most unconstrained chain segment which is the outermost branch end.[149] When the tip of the side arm relaxes and the chain gradually disentangles while collapsing deeper into its tube all the way to the branch point, this side arm does no longer contribute to the entanglement network constraining the branch segment. Now the relaxation of the formerly motion impeded branch segment close to the joint can occur, however the collapsed chain acts as a drag point with friction ζ_a and the reptation or further CLF relaxation is retarded due to the additional drag, see **Figure 3.8b**.[150]

The concept of hierarchical relaxation furthermore applies to multiply branched polymer topologies, and their relaxation can be regarded as cascading CLF from the outermost branching level to the inner branch points until the center of mass can diffuse. However, with so many molecular parameters involved in the complexity of a higher-generation branched architecture, making a generalized statement about the impact of hierarchical mechanism on relaxation is quite challenging. The diffusion of moderately branched, thus

highly entangled dendritic polymers will inevitably depend on the hierarchical relaxation. In contrast to that, an overly dense outer layer of chain ends will "shield" the inner branch points from being engaged in entangling with neighbouring molecules, thus converting the primitive path into a thick tube or even a spherical shape with little to no engagement of inner sections for building a physical network.
These contrary effects – on one hand slowing down relaxation by imposing additional hierarchical branch-point hopping, and on the other hand accelerating relaxation by decreasing entanglement probability due to shielding – is well known for dendrigraft polymers and the balance of these effects ultimately determines the polymers behavior in shear and elongational flow.[9]

3.4 Extensional Rheology

3.4.1 Polymer Melts in Elongational Flow

In the uniaxial elongational experiment, shown in **Figure 3.9**, a sample with length L is clamped on both ends and stretched with a constant velocity, v_x, along the main deformational axis, x, with a constant elongational rate, known as Hencky[151] strain rate, $\dot{\varepsilon}_\mathrm{H}$, **Equation 3.38**.[9,126,128]

$$v_\mathrm{x} = \dot{\varepsilon}_\mathrm{H} \cdot x \tag{3.38}$$

If the deformation is uniform from both ends, the center of the sample does not move ($v_\mathrm{center} = 0$), whereas the sample ends distance, L, increases with a velocity of v_x from the center, see **Figure 3.9a**.

$$v_\mathrm{end} = \dot{\varepsilon}_\mathrm{H} \cdot \frac{L}{2} \qquad \text{and} \qquad \frac{dx}{dt} = \dot{\varepsilon}_\mathrm{H} \cdot x \tag{3.39}$$

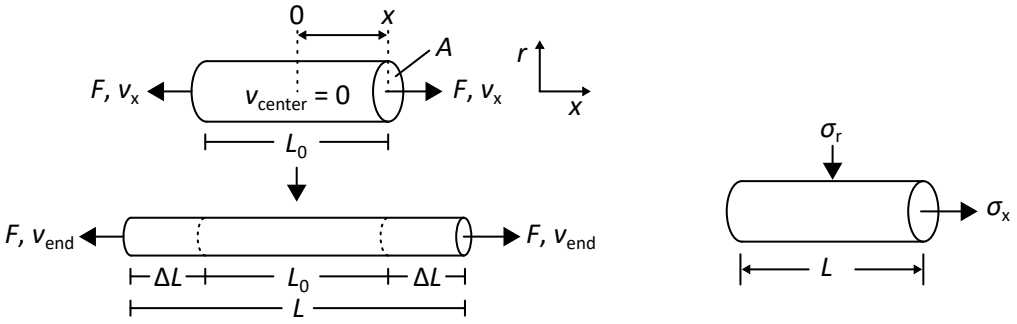

(a) Uniaxial deformation of a cylindrical sample. **(b)** Components of the extensional stress, σ_ext.

Figure 3.9: Schematic illustration of the uniaxial extension of a rod in deformation direction x in a cylindrical coordinate system.[11]

Integration over the whole stretching range ($2\,\Delta L$) from L_0 to L leads to **Equation 3.40**, with the Hencky strain, ε_H, as the logarithmic unit of measure for extension.

$$\dot{\varepsilon}_{\mathrm{H}} \cdot t = \varepsilon_{\mathrm{H}} = \int_{L_0}^{L} \frac{1}{x} dx = \ln(\frac{L}{L_0}) \quad \Leftrightarrow \quad L = L_0 \cdot \exp(\dot{\varepsilon}_{\mathrm{H}}\, t) \tag{3.40}$$

In common polymer melt processing techniques, often elongations in the range of several hundred percent occur, corresponding to a typical Hencky strain of $\varepsilon_{\mathrm{H}} \approx 2 - 3$.[9,119] Inserting Equation 3.40 into Equation 3.38 results in **Equation 3.41** as an expression for the sample end velocity, v_{end}.

$$v_{\mathrm{end}} = \frac{1}{2} \dot{\varepsilon}_{\mathrm{H}} \cdot L_0 \cdot \exp(\dot{\varepsilon}_{\mathrm{H}}\, t) \tag{3.41}$$

A constant extension rate during the elongation of the sample is only achieved if the sample end velocity v_{end} increases exponentially, which is a challenge when it comes to the technical instrumentation in extensional rheometry (see Section 3.4.3).
While the sample is stretched bidirectionally with an axial stress σ_{x}, the sample's surface experiences an uniform normal stress, σ_{r}, in the radial plane (**Figure 3.9b**). The resulting extensional stress, σ_{ext}, (also called tensile stress), defined as the difference between the axial stress and the stress acting on the free surface, is the force, F, per unit area, A, acting on the end of the sample.

$$\sigma_{\mathrm{ext}} = \sigma_x - \sigma_r = \frac{F}{A} \tag{3.42}$$

Polymer melts can be considered as incompressible, therefore the sample volume, $V = \pi R_0^2 L_0$, is treated as constant over time, t.

$$V = V_0 = A(t)\, L(t) \tag{3.43}$$

According to the exponential increase in sample length, $L(t)$, the cross section area, $A(t)$, is decreasing exponentially, according to **Equation 3.44**.

$$A(t) = A_0 \cdot \exp(-\dot{\varepsilon}_{\mathrm{H}}\, t) \tag{3.44}$$

Then, the extensional stress, σ_{ext}, can be expressed as **Equation 3.45**.

$$\sigma_{\mathrm{ext}} = \sigma_{\mathrm{x}} - \sigma_{\mathrm{r}} = \frac{F \cdot \exp(\dot{\varepsilon}_{\mathrm{H}}\, t)}{A_0} \tag{3.45}$$

In analogy to the viscosity in shear (see Equation 3.7), the transient extensional viscosity, η_{E}^{+}, also called tensile stress growth coefficient, can be defined as **Equation 3.46**.[9]

$$\eta_{\mathrm{E}}^{+} = \frac{\sigma_{\mathrm{ext}}(t, \dot{\varepsilon}_{\mathrm{H}})}{\dot{\varepsilon}_{\mathrm{H}}} \tag{3.46}$$

At low extensional rates or long times, for a viscoelastic material with a Poisson's ratio $\mu = 0.5$ (constant volume in uniaxial tension) a relationship with a factor of 3 is found between the shear viscosity, $\eta_{\mathrm{S}}^{+}(t)$, and the uniaxial extensional viscosity, η_{E}^{+}, see **Equation 3.47**.[9]

$$\eta_{\mathrm{E}}^{+}(t) = 3 \int_0^t G(t)\, dt = 3\, \eta_{\mathrm{S}}^{+}(t) \tag{3.47}$$

This dependence is also called "Trouton ratio" ($Tr = \eta_E^+/\eta_S^+ = 3$)[152] and is useful to normalize extensional viscosity data. Moreover, it can be used as an indicator to assess the quality and reliability of the elongational experiment by comparison with the linear viscoelastic (LVE) behavior in shear, as shown in **Figure 3.10**.

In case the transient extensonal viscosity, η_E^+, increases in time and exceeds the factor of 3, a strain hardening behavior is observed, see the following **Section 3.4.2**.

This strain hardening behavior typically occurs in polymer melts of long chain branched (LCB) topologies. Vice versa, if the viscosity decreases below the LVE prediction when the melt is elongated, the polymer shows strain softening behavior which is commonly observed in linear or barely entangled polymers.[9]

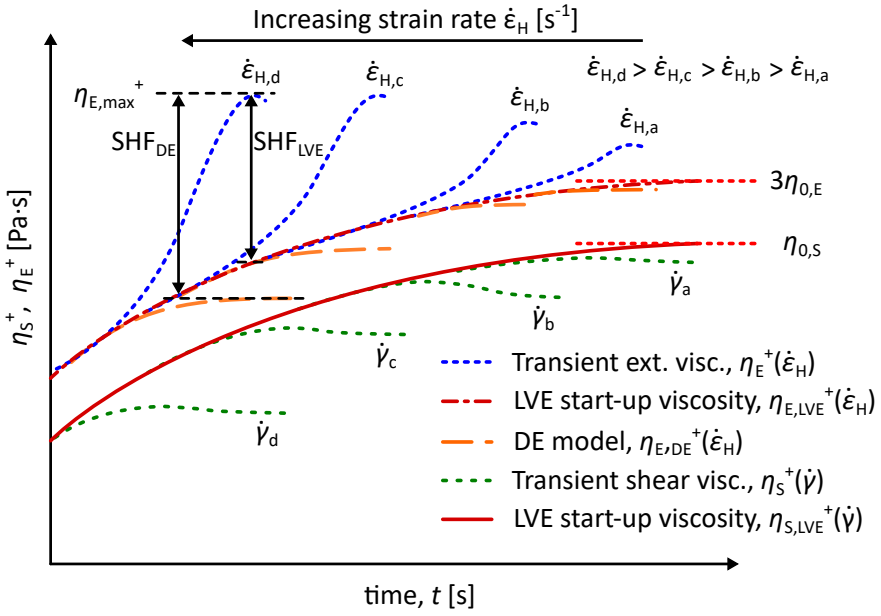

Figure 3.10: Schematic illustration of the transient extensional viscosity, η_E^+ (blue), and transient shear viscosity, η_S^+ (green), of a typical viscoelastic polymer melt at different shear, $\dot{\gamma}$, and extensional Hencky strain rates, $\dot{\varepsilon}_H$. In case the $\eta_E^+(t, \dot{\varepsilon}_H)$ exceeds the linear viscoelastic (LVE) start-up viscosity curve (red), the material is strain hardening, quantified by the strain hardening factor (SHF). In the slow flow regime, at small rates, both shear and extensional LVE material functions converge to the zero-shear viscosity, which differs by a factor of 3, called "Trouton ratio", with $\eta_{0,E}^+ = 3\,\eta_{0,S}^+$.[153]

3.4.2 Quantification of Strain Hardening

When it comes to processing polymers into filaments or sheets, strain hardening is beneficial as inhomogeneities in thickness are mitigated when the material is stretched. For example, if in film blowing, due to material unevenness, a smaller cross section area locally experiences a stronger elongational stress, the strain hardening counteracts with an increasingly resistive force against further decrease of the wall thickness due to excessive strain. In that sense the hardening resembles a self-healing behavior to compensate inhomogeneities and to reach thin, light-weight material structures.[119]

In contrast, inhomogeneities in non-strain hardening polymer melts are amplified with increasing elongation, which leads to premature failure of the material, e.g. filament or film rupture.[9,119,126]

To quantify the strain hardening and to compare the resulting material properties, the strain hardening factor (SHF) is introduced and defined in **Equation 3.48** as the ratio of the maximum (steady state) tensile stress growth coefficient (i.e. extensional viscosity), $\eta^+_{\mathrm{E,max}}(\dot{\varepsilon}_\mathrm{H})$, to the one predicted by the Doi-Edwards (DE) model, $\eta^+_{\mathrm{DE,max}}(\dot{\varepsilon}_\mathrm{H})$, see also Figure 3.10.

$$\mathrm{SHF} \equiv \frac{\eta^+_{\mathrm{E,max}}(t, \dot{\varepsilon}_\mathrm{H})}{\eta^+_{\mathrm{E,DE}}(\dot{\varepsilon}_\mathrm{H})} \tag{3.48}$$

The Doi-Edwards prediction and its use as the basis for the calculation of strain hardening will be explained in more detail in the following **Section 3.4.2.1**.

Since strain hardening behavior is important for melt stability in elongational processes, it has also a positive effect on the cell wall stability and expandability of polymer foams. Although the elongation in foaming is biaxial (bi), there is a relation to the extensional viscosity that can be measured in uniaxial direction (uni), expressed by **Equation 3.49**.[128]

$$\eta^+_{\mathrm{E(bi)}} = 2\,\eta^+_{\mathrm{E(uni)}} \quad \text{and} \quad \eta_{0,\mathrm{E(bi)}} = 2\,\eta^+_{0,\mathrm{E(uni)}} = 6\,\eta^+_{0,\mathrm{S}} \tag{3.49}$$

Therefore, strain hardening occurring in biaxial deformation is directly reflected in uniaxial elongational experiments,[119] and consequently can be quantified with relatively simple instrumentation (see **Section 3.4.3**), since technically challenging biaxial rheometers are not fully developed and still unsuitable for routine use.[9]

3.4.2.1 Doi-Edwards (DE) and Molecular Stress Function (MSF) Model

To evaluate the degree of nonlinearity of a deformation, the Weissenberg[13] number, Wi, a dimensionless group as the product of a characteristic time, τ, of the fluid and a characteristic deformational rate, $\dot{\gamma}$ or $\dot{\varepsilon}$, gives a simple tool in behavioral prediction or correlation of data, see **Equation 3.50**.[154]

$$Wi = \dot{\gamma}\tau = \gamma_0\omega\tau \text{ (shear)} \qquad \text{or} \qquad Wi = \dot{\varepsilon}\tau \text{ (extension)} \tag{3.50}$$

When a (e.g. uniaxial) shear or extensional strain rate, $\dot{\gamma}$ or $\dot{\varepsilon}$ respectively, is applied to a polymer system in its relaxed, equilibrium state with a rate much faster than the longest relaxation rate, e.g. reptation relaxation, but slow compared to the segmental (Rouse) relaxation, i.e. $1/\tau_\mathrm{d} < \dot{\varepsilon} < 1/\tau_\mathrm{R}$, the Gaussian conformation of the chain segments within the "blobs" can be restored at any time, see **Figure 3.11a**.
In contrast, the tubular superstructure can only respond at that excitation rate with re-orientation, as shown in **Figure 3.11b**. Here, the characteristic time of reptation, $\tau = \tau_\mathrm{d}$, decribes the first onset of nonlinear behavior at low frequencies matching $Wi \approx \dot{\gamma}\tau_\mathrm{d}$.

The DE model is based on the tube theory of Doi and Edwards,[131,132] and in non-linear deformation, e.g. extensional flow or stress overshoot in shear flow, it assumes the stress to result solely from those orientational changes.[155]

[13] Another dimensionless group which looks similar to the Wi is the Deborah number, $De = \dot{\gamma}\tau$ or $\omega\tau$. Whereas the Weissenberg number is intended to describe the onset of nonlinearity of a material's rheological response, the Deborah number is a measure to describe when an elastic contribution to a viscous material is obtained upon deformation, i.e. the onset of viscoelasticity.[154]

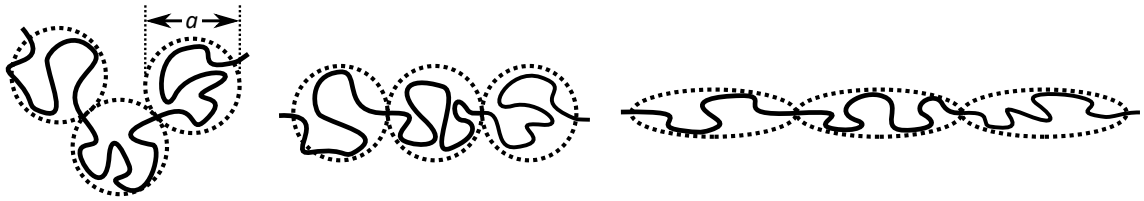

(a) Relaxed. $\dot{\varepsilon} < 1/\tau_{\mathrm{d}}$ **(b)** Oriented. $1/\tau_d < \dot{\varepsilon} < 1/\tau_{\mathrm{R}}$ **(c)** Stretched. $\dot{\varepsilon} > 1/\tau_{\mathrm{R}}$

Figure 3.11: Degree of chain deformation assessed via the Weissenberg number in shear ($Wi = \dot{\gamma}\tau$) or extension ($Wi = \dot{\varepsilon}\tau$), illustrated on the blob model. **(a)** The applied strain is lower than the inverse reptation time τ_{d}. The tube and the chains within the tube segments are relaxed at any time. **(b)** The strain exceeds the reptation time and the tube is re-oriented. **(c)** The strain exceeds the segmental Rouse relaxation time. Under fast deformation conditions, the polymer itself gets stretched while the tube diameter decreases.

However, tube orientation is not the only molecular process happening in steady-state shear and elongational flows and the Doi-Edwards theory does not take into account tube diameter reduction associated with chain stretching beyond the equilibrium contour length of the tube, see **Figure 3.11c**, which is the major origin of strain hardening. As a result, elongational viscosity predictions for linear polymers are underestimated by DE and reach an early plateau, in particular at fast rates when orientation is slow and lags behing stretching.[9] This is especially the case when it comes to more complex systems like polydisperse polymers or the presence of branching, where the theory fails inevitably for a full quantitative description because of the not-consideration of branch point withdrawal. That means, when the tube is stretched, only free chain ends of the backbone can retract back into their tube. The retraction of deeper backbone segments is retarded by branch points and subject to entropically favorable side chain dynamics.[156]

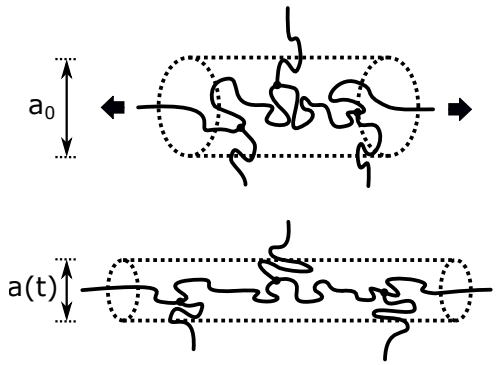

Figure 3.12: Uniaxial deformation of a tube segment and change in the tube diameter from undeformed a_0, to deformed $a(t)$. The oriented backbone tube is stretched, while the side chains, perpendicular to the direction of deformation, are compressed.

As a consequence, elongational viscosity predictions for linear polymers are underestimated by the DE theory and reach an early plateau, especially at fast rates when orientation is slow and lags behind stretching. This plateau was suggested by Wagner et al.[157] to be taken as the basis for the quantification of strain hardening (see Equation 3.48) as the DE prediction accounts for the the re-orientation effect only and any viscosity upturn deviation is attributed to this chain stretching. The definition of strain hardening as an upturn above

the LVE (cf. Hepperle et al.[158] and López-Barrón et al.[159]) is not recommended as it does not quantify the stretching effect. Nonetheless, the definition SHF $= \eta^+_{\mathrm{E,max}}/\eta^+_{\mathrm{E,LVE}}$ is also widely used, because it does not require mathematical simulation of the DE model and still gives a simple but very good estimation on the extent of strain hardening.

The DE model can be extended by a so called molecular stress function (MSF), taking into account the structural-molecular characteristics and the change in tube diameter due to stretching or compression, as exemplarily shown in **Figure 3.12**, and ultimately leading to very good predictions of the steady-state elongational viscosities via the MSF model.[160–162] Moreover, the MSF constitutive equation, originally developed by Wagner et al.[163] from the slip-link model, also proved useful for predicting other rheologically nonlinear phenomena, e.g. in medium and large amplitude oscillatory shear (MAOS and LAOS), as well as in transient shear flow for simple linear and topologically more complex polymer systems.[164,165]

The mathematical approach of the MSF constitutive **Equation 3.51** can be expressed as a generalization of the DE model and will be briefly covered in the following paragraph.[14] The extra stress tensor, $\sigma(t)$, building up from a time t' of stress-free state with equilibrium tube diameter, until a time t when the stress is measured, is given by Equation 3.51,

$$\sigma(t) = \underbrace{\int_{-\infty}^{t} m(t-t')}_{\mathrm{DE}} \underbrace{f^2(t,t')}_{\mathrm{MSF}} \underbrace{\boldsymbol{S}^{\mathrm{IA}}_{\mathrm{DE}}(t,t')\, dt'}_{\mathrm{DE}} \tag{3.51}$$

with the Maxwell viscoelastic memory function, $m(t-t')$ (**Equation 3.52**), and measure of strain, $\boldsymbol{S}^{\mathrm{IA}}_{\mathrm{DE}}(t,t')$ (**Equation 3.53**), both originating from the DE Equation 3.51 (underlined as "DE").
As already mentioned above, the molecular stress function, $f(t,t')$ (Equation 3.51, underlined "MSF"), is the extension taking tube stretching into consideration.

The memory function, $m(t-t')$, is obtained from the relaxation spectrum, $\{g_i, \tau_i\}$ (see Section 3.2.1, Equation 3.26 and 3.27), by fitting the Maxwell model to the LVE data.

$$m(t-t') = \frac{\partial G(t-t')}{\partial t'} = \sum_{i=1}^{N} \frac{g_i}{\tau_i} \exp\left(\frac{t-t'}{\tau_i}\right) \tag{3.52}$$

The strain measure, $\boldsymbol{S}^{\mathrm{IA}}_{\mathrm{DE}}(t,t')$, of the DE model is a relative orientation tensor, that assumes the stress tensor, $\sigma(t)$, to be the result of a mere orientational change via tube segment rotation.[166] The notation involves the independent alignment approximation (IA), assuming all chain segments – even though molecularly coupled to each other – to deform independently from its neighbors, which reduces the complexity and enables computability.[10]

$$\boldsymbol{S}^{\mathrm{IA}}_{\mathrm{DE}}(t,t') = 5\,\boldsymbol{S} = 5\left[\left(\frac{1}{J-1}\right)\boldsymbol{B} - \left(\frac{1}{(J-1)(tr(\boldsymbol{C})+13/4)^{0.5}}\right)\boldsymbol{C}\right] \tag{3.53}$$

[14] For detailed derivation and further reading into the topic of the DE and MSF theory, the reader is referred to textbooks[166] and following citations in this chapter.

$$\text{with} \quad J = tr(\boldsymbol{B}) + 2(tr(\boldsymbol{C}) + 13/4)^{0.5} \tag{3.54}$$

The approximation by Curie[167] includes the Cauchy and Finger tensors $\boldsymbol{C}$ and $\boldsymbol{B}$, respectively, with their traces[15] $tr(\boldsymbol{C})$ and $tr(\boldsymbol{B})$.

The molecular stress function, $f(t,t')$, represents the relative tension in the macromolecular chain, which increases by decreasing tube diameter from its equilibrium state, a_0, to a reduced diameter, $a(t,t')$; basically it's the inverse of the relative tube diameter, a/a_0, see **Equation 3.55**.

$$f(t,t') = \frac{a_0}{a(t,t')} \tag{3.55}$$

The mathematically separate treatment of the stress function is only possible because of the underlying assumptions: Segment rotation is an affine deformation and tube elongation is orientation independent, i.e. all chains undergo the same isotropic extension with a stretch factor, f.[157,166]

As the values of the tube diameter are not directly accessible, finding a proper expression for f needs to be circumvented. Therefore, the square of the relative tension, i.e. square of the stress function, f^2, is introduced into Equation 3.51 as related to the free strain energy stored in the polymer system via decreasing entropy due to orientation. The solution of f^2 is found by solving an evolution equation based on energy balance.[157,168]

Depending on the polymer system and its topology, numerous different evolution equations have been described, each specific from suitable assumptions and approximations about structural parameters,[169] and compared to experimental results, e.g. from linear monodisperse[170], bidisperse[171] and polydisperse[172], to SCB and LCB[173] polymer systems and blends thereof[174], as well as model comb[155,162] and pom-pom[175,176] molecules with hierarchical relaxation modes[177].

For example, Abbasi et al.[120,164,168] proposed an evolution **Equation 3.56**, which was verified with a variety of linear and branched polymers showing good quantitative description.[16]

$$\frac{\partial f^2}{\partial t} = \beta\dot{\varepsilon} f^2 \left(S_{11} - S_{33} - \frac{f^2 - 1}{f^2_{\max} - 1}\sqrt{S_{11} + \frac{1}{2}S_{33}} \right) \tag{3.56}$$

The key point to be emphasized by this example is that the molecular stress function is only comprised of two nonlinear scalar parameters, β and $f^2_{\max}$, serving as fitting parameters for the uniaxial stress growth coefficient data and connecting the strain hardening criteria with the characteristics of the molecular structure, and in this case the branching in particular. The parameter $f^2_{\max}$ governs the steady-state value (maximum) of the viscosity in extensional flows, while the parameter β governs the slope of the extensional viscosity. Moreover, β is closely related to the branching structure as it represents the ratio of the

[15] The trace is the sum of the diagonal elements of the 2nd order tensor's matrix: $tr(\boldsymbol{A}) = \sum_{i=1}^{n} a_{ii}$.

[16] The MSF model for LCB polymers, proposed by Abbasi et al.[120,164,168], assumes the branch segments which are part of the backbone tube to be compressed, while the main part outside the tube to be stretched due to frictional motion of the outer branch tube via entanglement interacion.

total (backbone and branch) entanglement number of the molecule, Z, to the entanglement number in the stretched tube, which precisely is Z_{bb} of the backbone, see **Equation 3.57**.

$$\beta_{\mathrm{definition}} = \frac{Z}{Z_{\mathrm{bb}}} = \frac{Z_{\mathrm{bb}} + Z_{\mathrm{br}} N_{\mathrm{br}}}{Z_{\mathrm{bb}}} = 1 + \frac{Z_{\mathrm{br}} N_{\mathrm{br}}}{Z_{\mathrm{bb}}} = \frac{M_{\mathrm{w}}}{M_{\mathrm{w,bb}}} = \phi_{\mathrm{bb}}^{-1} \tag{3.57}$$

3.4.3 Instrumentation

Due to technical challenges in implementation, progress in rheometry investigating elongational flow happened mostly in the last two decades - compared to relatively simple and therefore earlier developed instrumentational setups for shear rheology.[9,119]
Pioneering experimental work was made by Cogswell[178] using the principle of a tensile testing machine with fixed clamps on polymer melts and applying constant stress, resembling a creep-extension. Improvements were made with a servomotor controlling the speed of the pulling rod in Münstedt's[179] Tensile Rheometer (MTR), thus a uniform accelerated velocity with a constant Hencky strain rate up to $\dot{\varepsilon}_{\mathrm{H}} = 5\,\mathrm{s}^{-1}$ could be achieved. The first experimental machine leading to a commercial Rheometrics Melt Extensional Rheometer (RME) was based on Meissner's[180] horizontal design with two pairs of toothed wheels in fixed distance pulling the sample from both sides. This setup made use of the definition of the Hencky strain, providing a constant elongation rate in a simple way by constant wheel velocity. Even though this allowed the machine to be much more compact in size than previous models, it still had some drawbacks with handling and relatively large amounts of material needed.[119]

3.4.3.1 Extensional Viscosity Fixture (EVF)

It was not until the development of fiber windup rheometers, namely the Sentmanat Extensional Rheometer (SER, from Xpansion Instruments)[181,182] as well as its technically similar Extensional Viscosity Fixture (EVF from TA Instruments)[183,184], that extensional rheometry became a viable characterization method for routine laboratory work. Both devices can be attached to conventional rotational rheometers and therefore offer the huge advantage of a relatively simple and cost effective possibility to perform additional uniaxial elongation tests of polymer melts on already existing host equipment. The SER and EVF make use of the same working principle, with two drums in fixed distance driven by the motor via gears in counterrotating motion. The sample is winded up from both sides and stretched on a constant length (cylinder distance) L_0 during the extension. Analoguous to the Meissner design, a constant strain rate $\dot{\varepsilon}_{\mathrm{H}}$ is achieved by a uniform velocity of the drums.

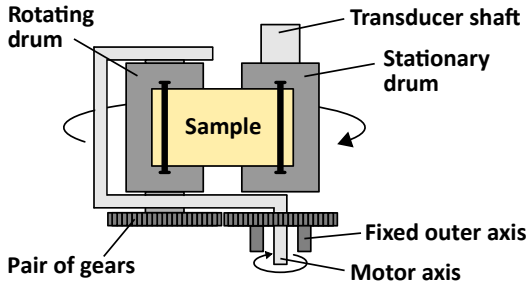

(a) The stationary drum (upper geometry part) is directly coupled with the torque transducer, while the rotating drum (lower geometry part) is connected to the motor through a pair of gears.

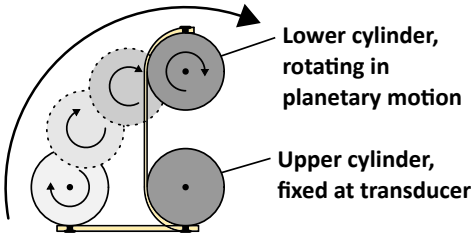

(b) The lower drum moves in a circular orbit around the fixed drum by simultaneously rotation on its own axis, ensuring uniform sample deformation at constant extensional rates $\dot{\varepsilon}_H$.

Figure 3.13: Schematic functional principle of the Extensional Viscosity Fixture (EVF) for ARES-G2 rheometer showing **(a)** the geometry setup, and **(b)** the planetary motion mechanism for achieving a logarithmic strain (Hencky strain), ε_H, via keeping a constant rotational speed and strain rate, $\dot{\varepsilon}_H$.

The extensional measurements in this work were performed on the EVF geometry, see **Figure 3.13**. The sample is attached at both ends, each to one cylinder, **Figure 3.13a**. While the drum geometry in the motor axis is fixed at the torque transducer, the other drum rotates in planetary motion around the stationary one and therefore elongates the sample uniform in both directions, **Figure 3.13b**. Due to the separation of rotating compounds with motor and gears, the extensional force caused by direct material response pulling at the transducer is not affected by gear friction as in the case of the SER. Due to the drum dimensions and distance, the EVF as well as the SER are limited to a maximum Hencky strain of up to $\varepsilon_H = 4.3$. However, this only accounts for samples not thicker than 0.7 mm and mostly Hencky strains between 3 and 4 are the practical limit until after one drum revolution the stretched sample comes into contact with its ends or the retaining brackets. For samples breaking at much higher Hencky strains, testing at a filament stretch rheometer (e.g. VADER1000 with $\varepsilon_{H,max} \sim 6$[185]) might be more suitable.

Recently, a new horizontal design of a fiber windup rheometer was presented, developed by Li et al.[186] using the ARES-G2 rotational rheometer as the host machine. Instead of attaching the samples vertically to the drums like for the SER and EVF, where they are prone to gravitational sagging effects, the new horizontal extensional rheometer (HER) offers the possibility to attach the sample from below the counterrotating drums where they are supported by a lubricated platform and giving the big advantage to measure extensional viscosities as low as 500 Pa·s, compared to $\sim 10^4$ Pa·s for the EVF/SER. With respect to the design, the HER can be seen as a technical hybrid of the RME and the SER, as the transducer is connected to the drive wheel, thus having to take inherent (e.g. gear) friction into account. However, the new testing device, even sufficiently validated within a wide range of viscosities, has not reached commercial status yet and high molecular weight PS – especially branched ones – exhibits good melt strength for testing in vertical devices.

4 Fundamentals of Polymer Foaming

The following chapter is dedicated to introduce the principles of physical foaming of thermoplastic polymers. This complex topic is broken down into first explaining the morphological characteristics and properties of the cellular structure, and then the common processing methods and foaming technologies are briefly presented. Thereafter, the stages of the foaming process are highlighted with the focus on the here employed one-step batch foaming method.
Finally, the historical and technical aspect of commercial polystyrene foam production is summarized, closing the theoretical part of the thesis.

4.1 Introduction

Amongst the solid foams, polymeric foams are the biggest representative of solid cellular materials. With a global market share of about 120 billion USD (in 2020),[187,188] they exceed the metal foam market, that has only a global share of about 70 million USD (in 2020),[189] by more than three orders of magnitude. Building and construction (∼30 %), automotive (∼20 %), as well as packaging applications (∼15 %) are the major market segments and make up about 75 % in terms of revenue.[188]

Owing to their wide variety in chemical composition, thermal and mechanical behavior, the processing of polymers into cellular materials enables a broad spectrum of foam properties which can be tuned according to processing techniques, conditions and additives. Depending on the cellular morphology with isolated air pockets (closed-cell foams) or continuous pores (open-cell foams), the internal foam structure can block heat convection or accommodate fluids, respectively. Furthermore, the free volume allows elastic or inelastic deformation of the polymer framework to dissipate energy or provides structural stability at low density. From everyday objects to hightech engineering materials, those main features of foams, i.e. thermal insulation, absorbency, energy dissipation, high relative strength at light weight, all on their own or combined define their application.[4,5,7,190]

Table 4.1: Examples of different ways to classify foams with respect to their cellular structure or manner of preparation.

Category	Possible classification
Cellular structure:	
Morphology	open-, mixed-, closed-cell
Stiffness	rigid, flexible
Density (VER) [a]	high (≤4), medium (≥4–10), low density (≥10–50)
Cell size (µm) [b]	macro- (∼10), micro- (<10), nanocellular (<1)
Preparation:	
Foaming method	mechanical, chemical, physical
Processing	batch, extrusion, injection molding

[a] The (unitless) foam *relative* density, $\rho_{rel} = \rho_f/\rho_p$, is the inverse of the volume expansion ratio, VER = $\rho_p/\rho_f \approx 1/\rho_f$, for polymeric foams.[8] [b] The cell sizes shown represent the rough order of magnitude. The classification often depends on the literature which also considers the cell density as a criteria.

Polymer foams can be categorized in various ways with respect to their appearance, macro- or microscopic properties, but also their manner of production.[6] **Table 4.1** gives an overview of possible classifications which will be covered in the course of this chapter.

4.2 Polystyrene Foams

The first description of polystyrene dates back to 1839 when a Berlin pharmacist, Eduard Simon found, that the oily liquid distilled from storax resin and which he named "styrol", increased in viscosity when stored for days and eventually turned solid after months. However, it was not until the modern age of polymer science, estabished by the work of Hermann Staudinger (ca. 1920), when the auto-polymerization of styrene was recognized as the formation of macromolecular chains from the monomer.[191] Even though at that time academic research just started to understand the chemical nature of PS, the properties already gained industrial interest with respect to possible applications. From 1930 on, nearly 100 years after the discovery of PS, IG. Farben (a company conglomerate of six companies, including i.a. BASF, Bayer, Hoechst and Agfa)[192] started the development of large-scale extrusion of PS, followed by Dow Chemicals in USA, in the mid-1930s.[1,7] In those early years of science and advancements in polymer chemistry, the versatility of PS became clear, when in 1931 Munters and Tandberg[193], two swedish inventors treated PS with blowing gases and filed a patent application for the production of "porous or cellular articles or materials" from macromolecular substances for heat insulation.[6] This method was rediscovered by researchers of Dow Chemicals in 1941 and the company obtained a license to produce lightweight, insulating PS that was patented and traded under the Styrofoam® brand name.[6,50] Few years later, chemical engineer Stastny impregnated beads of PS with aliphatic hydrocarbons and invented pre-expanded PS spheres for molding and extrusion. This processing method, patented in 1949 by the BASF, has ever since been a source of product developments, e.g. Styropor® and Neopor®.[190]

Even though the European demand for PS ranks only at the sixth place after PE (incl. LDPE and HDPE), PP, PVC, PU and PET,[194] however in foamed condition it is still the market dominating polyolefin. In comparison to all synthetically produced foams, PS consistently ranks second behind PU. The global market for all PS is estimated to about 30 billion USD,[195] of which about 10 billion USD (∼1/3) is dominated by the expanded polystyrene (EPS) market segment.[196]

4.2.1 Expanded Polystyrene (EPS)

The production of expanded polystyrene (EPS) foam begins with the free-radical suspension polymerization of styrene in water, which yields small, compact PS spheres with an average diameter of ∼200 µm. The dry beads are then impregnated in an agitation reactor with a low-boiling hydrocarbon, mostly pentane (or butane) as blowing agent. In the next step, those raw beads are pre-expanded above 90 °C with steam. The puffed beads, now 40–50 times their original size, are then cured for 6–12 h. In this time, the cooling down of the blowing agent and water vapor creates a slight vacuum which is compensated by diffusion of air into the PS. Finally, the cured PS are fed into a mold and steamed again to further expand the residual blowing agent and inflate the beads until they completely fill out the mold cavity and agglutinate and melt into each other at their surface. The resulting rigid closed-cell foam is tough and has a porosity of 96–98 %[17] and a density of 10–30 kg/m^3.[7,190]
The shape of the solidified EPS foam depends on the form of the mold which allows to create a nearly infinite variety of EPS product designs that can be costum tailored for packaging or insulation to adopt the shape of the enclosed object, e.g. interior helmet padding or exterior cushioning for shipping fragile devices. Furthermore, especially molded in blocks, it's preferrably used for thermal insulation in construction.[5,190]

4.2.2 Extruded Polystyrene (XPS)

In extruded PS, the blowing agent CO_2 is fed into the extruder under pressure and the gas-accumulated polymer is expelled from the die. The wide-slit nozzle where the gas expands forms a continuous, rectangular foam block of a thickness technically limited to 2 m. Those extruded, closed-cell and light-weight foam blocks are then readily cut into insulation boards for interior or exterior wall panelling.[7] Furthermore, due to their relatively high density which is in the range of 30–34 kg/m^3 and thus slightly higher than that of EPS foams, they also exhibit enough stiffness and prove useful for model building.[8]

4.3 Foam Structure

The foam properties, like density, mechanical strength, or thermal conductivity, can be macroscopically analyzed and are highly governed by the microscopic structure and porosity

[17] The porosity is a measure of the foam volume fraction that is occupied by air. It commonly expresses the void fraction, $\phi_{\text{void}} = 1 - \rho_{\text{rel}} = 1 - \rho_{\text{f}}/\rho_{\text{p}}$, as volume percentage (vol%).[5,8]

of the polymer framework with cell morphology and cell size among the main important structural features.

4.3.1 Cell Morphology

The gas phase of open-cell foams is continuous and traversed by the polymer like a three-dimensional interconnected network of struts, resulting in a very high material porosity that is relatively soft. Apart from increased flexibility, the permeability for gas or liquids is often a desirable feature or even primary reason for the choice in application when it comes to soaking or filtering properties. In closed-cell structures, on the other hand, the gas is trapped in discrete pockets and the voids inside the foams are isolated via cell walls of the polymer. Therefore, closed-cell foams are in general more dense but excel in applications where structural integrity, high dimensional stability, and insulation combined with low density are key properties.[5]

Typically, the polygonal structure of the polymer framework, composed of vertices, edges, and faces is disordered and the cells exhibit a size distribution.[5] An idealized cell structure has been described by Weaire and Phelan[197], who discovered by computation a foam structure that was 0.3 % smaller in surface area than the one proposed by William Thomson (a.k.a. Lord Kelvin)[198] in 1887. Up to 1994, Thomsons structure was accepted as the optimum arrangement of polyhedrons with respect to a maximum volume and simultaneously minimum surface area.[18] His truncated octahedron had 8 hexagonal and 6 quadratic faces, resulting in a total of 14 neighboring cells, whereas the newly discovered Weaire-Phelan structure consisted of a regular arrangement of distorted dodecahedrons (12 pentagonal faces) and irregular tetradecahedron (12 pentagonal faces + 2 hexagonal faces = 14 polygonal faces) with an average total of 13.5 neighbor polygons.[199] This idealization is considered to reflect the architecture of real foams with best approximation, as structural investigations of foams also almost exclusively found pentagonal (55–65 %) and hexagonal (∼20 %) faces over a small portion of quadratic (10–24 %) shapes. For example, enclosed soap foam bubbles have an average count of 14 surrounding bubbles and PU foam cells are mostly surrounded with a number of 13 neighbors.[5]

4.3.2 Thermal Conductivity and Knudsen-Effect

The thermal conductivity of a cellular material, e.g. a polymeric foam, λ_f, can be expressed in **Equation 4.1** as a sum of individual contributions to the total heat transfer.[4,200]

$$\lambda_f = \lambda_s + \lambda_g + \lambda_c + \lambda_r \tag{4.1}$$

For low foam densities, the conductivity of the solid polymer frame, λ_s, becomes negligible. The same accounts for the heat convection within the cells, λ_c, since the direct heat transport due to the movement of the fluid (i.e. gas molecules) is already blocked or

[18] The search for an optimum arrangement of polyhedral cells to minimize the surface area of a given bubble volume, i.e. to find the energetically most efficient soap bubble, is known as “Kelvin problem”, posed by William Thomson in 1887.

tremendously reduced at cell sizes below the mm-dimension[19], which most foams anyway comply. The radiative term, λ_r, can be reduced by shielding or using fillers or paints that reflect or extinct radiation. Then, the conduction through the gas phase, λ_g, remains as one major factor to improve the insulating properties, of which reducing the cell size is considered as the most advantageous approach.[190]

With the focus towards nanocellular foams of less than 1 µm cell size (and 10^{15}–10^{16} cells/cm^3), it is expected to achieve unique material properties of which one of those is the significantly reduced thermal conductivity, making use of a diffusion phenomenon called Knudsen effect.[201,202] When the pore size is reduced and approaches the mean free path of gas molecules (ca. 70 nm), the gas molecules collide with the cell walls more frequently than with other gas molecules inside the pore, as illustrated in **Figure 4.1a**.[203,204]
As a consequence, the heat conductivity decreases quite drastically, as can be seen from **Figure 4.1b**, that shows the theoretical prediction[205] which further was found to be in agreement with experimental data.[200]
For example, the decrease of the cell size to 100 nm reduces the thermal conductivity from ca. 0.025 mW/mK to less than 0.01 W/mK, potentially being 2–3 times more energy efficient when used as high performance insulation compared to conventional micro- or macrocellular foams.[200,206]

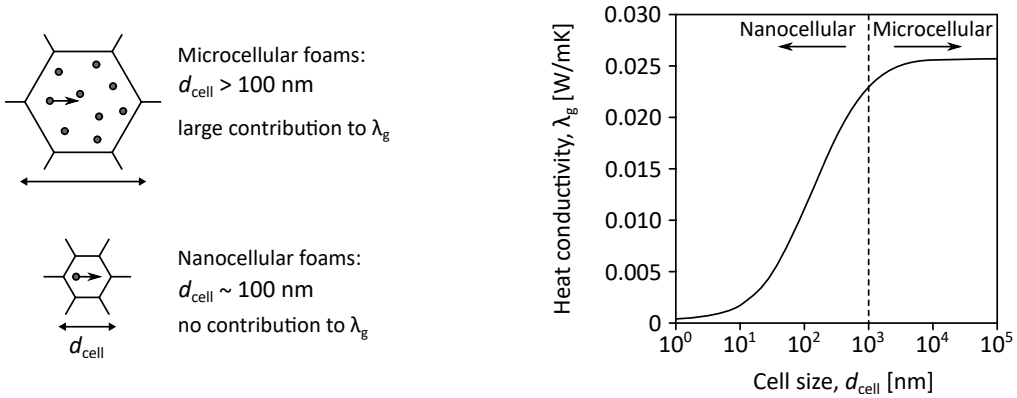

(a) Knudsen effect.

(b) Thermal conductivity vs. cell size.[205]

Figure 4.1: Consequence of the Knudsen effect on the thermal conductivity of the gas phase, λ_g. Neglecting contributions of the solid frame and excluding radiative contribution, microcellular polymer foams have a conductivity of about 0.025 W/mK, as found at standard conditions for PS with a relative density of 0.025.[190]

However, not only the cell size is important for the foam properties and good insulation, but furthermore the porosity, that means the free volume. If the pore diameters are low, but also the number of voids, the foam is rather dense and the heat transfers through the solid phase. Vice versa, when the density is very low, the polymer does not contribute to the heat transfer, but the material becomes sufficiently transparent for infrared radiation.

Optimum balance of solid conduction and radiation is expected around 85 % porosity. (equal to a relative density of $\rho_{rel} = \rho_f/\rho_p = 1 - \phi_{void} = 0.15$, see[17]).[204]

[19] The convective movement is already significantly reduced at cell sizes below 2 mm (open-cell) and 4 mm (closed-cell).[200]

This high porosity of 60–80 % has been achieved for cell sizes of 100 nm or less using acrylic copolymers and blends.[207–209]
The major challenges in achieving such high porosity combined with low cell size is on one hand the growth of bubbles from a high number of nuclei and on the other hand the formation of a huge inner surface that necessitates the stabilization of thin cell walls without cell coalescence. For example[20], if the cell size of a foam with 80 % porosity is reduced from 200 nm to 100 nm, the thickness of the cell walls has to decrease to 1/3 from 15 nm to 5 nm.[204,209] This emphasizes the importance of polymer dynamics and strength in melt and solid state, as the wall sizes approaching macromolecular chain dimensions.

4.4 Methods of Foaming

4.4.1 Mechanical, Physical and Chemical Foaming

Porous polymer structures can be produced mechanically without a blowing agent or by expansion of a blowing agent dissolved in the polymer which is then physically or chemically released. Technically, all of those methods can be utilized in batch or continuos processes.

In mechanical foaming, the gas is dispersed into a liquid polymer system by vigorously whipping or insufflating a gas from an external source. Therefore, in contrast to chemical and physical foaming, the bubbles are not created by expansion of small molecules due to pressure, but rather by entrapping the gas in the polymer matrix. To fixate the cellular structure, the polymer melt, solution or suspension is hardened by catalytic or thermal reaction, or both. This method is commonly used for the production of thermoset foams from urea resins or elastomer light-weight natural rubber materials from latex.[210]

The blowing agents in physical foaming are volatile gases or liquids. Under pressure, gases can be dissolved in a polymer. If the pressure in the system then is reduced, the solubility of the gas in the polymer matrix decreases and the gas phase separates. In order to restore the pressure balance, the gas trapped inside the polymer expands. In case of low-boiling liquids which are mixed into the polymer, the application of heat leads to a phase transition into gaseous state and thus generating a pressure. Usual industrial blowing agents in physical foaming are nitrogen, carbon dioxide or air, or small-molecule aliphatic C_4- and C_5-hydrocarbons. The usage of hydrochlorofluorocarbons (HCFC), which were preferred blowing agents before the 1980s due to their solubility, volatility and non-toxic nature, was internationally banned by the Montreal Protocol[211] in 1987 to protect the ozone layer from man-made, volatile organohalogen compounds which were found to be highly ozone depleting.[6,7,190]

Chemical foaming uses the thermal decomposition of the blowing agent which releases gaseous nitrogen or carbon dioxide. The blowing agent can be added seperately as thermally instable compound. Commonly used are azide groups, where the decomposition into N_2 and/or CO_2 is activated by heat.[7,190] Furthermore, the blowing agent can be already an integral part of the monomer which exothermically eliminates the gas molecule during

[20] Using a cubic cell model foam.[204,209]

polymerization or crosslinking reaction. This is specifically used in polyurethane (PU) foams, where a small amount of water is added to decompose the isocyanate group that releases carbon dioxide while forming an amine group.[4,7]

4.4.2 Batch Foaming, Extrusion Foaming and Foam Injection Molding

Foaming can be performed in a discontinuous, continuous or semi-continuous process that are represented by batch foaming, extrusion foaming and foam injection molding, respectively. **Table 4.2** gives a rough overview of the different procedures and compares the technical advantages and properties of the resulting foams.

In the discontinuous process of batch foaming, the polymer is placed into an autoclave system, i.e. a high pressure vessel with temperature control. The polymer is saturated under pressure with the gaseous blowing agent at a specific temperature. Upon decompressurization of the autoclave, the polymer expands and the foam solidifies within seconds. The advantage of this method is the versatility in foam shapes that can be produced using the corresponding negative mold. Furthermore, the autoclave setup is not only technically simpler without moving parts – as compared to the extrusion –, but also less processing parameters have to be considered. Therefore, batch foaming is suitable in experimental, small-scale studies to specifically investigate the polymer-gas interaction, the nucleation or bubble growth while reducing the complexity of the foaming process. In contrast to extrusional techniques of foaming (see below), that necessitate continuous control over polymer and gas feed, screw velocity, as well as melt, dye and post-extrusion aging temperature (i.e. balance of heating and cooling), in batch foaming those parameters do not have to be adjusted and optimum foaming windows are easier to find. On the other hand, conventional batch foaming prepared by gas sorption via external pressure is more time-consuming, as the specimen has to be exposed to the external pressure for an extended period of time until the polymer is homogenously saturated with blowing agent. Due to the diffusive mechanism, the saturation time is increasing with increasing sample dimensions. This issue however can be circumvented by premixing the polymer with chemical or physical blowing agents prior to autoclave treatment, which is performed as bead-foaming method.[5,190,210] An industrial example of this method is the commercial production of expanded polystyrene (EPS), see also **Section 4.2.1** (p. 52).

Along the evolution of thermoplastic polymer processing in extrusion, continuous foaming developped as a technological extension around the 1940s. From first patents to yield "synthetic spongy materials" of PE and PS and further advancements in mixing, material transport, pumping, screw and die design, foam extrusion co-evolved to a well-adopted method to produce cellular, light-weight materials, especially since the 1970s when automation and control over processing parameters met conditions and operation windows required for such a complex field of science and engineering.[6]
Nowadays, foam extrusion units can combine nearly all features of regular extrusion technology, including reactive mixing operations, devolatilization and crosslinking. Depending on the die geometry, the foamed extrudate is molded into simple base shapes in excellent speed and with high energy efficiency. Therefore, the continuous production of cellular

plastics in e.g. sheets, blocks, cylinders or tubes is also a cost-efficient way to manufacture insulation, cushioning and protection material mostly consisting of PS (e.g. XPS, see also Section 4.2.2), PVC, PE, PP and – recently more trending – PET.[6,212,213]

Table 4.2: Comparison of foaming processes. Criteria are simplified and show the general, relative trend with respect to conditions, applications, dis-/advantages and resulting foam properties,[214,215] although exceptions might exist.

	Foaming Process		
Criteria	Batch	Extrusion	Injection molding
General:			
Type	discontinuous	continuous	semi-continuous
Purpose	foam studies	commercial	complicated foams
Relevance	lab scale	large scale	large scale
Material:			
Amount	small (g)	large (kg)	large (kg)
Additives	before foaming	during process	during process
Blowing agent	mostly physical	chem. & phys.	chem. & phys.
Foam properties:			
VER	rather high	low to high	low/moderate
Cell density [a]	10^6–10^{16}	10^4–10^{11}	10^4–10^8 cells/m^3
Cell distribution	uniform	uniform or gradient	mostly gradient
Skin layer (µm)	thin ($\lesssim 100$)	thin ($\lesssim 100$)	thick ($\gtrsim$500)[215–218]
Equipment:			
Hardware	autoclave	extruder	extruder+mold
Screw type	–	single/double	reciprocating
Tooling cost	cheap	expensive	most expensive
Parameters:			
Gas loading	below T_g	above T_g	above T_g
Pressure (max)	400 bar	250 bar	350 bar
Saturation	moderate/high	low to high	low/moderate
Flexibility	low	high	high
Shear stress	no shear	shear (screw)	shear (screw)
Effort:			
Complexity	lowest	medium	highest
Output/time	very low (g–kg/h)	high (kg–t/h)	moderate (kg/h)

Foam injection molding is similar to conventional injection molding, however the blowing agent is either supplied with an additional gas dosing unit in physical foaming or pre-mixed in the polymer matrix for chemical foaming. The injection molding is technically more complex than the extrusion of foams.[215] Additional critical points are the back pressure which has to be applied to avoid instabilities in dosing of the polymer and pre-mature expansion of gas in the plasticization unit of the barrel. Unlike in foam extrusion, the screw

not only rotates, but also moves in axial direction. Secondly, the shut off of the nozzle has to be precisely timed with the injection cycle to prevent polymer leaking and gas loss causing excessive pressure fluctuations. Finally, also the mold has to be customized to the injection machine specifications and the solidification of the foam requires environmental control of temperature and cycle time.[219]

4.5 Stages of the Foaming Process

The foaming process can be divided into different stages, that are illustrated in **Figure 4.2** on the example of physical one-step batch foaming,[4] upon which the here performed foaming experiments are based on. However, the principles also apply to the abovementioned continuous processes like foam extrusion and injection molding. Those stages are now briefly summarized, but will be addressed more extendedly in the following sections.

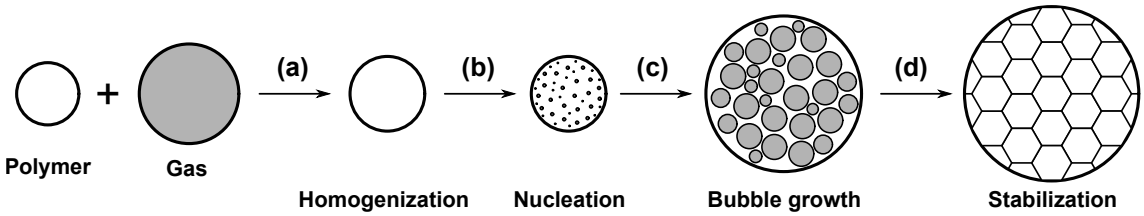

Figure 4.2: Schematic illustration of the stages of the foaming process.[4] **(a)** Homogenization of the polymer with the blowing agent under elevated pressure (and temperature). **(b)** Nucleation by sudden depressurization or temperature increase. The system transitions to a stable two-phase system. **(c)** Bubble growth and expansion of the foam due to the internal bubble pressure. **(d)** Foam vitrification and cell stabilization by reversed plasticization. Over time the blowing agent is exchanged by the surrounding air via diffusion.

First, the polymer is homogenized with the gaseous blowing agent under elevated pressure. The gas molecules diffuse into the polymer and lead to a swelling effect of the sample, see **Figure 4.2a**. With increasing gas sorption, the polymer-gas mixture is also increasingly plasticized and the glass transition temperature, T_g, decreases. The sorption is often conducted at elevated temperatures well above the T_g of the pure polymer, with the advantage of much faster gas saturation. After the polymer is saturated, bubble nucleation can be induced by sudden depressurization (one-step batch foaming) or by temperature increase (two-step batch foaming), see **Figure 4.2b**. Both ways can shift the thermodynamic equilibrium and the previously homogenous mixture phase separates into a thermodynamically stable two-phase system. Thereafter, further gas molecules diffuse into the bubble nuclei and the excess pressure drives the bubble expansion to restore the equilibrium between internal and external pressure, see **Figure 4.2c**. During the expansion, the polymer depletes of dissolved gas molecules and consequently the plasticizing effect is reversed. The viscosity increases and the growing bubbles are frozen in and the cell walls stabilize, see **Figure 4.2d**.

4.5.1 Sorption, Saturation and Plasticization

The random conformation of a polymer chain creates free volume within the polymer matrix. Those voids can be occupied by small molecules, i.e. blowing agents, which diffuse under pressure into the polymer. The solubility of the gas depends on the affinity of the gas-polymer interactions and the applied conditions of temperature and pressure. Simultaneously, the gas molecules act like a plasticizer on the polymer matrix.[8]
Therefore, the process of polymer-gas homogenization can be briefly summarized as an influence of a) the diffusion of the gas, b) the solubility of the gas, and c) the plasticization effect.

In amorphous polymers (e.g. PS) the solubility of a gas (e.g. CO_2) can be described by **Equation 4.2**, known as the "dual sorption model", where the overall equilibrium gas concentration, c_g, is a sum of a Henrian contribution term, C_H, and a Langmuirian contribution term, C_L.[8,220,221]

$$c_g = C_H + C_L = H\,p + \frac{C'_L\,b\,p}{1 + b\,p} \tag{4.2}$$

This model considers two populations of gas molecules, however both in equilibrium to each other. One gas population has high diffusional mobility and its molecules get trapped among the chains while pushing the chains apart. The other population's mobility is rather restricted, as they are absorbed by occupying the free volume. Hence, the former population follows Henry's law, which states that – in ideal systems – the amount of dissolved gas within a liquid, e.g. viscous polymer, is proportional to its partial pressure, p, outside the liquid. The proportionality is Henry's law constant, $H = C_H/p$.[8] The latter mentioned population of gas molecules is described by the absorption model of Langmuir, with C'_L as the Langmuir total absorption capacity constant and b as the affinity constant.[220–222]

Most polymer-gas systems exhibit non-ideal sorption behavior with a convex or concave function. For example, if the solubility follows a concave trend, i.e. $\Delta c/\Delta p$ decreases, the gas solubility approches a maximum and an increase in pressure does barely affect the amount of gas that is already dissolved in the polymer.[8]
The gas solubility is further influenced by the temperature (H and $C'_L\,b = f(T)$), that can be expressed by the van't Hoff **Equation 4.3**, here at the example of Henry's constant, $H(T)$.

$$H(T) = H^\circ \exp\left[\frac{-\Delta H}{R}\left(\frac{1}{T} - \frac{1}{T^\circ}\right)\right] \tag{4.3}$$

For example, the solubility of of CO_2 in PS decreases with temperature, whereas N_2 exhibits better solubility, as shown in **Figure 4.3**. However, the PS-CO_2 system still has one order of magnitude higher affinity than the PS-N_2 system, which is one of the reasons why CO_2 is the preferred gaseous blowing agent when it comes to PS foaming. A higher mass uptake of blowing agent not only results in a higher gas volume, i.e. expansion, but also improves the nucleation.[8]

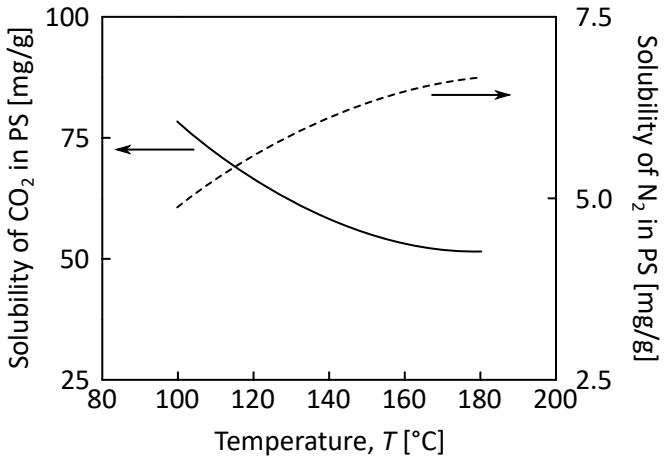

Figure 4.3: Solubility of carbon dioxide (CO_2) and nitrogen (N_2) in polystyrene (PS) at a saturation pressure of about 120 bar. The solubility of CO_2 is about one order of magnitude higher than compared to N_2. Adapted from Gendron[8], with data found in Sato et. al[223].

While Henry's law applies to the saturation of the polymer with (gaseous) blowing agent, the sorption kinetics itself follow a diffusive mechanism, that can be classically described by Fick's law. Influential factors are the rubbery or glassy state of the polymer, plasticizers, as well as the presence of crosslinking, crystallinity or fillers. In the latter cases, not only the gas solubility is decreased, but diffusive transport only happens in the amorphous fractions, whereas crystalline and filler regions act as a barrier and add a turtuosity contribution that accounts for the extended diffusion path around these "obstacles".[8]
Diffusion coefficients can be determined on theoretical basis (e.g. the free volume model or the molecular model) or be obtained experimentally (e.g. the half-time method or the moment method). For an overview of the different methods and references to further literature, the reader is referred to Gendron[8].

The presence of small-molecule blowing agents reduces the polymer-polymer interactions, thus act like plasticizers, decreasing (in first approximation) the glass transition temperature, T_g, linearly with gas solubility.[8,224] In that regard, the influence of gas molecules can be decribed by the molecular model successfully developped by Chow[225], who investigated the T_g-depression at the example of PS with different diluents.

As a consequence of the plasticizing effect, also the viscosity of the polymer-gas mixture decreases. Handge and Altstädt[224] extended the TTS principle (see also Section 3.2.2) by the gas pressure and concentration (i.e. formulating a "time-temperature-pressure-concentration superposition principle") and could show that the shift behavior could be expressed by a shift factor $a_{T,p,c}$, obtained by applying the WLF **Equation 4.4** (cf. Equation 3.28).

$$\eta_{T,p,c} = a_{T,p,c} \cdot \eta_{T_{ref},p_{ref},c_{ref}} \quad \text{with} \quad \ln a_T = \frac{-C_1\,[T - T_g(p,c)]}{C_2 + T - T_g(p,c)} \tag{4.4}$$

4.5.2 Nucleation

In physical foaming, a polymer/gas system which is in equilibrium at high pressure to keep the gas dissolved in the polymer, will transition to a stable two-phase system (solid/gaseous) when the pressure is released. The sudden pressure reduction triggers the phase separation and the system in supersaturated state falls into the metastable zone between the binodal and the spinodal. For a system of polymer/CO_2, due to the location of the spinodal, a pressure drop inherently results in nucleation.[4,204] If the thermodynamic conditions are only changed gradually, no foaming will take place, because the diffusion of the gas and escape through the surface is sufficient to restore equilibrium. Only in case of an adequate disturbance of the thermodynamic condition, the gas tends to undergo the desired phase separation for foaming.

A stable bubble is only formed if the nucleus exceeds a critical radius R_c. According to **Equation 4.5**, this radius depends on the surface tension σ, as well as the pressure of the bubble, p_b, and the system, p_{sys}.[8]

$$R_c = \frac{2\sigma}{p_b - p_{sys}} = \frac{2\sigma}{\Delta p} \tag{4.5}$$

After a critical radius of the bubble nucleus is reached, energy dissipation is favored by bubble growth, as shown in **Figure 4.4**.

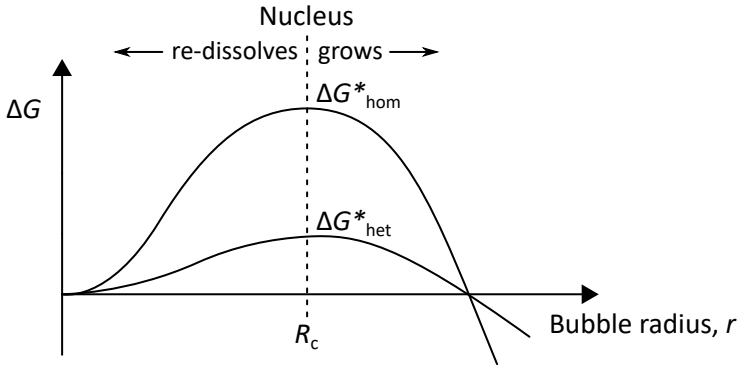

Figure 4.4: Homogenous (hom) and heterogenous (het) energy barrier, ΔG^*, of a critical bubble radius, R_c, to form a stable nuclei for further bubble growth.[12,203].

In contrast to the homogenous nucleation, the energy barrier for heterogenous nucleation, ΔG^*_{het}, is reduced. In consequence, more stable nuclei are generated at a faster rate, resulting in a higher cell density of the foam.

Homogeneous Nucleation

Homogenous nucleation happens, if gas molecules dissolved in a polymer congregate for a sufficient time to form a stable nucleus above a critical diameter, R_c (ca. 10–100 nm). The rate of bubble formation as a kinetic phenomenon can be described by the classical nucleation theory (CNT). Originally developped for liquid/gaseous systems, the CNT

expresses the energy of a system, ΔG_{hom}, as a sum of a contribution of the bubble volume, V_{b}, proportional to the pressure difference, Δp, and a contribution of the product of bubble surface, A_{bp}, and surface energy, σ_{bp}, of the polymer-gas interphase, see **Equation 4.6**.[12]

$$\Delta G_{\mathrm{hom}} = -V_{\mathrm{b}}\Delta p + A_{\mathrm{bp}}\sigma_{\mathrm{bp}} \tag{4.6}$$

The excess energy, ΔG_{hom}, approaches a minimum, if the cavity of the polymer is spherical, which is always the case for isotropic σ_{bp}. Then, with the radius, r, Equation 4.6 can be written as

$$\Delta G_{\mathrm{hom}} = -\frac{4}{3}\pi r^3 \Delta p + 4\pi r^2 \sigma_{\mathrm{bp}} \tag{4.7}$$

Differentiation of **Equation 4.7** with respect to r results in the critical radius, R_{c}, see Equation 4.5, and gives the Gibbs free energy $\Delta G^*_{\mathrm{hom}}$ for the homogenous formation of a critical nucleus, where in first approximation Δp can be equaled with the saturated vapor pressure.[12]

$$\Delta G^*_{\mathrm{hom}} = \frac{16\pi}{3\Delta p^2}\sigma^3_{\mathrm{bp}} \tag{4.8}$$

According to Colton and Suh[226,227], by applying an Arrhenius law and inserting of **Equation 4.8**, the homogenous nucleation rate (bubble formation rate), J_0, can be expressed as **Equation 4.9** with the gas concentration, c_0, and the frequency factor, f_0, of the gas molecules which enter the nucleus by diffusing out of the polymer matrix.

$$J_0 = f_0\, C_0 \exp\left(-\frac{\Delta G^*_{\mathrm{hom}}}{k_{\mathrm{B}}T}\right) \tag{4.9}$$

From this theory it follows, that an increase in saturation pressure, i.e. pressure difference, the Gibbs free energy decreases and thus the number of bubble nuclei increases. Furthermore, the presence of a surface-active agent dissolved in the polymer will reduce the surface tension and therefore also lower the energy barrier with the result of a higher nucleation rate.

Once a nuclei is formed, it still might collapse in the early stage or the bubble possibly does not survive throughout the foaming process. Due to Ostwald ripening, a thermodynamically-driven phenomenon where large bubbles grow at the expense of small bubbles, or cell coalenscences with two bubbles merging together, the effective number of bubbles ending up as a stabilized cell in the final foam, N_{cell}, will always be lower than the total number of nuclei, N_0, initially generated over time t, see **Equation 4.10**.[204]

$$N_{\mathrm{cell}} < N_0 = \int J_0(t)dt \tag{4.10}$$

When it comes to experimental evaluation with simple binary systems of polymer/CO_2, the CNT rather describes qualitative trends for pressure, temperature and gas concentration effects on the cell nucleation density than being useful for quantitative predictions. A major shortcoming of the CNT is the inadequate capture of the polymer-CO_2 interaction at the bubble interface.[204]

Heterogeneous Nucleation

In heterogenous nucleation, the nuclei of the gas bubbles are formed at the interphase of a polymer and an additive which is blended, but not dissolved in the polymer. In analogy to the abovementioned homogenous nucleation, the bubble nucleation within this liquid/solid system can also be decribed by the CNT via **Equation 4.11**,[12,226]

$$\Delta G^*_{\mathrm{het}} = \Delta G^*_{\mathrm{hom}} \cdot S(\theta) \tag{4.11}$$

in which the Gibbs Free energy, $\Delta G^*_{\mathrm{het}}$, for heterogenous nucleation depends on an additional surface factor, $S(\theta)$. This factor is a monotone function of the contact (or wetting) angle, θ ($0° \leq \theta \leq 180°$), see **Figure 4.5**, and is described by **Equation 4.12**.

$$S(\theta) = \frac{1}{4}(2 + \cos\theta)(1 - \cos\theta)^2 \tag{4.12}$$

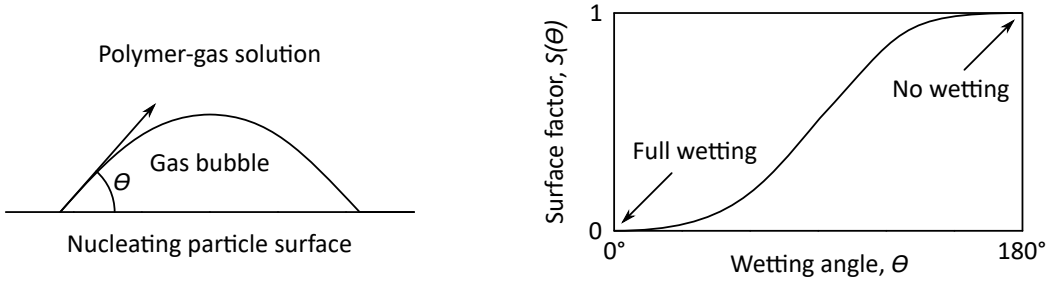

(a) Wetting angle, θ, using nucleating agents.[12]

(b) Surface factor, $S(\theta)$, as a function of the wetting angle, θ.

Figure 4.5: Heterogenous nucleation at the surface of a nucleating agent particle.

The contact angle is a measure of the wettability of a solid by a liquid and is a result of the surface tensions and interfacial energies of the respective compounds. Quantitatively, the wetting phenomenon can be described by Young's **Equation 4.13**.

$$\cos\theta = \frac{\gamma_{\mathrm{s}} - \gamma_{\mathrm{sl}}}{\gamma_{\mathrm{l}}} \tag{4.13}$$

with γ_{s} as the free specific surface energy of the solid (particle) with respect to the surrounding gas, γ_{sl} as the specific interfacial energy between the solid and the liquid phase, as well as γ_{l} describing the surface tension of the liquid towards the surrounding gas.[228] Therefore, according to Equation 4.11 and Equation 4.12, the presence of an interface can drastically reduce the energy barrier for nucleation, resulting in a higher nucleation rate, J_1, that can be expressed as **Equation 4.14** (in analogy of Equation 4.9), with C_1 and f_1 as concentration and frequency factor of gas molecules, respectively.[214]

$$J_1 = f_1\, C_1 \exp\left(-\frac{\Delta G^*_{\mathrm{het}}}{k_{\mathrm{B}} T}\right) \tag{4.14}$$

It should be mentioned that the occurence of heterogenous nucleation of course does not exclude additional homogeneous nucleation. Even if the heterogenous mechanism is favored,

homogeneous generation of nuclei can still occur in areas of the gas/polymer that are distant to the surface of the nucleating agent and thus unaffected by heterogenous nucleation. Therefore, the nucleation of a dissolved gas in a polymer matrix that contains a second phase-forming component, generally takes place both homogenously and heterogenously.

4.5.3 Bubble Growth

After the nucleation, the bubble growth is the second phase of foaming. However, both phases can happen simultaneously, that means during the growth phase also new nuclei can emerge.
Once phase separation is triggered by reducing the system pressure and a stable bubble nuclei is formed, more and more gas escapes the plasticized polymer melt and diffuses through the surface of the polymer-gas interphase into the bubble. The expansion of the bubble is then a result of the difference in system pressure (outside the sample) and internal pressure within the bubble of entrapped gas molecules. The mathematical description of this growth phase is rather complex, considering the number of mutually interacting physical quantities involved. The diffusion of gas molecules out of the polymer melt creates a concentration gradient in the solution shell around the bubble. Furthermore, the shear and extensional viscoelastic properties of the polymer come into effect, which in turn change with progressing foam expansion due to the decreasing plasticizing effect. On top of that, also the system temperature decreases which is a result of the Joule-Thomson thermodynamic effect when gas expands.

Based on the underlying physics, Amon and Denson[229] developped a model to simulate the growth dynamics of closely spaced spherical bubbles under isothermal conditions. This so-called “cell model” combines several types of equations (e.g. continuity, momentum, diffusion and mass balance equations), and can be solved numerically with appropriate initial and boundary conditions to obtain the dimensional growth of the bubble over time. The assumptions and derivations of governing equations cannot be covered here in detail, but the basic idea should be adressed schematically in **Figure 4.6** at the example of a nucleated bubble in the sperical coordinate system.
The bubble is assumed to be surrounded with a shell of the viscoelastic polymer of finite volume and also the gas concentration is limited. After nucleation the gas diffuses into the gas bubble, resulting in a gradient between the surface gas concentration, $c_R(t)$, of the bubble and the gas concentration at radial position, r, at time t. The radii $R(t)$ and $R_{\text{shell}}(t)$ signify the the boundaries of inner and outer polymer-gas solution shell positions.[230]

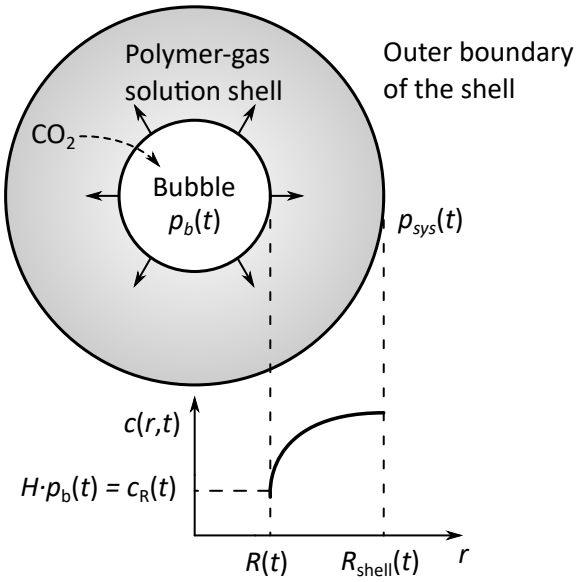

Figure 4.6: Illustration of the "cell model" to simulate the bubble growth. The nucleated bubble expands in radial direction, r, due to the internal bubble pressure, $p_\mathrm{b}(t)$, that is further related to the gas concentration dissolved at the polymer-gas interface by Henry's law, $c_\mathrm{R}(t) = H \cdot p_\mathrm{b}(t)$. Adapted from Leung et al.[230] and Ataei et al.[231].

These assumption eventually are leading to the integrated momentum **Equation 4.15** for the polymer/gas solution surrounding the gas bubble with pressure p_b; the (external) system pressure is p_sys, and γ and R are the bubble surface tension and radius, respectively.[230]

$$p_\mathrm{b}(t) - p_\mathrm{sys}(t) - \frac{2\gamma}{R} + \int_{R(t)}^{R_\mathrm{shell}(t)} \frac{\tau_{rr} - \tau_{\theta\theta}}{r}\, dr = 0 \tag{4.15}$$

Herein, the viscoelastic properties of the polymer/gas solution are expressed via the stress components τ_{rr} and $\tau_{\theta\theta}$ in radial, r, and angular direction, θ, respectively. Both stress components can be derived by a Lagrangian coordinate transformation and present as a set of differential equations (now shown here) that include the relaxation time, and the viscosity of the polymer/gas-solute system.[230,232]
In a more simplified version, at the example of a newtonian fluid, the stress, $\tau_{rr} - \tau_{\theta\theta}$, can be expressed via **Equation 4.16**,[229] (cf. Equation 3.45 and 3.46)

$$\tau_{rr} - \tau_{\theta\theta} = \frac{F}{A} = \eta_\mathrm{bi} \cdot \dot{\varepsilon} \tag{4.16}$$

and therefore shows, that the expansion of the bubble is governed by the biaxial extensional viscosity, η_bi, with $\dot{\varepsilon}$ being the elongation strain rate.

Leung et al.[230] used a batch foaming visualization system with high speed camera to in-situ observe and track the nucleation and growth process of bubbles in a pressurized PS/CO_2 system. By comparing the experimental growth profiles with their simulation, they found that the cell model could quite precisely predict the bubble growth behavior and concluded most of the physics to be mathematically correctly represented.
However, it should be emphasized that this model is only valid in the initial stage of growth in isothermal conditions when the temperature is sufficiently high and the Joule-Thomson

effect is negligible. Moreover, it only considers isolated, spherical bubbles and does not take into account converging cells and cell wall formation which might heavily change the gas diffusion or viscoelastic flow profile of the polymer.

4.5.4 Cell Stabilization

As already mentioned above, as soon as the system phase separates and the blowing agent diffuses into the bubbles, the polymer matrix gets depleted of its plasticizing gas and the melt viscosity increases. In polymers that exhibt strain hardening behavior, additional cell stabilizing effects come from the increase of the extensional viscosity at extensional times when the strain hardening sets in. Both superpositional effects are illustrated in **Figure 4.7**.[8]

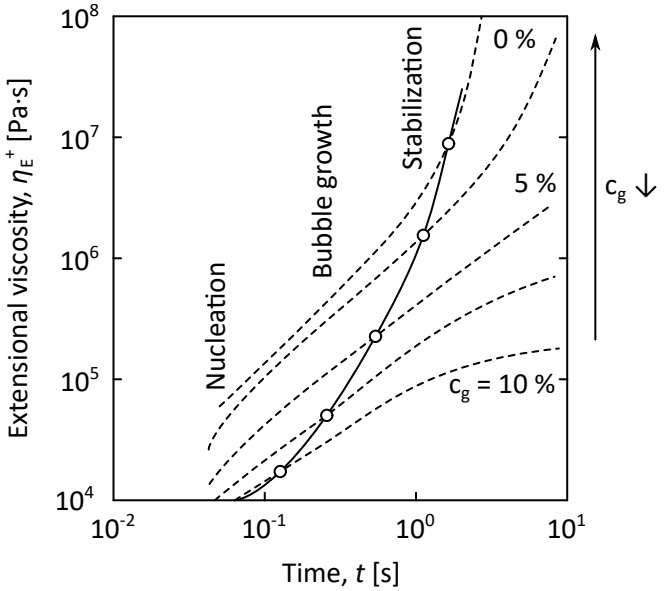

Figure 4.7: Illustrative example of the increase in the melt extensional viscosity, η_E^+, during the foaming process. The dashed lines show the extensional viscosity, η_E^+, at different gas concentrations, c_g. While the viscosity of the (e.g. branched PS-CO_2) system gradually increases with progressive gas depletion, the cell structure is additionally stabilized in the later phase of the bubble growth due to strain hardening. The solid line highlights the superpositional effect of loss in plasticizing blowing agent and onset of strain hardening. Adapted and modified from Gendron[8].

Due to the loss of the plasticizing gas, the T_g rises to that of the unsaturated condition. Thereby, the relaxation of polymer chains in the melt freezes, the surface tension vanishes and the system stabilizes. Under certain circumstances, the growth of bubbles can surpass the maximum tensile stress of the cell walls leading to rupture and therefore lower effective nucleation density, or in extreme cases to open-cell structure.

In contrast to thermoplastic polymer foaming, elastomer (or thermoset) foams gain structural stability by crosslinking during the foaming process. So, if they exhibit low glass transition, cellular materials of elastomers combine both flexibility and structural stability. Therefore, the glass transition temperature not only determines the polymers processing conditions, its physical product properties and application.

5 Model Comb Polystyrenes

This chapter introduces the practical part of this thesis, that begins with the investigation of the structure-property relationship on the basis of model comb polstyrenes. In the scope of this chapter is the systematic variation of the number of branches, with other molecular parameters like backbone and branch length remaining the same. The influence of the branch density on the melt behavior is investigated, and the rheological properties serve to explain the origins of foamability. Moreover, an optimum number of branches is found that results in highly expandable foams and also strongly correlates with the strain hardening.

The chapter covers results that have been published in parts in[120,233–235]. The figures and tables have been reproduced and modified with permission of the copyright holders.

5.1 Synthesis of Model Comb Polystyrenes (Comb PS)

First, a series of model comb PS with the same backbone (290 kg/mol) and side chain length (44 kg/mol), but different branch density is synthesized. The average number of the well-entangled branches per backbone molecule ranges from 3 to 190.

As previously discussed in Section 2.2, the strategy of utilizing anionic polymerization combined with the grafting-onto method provides the most control over structural characteristics when it comes to the synthesis of model comb topologies. The independent polymerization of backbone and side chain components is reproducible and allows full characterization of their molecular weights and dispersities. When it comes to homopolymer comb PS, the functionalization of the backbone with haloalkyl- or carbonyl groups offer a suitable way to create potential branching points (as briefly mentioned in Section 2.2.3). In general, the haloalkyl-groups are introduced via chloromethylation, as one of the early synthetic routes employed to achieve comb PS topologies.[236,237] However, this method is accompanied by the disadvantage of the formation of highly toxic and carcinogenic intermediate products like chloromethyl methyl ether (CMME). But more importantly, it suffers from low control over the degree of functionalization, lack of reproducibility and a fairly significant tendency to unwanted crosslinking during grafting with living anions due to halogen-metal exchange side reactions and dimeric termination.[238] In a later approach, aromatic functionalization via Friedel-Crafts (FC) acetylation was applied by Li et al.[81,82]

on polystyrene to synthesize "arborescent" (i.e. dendrigraft) PS-based graft topologies. The greater control of degree of functionalization, reproducibility and repeatability to achieve higher generation grafted PS, makes the FC acetylation a suitable tool for PS functionalization,[239] and proved by Kempf et al.[105] as especially advantageous in the synthesis of comb PS with a low and moderate degree of branching (e.g. 2–30 braches per backbone molecule).
Therefore, this work continues on the synthetic strategy of FC acetylation and grafting-onto and extends its use to realize a wide range of branching density up to highly branched comb PS with bottlebrush-like structures in the scope of this Chapter. Moreover, this approach was employed for branch-on-branch ("bob") PS with dendrigraft topologies, that were synthesized for **Chapter 6**.

The lengths of the backbone and side chains were kept constant, with the number of branches as the only variable. The choice in molecular weights of each component was based on the following considerations:

1.) The ratio of backbone and side chain length: The molecular weight of the backbone had to be significantly higher than the molecular weight of the branches to keep a comb-like aspect ratio, $M_{w,bb} \gg M_{br}$.[21] In addition it is easier to separate the comb product from residual, excess side chains, that is mandatory when using the grafting-onto approach.

2.) The length of the side chains: The objective was the investigation of long chain branching. Therefore, the side chains should be well-entangled, however, not excessively increasing the total molecular weight of the comb PS. For this reason, a relatively low number of entanglements, $Z_{br} \approx 3$, deemed appropriate.

3.) The length of the backbone: The molecular weight should also be well-entangled and longer than the branches (see 1.). However, it needs to be considered that the zero shear viscosity increases still with $\eta_0 \propto M_w^{3.4}$, so $M_w < 500\,\mathrm{kg/mol}$ would suit.

5.1.1 Polymerization, Functionalization and Grafting-Onto

The general reaction scheme for the synthesis of a series of comb PS is shown in **Figure 5.1**. Polymerization and grafting were carried out under strict Schlenk conditions (i.e. high-vaccum and argon inert gas atmosphere), while the acetylation, even though not very sensitive to air or impurities, was still kept in a dry reaction environment; specific details are described in **Appendix A.1**.

[21] A backbone of similar or double the M_w of that of the branches will more resemble star-like topologies.

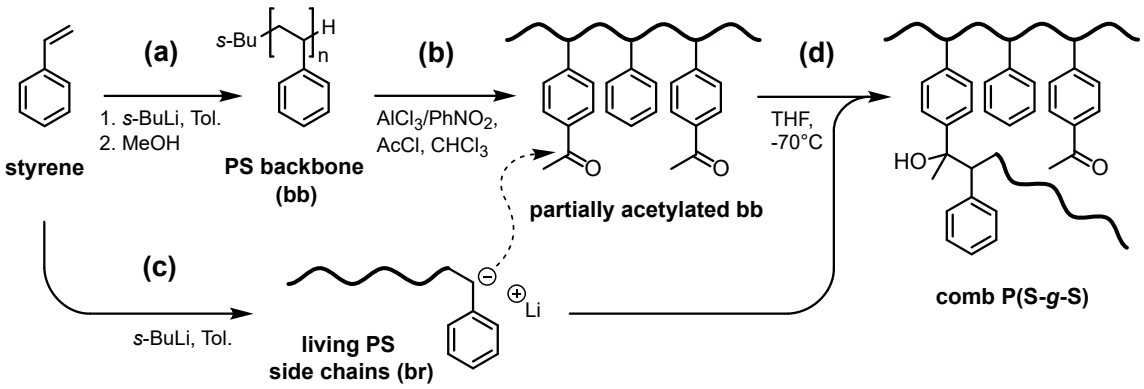

Figure 5.1: Reaction scheme for the synthesis of model comb poly(styrene-*g*-styrene) ("comb PS"). **(a)** Anionic polymerization of the backbone (bb). **(b)** Partial Friedel-Crafts (FC) acylation of the backbone with acetyl chloride. **(c)** Anionic polymerization of living side chains (i.e. branches, br). **(d)** Grafting of the living side chains onto the acetylated backbone in a nucleophilic addition reaction. Excess side chains are terminated with MeOH and removed via precipitation fractionation in a mixture of THF/MeOH. Details are described in **Appendix A.1.2**. Reproduced and modified with permission.[120] Copyright 2017, American Chemical Society.

In the first step, **Figure 5.1a**, the well-entangled backbone (bb) was anionically polymerized with low dispersity ($Đ = 1.1$) and a molecular weight of $M_{\mathrm{w,bb}} = 290\,\mathrm{kg/mol}$.
In the following acetylation reaction **Figure 5.1b**, carbonyl groups were introduced onto the backbone via a FC reagent/catalyst system of acetyl chloride/aluminium chloride ($AcCl/AlCl_3$) in chloroform ($CHCl_3$). The reaction mechanism is commonly known as electrophilic aromatic substitution (Ar-S_E), involving the formation of a σ-complex with the acylium ion intermediate ([Me-C^+=O]) and subsequent proton elimination. Due to the positive inductive effect (+I) of the alkyl backbone chain, the substitution is slightly activated and *o*/*p*-directed.[240] However, the space-occupying backbone on and the bulky complex formed by the reagent-catalyst system[22], guides the acetyl group exclusively into the sterically more accessible *p*-position, as found for acylated (i.e. acetylated) PS.[241–243] Additionally, the -I/-M effect of the introduced acetyl group leads to a strong deactivation, thus only monosubstitution of the phenyl group occurs.[239,240]
As all phenyl groups are equivalent in reactivity, with substoichiometric acetlyation agents the functionalization happens randomly with a statistical distribution along the backbone. A maximum degree of functionalization of ∼13 mol% could be achieved, while higher conversions were prone to crosslinking side reaction.
The polymerization of the side chains occured under the same conditions as the polymerization of the backbone, with the sole difference that the polystyryl anions were not terminated, see **Figure 5.1c**. Merely a small sample (ca. 5 mg) was taken to analyze the molecular weight ($M_{\mathrm{w,br}} \approx 44\,\mathrm{kg/mol}$) and dispersity ($Đ \approx 1.0$). The rest of the side chains were kept alive for the grafting reaction to undergo nucleophilic addition with the carbonyl groups, see **Figure 5.1d**.
However, due to the basicity of the anions and the slightly protic behavior of the α-carbon hydrogens at the acetyl-CH_3 group, even with (∼1.5-fold) excess amount of living anions,

[22] The catalyst consists of $AlCl_3$ and nitrobenzene ($PhNO_2$), with the latter increasing the solubility of the former in relatively non-polar solvents like $CHCl_3$.

the grafting does not yield full conversion. The persisting yellow/orange coloration of the reaction mixture until termination and restoration of carbonyl groups after work-up (proven by NMR, see Section 5.1.3.3) strongly suggests deactivation of a relative amount of the C=O double bonds by enolate formation[23].[81] In short, all carbonyl groups are converted, either into branch points or enolates, however the latter being reversible upon termination. This side reaction is reported to be widely independent of the reaction conditions (e.g. temperature, solvent, salt additives, and reaction time), with grafting yields found to be in the range of $\sim 65\,\%$.[81]

5.1.2 Fractionation

The grafting-onto approach with an excess amount of living side chains requires the separation of the residual, unreacted linear chains from the comb PS product after termination of the reaction. Due to the great difference in molecular weight, precipitation fractionation proved as a valid method in the separation of the raw product on a preparative, multi-gram scale. Using a solvent/non-solvent system of THF/MeOH and successively increasing the amount of non-solvent beyond the cloud point, the solution separated into a highly viscous gel phase, enriched in a high molecular weight graft PS fraction and in a low viscous sol phase with predominantly linear, low molecular weight side chains (see also **Appendix A.1.2.4**). The quality of the separation, i.e. the purity of either the precipitate or supernatant phase depends on: a) the molecular weight difference, b) the ratio of solvent/non-solvent, as well as c) the dilution ratio of the raw product in those, and d) the time which was given to the mixture for phase separation until further proceeding with segregation of both phases via decanting.[244] The partition equilibrium, especially of the shorter chains in both fractions necessitates the repeating of the fractionation step, with each iteration further depleting the gel-phase of low molecular weight impurities. In this way, high purities of >99% comb PS and almost full recovery of converted backbone could be achieved. Generally, for the purification of combs with a high degree of branching, less fractionation steps had to be applied.

5.1.3 Molecular Characterization

The investigation of structure-properties relationship requires thorough knowledge on the topological characteristics of the polymer. As in the case of the grafting-onto method, the target length of the backbone (bb) as well as of the branches (br) can be quite precisely predetermined by the monomer/initiator ratio. Furthermore, their molecular weights ($M_{\mathrm{w,bb}}$ and $M_{\mathrm{w,br}}$) and low dispersities ($Đ$) can be proven seperately via size exclusion chromatography (SEC) analysis. However, after successful grafting, the degree of branching quantified by the number of branches per backbone molecule, N_{br}, remains as the last parameter to determine the structure of a comb molecule.

[23] Enolate formation happens upon proton abstraction from the CH_3-moiety of the acetyl group. The proton abstracting anion is terminated, however, the acetyl functionality is restored after protic workup. For a schematic illustration of the mechanism the reader is referred to Li et al.[81]

Generally, for homopolymer grafted PS, in this thesis four different methods have been employed to quantify N_{br}, as briefly summarized hereinafter:

1.) **SEC-MALLS:** The absolute value of M_w of the purified comb-PS is determined via a multi-angle laser light scattering (MALLS) detector, where N_{br} is back-calculated from $M_{w,bb}$ and $M_{w,br}$, see **Section 5.1.3.1**.

2.) **SEC trace:** After termination of the reaction mixture, the peak area ratio of the product peak vs. residual side chain peak is analyzed. If the total amount of styrene converted into backbone (m_{bb}), resp. side chain (m_{br}) polymer is known, as well as their molecular weights ($M_{w,bb}$ and $M_{w,br}$), the amount of side chains appearing in the comb product peak enables the calculation of the number of reacted side chains attached per backbone molecule, see **Section 5.1.3.2**.

3.) **NMR:** Nucleophilic addition reaction partially converts the carbonyl groups of the functionalized backbone into alcohols, so the decrease of methyl-^{1}H signal at the α-carbon of the acetophenone-like structure vs. the increase of phenyl rings, i.e. aromatic ^{1}H signal due to additional styrene units, can be quantified via NMR, see **Section 5.1.3.3**.

4.) **Gravimetry:** The increase in absolute mass from backbone (m_{bb}) to comb product (m_{comb}) is directly related to the number of side chains reacted with the backbone precursor. In knowing the precursor molecular weights, i.e. $M_{w,bb}$ and $M_{w,br}$, the average number of side chains can be calculated.

From the abovementioned methods, the gravimetric method is, theoretically, the most simple way to calculate an average number of branches, N_{br}, as no analytical instrumentation (except a balance) is needed. However, the drawback of this method is that it necessitates thorough purification of the comb and is only accuarate if the product can be losslessly recovered during the fractionation process, which highly depends on the difference in M_w of the comb and $M_{w,br}$ of the side chains, including various other factors as mentioned in Section 5.1.2. Due to this challenge, the gravimetric method was not applied for the comb PS series in this chapter.[24]
The comb series PS290-N_{br}-44 (following the nomenclature PS$M_{w,bb}$-N_{br}-$M_{w,br}$, with all M_w in kg/mol) was characterized with respect to the average number of branches, N_{br}, via SEC-MALLS, SEC trace and NMR. For comparison, the results are summarized in Table 5.1, p. 5.1.

5.1.3.1 SEC-MALLS

Size exclusion chromatography (SEC) is the standard method to determine molecular weights, which separates polymers according to their effective hydrodynamic volume in solution. In comparison to linear polymers, branched topologies with same molecular

[24] However, the gravimetric method proved as a valid option to characterize the number of short chain branches (SCB) or long chain branches (LCB) in Chapter 6, as for those densely branched structures high recovery purification could be achieved with reasonable effort.

weights exhibit a lower hydrodynamic volume due to their more dense chain conformation, and therefore traverse the separation column at higher elution volumes, V_e.
With a calibration based on linear polymer standards, that measures the molecular weight via the intensity of UV and DRI detector signals as function of V_e, apparent molecular weights of branched polymers will always be reported lower than their true value. Therefore, SEC alone as a relative method coupled with a UV or DRI detector is insufficient for the characterization of polymers whose topology strongly deviate from a linear chain. The additional combination of the analytical SEC instrument with a multi-angle laser light scattering (MALLS) detector allows the determination of absolute molecular weights according to the Zimm **Equation 5.1**,[245,246] based on the static light scattering (SLS),[44]

$$\frac{K\,c}{R_\theta} = \frac{1}{M_w\,P(\theta)} + 2\,A_2\,c \tag{5.1}$$

with the polymer concentration, c, the Rayleigh ratio, R_θ, the weight-average molecular weight, M_w, and the second virial coefficient, A_2. The optical constant, K, is expressed by **Equation 5.2**,

$$K = \frac{4\,\pi^2\,n_0^2\,(dn/dc)^2}{\lambda_0^4\,N_A} \tag{5.2}$$

with the refractive index, n_0, of the solution at the wavelength, λ_0, the specific refractive index increment, dn/dc, and the Avogadro number, N_A.[44]
The scattering factor, $P(\theta)$, in Equation 5.1 is defined in **Equation 5.3**, and therefore a function of the mean-square radius of gyration, R_g^2, and the scattering vector, q. The scattering vector is expressed in terms of the scattering angle, θ.

$$\frac{1}{P(\theta)} = 1 + \frac{q^2\,R_g^2}{3} \qquad \text{with} \qquad q = \frac{4\pi}{\lambda}\sin\left(\frac{\theta}{2}\right) \tag{5.3}$$

When performed in an online SEC setup, the MALLS intensity is measured for each volume increment, i.e. molecular weight fraction, at multiple angles. Although the second virial coefficient, A_2, of the solution cannot be determined due to the lack of a known concentration series, however the high dilution of the solute polymer allows to assume the concentration to be zero ($c \approx 0$) for an appropriate approximation. Therefore, the second virial coefficient, A_2, vanishes and the extrapolation of $c \to 0$ gives the inverse of the molecular weight at the interception of the Kc/R_θ axis and the radius of gyration as proportional to the slope in a Zimm plot where Kc/R_θ is plotted vs. $q^2 + kc$, according to **Equation 5.4**.

$$\left(\frac{K\,c}{R_\theta}\right)_{c\to 0} = \frac{1}{M_w} \tag{5.4}$$

All combs of the PS290-N_{br}-44 series have been analyzed via SEC-MALLS, as shown in the overlay of the SEC elugrams in **Figure 5.2**. The specific details about the instrument setup, sample preparation and measurements are described in **Appendix A.1.5.1**.

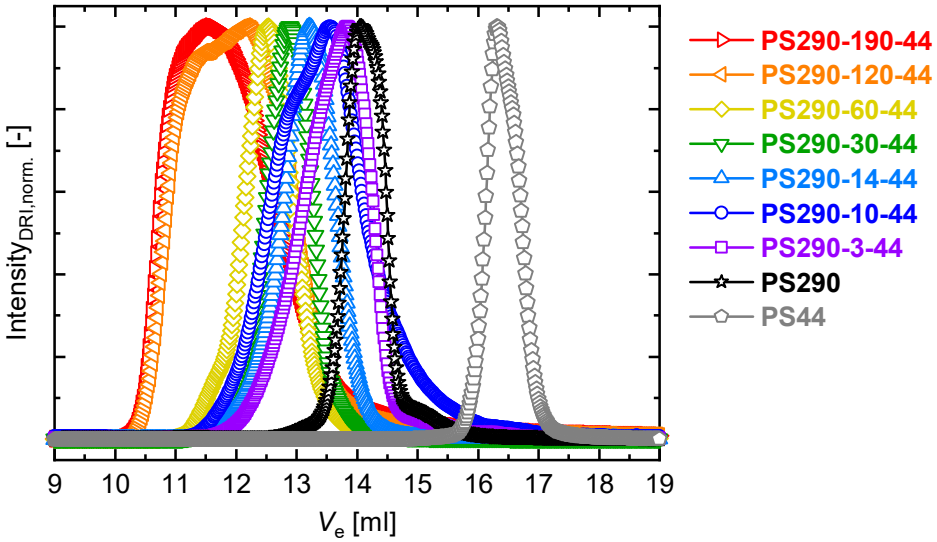

Figure 5.2: Overlay of elugrams (normalized DRI intensity vs. elution volume, V_e) of the purified comb PS290-N_{br}-44 series, the backbone PS290 and the isolated side chains PS44, measured by SEC-MALLS. The sample names are defined as PS$M_{w,bb}$-N_{br}-$M_{w,br}$ with M_w as the weight-average molecular weight in kg/mol. Results are summarized in **Table 5.1**. The measurements were performed in THF at 25 °C using a flow rate of 1 ml/min and a sample concentration between 0.7 to 3 mg/ml. Reproduced and modified with permission.[120] Copyright 2017, American Chemical Society.

The molecular weights and dispersities which were analyzed via SEC-MALLS are reported (together with results from SEC trace and NMR method) in **Table 5.1** and the average number of branches per backbone molecule, N_{br}, was calculated according to **Equation 5.5**.

$$N_{br} = \frac{M_w - M_{w,bb}}{M_{w,br}} \tag{5.5}$$

5.1.3.2 SEC Trace

In the second method, N_{br} was obtained via the grafting yield using the SEC trace of the raw product before fractionation purification and comparing the peak area of the grafted polymer (i.e. comb), A_{comb}, to the total peak area of the grafted polymer and residual, ungrafted side chains, $A_{comb} + A_{sc}$. Based on the amount of polymerized backbone, m_{bb}, and side chains, m_{sc}, fed to the reactor and the information about their molecular weights, the number of grafted chains, $N_{br,SECtr}$, can be calculated from **Equation 5.6** and was also reported in Table 5.1.

$$N_{br,SECtr} = \frac{\left[\frac{A_{comb}}{A_{comb} + A_{sc}} \cdot (m_{bb} + m_{sc}) - m_{bb}\right] \cdot M_{w,bb}}{m_{bb} \cdot M_{w,br}} \tag{5.6}$$

5.1.3.3 ^{1}H-NMR

Proton NMR spectra were performed as the third method to calculate the number of branches per molecule. The ^{1}H-NMR spectra of the partially functionalized backbone prior to grafting, as well as the purified comb PS was analyzed with respect to the initial

and residual degree of acetylation due to unconverted functional groups. **Figure 5.3** exemplarily represents the NMR spectra for a partially acetylated backbone with $N_{ac} = 157$ before grafting and the same sample named PS290-60-44 after the grafting with $N_{br} = 60$ side chains of $M_{w,br} = 44\,kg/mol$.

The peak integral A_1 at $\delta = 2.5\,ppm$ corresponds to the methyl-^{1}H at the α-C atom, whereas A_2 at $\delta = 7.4$–$7.7\,ppm$ is related to the *o*-aromatic protons of the acetyl group and the ratio of A_2/A_1 is supposed to be 2/3, as indicated in **Figure 5.3a**. The aromatic protons of the unfunctionalized styrene units, as well as the protons *meta* of the acetyl group show as peak A_3 at $\delta = 6.2$–$7.3\,ppm$.

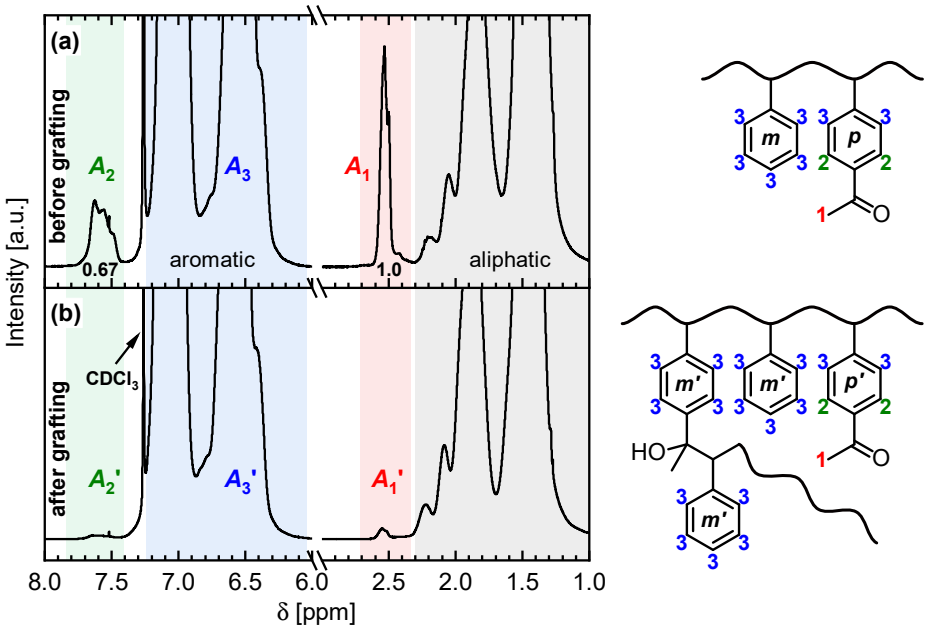

Figure 5.3: ^{1}H-NMR at 400 MHz of **(a)** acetylated PS290 with $N_{ac} = 157$ carbonyl groups per backbone molecule before grafting with side chains (Equation 5.7), and **(b)** the same sample purified after the grafting reaction with side chains of $M_{w,br} = 44\,kg/mol$, resulting in PS290-60-44. The number of branches $N_{br} = 60$ was calculated from the residual degree of functionalization after grafting (Equation 5.9). The integral ratio of methyl-^{1}H vs. *o*-aromatic ^{1}H related to the acetyl groups should be $A_2/A_1 = 2/3$, as shown in (a). Reproduced and modified with permission.[120] Copyright 2017, American Chemical Society.

With the amount of acetylated styrene units, p, and the amount of non-functionalized phenyl rings, m, the degree of acetylation, that means the mole fraction of acetyl groups to the total amount of styrene units, can be calculated using **Equation 5.7**.

$$\frac{p}{m+p} = \frac{5}{3}\frac{A_1}{(A_3 + A_1)} \tag{5.7}$$

The total number of acetyl groups, N_{ac}, of the functionalized backbone, Figure 5.3a, is then simply given by **Equation 5.8** with the degree of polymerization, $n_{bb} = M_{w,bb}/M_{styrene}$, and also reported in Table 5.1.

$$N_{ac} = n_{bb} \cdot \frac{p}{m+p} = n_{bb} \cdot \frac{5}{3}\frac{A_1}{(A_3 + A_1)} \tag{5.8}$$

The reaction of the acetylated backbone into comb PS changes the relative peak integrals, indicated as primed symbols in **Figure 5.1b**. The nucleophilic attack converts the carbonyl functionality into alcohol groups, thus shifts the chemical environment of the methyl group (CH_3) and decreases the peak integrals of the residual CH_3 groups to A'_1. Moreover, additional phenyl groups of the grafted side chains increase the relative peak integral A'_3 of the aromatic protons in relation to A'_1. From the presence of residual acetyl functionalities and the relative changes at conversion, the number of reacted side chains can be calculated via **Equation 5.9**, where n_{bb} and n_{br} is the degree of polymerization of the backbone and side chains, respectively.

$$N_{\mathrm{br,NMR}} = \frac{\frac{5}{3}\, n_{\mathrm{bb}} \left[\frac{A_1}{A_3 + A_1} - \frac{A'_1}{A'_3 + A'_1} \right]}{1 + \frac{5}{3}\, n_{\mathrm{br}}\, \frac{A'_1}{A'_3 + A'_1}} \tag{5.9}$$

Conversion of functional C=O groups and relative "dilution" with aromatic protons from side chains significantly lowered the relative peak intensities of A'_1 and A'_2, thus making the NMR analysis especially challenging for densely grafted and bottlebrush topologies with high number of branches. In the shown example of PS290-60-44, the A_2/A_3 ratio lowered to A'_2/A'_3 in approximately one order of magnitude from 2.4×10^{-2} to 2.2×10^{-3}. Even though using a 600 MHz NMR with helium cooled NMR probe for samples with $N_{\mathrm{br}} \geq 30$ to improve the signal-to-noise ratio, the ill-defined baseline in the NMR graph was a major source of uncertainties.

5.1.4 Concluding Remarks on Synthesis and Characterization

For the comb PS290-N_{br}-44 series, the reported number of branches, N_{br}, refers to the SEC-MALLS results. Furthermore, SEC-MALLS is more accurate at higher molecular weights (higher degrees of branching) as scattering intensity increases. Comparing the results of the SEC-MALLS with $N_{\mathrm{br,SECtr}}$ and $N_{\mathrm{br,NMR}}$ determined by the SEC trace of the raw product and ^{1}H-NMR, respectively, shows congruency within all three methods of measurements of branches per comb molecule and deviations are considered to be within the range of experimental reproducibility.

It is worth mentioning that the grafting yield achieved in the synthesis of comb PS increased with branching density, e.g. only ∼20 % for $N_{\mathrm{br}} = 3$ and 10, but ∼60–66 % for $N_{\mathrm{br}} = 120$ and 190. Therefore, considering that approximately one-third of functionalities does not participate in grafting, a theoretical maximum yield (∼65 %) was reached for densely grafted combs, which is in accordance with literature.[81]

The lower grafting yield for low degrees of branching might be attributed to a lower amount of living PS side chains fed to the reactor. Even though the PS anions were still in excess quantities (∼1.5-fold) compared to the number of acetyl groups, for a lower total number of functional groups per backbone molecule, also a lower total concentration of active chain were polymerized. Therefore, the solution of anions is more sensitive to impurities terminating the reaction, whereas a higher concentrations of living anions tolerate more impurities. Those impurities originate from improper preparation of reagents and solvents

or might be introduced via leakages during the grafting reaction. On the other hand, a possible explanation for high yields which were achieved in later stages of the synthesis could be the increased experience which contributed to e.g. optimization of reactor setup, working steps, salt and solvent concentrations as well as reaction time and monitoring.
In further projects, e.g. like the synthesis of dendrigraft-type branch-on-branch (bob) model PS (see Chapter 6), the same grafting technique was used and high yields of ∼60 % have also been achieved consistently.

5.2 Overview of Molecular Parameters

Figure 5.4 gives an over overview of the molecular parameters to characterize the topological structure of the synthesized comb- and bottlebrush-like PS.

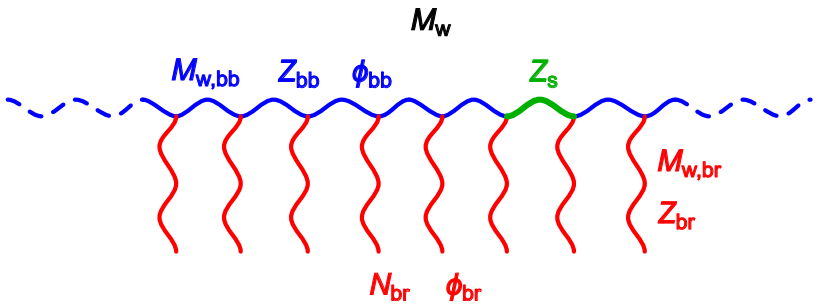

Figure 5.4: Structural parameters of comb- and bottlebrush-like PS.

Those parameters are the total molecular weight, M_w, that consists of the backbone molecular weight, $M_{w,bb}$, and the branch molecular weight times the number of branches, $M_{w,br} \times N_{br}$. Furthermore, the length of the backbone and branches can also be described by the number of entanglements, Z_{bb} and Z_{br}, respectively. The segment entanglement number, Z_s, is a measure of the branch point distance. Another important parameter often used to describe scaling laws in rheology is the backbone volume fraction, ϕ_{bb}, or the branch volume fraction, ϕ_{br}. The mathematical relationships of those structural parameters are described in **Table 5.1**, that gives an overview of the synthesized comb and bottlebrush PS samples.

In this chapter, in total two series of comb PS were synthesized. The first (main) series with well-entangled long chain branches (LCB) were named comb PS290-N_{br}-44 and used for rheological and foaming experiments.
The second series was a small set of comb PS290-N_{br}-6 with unentangled short chain branches (SCB) to complement rheological data.

Table 5.1: Molecular and structural characteristics of the synthesized model comb PS290-N_{br}-44 series and PS290-N_{br}-6* series. Reproduced and modified with permission.[120] Copyright 2017, American Chemical Society.

Sample name [a]	**Backbone (bb)**			**Branches (br)**					**Comb**		**Struct. Charact.**		
PS$M_{\mathrm{w,bb}}$-N_{br}-$M_{\mathrm{w,br}}$	$M_{\mathrm{w,bb}}$ [b]	$Đ_{\mathrm{bb}}$ [b]	N_{ac} [c]	$M_{\mathrm{w,br}}$ [b]	$Đ_{\mathrm{br}}$ [b]	N_{br} [d]	$N_{\mathrm{br,SECtr}}$ [e]	$N_{\mathrm{br,NMR}}$ [f]	M_{w} [b]	$Đ$ [b]	ϕ_{bb} [g]	Z_{s} [h]	Topology [i]
PS290	290	1.10	0	–	–	–	–	–	290	1.10	1	20	linear
PS290-3-44	290	1.10	13	45	1.07	3	n.a.	3	420	1.11	0.68	5.06	LC
PS290-10-44	290	1.10	60	44	1.05	10.4	13	10	750	1.15	0.40	1.72	DC
PS290-14-44	290	1.10	31	45	1.07	13.8	15	15	900	1.08	0.32	1.36	DC
PS290-30-44	290	1.10	86	43	1.03	29.8	35	33	1600	1.03	0.18	0.65	DC
PS290-60-44	290	1.10	157	44	1.05	59.5	66	62	2900	1.03	0.099	0.33	DC
PS290-120-44	290	1.10	181	44	1.05	120	88	122	5570	1.11	0.052	0.17	DC
PS290-190-44	290	1.10	331	44	1.05	189.3	201	205	8620	1.07	0.034	0.10	LB
PS290-50-6*	290	1.10	86	6	1.04	51	n.a.	52	590	1.09	0.49	0.39	DC
PS290-90-6*	290	1.10	157	6	1.06	93	n.a.	85	830	1.07	0.35	0.22	DC

[a] All weight-average molecular weights in [kg/mol]. [b] Measured by SEC-MALLS. [c] Number of styrene units acetylated as potential coupling sites for grafting reaction, measured by ^{1}H-NMR. [d] Number of branches, $N_{\mathrm{br}} = (M_{\mathrm{w}} - M_{\mathrm{w,bb}})/M_{\mathrm{w,br}}$, as calculated from M_{w}, measured by SEC-MALLS. [e] Number of branches, $N_{\mathrm{br,SECtr}}$, as calculated from SEC trace by comparing the peak area of the comb fraction to the area of residual side chain fraction from the raw product directly after termination of the reaction. [f] Number of branches, $N_{\mathrm{br,NMR}}$, calculated as reacted carbonyl groups from residual acetyl functionality after grafting, measured by ^{1}H-NMR. [g] Backbone volume fraction, $\phi_{\mathrm{bb}} = M_{\mathrm{w,bb}}/M_{\mathrm{w}}$. [h] Segment entanglement number, calculated by $Z_{\mathrm{s}} = Z_{\mathrm{bb}}/(N_{\mathrm{br}} + 1)$, where $Z_{\mathrm{bb}} = M_{\mathrm{w,bb}}/M_{\mathrm{e}} = 20$ with $M_{\mathrm{e}} = 14.5\,\mathrm{kg/mol}$. [i] Topologies of loosely-grafted comb (LC), densely-grafted comb (DC) and loosely-grafted bottlebrush (LB), as determined using scaling analysis of Sheiko et. al[247–249] (see Appendix A.1.5.3, Table A2 and A1). *Comb PS290-N_{br}-6 series was not used for foaming, but rheologically characterized (see Section 5.3.1.6) and furthermore used in Chapter 7.

5.3 Rheology of Comb and Bottlebrush-like PS Topologies

This section highlights the rheological properties of the model comb PS290 series, starting with the linear viscoelastic properties, investigated via small amplitude oscillatory shear (SAOS). Thereafter, nonlinear viscoelastic properties are analyzed in uniaxial elongation.

5.3.1 Linear Viscoelastic Properties – SAOS

Linear viscoelastic properties were explored via small amplitude oscillatory shear (SAOS) experiments performed on an ARES-G2 rheometer using a parallel plate geometry and within a frequency range of $\omega = 100$ to 0.01 rad/s and temperature range between 130 °C and 230 °C. The mastercurves over the entire frequency spectrum were obtained applying the TTS-principle and shifted to a reference temperature of $T_{\text{ref}} = 180\,°\text{C}$[25] using the WLF equation (see Section 3.2.2). For details about sample preparation and specific measurement conditions, the reader is referred to **Appendix A.1.6**.

Prior to recording dynamic frequency sweep (DFS) data, the thermomechanical stability of the tertiary alcohol function of the branch points was investigated using a test sample and performing time-sweep measurements at 0.1 rad/s and $\gamma_0 = 0.25$ at 230 °C under nitrogen air flow. To ensure reproducibility of results, especially at long measurement times and to exclude degradation effects (i.e. chain scission or crosslinking), the storage and loss moduli, G' and G'', respectively, were tracked for 10^4 s and the change observed was less than 5 %.[26]

The linear viscoelastic data for all samples listed in **Table 5.1** are shown in **Figure 5.5**, using the frameworks of **(a)** the (elastic) storage, G', and (viscous) loss, G'', moduli, **(b)** the complex viscosity, $|\eta^*|$, with extrapolation to the zero-shear viscosity (ZSV), η_0, via the Maxwell model, **(c)** the relationship between G' and G'' as the phase angle, δ, as a function of angular frequency, ω, and **(d)** δ versus the complex modulus, $|G^*|$, displayed as a van Gurp-Palmen (vGP) plot.

[25] The uniaxial extensional measurements were also performed at $T = T_{\text{ref}} = 180\,°\text{C}$.

[26] Further and in-depth stability studies on comb PS310-100-40 (synthesized for Chapter 6) with the same branch point functionality, were performed using TGA, SAOS, NMR and FTIR methods to analyze sample alteration in topology and chemistry and to determine preventive effects. It was concluded that branched PS made from grafting onto acetylated substrate were sufficiently stable using sample preparation and measurement procedures as described in Appendix A.1.6. The thermorheological stability measurements were performed and analyzed by Dr. M. Cziep (unpublished results).

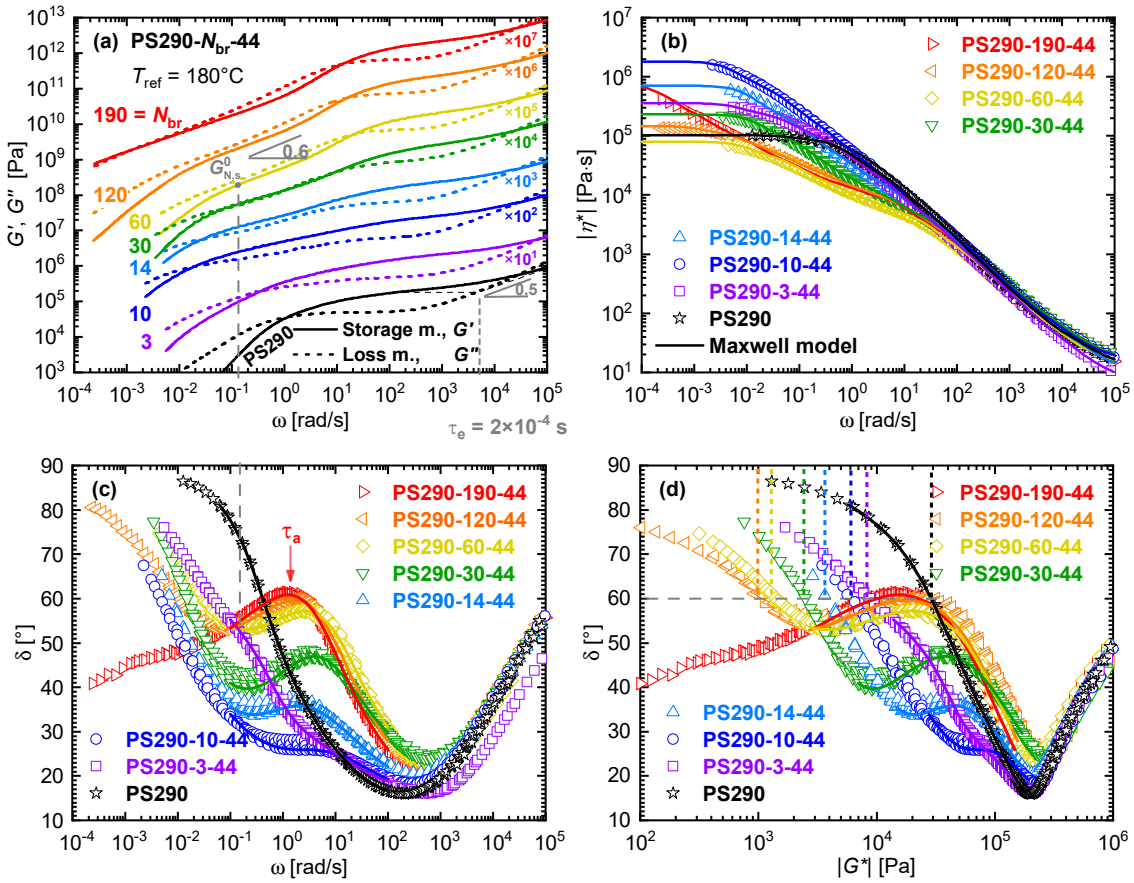

Figure 5.5: Linear viscoelastic mastercurves from SAOS data of the comb PS290-N_{br}-44 series at a reference temperature of $T_{ref} = 180\,°C$. **(a)** Storage, G', and loss modulus, G''. **(b)** Complex viscosity, $|\eta^*|$, with Maxwell model fitting (solid lines) to obtain the zero-shear viscosity, η_0, at $|\eta^*|_{\omega\to 0}$. **(c)** Phase angle, δ, vs. angular frequency, ω. **(d)** van Gurp-Palmen plot, δ vs. complex modulus $|G^*|$, with solid lines being DFS data directly obtained at T_{ref}.
The calculation of the entanglement relaxation time, τ_e, and the diluted modulus, $G^0_{N,s}$, is graphically illustrated in **(a)** and **(c)** for PS290 and PS290-60-44, respectively. The dominant arm relaxation time, τ_a, as the local maxima of δ is shown in **(c)** at the example of PS290-190-44. The complex modulus at a phase angle of 60°, $|G^*|_{\delta=60°}$, is analyzed as a criterion for branching content as graphically shown in **(d)** by the dashed lines.
Reproduced and modified with permission.[120] Copyright 2017, American Chemical Society.

5.3.1.1 Plateau Modulus and Entanglement Molecular Weight

The entanglement molecular weight of linear PS, $M_e = 4/5(\rho RT/G^0_N) = 14.5\,kg/mol$, (see Equation 3.30) at $T = T_{ref} = 180\,°C$ was calculated using the plateau modulus of the PS290 backbone, $G^0_N = 2.02\cdot 10^5\,Pa$, which is defined as the value of G' where the phase angle δ has a minimum. The entanglement relaxation time for PS290, $\tau_e = 1/\omega_e = 2\cdot 10^{-4}\,s$, which is the Rouse time corresponding to an entanglement segment, was estimated using an empirical approach, simply defined by Ferry[143] as the crossover between the horizontal plateau modulus (G^0_N) line and the loss modulus (G''), as graphically indicated in **Figure 5.5a**.[27]

[27] Several alternative methods to determine τ_e from theoretical considerations or experimental data are known, as reviewed by Szántó and Vogt.[250]

5.3.1.2 Reptation Time

While the second crossover frequency region (end of the rubber plateau region) provides information about the segmental entanglement relaxation characteristics on short time scales, the first crossover in the low frequency region, when $G' \geq G''$, is related to the size and relaxation dynamics of the whole molecule. Linear PS290 shows a clear crossover of G' and G'' with transition into the terminal region where $G' \propto \omega^2$ and $G'' \propto \omega^1$. This crossover was also observed for loosely and densely grafted combs with $N_{\mathrm{br}} \leq 30$ (see Figure 5.5a) and is attributed to the relaxation of the innermost backbone segments via the reptation mechanism. The shift of the crossover to lower frequencies for sparsely branched combs indicates that the reptation process is slowed down by the branches as a consequence of the hierarchical relaxation (see also Section 3.3.6). However, this shift is observed to be the highest for PS290-10-44, but reverts for higher number of branches and the crossover gets less pronounced until no crossover is observed for densely grafted comb and bottlebrush PS with $N_{\mathrm{br}} \geq 60$. The power law dependency of $G' \sim G'' \sim \omega^{0.6}$ (indicated in Figure 5.5a for PS290-60-44) is associated with the presence of Rouse-like relaxation behavior of the inner backbone segments supported by dynamic dilution of the branches rather than diffusive reptation-like motion.[28]

5.3.1.3 Complex Viscosity and Zero-Shear Viscosity

The absolute value of the complex viscosity is shown in **Figure 5.5b** along with Maxwell model fittings from the discrete relaxation spectra (g_i, τ_i; see Section 3.2.1) to obtain the zero-shear viscosities (ZSV), η_0, by extrapolating the data to the low frequency region via $\eta_0 = \sum g_i \tau_i$. This ZSV plateau increases from ca. 10^5 Pa·s for PS290 to a maximum of ca. $2{\cdot}10^6$ Pa·s for PS290-10-44, until it decreases again to reach a minimum for PS260-60-44 with η_0 being slightly lower than the backbone. For higher degrees of branching, i.e. $N_{\mathrm{br}} > 60$, a second increase is observed. It is notable, that even for dense comb (DC) PS with $N_{\mathrm{br}} = 120$ in the high branching range, the ZSV is still within the experimentally accessible range, whereas a transition to loose bottlebrush (LB) conformations does not seem to approach a steady state value in viscosity at low frequencies. The experimental limits towards long relaxation times were exceeded, even when making use of the TTS principle. Therefore, the plateau estimated by the Maxwell model is expected to have a higher degree of uncertainty. The ZSV values were extracted and summarized in **Figure 5.6**.

When focusing on the intermediate frequency regime ($\omega \sim 1\,\mathrm{s}^{-1}$), a weakly pronounced plateau with a lower slope is related to the branch relaxation. This characteristic time, τ_{br}, is more clearly observed as a relative maximum in **Figure 5.5c**.

5.3.1.4 Backbone, Branch Relaxation and Diluted Modulus

The replot of the SAOS data (G' and G'') in terms of phase angle, δ, visualizes the underlying relaxation dynamics in the high- and low-frequency regions, with two relative

[28] Molecular theories predict for ideal melts an exact power law exponent of 0.5, $G'_{\mathrm{Rouse}} \sim G''_{\mathrm{Rouse}} \sim \omega^{0.5}$, while real melts (like PS) are known to depart slightly higher, with $G'' > G'$.[251]

minima in δ related to rubbery plateaus corresponding to entangled chains and diluted backbone. While linear PS290 only displays one minimum (where the plateau modulus $G^0_N = G'|_{\delta=\min}$ is defined), branching induces a second minimum accounted for backbone dilution. This minimum at low frequencies, related to the second plateau of G' and not always visually pronounced in the mastercurve, defines the diluted modulus, $G^0_{N,s}$, which was also summarized in **Figure 5.6**. However, for PS290-3-44 these minima merged, with the second, local minimum merely exhibiting a shoulder towards the intermediate-frequency domain. Hereby it is important to mention, that randomly grafted LC conformations have a significant variance in branch distribution along the backbone, whereas a more even branch point spacing is statistically favored at higher grafting densities of DC and even more LB (and DB) conformations. For example, with $N_{ac} = 13$ potential coupling sites, PS290-3-44 can adopt symmetric, almost H-shaped structure or might be topologically skewed to an assymetric comb-shape or asymmetric star-shape, changing the microscopic branch density and segment spacing accordingly. Furthermore, the dispersity of the comb ($Đ = 1.11$) has to be considered as another factor of structural inhomogeneity. Using the relationship between the dispersity index and the standard deviation[29] of molcular weight, results in an uncertainty of $N_{br} = 3 \pm 3$ branches which is no or double amount of branches from the average. In addition, he dispersity of the backbone partially also contributes to this deviation. The indistinguishability of the second, local minimum is in agreement with findings of Kempf at al.[105] for comb PS with $N_{br} \leq 5$.

5.3.1.5 Van Gurp–Palmen Plot

Another replot of the SAOS data is given by the phase angle, δ, vs. the absolute value of the complex modulus, $|G^*|$ (see **Figure 5.5d**). This plot is also known as van Gurp-Palmen (vGP) plot and has the advantage that, compared to the mastercurves, dynamic-mechanical properties are displayed frequency and temperature independent when TTS holds.[252] Because the longest relaxation time is closely related to the chain length, the vGP plot is also molecular weight independent.[30] Trinkle and Friedrich[253] found, that for linear polymers the width of the curve is primarily governed by the dispersity, $Đ$, and a quantitative description is best given for $\delta = 60°$. This criterion, $|G^*|_{\delta=60°}$, was furthermore found to be a distinguishing value for LCB content in blends of industrially synthesized, linear and branched PP. However, in contrast to monodisperse model branched polymers,[254] no clear second minimum was observed, neither in δ vs. ω, nor in the vGP plot, supposedly as a result of the high dispersity of $Đ = 3$–8.[14]

The vGP plot of the comb PS290-N_{br}-44 series was also investigated with respect to $|G^*|_{\delta=60°}$, not only because these combs showed a clear deviation from linear PS at $\delta = 60°$, but also because there is a single value for $|G^*|$, except for the loosely grafted bottlebrush PS290-190-44, where the value can not be detected. Figure 5.5d graphically shows the $|G^*|$ values (vertical lines) where $\delta = 60°$ (horizontal line) intersects the experimental data.

[29] Standard deviation, $\sigma = M_n\sqrt{Đ - 1}$; with $M_n \approx 380\,\text{kg/mol}$.

[30] Furthermore, normalization of $|G^*|$ to the plateau modulus, G^0_N, allows the comparison of polymers having different chemical contitution and tacticity.[253]

The respective complex moduli are extracted and furthermore reported in **Figure 5.6**.

5.3.1.6 Summary of Linear Viscoelastic Properties

Finally, **Figure 5.6** summarizes the experimental SAOS data of the comb PS290-N_{br}-44 series extracted from Figure 5.5a–d. The depicted data combines the frameworks of the zero-shear viscosity, η_0 (Section 5.3.1.3), the diluted modulus, $G^0_{N,s}$ (Section 5.3.1.4), and the absolute value of the complex modulus at a phase angle of $\delta = 60°$, $|G^*|_{\delta=60°}$ (Section 5.3.1.5), as a function of the total molecular weight, M_w (bottom x-axis), which is directly related to the number of branches, N_{br} (top x-axis).
The graph was supplemented by further data of two additional comb PS from Kempf et al.[105] with $N_{br} = 5$ and 29, due to structural similarity in backbone, $M_{w,bb} = 275$ kg/mol, and branch molecular weights, $M_{w,br} = 42$ and 47 kg/mol, respectively. Here, they are named PS275-5-42 and PS275-29-47.[31] Furthermore, comb PS310-100-40 data, synthesized in Chapter 6 was also added.

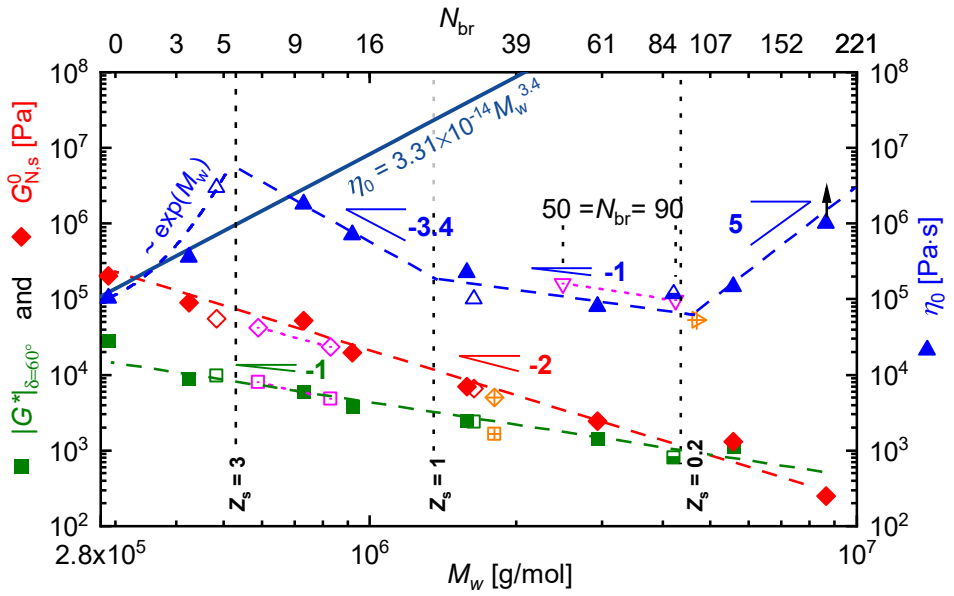

Figure 5.6: Complex modulus at $\delta = 60°$, $|G^*|_{\delta=60°}$ (■); diluted modulus, $G^0_{N,s}$ (◆); and zero-shear viscosity, η_0 (▲), as a function of total weight-average molecular weight, M_w (bottom x-axis), and respective number of branches, N_{br} (top x-axis) for comb PS290-N_{br}-44. Hollow symbols (△, etc.) are data of comb PS275-5-42 and PS275-29-47 from Kempf et al.[105]; and half-filled symbols (▲, etc.) are data of comb PS310-100-40 (see Chapter 6). The η_0 values of PS310-100-15 (crossed symbols, ⋈), and PS290-50-6 and PS290-90-6 (dotted symbols, ▽) with barely and unentangled side chains, respectively, are plotted against N_{br}. Dashed lines serve as guide to the eye and slopes are scaling exponents which are explained in the main text. The borders of the different scaling regimes are marked with vertical lines referring to the number of entanglements between branch point segments, Z_s. Reproduced and modified with permission.[120] Copyright 2017, American Chemical Society.

[31] Both comb PS data appear in the work of Kempf et al.[105] with similar nomenclature. However, PS275-29-47 originates from the Roovers series and was there named "C742".[236]

Even though the structural features were not identical with respect to the branch molecular weight, comb PS310-100-15 with barely entangled side chains ($M_{w,br} \approx M_e = 14.5\,kg/mol$), and combs PS290-50-6 and PS290-90-6 with unentangled short chain branches ($M_{w,br} < \frac{1}{2} M_e$) complete the summarizing picture in Figure 5.6.[32] It needs to be mentioned, that for those 3 combs with $M_{br} \not\approx 44\,kg/mol$, the total molecular weigth scale (bottom x-axis) does not match the branch number scale (top x-axis). Therefore, (except of the data of $|G^*|$ and $G^0_{N,s}$), the zero-shear viscosities are plotted as a function of number of branches, thus referring to the upper x-axis. This approach is intentionally used to relate the rheological behavior and scaling laws, in particular of η_0 to structural characteristics like entanglements (as $Z_{bb} \approx Z_s N_{br}$ still holds), rather than the absolute polymer weight that has no specific topological information.

The solid line represents the ZSV for linear PS at $T_{ref} = 180\,°C$ as a function of the molecular weight, $\eta_0 = 3.31 \cdot 10^{-14}\, M_w^{-3.4}$.[255] From this graph it can be seen that comb PS with the same molecular weight and N_{br} between 3 and 10 branches per backbone, i.e. segmental entanglement number $Z_s = 2$–5, have zero-shear viscosity values exceeding η_0 of their linear reference with same molecular weight, i.e. $\eta_{0,comb} \geq \eta_{0,lin}$. This strong increase, which seems to follow $\eta_0 \sim \exp(M_w)$, reflects also the rheological behavior found for star polymers with sufficiently well-entangled arms, where $\eta_0 \sim \exp(M_{arm})$ and is attributed to the suppressed reptation due to hierarchical relaxation. The exponential increase with M_w reaches an estimated maximum of η_0 around $N_{br} \approx 6$ or $Z_s \approx 3$ and is therefore in agreement with model comb simulations of Inkson et al.[256] for a minimum of 6 branches per backbones with $Z_{bb} \approx 20$ entanglements. Recently, Ahmadi et al.[257] synthesized branched poly(*n*-butyl acrylates) and upon rheological investigastion, sparsely grafted ($N_{br} \approx 2$–5) P*n*BA combs with even slightly to well-entangled side chains presented higher ZSV than their linear analogues, whereas more densely grafted P*n*BA exhibited significantly reduced ZSV. Similar exponential behavior at low branching numbers has also been found for LCB star polyisoprenes.[258,259]
Following the scaling analysis by Sheiko et al.[247–249] (as summarized for PS290-N_{br}-44 in Table A2), indicates that the entanglement number of the branch segments with $Z_s = 3$ ($\widehat{=} N_{br} = 6$ in this comb PS series) signifies a transition point from loosely grafted (LC) to densely grafted comb (DC) conformation.

Increasing the number of branches to $N_{br} > 6$, but within the entangled branch point spacing, $1 < Z_s < 3$, decreases the zero-shear viscosity with a scaling exponent of -3.4, i.e. $\eta_0 \sim M_w^{-3.4}$. The number of chain ends increase and therefore the ability to relax via CLF mechanism, which is more effective and strongly counteracts the inhibition of reptation based on hierarchical terms. Then, the reptation of the diluted backbone resembles more the diffusion of a linear chain with the volume fraction, ϕ, in a matrix of short chains. Applying this analogy of a diluted entangled linear polymer solution with the plateau modulus and longest relaxation time scaling with $G^0_N \propto \phi^2$ and $\tau_d \propto \phi^{1.4}$, respectively, then consequently, according to **Equation 5.10**[260,261],

[32] For the full SAOS data the reader is referred to Figure 6.3 (PS310-100-15) and Figure A.2.1 (PS290-50-6 and PS290-90-6).

$$\eta_0 = G_N\,\tau \equiv G_N^0\,\tau_d\,\phi^{3.4} \tag{5.10}$$

the zero-shear viscosity, η_0, is proportional to the volume fraction as $\phi^{3.4}$, where G_N^0 and τ_d refers to the undiluted ($\phi = 1$) polymer in the melt state.

Therefore, the slope created by comb PS with $N_{br} = 10$ and 14 supports the scaling law of $\eta_0 \sim \phi_{bb}^{3.4} \sim M_w^{-3.4}$ proposed in theoretical studies for combs with $Z_{bb} \geq 20$ and $2 < Z_{br} < 10$.[256] This power law dependency seems to be valid up to a molecular weight where the number of branches $N_{br} < Z_{bb} = 20$.

When the number of branches is further increased, so that the backbone chain section between two branch points falls shorter than one entaglement, i.e. $Z_s < 1$, then η_0 still scales with a decreased power law. However, the slope of -1 is less steep. A proportionality of $\eta_0 \sim \phi_{bb}^{1} \sim M_w^{-1}$ is observed for $N_{br} = 30$ and 60, with the latter, PS290-60-44 with $Z_s \cong 0.3$ reaching a zero-shear viscosity as low as its backbone precursor even with a remarkable 10-times of the molecular weight. It should be mentioned that the scaling of the decreased slope is a first approximation, while it is still possible that the zero-shear viscosity follows a slightly different scaling towards M_w or most probably has transition regions outside its range of $1 > Zs > 0.2$ and with variable slopes.

Comb PS310-100-40 with structural similarity to the PS290-N_{br}-44 series comes close to a branch point spacing of $Z_s = 0.2$ entanglements. However, the zero-shear viscosity, even well in the expectable order of magnitude, is slightly higher than predicted from Figure 5.6.

Interestingly, even for comb PS290 with $N_{br} = 50$ and 90 unentangled side chains of $M_{w,br} = 6$ kg/mol, when relating their PS290 backbone segment structure to the number of branches (top x-axis), both data points still show a slope which relates to a power law dependency of -1 in the range of $0.4 > Z_s > 0.22$. When relating both samples, PS290-50-6 and PS290-90-6 to M_w (bottom x-axis), which shifts both data points to the left (not shown in the graph), still a scaling of $\eta_0 \sim M_w^{-1} \sim \phi_{bb}^{1}$ applies. It must be expected that for PS290-N_{br}-6 this scaling of -1 follows a much broader range in molecular weight or number of branching, i.e. backbone segment entanglements. However, in lack of data this range can not further be narrowed down.

Including PS310-100-15 (with barely entangled side chains) in the set of data, a backbone section of $Z_s = 0.2$ entanglements between branch points seems for a ~290 kg/mol PS backbone and a branch molecular weight of $\frac{1}{2}M_e \leq M_{w,br} \leq 3M_e$ to result in similar zero-shear viscosities of below $\eta_{0,comb} \leq \eta_{0,linear} \approx 10^5$ Pa·s.

For the comb PS290-N_{br}-44 series, a further increase in branches well above $N_{br} = 100$, and as a consequence thereof transition into the loosely-grafted bottlebrush (LB) conformation region, drastically increases the η_0 with a power law exponent of > 5, which means that $\eta_0 \sim M_w^5 \sim N_{br}^5 \sim \phi_{bb}^{-5}$. However, this is just an estimate lower value because the experimental data of PS290-190-44 in terms of ZSV is most likely underreported due to the very long relaxation time of the bottlebrush-like molecule that is beyond a reasonable measurement window, even when using TTS.

In contrast to η_0, which depends strongly on the structural parameters, from Figure 5.6 it is observed that the complex modulus at $\delta = 60°$, $|G^*|_{\delta=60°}$, as well as the diluted modulus, $G^0_{N,s}$, are not sensitive to conformational changes of the molecule which result from the side chain crowding. Both scalings of $|G^*|_{\delta=60°} \sim M_w^{-1}$ and $G^0_{N,s} \sim M_w^{-2}$ seem to show universality when comparing comb- and bottlebrush-like molecular structures with the same (or similar) backbone length but totally different side chain length as in the example of well-entangled LCB comb PS290-N_{br}-44, unentangled SCB combs PS290-N_{br}-6 and PS310-100-14 with barely entangled side chains.

From the strong molecular weight dependency and direct correlation with the branching content, it is evident that the complex modulus $|G^*|_{\delta=60°}$, which has been suggested as feasible criteria to provide rheological information about dispersity,[253] has a broader utilization towards topological information and in particular towards the degree of branching, as becomes clear from **Equation 5.11**. Its applicability with respect to a bigger variety of structural parameters still has to be validated.[33]

$$|G^*|_{\delta=60} \sim M_w^{-1} \sim \phi_{bb} \sim \phi_{br}^{-1} \sim N_{br}^{-1} \quad \text{(for high } N_{br}\text{)}; \quad \text{with} \quad \phi_{bb} = \frac{M_{w,bb}}{M_w} \tag{5.11}$$

The diluted modulus, $G^0_{N,s}$, also gradually decreases with increasing molecular weight due to more side chains. Although the backbone appears to be more confined and the diffusion in the longitudinal direction (reptation) is restricted by the branch points, the entire molecule possesses more chain ends that provide increasingly efficient relaxation via the CLF mechanism and a larger tube for transversal motion, as compared to its linear analogue.

The dilution concept of a polymer chain, either in a solvent, or a matrix of oligomers or lower M_w chains, can also be applied to this case when the backbone tube is diluted by covalently connected side chains that relax by a fast CLF mechanism (see also DTD theory in Section 3.3.5). The reduction of the plateau modulus (in analogy of Equation 3.37 for solvent-like molecules) is then fundamentally described by the volume fraction representing the backbone, ϕ_{bb}, according to **Equation 5.12**.

$$G^0_{N,s} = G^0_N \, \phi_{bb}^{1+\alpha} \quad \text{with} \quad \alpha = 1 \text{ to } 4/3 \tag{5.12}$$

For these comb PS, the experimental finding of the diluted modulus being proportional to $M_w^{-2} \sim \phi_{bb}^2$, calculates for the dilution exponent $\alpha = 1$. This scaling is in good agreement with theoretical and experimental dilution studies[34] who found values of $\alpha = 1$ and 4/3, depending on i.a. the topological system (linear, star, comb, etc.), the chemical composition, the polymer-solvent molecular weight difference and the magnitude of dilution. Both values

[33] The complex modulus at a certain phase angle was also used as an approach to quantify the branching content in dendrigraft PS. Even though $\delta = 60°$ was not applicable due to the shape of the curve in the vGP plot, different phase angles, in particular $\delta = 45$–$55°$, showed a strong correlation with the volume fraction of the outermost branching layer, see Chapter 6 and specifically Section 6.2.1.4.

[34] It should be mentionend that there is already a 20-year old discussion about the "proper" dilution exponent value of α. For a more detailed review about the disputed issue of this aspect of the tube theory, the reader is referred to Hall et al.[262]

have also been used in tube theories with one or the other showing better prediction of experimental data.

To gain more insight into the dilution behavior of linear PS, and the LCB and SCB comb PS series presented here, in a seperate study the branched PS290-N_{br}-44 and its linear backbone precursor PS290 have been blended with linear, side chain-size PS of $M_w = 44\,kg/mol$. Whereas the linear backbone precursor PS290 showed an exponent of $\alpha = 4/3$, which falls also well in the range of the expected dilution exponents, in contrast, the comb PS backbones, that were already diluted by the branches and which were further diluted by linear chains, presented a dilution exponent of $\alpha = 0$. Those DTD effects of the branches and "free" side chains will be covered more extendedly in Chapter 6, and specifically in **Section 6.2.1.3**.

5.3.2 Nonlinear Viscoelastic Properties – Uniaxial Elongation

Uniaxial extensional experiments were performed on an ARES-G2 rheometer using an extensional viscosity fixture (EVF) geometry set. The transient stress growth coefficient (extensional viscosity, η_E^+) was measured at $T = 180\,°C$ at different extensional rates from $\dot{\varepsilon}_H = 10\,s^{-1}$ down to slow rates at $\dot{\varepsilon}_H = 0.001\,s^{-1}$. For details about the sample preparation and specific measurement conditions, the reader is referred to **Appendix A.1.6**.

5.3.2.1 Extensional Viscosity

The extensional data of the comb PS290-N_{br}-44 series in Table 5.1 is shown in **Figure 5.7** as tensile stress growth coefficient, η_E^+, versus stretch time, t, for different extensional rates. The envelope of the linear viscoelastic behavior (LVE) was predicted by the relaxation modes of the multi-mode Maxwell fitting from the SAOS data (Figure 5.5) via Equation 5.13.[35]

$$\eta_{E,LVE}^+ = 3 \sum_{i=1}^{N=10} g_i\,\tau_i \left(1 - \exp\frac{-t}{\tau_i}\right) \tag{5.13}$$

As can be seen from **Figure 5.7a**, the extensional viscosity, η_E^+, of linear PS290 closely matched the LVE predictions with little deviation, neither signifying hardening nor softening behavior during the elongational test. In contrast, all comb PS, **Figure 5.7b–h** show a significant upturn from the start-up LVE envelope, known as strain hardening behavior. This is even observed for very sparsely branched LC PS with only $N_{br} = 3$ side chains per molecule and over a broad range (∼4 decades) of extensional rates.
An increase in the number of branches to $N_{br} = 10$, 14, 30 and 60, **Figure 5.7c**, **d**, **e** and **f**, not only yielded in successively higher strain hardening, but also shifted the onset in strain hardening from $\dot{\varepsilon}_H = 0.01\,s^{-1}$ to lower extensional rates of $0.003\,s^{-1}$. A further increase in N_{br} towards the high region of densely grafted comb PS, represented by PS290-120-44, resulted in a very large degree of strain hardening. However, the extensional tests barely reached a steady-state value, i.e. a peaked maximum or plateau. This was even more

[35] Alternatively, by plotting $3\,|\eta^*|$ vs. the inverse of frequency, $1/\omega$, see Figure 5.5b, using the Trouton ratio, $Tr = 3\,\eta_E^+/\eta_S^+$, see also Equation 3.47 in Section 3.4.1.

so the case for loosely grafted bottlebrush PS290-190-44, where the stetching filament already ruptured at Hencky strains below 3, resulting in lower strain hardening, especially at high extensional rates $\dot{\varepsilon}_H \geq 0.03\,s^{-1}$ compared to PS290-120-44 with a lower degree of branching.

Figure 5.7 furthermore contains the stress growth coefficient curves of the Doi-Edwards (DE) and molecular stress function (MSF) model predictions to calculate the strain hardening criteria and compare the experimental results with molecular theories. The predictions of the DE and MSF model were performed by Dr. Mahdi Abbasi using a home-written MATLAB script and the dynamic-mechanical SAOS data.[120]

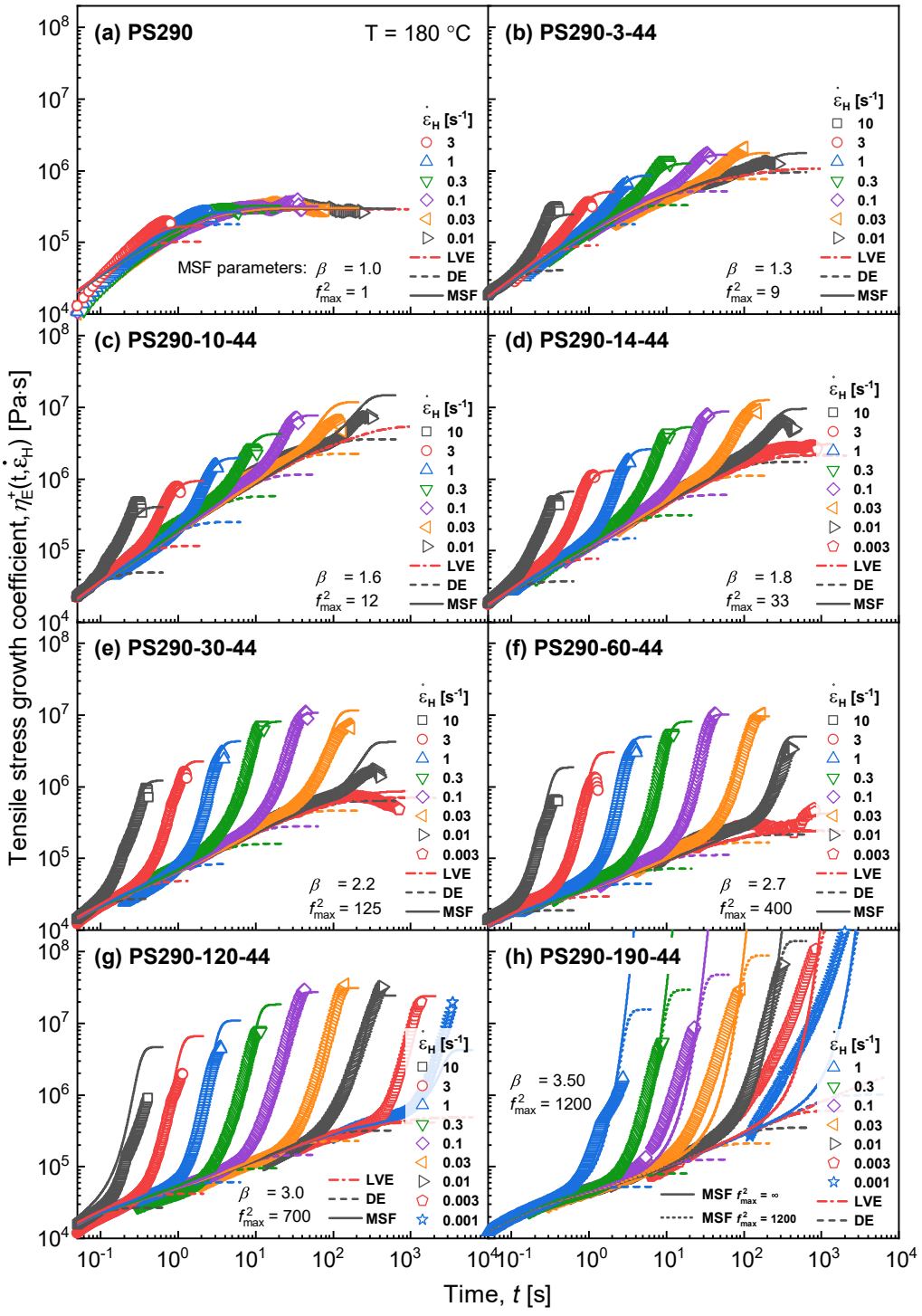

Figure 5.7: Tensile stress growth coefficient data, η^+_E. **(a)** Linear PS290 backbone. **(b)** Comb PS290-N_{br}-44 series with the same backbone (290 kg/mol) and side chains (44 kg/mol), but different N_{br}. Lines are LVE predictions from SAOS data (red dashed-dotted line), as well as predictions from the DE (dashed line) and MSF model (solid line) with fitting parameters β and f^2_{max}. Reproduced and modified with permission.[120] Copyright 2017, American Chemical Society.

5.3.2.2 Strain Hardening

The rheological behavior of the comb PS290-N_{br}-44 series in elongational flow is summarized in the framework of strain hardening in **Figure 5.8**, with the strain hardening factor, SHF $= \eta^+_{E,max}(\dot{\varepsilon}_H)/\eta^+_{E,DE}(\dot{\varepsilon}_H)$ (see also Section 3.4.2) as a measure to quantify the increase in viscosity during elongational deformation. The DE prediction, as the reference for strain hardening was based on Equations 3.51–3.54 (see Section 3.4.2.1) with the molecular stress function parameter, $f = 1$, which means the polymer tube is assumed to be oriented, but no stretching is considered.

For comparison, the experimental results (shown as symbols with dotted lines as guide to the eye) were complemented with the MSF predictions of the SHF $= \eta_{E,MSF}(\dot{\varepsilon})/\eta_{E,DE}(\dot{\varepsilon})$ (shown as smoothened, solid lines) that takes into account the tube diameter reduction and increase in elongational stress while streching.

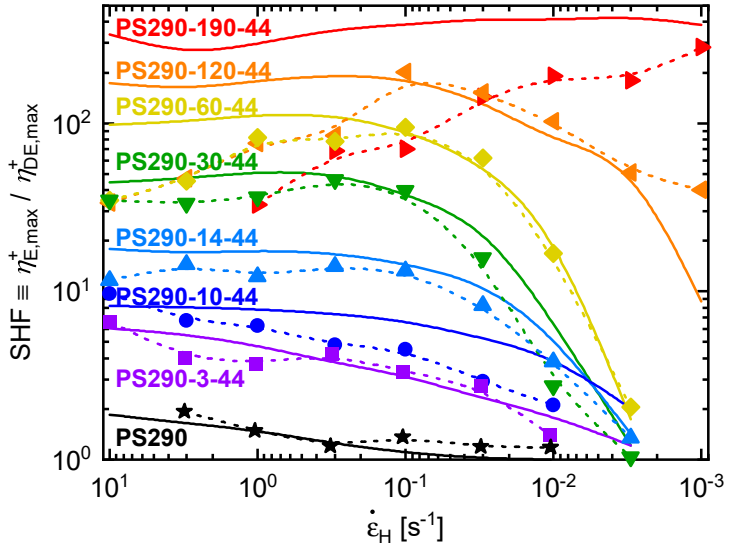

Figure 5.8: Strain hardening factor, SHF $\equiv \eta^+_{E,max}/\eta^+_{DE,max}$, as a function of the extensional rate, $\dot{\varepsilon}_H$, from short times (high strain rates) to long times (low strain rates), following the time order of the extensional data in Figure 5.7. Symbols are based on the maximum experimentally achieved stress growth coefficient, $\eta^+_{E,max}$, and dashed lines show the general trend as guide to the eye. Solid lines are predictions of the MSF model. Reprinted and modified with permission.[120] Copyright 2017, American Chemical Society.

Figure 5.8 shows that LCB in synthesized comb PS results in a significant increase in strain hardening well above the one of linear reference PS290. At the fastest rate, $\dot{\varepsilon}_H = 10\,s^{-1}$, the maximum of SHF ≈ 35 is reached for $N_{br} = 30$. Comb PS290-60-44 and PS290-120-44 show nearly the exact same SHF, however, at reduced strain rates, both samples surpass this value and reach their maximum at $\dot{\varepsilon}_H = 0.1\,s^{-1}$, with the latter achieving an extensional hardening above SHF $= 200$. This magnitude of strain hardening has never been reported for a comb- or bottlebrush-like topologies, especially not within Hencky strains below $\varepsilon_H = 4$, which marks the experimental limit for the elongational test with the EVF geometry.[36] A further increase in N_{br} to 190 does not result in a higher strain

[36] The Hencky strain and its instrumental limits are especially relevant in Chapter 6. The reader is referred to Section 6.2.2.1 for a more detailed discussion.

hardening, but shifts the maximum of the achievable SHF towards even lower strain rates. This seems to be at the expense of melt stability when the sample is elongated at short times, as the comb PS290-190-44 barely reaches a SHF of 30 and the stretched filament breaks already at Hencky strains below $\varepsilon_H = 3$ at rates of $\dot{\varepsilon}_H = 1$. This indicates that branched topologies with loose bottlebrush conformations are relatively stiff due to the side chain crowding and therefore the number of effective entanglements along the backbone tube or within the interacting branches is drastically decreased.[37] Consequently, whereas a moderate number of well-entangled branches, in this case up to $N_{br} \approx 120$, has a positive influence on the processability in elongational deformations in the melt state, the effect is reversed towards bottlebrush-like branch densities. Considering that those might not be suitable for industrial processing where the polymer melt is subject to rather high strain rates or large deformations (e.g. foaming, film blowing or fiber spinning), bottlebrushes still might have beneficial qualities in solution processing like electrospinning[106] or thin film casting.[267]

In case the branch crowding of the pure polymer is excessively high and the entanglements lose efficiency when it comes to the strain hardening, as seen at the example of PS290-190-44 when the optimum number of branches is passed, blending with less densely branched or even linear topologies present as a promising and simple way to enhance and tune the processability. This matter is explored in more detail in Section 7.6 on the example of comb-linear PS blends.

5.3.2.3 Molecular Stress Function Model, MSF

The molecular stress function model (MSF), introduced in Section 3.4.2.1 (p. 44), provides a constitutive equation (Equation 3.55) to simulate the extensional viscosities, η_E^+, using the nonlinear fitting parameters f_{max}^2 and β, that govern the maximum stress growth coefficient and the slope of the viscosity upturn from the LVE envelope, respectively. By fitting Equation 3.56 (p. 47) to the extensional viscosity[38] data, values for f_{max}^2 and β are obtained, as reported in Figure 5.7.[39]

Figure 5.9 displays the MSF parameters as a function of the number of branches, N_{br} (bottom x-axis), and segmental entanglement number between branch points, Z_s (top x-axis). The molecular definition of $\beta = \phi_{bb}^{-1}$ (see Equation 3.57, p. 48) makes the slope-governing parameter closely related to the branching structure. However, as can be seen from Figure 5.9, the monotonical increase of the experimental values of β with N_{br} (blue circles) is inadequately represented by molecular theories (blue dashed-dotted line), that overestimate the contribution of the branches, i.e. branching number. Therefore, β was empirically fitted with a logarithmic function, see **Equation 5.14**.[120]

[37] This is congruent with fatigue testing of a comb sample (PS290-60-44) in the solid state, which failed at a torsional deformation at $\gamma_0 = 2.5\%$ in an amplitude sweep test. A failure at this low strain is equivalent to a relatively low molecular weight, linear PS90 and suggests a high degree of brittleness due to the insufficient number of effective entanglements. In comparison, a PS900 with much lower molecular weight has a strain-at-break of $\gamma_0 = 4.5\,\%$.[263–266]

[38] Also known as tensile stress growth coefficient.

[39] All simulations were performed by Dr. Mahdi Abbasi.

$$\beta = 1 + \log\left(1 + \frac{Z_{\mathrm{br}}\, N_{\mathrm{br}}}{Z_{\mathrm{bb}}}\right)^{1.7} 1 + \log\phi_{\mathrm{bb}})^{-1.7} \tag{5.14}$$

Furthermore, the parameter f^2_{max} also increases monotonically with N_{br}. When plotted on a logarithmic scale, due to the similar manner curvature to β, also an empirical power law function in analogy of Equation 5.14 can be proposed, taking into account the logarithmic scale and the "shift" of the f^2_{max}-data relative to β.[120]

$$f^2_{\mathrm{max}} = 4\left(1 + \frac{Z_{\mathrm{br}}\, N_{\mathrm{br}}}{Z_{\mathrm{bb}}}\right)^{1.7} = 4\,\phi_{\mathrm{bb}})^{-1.7} \tag{5.15}$$

Equation 5.15 and its empirical derivation from Equation 5.14 suggest a dependency between f^2_{max} and β, both related to the same function of ϕ_{bb}.

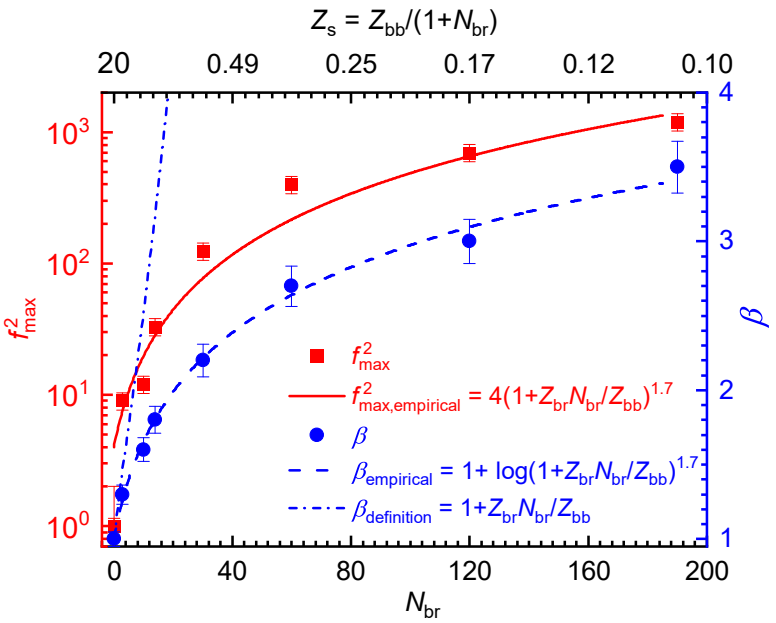

Figure 5.9: Nonlinear parameters f^2_{max} and β of the MSF model (Equation 3.55 and Equation 3.56, p. 47) as a function of the branching number, N_{br} (bottom x-axis) and segment entanglement number between branch points, Z_{s}, for comb PS with $M_{\mathrm{w,bb}} = 290\,\mathrm{kg/mol}$ and $M_{\mathrm{w,br}} = 44\,\mathrm{kg/mol}$. Reprinted and modified with permission.[120] Copyright 2017, American Chemical Society.

5.4 Foaming of Comb- and Bottlebrush-like PS Topologies

The anionically synthesized and rheologically characterized comb PS290-N_{br}-44, were saturated with a blowing agent in a pressure vessel and subsequently expanded by sudden pressure release in a one-step batch foaming process. The resulting foams were characterized with respect to their macroscopic foam properties and microscopic cell structure.

The foaming experiments were conducted in a batch reactor setup with carbon dioxide (CO_2) as physical blowing agent. In contrast to other blowing agents like volatile hydrocarbons (VHC, e.g. butanes and pentanes) or hydrochlorofluorocarbons (HCFC, also HFCs and

CFCs), it is proven to be environmentally friendly and safe to handle due to its non-toxicity and chemical inertness. Furthermore, the good solubility of CO_2 in PS (see Section 4.5.1, Figure 4.3), which is roughly one order of magnitude higher compared to other conventional gaseous agents (e.g. nitrogen),[8] potentially allows for higher volume expansions and lower foam densities. The possibility to carry out the foaming process at relatively moderate conditions makes the cost-efficient use of inexpensive CO_2, commercially available in gaseous, (supercritical) liquid or solid form (dry ice), not only interesting and thus wide spread in industrial application.[7] But moreover, it proved as suitable blowing agent to investigate saturation, micro- and nanocellular foaming behavior of polymers[202,204] and polystyrene[268–270] in particular and correlate those with their chemical composition[271,272], stereochemistry[273,274] or topology.[14]

5.4.1 One-Step Batch Foaming

5.4.1.1 Sample Preparation

Comparing the foaming behavior of branched and linear polymers and correlating it to structural characteristics requires the absence of impurities which not only might alter the rheology in bulk, but also to a greater extent affect the foaming process in terms of nucleation, bubble expansion or cell stability.[269] The presence of low molecular weight components and non-/polar functional groups places another interaction between the foaming agent and the polymer matrix.

In a recent study, Mahdi et al.[234] focussed on those influential effects of small amounts of impurities on the cell density of polystyrene foams. In order to assess the impact of those low molecular weight components, represented by oligomers or surfactants, they used commercial PS as well as lab-scale emulsion polymerized and anionically synthesized PS, and treated them with different purification methods. If, prior to foaming, the samples were either dissolved (e.g. in THF or dioxane) and the solvent was simply evaporated (in vacuum oven or freeze dryer), or the raw sample was extruded (via mini lab twin screw extruder), the foamed specimen had increased cell densities of 1–2 orders of magnitude and significantly decreased cell size as compared to their untreated, raw material. This improvement was majorly the case for samples of commercial or emulsion polymerized origin and to a much lesser extent for anionically polymerized PS, as the untreaded one already showed comparably high cell densities of $N_{\text{cell}} \sim 5 \cdot 10^8\,\text{cell/cm}^3$. Removing those impurities by repeated precipitation fractionation resulted in a further improvement towards higher cell densities of $\sim 10^9\,\text{cell/cm}^3$, albeit less distinct as compared to the first treatment method. Conversely to expectations, post-purification addition of small amounts of aliphatic surfactant or PS oligomer showed no significant influence, i.e. decrease in cell density. Mahdi et al.[234] concluded, that thoroughly homogenizing the sample matrix (e.g. via extrusion or solvent addition-evaporation) changes the spatial distribution of the surfactants or processing agents from micelle-like structures to randomly distributed and disordered molecules. Those surfactant-covered polymer-micelle particles, when melted and "frozen" into a solid sample, assumingly kept their thin film layer structure and reduced

the effective diffusion coefficient of CO_2, thus negatively affecting the diffusion-controlled nucleation mechanism towards lower cell densities.

Using the grafting-onto method with an excess number of side chains required in any case the samples to be purified for molecular characterization and rheology. Repeated precipitation fractionation (see Appendix A.1.2.4) ensured the removal of not only residual PS side chains but also other possible, lower molecular weight contaminants like oligomers and lithium salts.

5.4.1.2 Reactor Setup

The pressure vessel, a 300 ml stirred minireactor with a maximum pressure of $p_{max} = 180$ bar and maximum temperature of $T_{max} = 200$ °C, was modified for batch foaming. The stirring function and blade was removed and replaced by a fitted sample holder inset to be able to host a number of 2–3 samples.

The dried samples were vacuum press molded into rectangular, 1 cm^2-sized disks and perforated to hook them onto the wire of the sample holder. For details about sample preparation, reactor specifications and foaming procedure, the reader is referred to **Appendix A.1.7.1**. The hardware of the 180 bar batch foaming setup is shown and explained in **Appendix A.3.1**.

5.4.1.3 Implementation

In order to achieve low density foams through high volume explansion while also maximizing the cell density, a high degree of saturation and nucleation has to be ensured.[268] Therefore, the foaming process should be induced in a high pressures range at maximum pressure drop rates, i.e. fast gas expansion (see also Equation 4.9).[204] With respect to the technical and safety limit of the employed reactor type, all experiments were conducted at 180 bar and a depressurization time of ∼4 s at maximum valve opening speed.

Given a fixed pressure and depressurization rate, the foaming behavior is furthermore influenced by the temperature as additional processing parameter. In contrast to the pressure and depressurization rate, which by tendency should be maximized to improve the foaming outcome, there is a suitable temperature range (i.e. processing window), individual to the properties of the polymer, beyond which the foam quality decreases with regards to the volume expansion and/or cell size.
In pilot tests with linear polystyrene (PS290) this temperature was found to be in the range of $T_{foam} = 125$–145 °C and therefore above the glass transition point $T_g(PS) = 105$ °C (measured via DSC) of the pure polymer. It should be mentioned, that the sorption of the CO_2 into the polymer and the swelling effect under supercritical conditions[40], is plasticizing the PS and reduces the glass transition of the polymer-gas mixture well below the $T_g(PS)$.[276]
According to studies by Arora et al.[268] on the sorption of supercritical CO_2 in PS, the solubility of CO_2 at the chosen saturation pressure and temperature conditions (p_{sat} =

[40] Critical point of CO_2: $T_c = 304.2\,K \mathrel{\widehat{=}} 31.1\,°C$, $p_c = 73.8$ bar.[275]

180 bar and T_{sat} = 125–145 °C) is ca. 9 ± 1 g CO_2 in 100 g PS, which ultimately decreases the glass transition of the order of 45–50 °C.[225,276,277]

The foaming procedure in the 180 bar lab-scale autoclave is schematically summarized in **Figure 5.10**. The sample holder with the prepared sample specimen was placed into the flat bottom cylinder of the reactor and filled with crushed dry ice. Then the vessel was closed and the device was heated to the desired foaming temperature while adjusting the desired saturation pressure manually, **Figure 5.10a**). After an induction time of ∼30 min to reach the set temperature and pressure, the conditions were kept constant for ∼3 h to allow for the CO_2 to diffuse into the sample (**Figure 5.10b**).[41] Finally, the foaming was induced by sudden depressurization to atmospheric conditions (**Figure 5.10c**).

$$\mathrm{PS} + \mathrm{CO_{2\,(s)}} \xrightarrow[\substack{125\text{–}145\,^\circ\mathrm{C}\\ 180\,\mathrm{bar}\\ \sim 30\,\mathrm{min}}]{\textbf{(a)}} \mathrm{PS} + \mathrm{scCO_2} \xrightarrow[\substack{125\text{–}145\,^\circ\mathrm{C}\\ 180\,\mathrm{bar}\\ \sim 3\,\mathrm{h}}]{\textbf{(b)}} \mathrm{PS \cdot scCO_2} \xrightarrow[\substack{p = \mathrm{atm.}\\ \Delta \mathrm{t} = 4\,\mathrm{s}\\ \mathrm{T} \rightarrow \mathrm{r.t.}}]{\textbf{(c)}} \mathrm{PS_{foam}} + \mathrm{CO_{2\,(g)}} \uparrow$$

Figure 5.10: Operation procedure for the one-step batch foaming process in the 180 bar lab-scale autoclave. **(a)** Setting foaming conditions. Within about 30 min the dry ice ($CO_{2\,s}$) is turned into supercritical CO_2 ($scCO_2$). **(b)** Maintaining saturation conditions to allow full sorption of PS with $scCO_2$ (PS·$scCO_2$). **(c)** Induction of cell nucleation and bubble growth through sudden depressurization.

The immediate core temperature drop of the autoclave to about 20–30 °C below the set point is a consequence of the Joule-Thomson thermodynamic effect of expanding gases. This temperature reduction strongly affects the bubble growth phase by restricting the expansion time. When the system temperature falls below the glass transition temperature, T_g, of the CO_2-plasticized PS melt, the polymer solidifies before the internal bubble pressure can drive the foaming. Furthermore, the glass transition increases due to the phase separation and loss in plasticization, i.e. $T_g(\mathrm{PS \cdot scCO_2}) \rightarrow T_g(\mathrm{PS})$.[279]

5.4.2 Foaming Results

Figure 5.11 shows SEM images of the cell morphology of foamed linear and comb PS specimen, expanded at T_{foam} = 125 °C. From this low magnification, it can be seen, that the cellular structure is relatively homogeneous with monomodal cell sizes across the whole range of branching densities from linear (**Figure 5.11a**) to bottlebrush-like PS (**Figure 5.11h**). A comparison of those images in higher magnification, as shown in **Figure 5.12**, reveals that at low foaming temperatures branching had no distinct effect on the cell size, with average diameters of $d_{foam} \sim 20$ µm.

[41] The minimum contact time of PS in $scCO_2$ to fully saturate the sample was reported by Reverchon and Cardea[278] at similar conditions. Preliminary tests also found ∼3 h to be sufficient to ensure full saturationin the here presented foaming experiments.

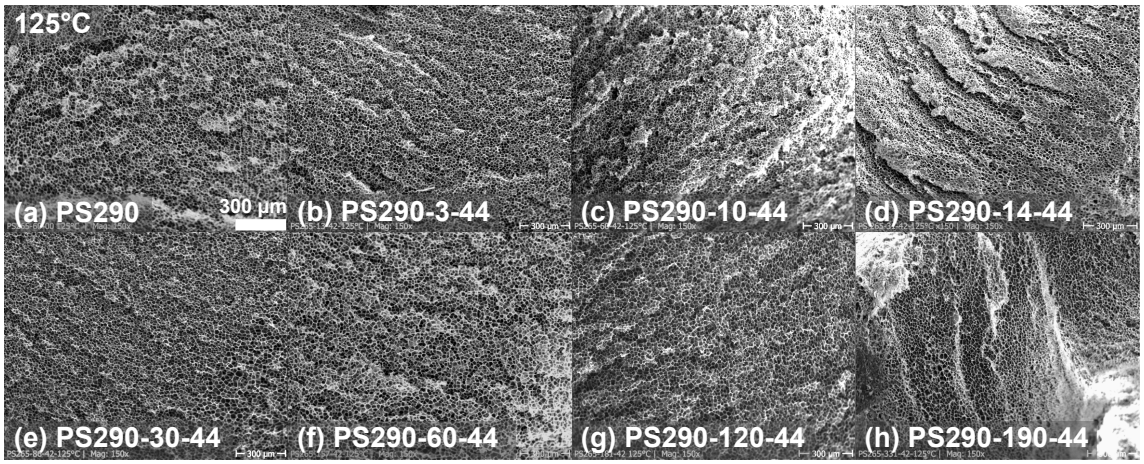

Figure 5.11: SEM images of the cellular structure of PS foams, expanded at 180 bar and 125 °C. **(a)** Linear PS290. **(b)**–**(h)** Comb PS290-N_{br}-44 series with number of branches from $N_{\mathrm{br}} = 3$ to 190. The pictures were taken at low magnification (×150). The scale bar shown in (a) represents 300 µm. Reproduced and modified with permission.[234] Copyright 2020, Elsevier.

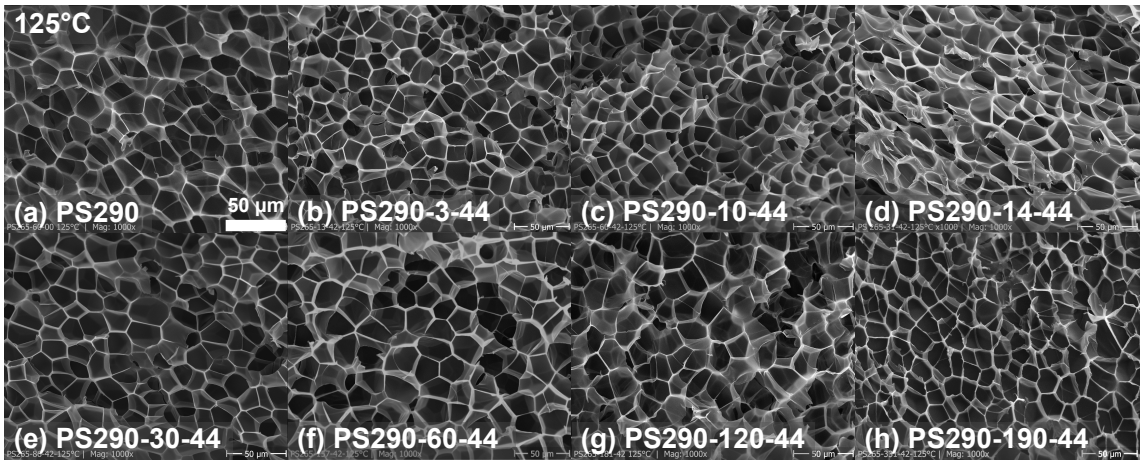

Figure 5.12: SEM images of the cellular structure of PS foams, expanded at 180 bar and 125 °C. **(a)** Linear PS290. **(b)**–**(h)** Comb PS290-N_{br}-44 series with number of branches from $N_{\mathrm{br}} = 3$ to 190. Same samples as in Figure 5.11, but higher magnification (×1000). The scale bar shown in (a) represents 50 µm. Reproduced and modified with permission.[235] Copyright 2020, Elsevier.

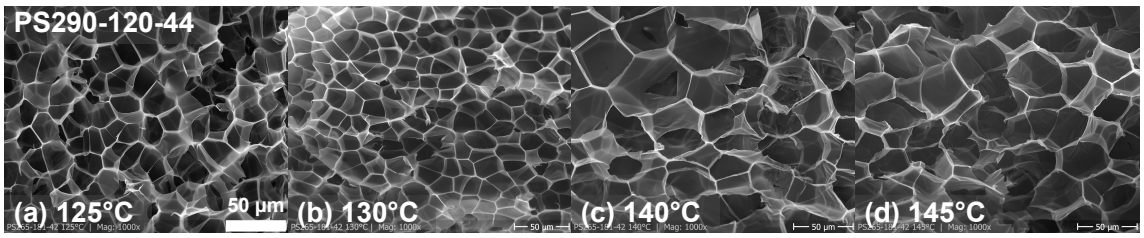

Figure 5.13: SEM images of the cellular structure of comb PS290-120-44 foams, expanded at different temperatures: **(a)** 125 °C, **(b)** 130 °C, **(c)** 140 °C, and **(d)** 145 °C. The pictures were taken at high magnification (×1000). The scale bar shown in (a) represents 50 µm. Reproduced and modified with permission.[235] Copyright 2020, Elsevier.

The effect of the foaming temperature, from 125 °C to 145 °C, on the cell size is shown in **Figure 5.13** at the example of comb PS290-120-44. This particular comb PS with an average of 120 branches per molecule exhibits sufficient melt strength to sustain thin cellular wall structures during bubble expansion, even at relatively high temperatures of 145 °C.

The quality of the foams were macroscopically assessed with respect to their density, ρ_{foam}, and volume expansion ratio, VER = ρ_{neat}/ρ_{foam} (expansion coefficient compared to the neat PS), and presented as a function of the foaming temperature in **Figure 5.14a** and **Figure 5.14b**, respectively.

The microscopic foam characteristics, analyzed via SEM images in terms of the average cell size, d_{cell}, and cell density[42], as number of cells, N_{cell}, per unit volume of neat, unfoamed polymer is shown in **Figure 5.14c** and **Figure 5.14d**.

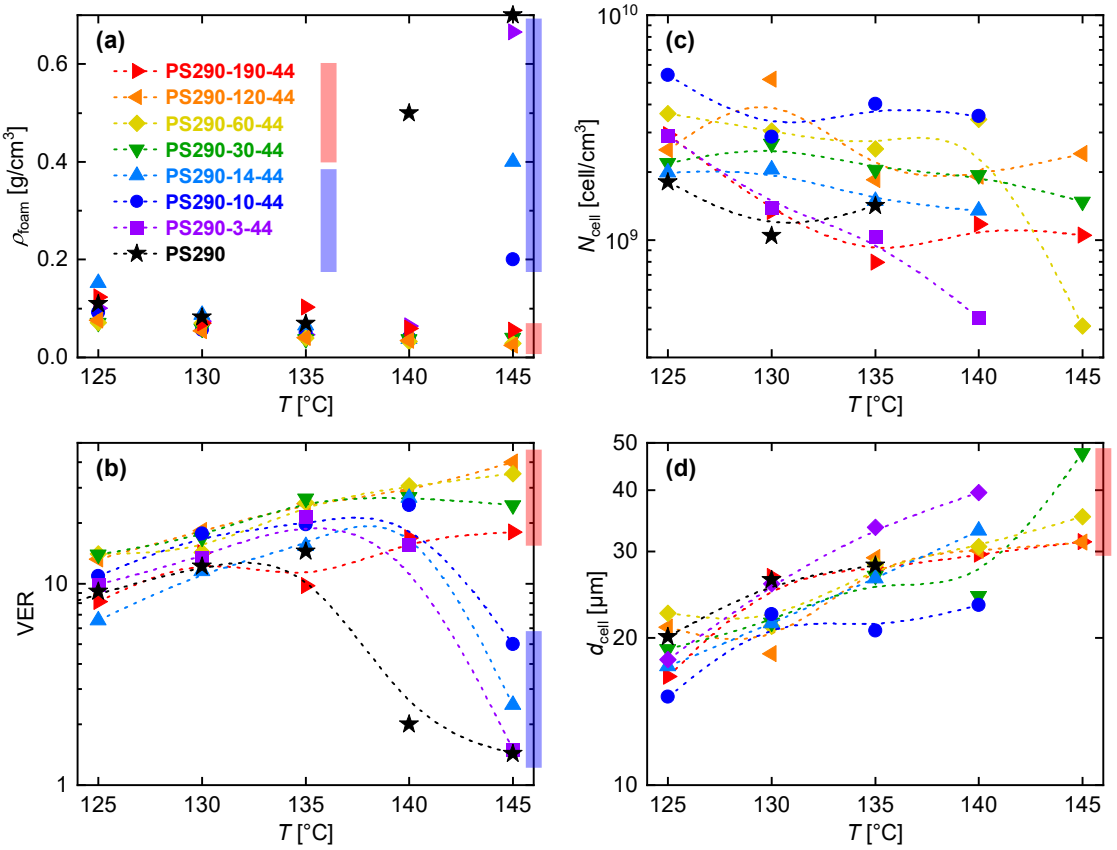

Figure 5.14: Effect of the temperature on the foaming properties of linear PS290 and comb PS290-N_{br}-44 with different number of branches, N_{br}. **(a)** Foam density, ρ_{foam}. **(b)** Volume expansion ratio, VER. **(c)** Cell density, N_{cell}. **(d)** Cell size, d_{cell}. Dashed lines are guide to the eye. Blue bars signify PS with linear, LC- and DC-PS conformation with $N_{br} \leq 14$, and red bars are DC- and LB-PS with $N_{br} \geq 30$ and LB-PS. Reproduced and modified with permission.[235] Copyright 2020, Elsevier.

[42] This can also be described as nucleation density, if all cells nucleated, expanded to bubbles without cell coalescence or cell wall rupture.

Foam Density and Volume Expansion

The density of a polymeric foam highly depends on the foaming conditions, i.e. saturation pressure and temperature at expansion. Very low foaming temperatures close to or even below T_g of the neat polymer promote a fast solidification in the early stages of the bubble growth phase, as the viscosity of the polymer-gas mixture is higher and the plasticizing effect of the blowing agent on the polymer is reversed faster with phase separation. In contrast, a high foaming temperature reduces the melt viscosity, thus lowers the stability of the cell walls and leads to premature cell coalescence and rupturing. In the extreme case, if the temperature is too high, the gas escapes without efficiently contributing to the expansion, or the foamed structure is not sufficiently solidified and partially shrinks. The optimum foaming temperature to achieve a low density foam with maximum expansion, therefore, is ultimately governed by the melt strength[43] (i.e. strain hardening), which is individual to the branching structure.

This dependency can be seen in Figure 5.14a as an over-all decrease in foam density, ρ_{foam}, from $T_{foam} = 125\,°C$ to $135\,°C$, related to the viscosity decrease which enables a higher bubble expansion until solidification. However, for increased temperatures above $140\,°C$, the melt strength of linear PS290 is insufficient to support the cellular structure of a low-dense foam, and the achieved volume (Figure 5.14b) barely doubles as compared to the unfoamed specimen. Consequently, at $145\,°C$ the foamability of linear PS is further reduced with close to no expansion. At this high temperature, also PS with loosely-grafted comb (LC) and densely-grafted comb (DC) conformation in the lower branching range up to $N_{br} = 14$ experience a drastic decrease in foam quality towards higher densities, however not as severely compared to linear PS due to their higher melt strength.

Figure 5.14a emphasizes a clear distinction between comb PS with DC conformation above $N_{br} \geq 30$ further sustaining high volume expansions at higher temperatures. Conversely, linear and DC conformations below $N_{br} \leq 14$ disproportionately lose foam size. This big disparity in foamability, that originates from strain hardening is congruent to the viscoelastic properties of the comb PS series in uniaxial extensional experiments, see Section 5.3.2. At high extensional rates of $\dot{\varepsilon}_H \geq 10^{-1}\,s^{-1}$, the strain hardening factor of PS290-30-44 and combs with more branches was at or well above SHF ≈ 30, whereas the SHF of PS290-14-44 barely exceeded 10 and was therefore minimum 3–4 times lower than that of comb PS with equal or more than $N_{br} \geq 30$ branches.

The volume expansion of PS290-120-44 at $T_{foam} = 145\,°C$ reached a value as high as VER ≈ 40. Considering that the maximum achievable volume expansion is restricted by the amount of blowing agent dissolved in the polymer, under those conditions at a fixed pressure of 180 bar, an upper theoretical limit of VER ≈ 45 exists.[44] This means that about 90 % of the CO_2 contributed to the bubble expansion with little amount of unused

[43] "Melt strength" is an elongational rheological property of a polymer melt and an engineering measure of its resistence to stretching and rupture. Melt strength can be measured e.g. with a Göttfert Rheotens, originally developed by Meissner.[10]. The strain hardening factor (SHF), e.g. obtained from uniaxial elongational measurements as an alternative but more clearly quantifiable parameter, can also be used to describe melt strength properties.[119]

[44] Calculated based on the gas solubility of $9 \pm 1\,g\,CO_2/100\,g$ PS at saturation conditions of $p = 180\,bar$ and $T = 125$–$145\,°C$.

gas escaping through the surface of the sample during the foaming stage. In contrast, linear PS290 at optimum conditions around 135 °C with VER ≈ 15 only reached a foaming efficiency of about 30 %.

Cell Density and Cell Size

Figure 5.14c shows the influence of the temperature on the cell density of the resulting foams. In the investigated temperature range of T_{foam} = 125–145 °C, most foam specimen, linear and branched PS, have cell densities in the order of $N_{cell} \sim 10^9$ cell/cm^3, which is in good agreement with Stafford et al.[269] who reported for purified commercial and lab-scale linear PS at similar conditions a cell density of 1–4 · 10^9 cell/cm^3, depending on the molecular weight and residual amount of impurities.

As a general tendency, the cell size increased with increasing temperature, which might be explained by the effect of cell coalescence due to a reduced viscosity. However, some values unexpectedly deviate from this behavior and there is no conclusive trend when the samples with different degrees of branching are compared. It is important to mention, that the calculation of the cell density is subject to several sources of error that all can affect the outcome significantly: a) the analyzed image represents just a relatively small cross section of the foam; b) the criteria to count a void as one cellular unit is subjective and a distinction is even more complicated if the cell walls enclosing a void are overly damaged from the sample preparation via fracturing; c) the volume expansion in the equation (see Equation A.3) relies on the accuracy of density measurement.
Nevertheless, from the SEM images of PS290, cellular structures were only obtained up to a maximum temperature of 135 °C, while branched PS290-N_{br}-44 with $N_{br} \leq 14$ achieved a foam-like morphology at an even higher temperature of 140 °C. Their foamability were only surpassed by highly branched DC-PS with $N_{br} \geq 30$ and LB-PS. In that sense, the cell density results are congruent with the foamability criteria deduced from the volume expansion ratio.

As mentioned before, the melt strength (quantified by the strain hardening) of the polymer dictates the structural stability of filaments in uniaxial, biaxial or planar flow, of which all occur during cell expansion and especially towards the end of the bubble growth phase. Accordingly, the strain hardening of highly branched combs support the cell walls and prevent cell coalescence. If the polymer exhibits insufficient melt strength to maintain the stability of nucleated bubbles in the growth phase, then the resulting cell size is an effect of cell coalescence and wall rupture, rather then pure cell expansion. As can be seen from Figure 5.14d, for comb PS with 190, 120 and 60 branches, between T_{foam} = 130 °C and the highest temperature at 145 °C where they still are foamable, the cell size from ∼25 µm to ∼30 µm does not significantly increase. In contrast, PS290-30-44 containing a lower number of branches at this temperature reached the highest cell size of $d_{cell} \approx 50$ µm. The increase in volume expansion of PS290-120-44 to VER ≈ 40 (see Figure 5.14b), while keeping a small cell density and cell size implies, that the cell wall thickness must be greatly reduced to support a higher total number of cells. A direct measurement of the cell wall thickness from the SEM image was not feasible. However, assuming polyhedral

cell structures, the cell wall thickness can be estimated, see Equation A.6, and results in a 50 % decrease from ca. 500 nm at $T_{\text{foam}} = 125\,^{\circ}\text{C}$ to ca. 250 nm at 145 °C.

5.5 Conclusive Summary: Structure–Property Relationship

The foamability and final foam quality of a thermoplastic polymer, as processed in the melt state, is a direct result of its flow behavior in the bubble growth phase. Assuming the same, homogeneous nucleation mechanism for polymers of identical chemical composition, but different topological features, then the bubble expansion, governed by shear and extensional flow, remains as the most influential factor on the outcome of foaming. Therefore, the polymer dynamics, which can be characterized by linear or nonlinear viscoelastic parameters, can provide a rheological fingerprint to connect the effect of molecular structure on the foaming properties.

Figure 5.15 graphically summarizes the rheological properties (on the left y-axis) in the framework of the linear viscoelastic parameter ZSV, η_0, in shear and the nonlinear viscoelastic criteria SHF in extensional flow, as well as the foam properties (on the right y-axis) in the framework of the VER and cell density, N_{cell}, and correlates them to the molecular structure, represented by the number of branches, N_{br}. The influential rheological factors on the bubble expansion with respect to the stages of foaming appear as follows: At the early stages, when a bubble nuclei is created and starts expanding, the polymer chains at the cell's surface experience small deformations within the linear viscoelastic regime. At this stage it can be assumed that a low viscosity, η_0, benefits the stabilization of nuclei and promotes their growth into small bubbles. On the contrary, the growth retarding force of the viscosity diminishes or delays the onset of bubble instabilities when the expansion time is longer.[280] Therefore, with progressing bubble growth, low viscosity has a negative impact on cell stabilization and is associated with poor foam quality. This has been consistently observed for linear PS290, which displays relatively high cell sizes at low VER and a foamability limited to temperatures of $T_{\text{foam}} < 135\,^{\circ}\text{C}$.

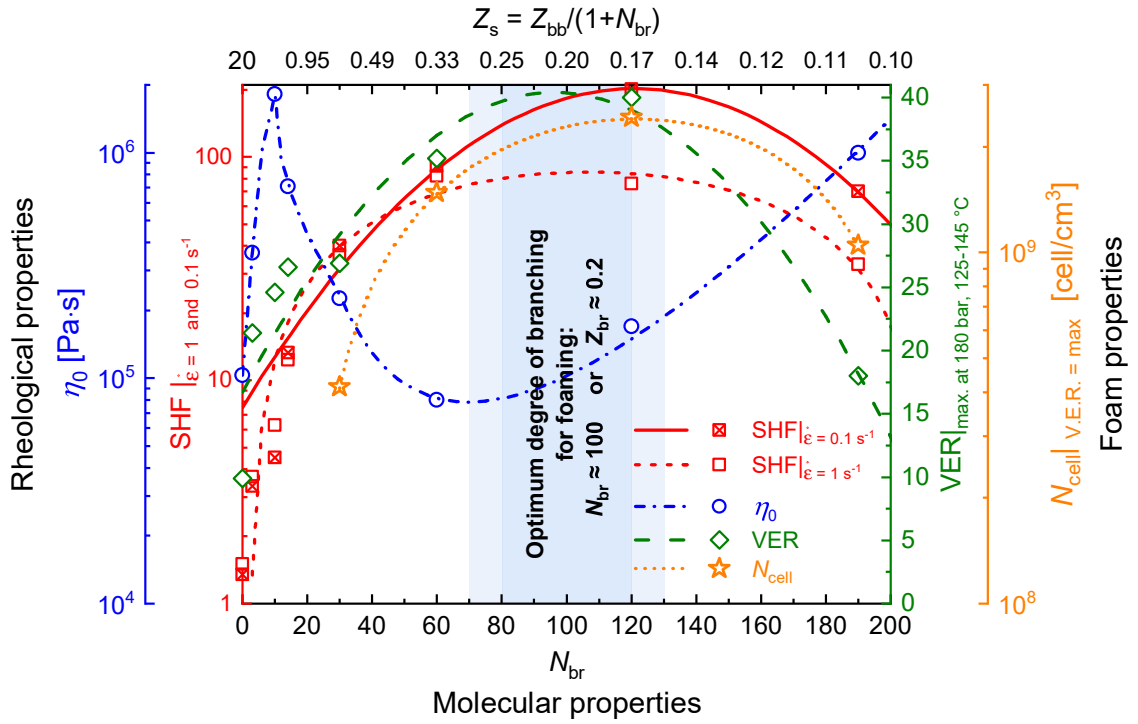

Figure 5.15: Effect of the molecular properties, represented by the number of branches, N_{br} (bottom x-axis), and segment number of entanglements, Z_s, on the rheological properties (left y-axis), represented by the zero-shear viscosity, η_0, and the strain hardening factor, SHF, at two extensional rates, $\dot{\varepsilon}_H = 1$ and $0.1\,s^{-1}$, all obtained from experiments at $T_{ref} = 180\,°C$. The foam properties (right y-axis) are represented by the maximum achievable volume expansion ratio (VER) and the related cell density $N_{cell}|_{VER=max}$ for foaming conditions of $p = 180$ bar and a temperature range of $T = 125$–$145\,°C$. Solid, dashed and dotted lines serve as guides to the eye. The maximum theoretically achievable V.E.R. is ~45, considering all dissolved CO_2 in the polymer sample contributes to the volume expansion. An optimum degree of branching for foaming of this comb PS series is indicated around $N_{br} \approx 100$, close to PS290-120-44 which correlates to the highest experimentally obtained VER and SHF. Reproduced and modified with permission.[235] Copyright 2020, Elsevier.

The presence of even very low amounts of $N_{br} = 3$ LCB already significantly improves the foamability towards higher VER at elevated temperatures owing to enhanced viscosity in both shear and extensional flow. Further addition of LCB, as seen up to PS290-120-44 with maximum strain hardening of SHF ≈ 200, benefits the later stages of foaming where melt stability is of paramount importance for cell stabilization until cell wall solidification. Even though η_0 for this comb PS is almost similarly low alike its backbone PS290, the elongational viscosity obviously has an even weightier influence, if the deformation field is within the nonlinear elongational regime. Therefore, a maximum SHF can be considered as a necessary prerequisite for the maximum achievable VER, while simultaneously diminishing cell coalescence, whereas an apparently reduced viscosity in shear does not have adverse effects on the volume expansion. In the case of LCB, cell stabilizing strain hardening during bubble growth outweighs possible minor negative influence of low η_0 on the expandability. At this point it is not clear if a low shear viscosity even might simultaneously improve the bubble formation in the nucleation stage. Undoubtedly, strain hardening during bubble expansion and thin cell wall formation, provided by LCB, is the key factor of foamability and reaching very low foam densities in microcellular, high cell density foam structures.

Consequently, the declining foam quality of the LB comb PS290-190-44 is then a result of its lower strain hardening, that comes with too many branches and inefficient entangling.

According to Figure 5.15, there is an optimum number of branches in a comb polymer to achieve the best foam expansion without compromising cell density, N_{cell}, which on the other hand is also closely related to the highest possible strain hardening. For the investigated LCB comb-PS series with $M_{\mathrm{w,bb}} = 290\,\mathrm{kg/mol}$ and $M_{\mathrm{w,br}} = 44\,\mathrm{kg/mol}$, this optimum is estimated to be found in the range of $N_{\mathrm{br}} \approx 100 \pm 20$, corresponding to $Z_{\mathrm{s}} \approx 0.2 \pm 0.05$ segmental entanglements between branch points.

Of course, this criteria of optimum N_{br} will be individual to each comb polymer series and will depend on the polymer type and specific molecular features with respect to the backbone and side chain lengths, i.e. number of entanglements.

The role of strain hardening as a requirement for good foamability was recently questioned by Weingart et al.[26], who found that a linear PP with no strain hardening delivered superior foamability in terms of low foam density and small cell morphology, as compared to LCB-PP that showed good strain hardening. The authors concluded, that the crystallization behavior from the onset of crystallization to the gelation and solidification is the most influential factor for good expandability and cell wall stability.
However, from the results in the presented work, strain hardening is undoubtedly the key driver for foamability in amorphous polymers and of paramount importance if other factors, like crystallization effects, do not govern the melt properties.

6 Model Dendrigraft Polystyrenes

This chapter takes branching – literally – "to the next level". Model dendrigraft polystyrenes with short chain branches (SCB) on long chain branches (LCB) are synthesized on the basis of a LCB comb PS precursor. The rheological properties of their branch-on-branch (bob) structure is investigated in SAOS and elongation. Foaming and comparison with the properties of SCB and LCB combs gives insights into influential rheological and topological parameters.

In the previous Chapter 5, the influence of comb- and bottlebrush-like topologies on the rheological and foaming properties were investigated and correllated to the molecular characteristics with respect to the number of branches. An increase in branching towards densely-grafted comb PS revealed to highly improve melt strength in elongational flow which translated to a maximum achievable volume expansion due to cell wall stabilization via strain hardening. However, excessive branching towards loosely-grafted bottlebrushes showed adverse effects in elongational and foaming performance and further improvement via more branch crowding at the backbone certainly cannot be expected.

Dendrigraft polymers offer another way to increase the branching content, but are – up to now – not sufficiently explored when it comes to their melt properties,[281–285] especially in elongational deformation.[283–285] Those highly branched topologies from the dendritic polymer family (see Section 2.3) have a defined branch-on-branch (bob) structure. With this, another generation of branching is achieved by grafting a second layer of branches onto the side chains of a comb or onto the arms of a star-shaped polymer. As one can expect, dendrigraft polymers are structurally diverse depending on the precursor topology and the statistically random or controlled grafting sites; therefore also different terms of nomenclature are used. However, the commonality is that their branches are considered as entangled, which discriminates dendrigrafts from dendrimers or hyperbranched polymers.

6.1 Synthesis of Model Branch-on-Branch PS (Bob PS)

The synthetic strategy of post-polymerization functionalization and successive side chain grafting offers a straightforward route to dendrigraft polymer architectures, with each branch layer serving as a precursor for higher-generation branching. As demonstrated for dendrigraft polystyrenes[77,81,286,287], polyisoprenes[93] and polybutadienes[94], as well as

various copolymer compositions[79,82,99,288,289], the cycle of functionalization, living anionic polymerization and grafting can be repeated and high molecular weights of 10^7 g/mol can be attained within only 2–4 grafting cycles.

The here presented synthesis of homopolymer branch-on-branch polystyrenes (bob PS) from comb PS is based on the Friedel-Crafts acetylation approach of Li and Gauthier[81] who synthesized two series of "arborescent graft polystyrenes" with up to three grafting generations, each with side chains of 5 and 30 kg/mol, respectively. However, they started with rather short backbones of also 5 and 30 kg/mol and relatively high degrees of acetylation, so the topological structure of their dendrigrafts assumingly resembled more a spherical, dendrimer-like structure rather than a comb-like conformation.

Their approach was adapted by first synthesizing a densely-grafted comb PS precursor with well-entangled LCB, analogously to the comb PS series from the previous Chapter 5 that was based on the same synthetic principles. However, a long backbone relative to the side chains ensured a comb-like aspect ratio. Successive grafting with a second layer of barely entangled SCB led to a multiply-branched PS with dendrigraft architecture.[45] The molecular weights of the backbone and LCB of the first graft generation, with $M_{w,bb} = 310$ kg/mol and $M_{w,lcb} = 40$ kg/mol respectively, were chosen to be of similar length like the comb PS290-N_{br}-44 series in the previous chapter. With a total entanglement number of the backbone of $Z_{bb} \approx 21$, a targeted grafting number of $N_{lcb} \approx 100$ LCB results in a segment entanglement number of $Z_s \approx 21/100 \approx 0.2$. Therefore, a low ZSV, η_0, is expected but already high melt strength, as concluded from Figure 5.15.
The molecular weight of the second layer of branches was decided to be much shorter, around the entanglement molecular weight, $M_{w,scb} \approx M_e \approx 15$ kg/mol, which ensured significant effect on the rheological behavior, but short enough to not excessively increase the molecular weight of the whole molecule, that is already high in the comb-stage. Another reason for the difference in LCB and SCB branch molecular weight was their characteristic relaxation behavior that was expected to also be different and thus rheologically distinguishable.

In total, a series of three samples of bob PS with the same comb precursor of $N_{lcb} = 100$ but different number of N_{scb} in the bob-stage were synthesized using anionic polymerization techniques. In the following sections, the synthesis is described. The molecular characteristics can be found in **Table 6.2**, p. 109.

6.1.1 Reaction Overview

Figure 6.1 gives a schematic overview of the synthesis of dendrigraft-type bob PS, with **(a)**–**(d)** as the first iterative cycle towards LCB comb PS (cf. Fig. 5.1). The second iterative cycle comprises reaction steps **(c)** and **(e)**–**(f)**, leading to the final bob PS with a corona of short chains. The depicted, simplified reaction scheme is representative in length scale, with respect to molecular weights ($M_{w,bb}$, $M_{w,lcb}$ and $M_{w,scb}$), functionalization (N_{ac}),

[45] To discriminate the different branch molecular weights and numbers for different graft generations, in this chapter the subindices "lcb" and "scb" were used to refer to long chain (LCB) and short chain branches (SCB), respectively.

and grafting number (N_{lcb} and N_{scb}), and shows the example of bob PS310-100-40-*g*-120-14 synthesized from the comb PS310-100-40 precursor by grafting (-*g*-) an additional, average number of $N_{scb} = 120$ SCB of $M_{w,scb} = 14\,kg/mol$ onto $N_{lcb} = 100$ comb LCB of $M_{w,lcb} = 40\,kg/mol$. Other bob PS of this series were targeted for higher branch density, ultimately achieving $N_{scb} = 240$ and 460 SCB.

The nomenclature of the bob PS is defined as PS$M_{w,bb}$-N_{lcb}-$M_{w,lcb}$-*g*-N_{scb}-$M_{w,scb}$.

An overview of the molecular characteristics of the synthesized linear PS, comb PS and bob PS is given in Table 6.2, which will be discussed later.

6.1.2 Functionalization and Grafting-Onto

The anionically polymerized, linear backbone PS310, **Figure 6.1a**, was FC-acetylated, resulting in a 6 mol% conversion, corrsponding to a total number of $N_{ac} = 167$ functionalized styrene monomer units, **Figure 6.1b**. Considering the conversion of only 2/3 of the acetyl groups into actual branch points due to enolate formation (see Section 5.1.1), this degree of acetylation was targeted to result – after grafting – in an expected, ideal range of $N_{lcb} \sim 100$ comb PS side chains. From this acetylated backbone, the LCB precursor comb PS310-100-40, **Figure 6.1c** and **d**, as well as SCB comb PS310-100-14 were synthesized, with the latter serving for comparison.

In the functionalization of comb PS310-100-40, with the intention of only few (1 to 5) second-layer SCB per LCB, the degree of acetylation was aimed towards 0.5–2 mol%, **Figure 6.1e**. Higher percentages of acetylation could not be achieved due to significant crosslinking, as recognized by a strong increase in viscosity of the reaction mixture and unsoluble reaction products when the concentration of FC acetylation reagents was increased.

The final grafting-onto step, **Fig. 6.1f**, resulted in a number of $N_{lcb} = 120$, 240 and 460 SCB onto acetylated comb PS310-100-40, all corresponding to 57–66 mol% conversion of functional groups with respect to the different degrees of acetylation of comb PS310-100-40. The achieved grafting yields were consistent with reports of Li et al.[81] who converted approx. 2/3 of acetyl functional groups of "arborescent" graft homopolymer PS into branch points. The competing enolate formation as occurring side reaction which is largely independent of reaction conditions has already been discussed in Section 5.1.1. Deviations of those grafting yields have been found to be more dependent on the density of functionalization and the molecular weight of the graft chains. Even though the nucleophilicity/basicity of the anions or the reactivity of the electrophilic carbonyl moiety is not affected by the molecular weight of the living branches, the length most likely is still an influential factor for the sterical accessibility of the functional group.

By endcapping the polystyryl anions with few units of isoprene[82] or 2-vinylpyridine[289] and grafting in the presence of LiCl, the yield for sterically unimpeded topologies can be increased towards 90 %. However, increased branch lengths and higher graft generations still negatively affect the amount of carbonyl conversion into branch points.[81] Furthermore, the comonomer units for endcapping may pose a thermomechanical weak link into the topology where the branches are attached and make them more prone to chain scission in high temperature conditions, e.g. during sample preparation, rheological tests and foaming.

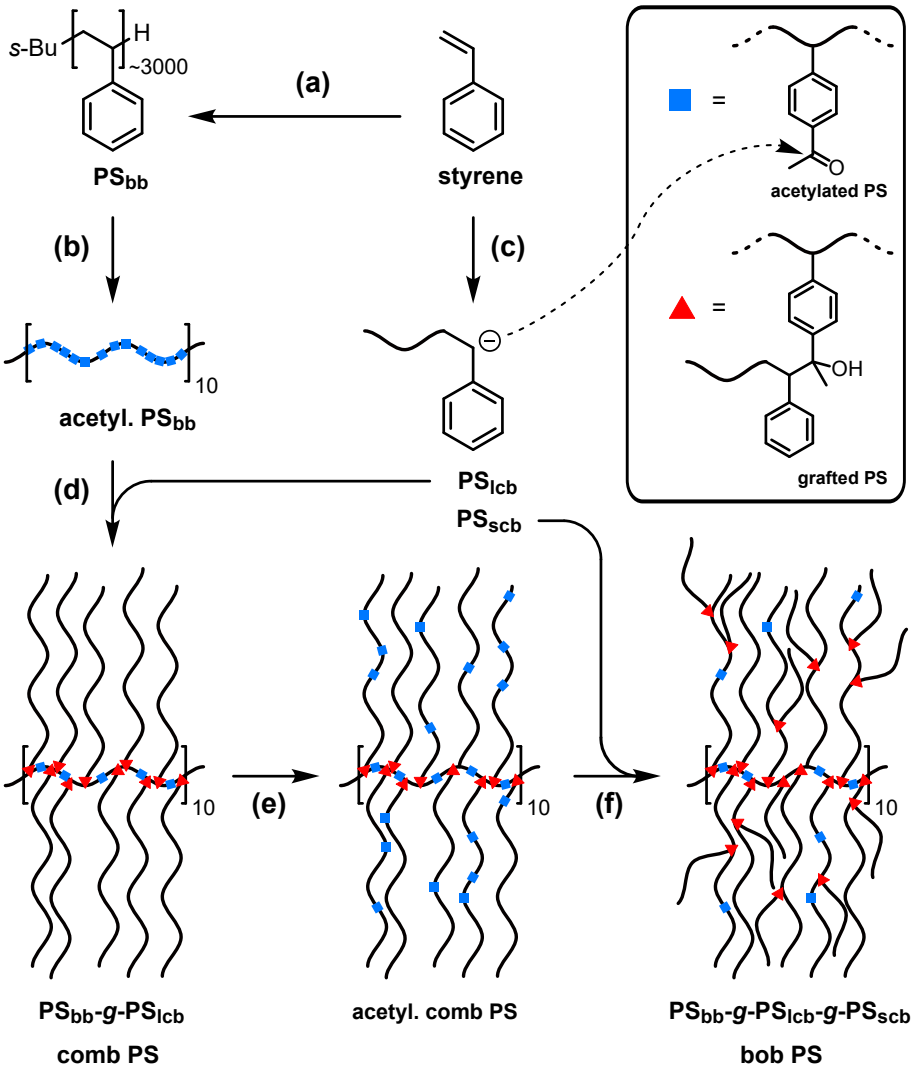

Figure 6.1: Reaction scheme for the synthesis of model branch-on-branch (bob PS) from comb PS. **(a)** Anionic polymerization of the backbone with $M_{w,bb} = 310\,kg/mol$. **(b)** Functionalization of the backbone via partial FC acetylation. **(c)** Anionic polymerization of living LCB (PS_{lcb}) and SCB (PS_{scb}). **(d)** Grafting of LCB onto the acetylated backbone. **(e)** Partial FC acetylation of the comb PS. **(f)** Grafting of SCB onto the acetylated comb PS precursor. The numbers and length scales are chosen to show a representative example of bob PS310-100-40-*g*-120-14.

As previously investigated, degradation of pure homopolymer comb PS (synthesized from acetylated substrates) can be widely avoided with proper sample preparation and measurement conditions (see Section 5.3.1).

The consistently similar grafting yields of about 60 % for all comb and bob PS indicate, that the synthesis of LCB comb or even highly dense SCB dendrigraft PS was – if at all – only minorly affected by sterical hindrance.[46]

It is important to mention that the acetylation is a random process. Therefore, the partial acetylation of comb PS310-100-40 (Figure 6.1e) will also result in additional functionalization of the backbone including the unconverted carbonyl groups from the comb synthesis stage.

[46] Furthermore, in this case the gained experience in synthesis and laboratory routine most likely is another non-negligible factor for the consistent grafting conversions, especially when compared to the first comb PS290-N_{br}-44 series (see 5.1.4).

However, due to the low volume fraction of the backbone of $\phi_{bb} \ll 10\,\text{mol}\%$, statistically more than >90 % of the functional groups will be found on the LCB of comb PS310-100-40 and therefore also >90 % of the $N_{scb} = 120$ SCB of the second stage will attach onto the comb PS side chains. This ratio is expected to be even higher in favor of branch-on-branch grafting considering the sterical accessibility of peripheral side chains vs. backbone core.[47]

Due to the regio-unselective acetylation, the position of the SCB on the LCB underlies also a variation. Apart from being – ideally – grafted mid-chain of the LCB, the SCB can also be attached to the apex (top) of the LCB resulting in a (nearly) linear, extended LCB of ∼55 kg/mol, or grafted close to the backbone. If the functional group is however close to the backbone, grafting results in a chain segment resembling a "barbwire" structure.[55]

6.1.3 Fractionation

The process of precipitation fractionation to purify comb PS from unreacted LCB, as well as – after the second step – bob PS from SCB, was conducted like previously explained for the comb PS series (see Section 5.1.2, p. 70). Due to the high difference in molecular weights of comb versus LCB ($M_{w,comb} \approx 100 \cdot M_{w,lcb}$) and in particular of bob versus SCB ($M_{w,bob} > 400 \cdot M_{w,scb}$), the addition of non-solvent MeOH strongly shifts the partition equilibrium of the high-M_w fraction towards the separation into a gel-phase. In contrast, the low-M_w compounds were still dissolved even at relatively high MeOH concentrations. Within 2–4 fractionation cycles, high purity (>99 %) and nearly full recovery of the branched product fraction was obtained.

6.1.4 Molecular Characterization

Comb and bob PS310 series synthesized in this chapter were molecularly characterized via SEC, giving apparent molecular weights based on hydrodynamic radii, as well as gravimetry, giving absolute molecular weights based on total mass increase. For comparison, the results are summarized in Table 6.2, p. 6.2.

6.1.4.1 SEC

The synthesized and purified SCB and LCB comb, as well as bob PS310 series were analyzed via SEC using a linear PS standard calibration. Therefore, the resulting number- and weight-average molecular weights, $M_{w,SEC}$, reported in Table 6.2, represent apparent values for linear PS with the same hydrodynamic radius.

Figure 6.2 shows the normalized molecular weight distribution of comb and bob PS310 series. The high-M_w branched polymers and the low-M_w side chains were very well baseline separated which positively affected the purity and recoverability via precipitation fractionation as explained before.

The molecular weights of the linear backbone and graft chains were within the exclusion limit of the analyical, single porosity colums below the maximum separable molecular

[47] This is a lower estimation for bob PS with $N_{scb} = 120$ SCB, so the probability of SCB found on LCB vs. backbone is even much higher than 90 % for the bob PS with $N_{scb} = 240$ and 460 SCB.

weight of $2.5{\cdot}10^3$ kg/mol. However, this separation range was insufficient to resolute the distribution of comb and bob PS. Therefore, a semi-preparative mixed bed column with a total exclusion limit of about $30{\cdot}10^3$ kg/mol was employed and calibrated with a set of linear PS standards with a maximum of $14{\cdot}10^3$ kg/mol to extend the range towards higher molecular weights.

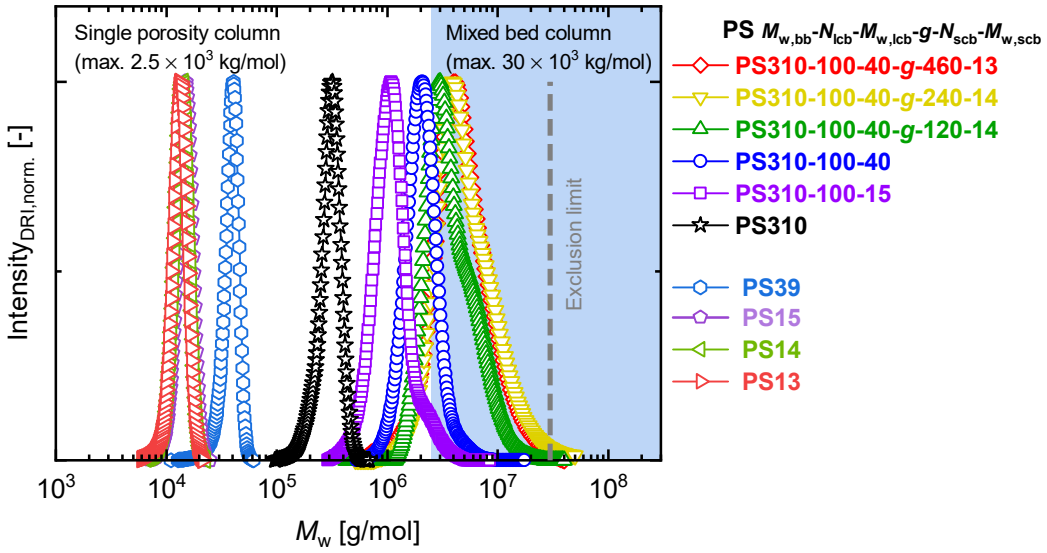

Figure 6.2: Molecular weight distribution of the purified dendrigraft bob PS310 series, as measured based on a linear PS standard calibration. Precursor linear PS310 backbone, LCB and SCB branches were measured with an analytical, single porosity column (max. $2.5{\cdot}10^3$ kg/mol). For the grafted comb and bob PS a semi-preparative mixed bed column (total exclusion limit max. $30{\cdot}10^3$ kg/mol) was used, calibrated with a set of linear PS standards with a maximum $M_w = 14{\cdot}10^3$ kg/mol. The measurements were performed in THF at 25 °C using a flow rate of 1 ml/min and an injected sample concentration between 0.5 to 2 mg/ml.

From Figure 6.2 it can be seen that the molecular weight distribution (MWD) broadens with increasing topological complexity. The comb PS with side chains of 15 and 40 kg/mol have relatively narrow MWD with dispersities of $Đ \approx 1.3$, which is also observed for the bob PS with the lowest grafting density of 120 SCB. However, for the bob PS with double the number of SCB, the MWD moderately increased to $Đ \approx 1.7$, but the highest branched bob PS had also a relatively low dispersity of $Đ \approx 1.3$. Broadening of the main peak with higher graft generations may be attributed to incresed topological complexity and statistical effects, but also might be caused by possible coupling reactions during the FC aromatic acetylation that will be discussed in **Section 6.1.6**.

6.1.4.2 Gravimetry

The simplest and arguably most straightforward method of determining the number of branches is achieved gravimetrically. The mass difference between the purified graft product recovered from fractionation and its precursor before the grafting reaction can be calculated and is attributed to the amount of grafted chains. If the molecular weight of acetylated precursor and branches is known, the mass increase can be directly converted into the number of added branches in the grafting-onto reaction.

The gravimetric method was previously used by Li et al.[81] who confirmed the grafting yield of comb- and dendrigraft-type PS obtained by SEC-trace method (see also Section 5.1.3.2). When comparing both methods, they reported deviations of ca. 2 percentage points for grafting yields of second-generation arborescent polystyrenes of 43 and 74 %. Due to the very good agreement, they further determined the grafting yield of highly branched PS gravimetrically as the molecular weight was too high that the dendrigrafts did not elute from the column and the SEC-trace method was inapplicable for characterization.

As already briefly mentioned in Section 5.1.3, the validity of the gravimetric method is only ensured with high recovery purification. The perfect baseline separation in the SEC (see Figure 6.1.6) between comb or dendrigraft product vs. precursor branches, due to 100 to 1000-fold molecular weight difference, indicates good fractionationability with little to no loss of linear or branched PS in the solvent or precipitate phase, respectively.

The number of branches reacted in the last grafting step, N_{gr}, was obtained by the mass of acetylated precursor, m_{ac}, and purified graft product, m_{gr}, as well as the molecular weights of the acetylated precursor, $M_{w,ac}$, and grafted side chains, $M_{w,gr}$, via **Equation 6.1**.

$$N_{gr} = \frac{(m_{gr} - m_{ac})\ M_{w,ac}}{m_{ac}\ M_{w,gr}} \tag{6.1}$$

Table 6.1 summarizes the gravimetric results and reports the molecular weight, $M_{w,gr}$, and the number, N_{gr}, of grafted chains. The grafting yield as the fraction of carbonyl functional groups which were converted into branch points was calculated via $\mathrm{mol\%_{gr}} = N_{gr}/N_{ac}$.

Table 6.1: Acetylation and grafting results after precipitation fractionation for comb and bob PS310 series. Comb PS310-100-40 (marked with *) served as precurser for dendrigraft bob PS.

	Acetylation			Grafting				
Sample name [a]	Precursor	N_{ac}	$mol\%_{ac}$	m_{ac}	m_{gr}	$M_{w,gr}$	N_{gr}	$\mathrm{mol\%_{gr}}$
PS310-100-15	PS310	167	6.0	4.07	30.8	15	103	62
PS310-100-40 (*)	PS310	167	6.0	5.63	53.0	39	98	59
PS310-100-40-*g*-120-14	*	188	0.5	5.05	7.23	14	123	66
PS310-100-40-*g*-240-14	*	405	1.0	3.65	6.66	14	236	60
PS310-100-40-*g*-460-13	*	802	2.0	2.85	7.13	13	461	57

[a] Samples labelled according to: PS$M_{w,bb}$-N_{lcb}-$M_{w,lcb}$-*g*-N_{scb}-$M_{w,scb}$. N_{ac}: Average number of acetyl groups per precursor substrate molecule, as measured by ^{1}H-NMR (see Section 5.1.3.3). $mol\%_{ac}$: Degree of acetylation as fraction of converted styrene units. m_{ac} [g]: Mass of acetylated precursor substrate used in grafting reaction. m_{gr} [g]: Mass of grafted product recovered after precipitation fractionation. $M_{w,gr}$: Molecular weight of branches added in grafting reaction. N_{br}: Average number of branches added after grafting reaction, determined gravimetrically by $N_{br} = [(m_{gr} - m_{ac})/M_{w,gr}]\ /\ [m_{ac}/M_{w,ac}]$, with $M_{w,ac}$ as the molecular weight of acetylated precursor. $\mathrm{mol\%_{gr}} = N_{gr}/N_{ac}$: Grafting yield.

Table 6.2: Molecular parameters of model comb and bob PS310 series. All molecular weights in kg/mol.

	Backbone (bb)			**Inner branches (lcb)**				**Outer branches (scb)**			**Total**			
Sample name [a]	$M_{w,bb}$	$Đ_{bb}$	$N_{ac,bb}$	$M_{w,lcb}$	$Đ_{lcb}$	N_{lcb}	$N_{ac,lcb}$	$M_{w,scb}$	$Đ_{scb}$	N_{scb}	M_w	$M_{n,SEC}$	$M_{w,SEC}$	$Đ_{SEC}$
PS310	310	1.14										290	310	1.14
PS310-100-15	310	1.14	167	15 [b]	1.03	103 [b]					1800	860	1150	1.33
PS310-100-40	310	1.14	167	39	1.03	98					4200	1630	2150	1.31
PS310-100-40-*g*-120-14	310	1.14	167	39	1.03	98	188	14	1.03	123	5900	3270	4240	1.30
PS310-100-40-*g*-240-14	310	1.14	167	39	1.03	98	405	14	1.03	236	7600	3850	6720	1.74
PS310-100-40-*g*-460-13	310	1.14	167	39	1.03	98	802	13	1.03	461	10100	4310	5500	1.28

[a] Sample labelled according to: PS$M_{w,bb}$-N_{lcb}-$M_{w,lcb}$-g-N_{scb}-$M_{w,scb}$. M_w = weight-average molecular weight. M_n = number-average molecular weight.
[b] In case of comb PS310-100-15, the brach molecular weight and branching number refers to $M_{w,scb}$ and N_{scb}, respectively.

6.1.5 Overview of Molecular Parameters

Table 6.2 summarizes the results of the characterization via SEC and gravimetry and lists the structural parameters of the linear backbone PS310, the SCB and LCB comb PS, as well as the bob PS series with 120, 240 and 460 outer SCB. All M_w used for the sample labelling (PS$M_{w,bb}$-N_{lcb}-$M_{w,lcb}$-g-N_{scb}-$M_{w,scb}$) are based on the SEC DRI trace and the branching numbers, N_{lcb} and N_{scb}, on the gravimetric results.

6.1.6 Concluding Remarks on Synthesis and Characterization

As previously mentioned in Section 6.1.4.1, even though the FC acetylation is less prone to crosslinking compared to the functionalization with CMME, still coupling is a possible side reaction at certain conditions. Even though the exact mechanism[48] is not clear, from literature[242,290–296] and own preliminary acetylation tests, several factors are known to facilitate the formation of secondary FC products. On one hand, the concentrations of the FC reagents, the dilution of the polymer in the chloroform solution and the attempted degree of acetylation plays a role. On the other hand, the molecular weight of the polymer also seems to influence the grafting outcome. Generally, coupling and crosslinking can be avoided to a great extent by a low acetylation level and at low concentrations. For example, the degree of acetylation of 6 mol% for this comb PS310 series was well below (half) the functionalization when compared to the highest branched comb PS290-190-44 (see Table 5.1) for which the backbone PS290 was functionalized with 331 acetyl groups corresponding to 12 mol%. However, a comb PS310-100-40 acetylated with only 2 mol% (for bob PS310-100-40-g-460-13) already showed to be prone to coupling side reaction, which indicates also a certain role of the molecular weight. With an even lower degree of acetylation, e.g. 1 % and 0.5 %, this unwanted reaction was largely avoided.

The differences in molecular weights reported by the gravimetric method and the SEC characterization are attributed to both techniques giving absolute vs. relative values, respectively. While the latter is based on the calibration of the column with linear PS standards, giving same molecular weights for same hydrodynamic radii, the former calculates M_w directly obtained from the weight difference of the acetylated precursor before grafting and the purified product after fractionation.
Due to the fact that branching increases the molecular density, the expected hydrodynamic radii are lower than compared to the gaussian chain conformation of a linear analogue with same molecular weight. Therefore, it is evident that the apparent $M_{w,SEC}$ values of comb PS are largely underestimated. This underestimation is even more the case for dendrigraft PS[49] with additional side chain crowding on top of the branches.[81] This becomes especially obvious for the number average molecular weight, $M_{n,SEC}$, for which the SEC only reports

[48] Rabek and Lucki[290] investigated the crosslinking of PS under FC conditions and reported the formation of strong charge-transfer (CT) complexes between the polymer, the catalyst ($AlCl_3$) and chlorinated solvents. They concluded that the solvent ultimately ends up as the coupling agent between the PS phenyl rings and expected the concentration of $AlCl_3$ relative to PS to be influential for the occurrence and degree of coupling.

[49] Gauthier et al.[297] reported for chloromethylated hyperbranched PS of $M_w > 10^7$ kg/mol and more than 5000 branch groups a structural stiffening towards hard sphere behavior in dilute to semidilute solutions.

a moderate increase from about 3300 kg/mol to 4300 kg/mol, even if the number of exterior branches nearly quadruples from $N_{scb} = 120$ to 460.

6.2 Rheology of Dendrigraft Bob PS Topologies

This section highlights the rheological properties of the synthesized model comb and denrigraft series, starting with the linear viscoelastic properties, investigated via small amplitude oscillatory shear (SAOS). Thereafter, nonlinear viscoelastic properties are analyzed in uniaxial elongation.

In contrast to the myriad of publications addressing the rheological behavior of comb- and bottlebrush-like topologies, up to date the literature that is found with focus on exploring the melt rheology of dendrigraft polymers is rather scarce.[281–285] Unlike the solution thermodynamics of the dendritic polymer family (i.e. dendrimers, hyperbranched and dendrigraft structures), the flow properties in the melt state are not a regular field of research. A reason might be the synthetic effort and lack of adequate amount of samples needed for experiments in the melt state. Moreover, there is another important limiting factor: Melt rheology is conducted well above T_g and often requires thermal conditions that might affect the architectural stability. The presence of functional groups, especially at the branch points, makes the polymer structure more prone to degradation. Since the relaxation of highly branched chains is retarded (hierarchical relaxation) and the rubber and terminal regimes are broadened towards low frequencies, using the TTS principle (see Section 3.2.2) necessitates a quite substantial increase in temperatures to capture information about the molecular dynamics at long time scales and might even not be applicable.

Comb PS from acetylated substrates did not show significant thermal degradation in SAOS or extensional tests if the sample preparation procedure was optimized, as already discussed in Section 5.3.1 with reference to the sample preparation described in Appendix A.1.6). Consequently, the synthesized dendrigraft PS were also appropriate candidates for investigating the linear and nonlinear melt rheology in oscillatory shear and elongational flow, respectively.

6.2.1 Linear Viscoelastic Properties (SAOS)

Linear viscoelastic properties of the here synthesized comb and dendrigraft PS310 series were explored via SAOS. Like in the previous investigation of the comb PS290 series from Chapter 5, the same measurement condition at $T_{ref} = 180\,°C$ were used to ensure experimental comparability. Therefore, sample preparation, measurement conditions, instrument operation and data processing are already described in Section 5.3.1.

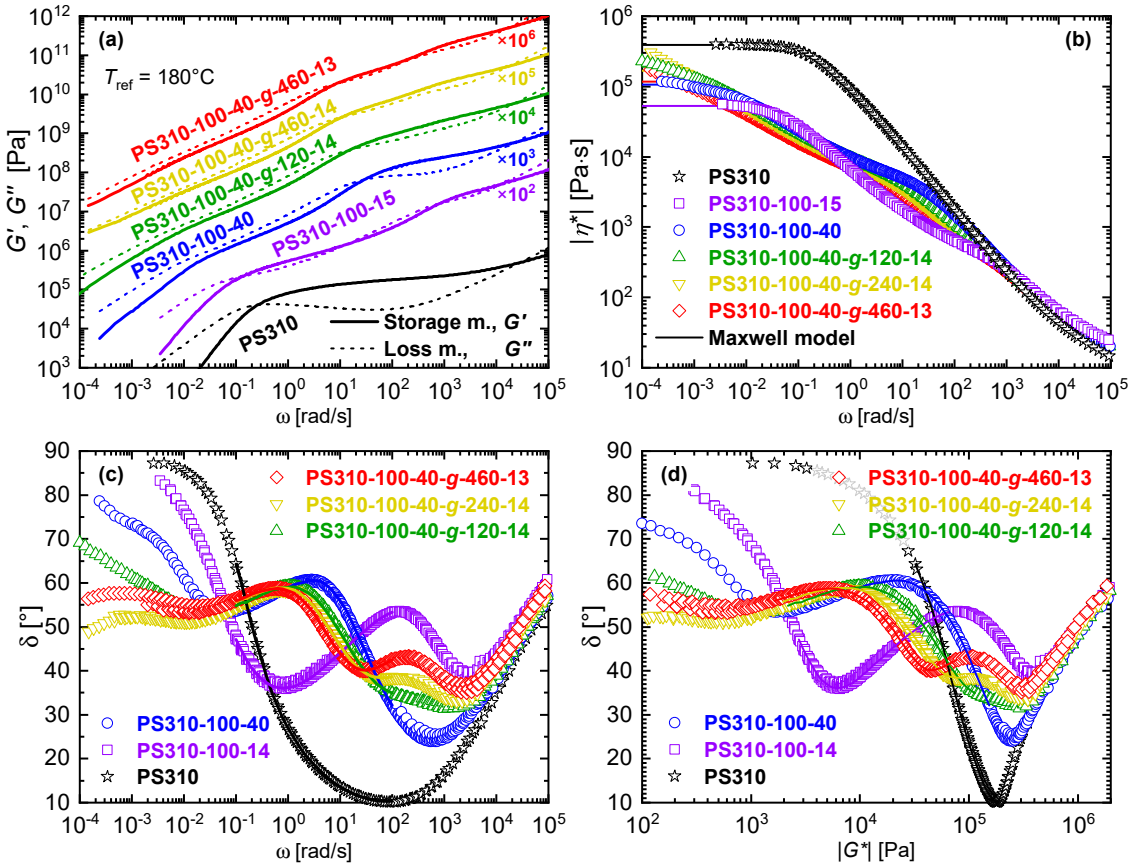

Figure 6.3: Linear viscoelastic mastercurves from SAOS data of linear PS310, comb PS310-100-$M_{w,lcb}$ and dendrigraft bob PS310-100-40-*g*-N_{scb}-$M_{w,scb}$ at a reference temperature of $T_{ref} = 180\,°C$. **(a)** Storage, G', and loss modulus, G''. **(b)** Complex viscosity, $|\eta^*|$, with Maxwell model fitting (solid lines) to obtain the zero-shear viscosity (ZSV), η_0, at $|\eta^*|_{\omega\to 0}$. **(c)** Phase angle, δ, vs. angular frequency, ω, and **(d)** van Gurp-Palmen plot, δ vs. complex modulus, $|G^*|$, with solid lines being DFS data directly obtained at T_{ref}.

Figure 6.3 shows the linear viscoelastic data for all samples from the linear PS310 backbone to the SCB comb PS310-100-15 and LCB comb PS310-100-40 precursor, as well as the bob PS series with $N_{lcb} = 100$ inner LCB and $N_{scb} = 120$, 240 and 460 outer SCB. The frameworks of the investigation comprised: **(a)** the mastercurves of the storage and loss moduli, G' and G'', respectively, **(b)** the complex viscosity, $|\eta^*|$, with extrapolation to the zero-shear viscosity, η_0, **(c)** the phase angle, δ, as a function of the angular frequancy, ω, and **(d)** the vGP plot as δ against the complex modulus, $|G^*|$. The following sections will address those frameworks in a closer look, describe and interpret the rheological data.

6.2.1.1 Mastercurves

The mastercurves of the PS310 backbone, see **Figure 6.3a**, shows the typical crossover of G' and G'' towards the terminal regime where $G' \propto \omega^2$ and $G'' \propto \omega^1$. The same scaling in the flow regime was also observed for SCB comb PS310-100-15, however the crossover is slightly shifted towards lower frequencies, indicating a deceleration of the reptation process as compared to the unbranched, linear backbone. The SCB comb furthermore shows two very distinct plateaus, where $G' > G''$, each with a clear crossover towards lower

frequencies, also reflected as very pronounced minima in the phase angle, δ, related to the backbone and branch relaxation, as seen in **Figure 6.3c**. No terminal region crossover for the densely grafted LCB comb PS310-100-40 is observed, which is in accordance with the results from the comb PS290 series showing also no crossover above a branching number of $N_{\mathrm{br}} \geq 60$.

Likewise, the bob PS series shows an even lower tendency for a crossover and the relaxation of the backbone is strongly dependent on the hierarchical relaxation from the outer SCB towards the inner LCB. The "flattening" of the power law dependency of G' and G'' in the terminal region indicates a Rouse-like backbone relaxation rather than a diffusive, reptation-like mechanism. Compared to both combs, the assignment of the relaxation behavior to specific chain dynamics of the multiply branched structure of dendrigraft PS is not obvious from the mastercurves. Therefore, the phase angle in **Figure 6.3c** provides a more distinct illustration of the relaxation modes. Whereas comb PS – in case of a significant number of sufficiently long branches – exhibits two minima, each higher generation of grafting is supposed to furthermore contribute additional chain dynamics. Thus, the hierarchical relaxation of those bob PS ideally will result in three distinctively different relaxation modes, each expressed as a minimum in δ vs. ω. In that sense, the relaxation behavior of bob PS is conform, showing 3 characteristic minima in δ corresponding to the backbone, LCB and SCB dynamics, respectively. However, the distinctness of the second minimum related to the dynamic dilution oft the LCB decreases with a lower number of SCB, so that bob PS with 120 SCB merely has a shoulder rather than a clear minimum as compared to higher branched bob PS with 240 and 460 SCB. Analogous to comb PS, the minimum at lower frequencies merges into the one at higher frequencies for insufficient branching density, corresponding to a low dilution effect.

6.2.1.2 Zero-Shear Viscosity

The absolute value of the complex viscosity, $|\eta^*|$, is shown in **Figure 6.3b**. In contrast to the linear and comb PS, that approach a plateau value for the zero-shear viscosity (ZSV) at low frequencies ($\eta_0 = \text{const.}$ for $\omega \to 0$), the ZSV for PS with dendrigraft topology did not approach a steady state value within the experimentally accessible range for measurement temperatures as high as 240 °C and data acquisition times in the order of hours. Comparable to the loss of a ZSV plateau for the transition from a dense comb PS290-120-44 towards a loose bottlebrush PS290-190-44 (see Figure 5.5b), more branches on the comb PS310-100-40 also manifests in a tremendously slowed down relaxation. Therefore, the zero-shear viscosit, η_0, of dendrigraft-type bob PS was estimated from the Maxwell model fittings obtained from the discrete relaxation spectra, but still the values are expected to be higher with a rather significant uncertainty.

Figure 6.4 visualizes the zero-shear viscosity, η_0, vs. the total molecular weight, M_{w}. Interestingly, comb PS310-100-15 with barely entangled SCB of $M_{\mathrm{w,scb}} \approx M_{\mathrm{e}}$ has a significantly lower η_0 than the unbranched backbone, as well as the comb PS310-100-40 with well entangled side chains. Consequently, when considering a backbone with a fixed number of branch points of $N_{\mathrm{br}} \approx 100$, conversely to the increase of the chain length of

the arm, η_0 has to decreases and undergoes a minimum. Presumably, at a certain branch length the CLF mechanism of the side chains becomes increasingly less effective to relax the backbone because the fraction of the fast-relaxing chain ends decreases relative to the inner parts close to the backbone where the retraction of the chain is entropically unfavored. Both comb PS310 with well- and unentangled side chains have a backbone segment entanglement number of $Z_s \approx 0.2$ between the branch points which was previously discussed at the example of the comb PS290 series as marking a significant value in branch point spacing, see Figure 5.6.

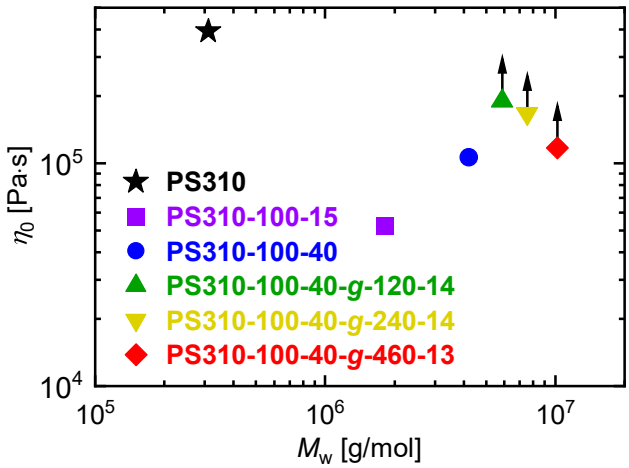

Figure 6.4: Zero-shear viscosity (ZSV), η_0, as a function of the total weight-average molecular weight, M_w at a reference temperature of $T_{ref} = 180\,°C$. Arrows indicate that the ZSV for bob PS310 are higher than experimentally accessible via TTS; values are based on the Maxwell model.

Further grafting of SCB onto LCB, i. e. the transition from comb to dendrigraft generation, also increases the ZSV, but the trend seems to revert with an increasing number of SCB above $N_{scb} > 120$. However, due to the instrumental and experimental limits accessing lower frequency regions, these values for bob PS are a mere estimate from the Maxwell model and should be taken with care.

6.2.1.3 Diluted Modulus

The cascade-like branched structure of dendrigraft PS with two branch layers leads to three minima in the phase angle, δ, as presented in **Figure 6.3c**. The first and second minimum are assigned to the dynamic dilution of the backbone of $M_{w,bb} = 310\,kg/mol$ and the inner long chain branches of $M_{w,lcb} = 40\,kg/mol$, respectively, with the former being influenced by the relaxation of the inner LCB and the latter dependent on the outer SCB relaxation dynamics.

Analogously to the backbone dilution of comb PS, for each minimum of bob PS a diluted modulus, $G^0_{N,s}$, is defined as the storage modulus at the frequency of this minimum of the phase angle, $G'|_{\delta=min}$. The extraction of the diluted moduli is exemplarily shown in **Figure 6.5a**.

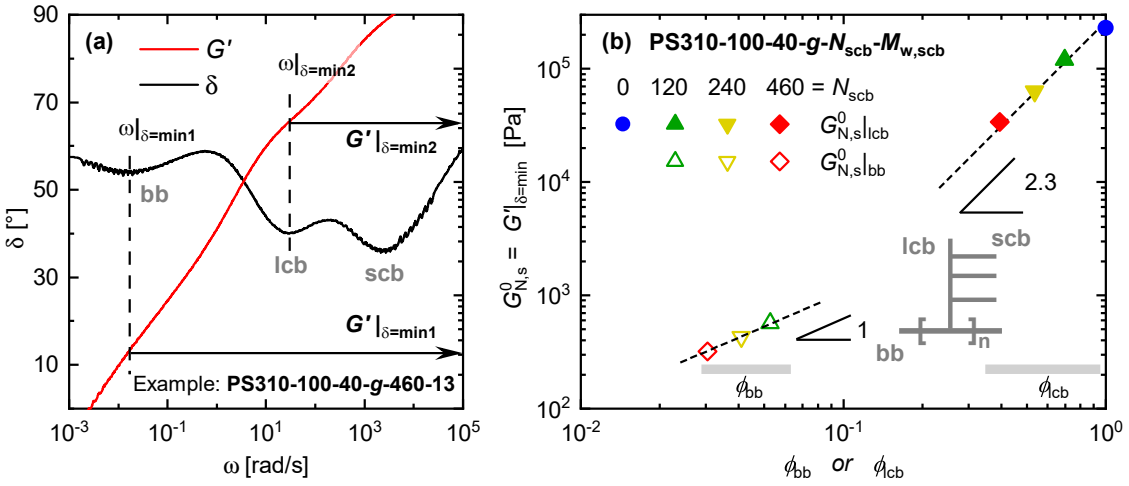

Figure 6.5: Investigation of the diluted modulus, $G^0_{N,s}$, of the bob PS310 series with backbone, LCB and SCB relaxation showing 3 distinct minima in the phase angle, δ. **(a)** Graphical illustration of the determination of $G^0_{N,s}$, defined as the storage modulus, G' (right y-axis), at the angular frequency, ω, where δ (left y-axis) has a minimum, $G^0_{N,s} \equiv G'|_{\delta=\min}$, at the example of bob PS310-100-40-*g*-460-13. **(b)** Diluted modulus as a function of the volume fraction for the bob PS backbone, $G^0_{N,s}|_{bb}$ vs. ϕ_{bb} (◇, etc.); as well as for the bob PS LCB, $G^0_{N,s}|_{lcb}$ vs. ϕ_{lcb} (◆, etc.), and their comb PS precursor (●).

For clarity and simplification, the first and second minima are now defined as the "backbone" (bb) and "LCB" (lcb) diluted modulus, $G^0_{N,s}|_{bb}$ and $G^0_{N,s}|_{lcb}$, respectively, see **Equations 6.2** and **6.3**.

$$G'|_{\delta=\min 1} \equiv G^0_{N,s}|_{bb} \propto \phi_{bb}^{1+\alpha} \tag{6.2}$$

$$G'|_{\delta=\min 2} \equiv G^0_{N,s}|_{lcb} \propto \phi_{lcb}^{1+\alpha} \tag{6.3}$$

According to the dilution concept (see also Section 5.5, Equation 5.12 and Section 7.3, Equation7.7), the plateau modulus is a function of the volume fraction of the polymer chain, ϕ_p, that is affected by the dilution.

In case of the backbone, both branching layers of LCB and SCB influence the relaxation and even though not directly connected, the SCB still "communicate" their chain dynamics to the backbone via the LCB. Therefore, the dilution of $G^0_{N,s}|_{bb}$ is a function of the volume fraction of the backbone, ϕ_{bb}, see Equation 6.2.

When it comes to the dilution of the LCB which is connected to – or one might say "trapped" between – both backbone and SCB, the circumstances are different. On one hand, the fast CLF relaxation of the SCB dilutes the LCB. On the other hand, the dynamics of the backbone, at which the LCB is attached to, are tremendously slowed down due to the hierarchical relaxation imposed by all braches. Therefore, compared to the time scale of the motion of the SCB, the backbone branch points can be considered as static for the LCB. As a consequence, the dilution of the LCB is supposed to be only a function of its own volume fraction, ϕ_{lcb}, amongst the surrounding SCB, as expressed by Equation 6.3.
Figure 6.5b summarizes the diluted moduli of the bob PS310 series for both, the backbone

and LCB as a function of their respective effective[50] volume fraction within the dendrigraft structure.

The dilution of the LCB results in a power law dependency of 2.3 which equals a dilution exponent of $\alpha = 1.3$. In that respect, the LCB – even though immobilized at one side by the "static" backbone – behave within the expected range of $\alpha = 1$–$4/3$ from the concept of the dynamic tube dilution (DTD), as found for branched (stars, combs) and diluted linear and star-linear blend polymer systems, see also Section7.3.[9,262]

Moreover, when compared to the scaling laws founds for other dendritically branched structures in literature, van Ruymbeke et al.[282] also consistently reported α of the effective outer layer dilution to fall between the 1 and 4/3. Even though the data of the investigated Caylee-tree topologies was inconclusive about the exact value, it appeared that the slope towards higher volume fractions of unrelaxed inner layer branches suggested $\alpha = 4/3$. However, Lee et al.[283] reported for similar Caylee-tree architectures a deviations towards lower values, $\alpha \leq 1$.

Because such a hierarchical dynamic dilution behavior is profoundly governed by the presence of entanglements (or lack thereof) on all levels of branching, the absolute size and number of chain segments, as well as the relative proportions of the topological constitution for sure play a crucial role in even being able to rheologically detect and interpret certain chain dynamics in multiply branched polymers. In that sense, dendrigraft polymers are considered as unique in showing the hierarchical relaxation that can be distinctively discriminated via rheology and emphasize the relevance of SAOS for the investigation of molecular branching.

When it comes to the backbone dilution, the rheological data is more noisy at low frequencies and the minima are not very pronounced and rather broad. This makes the determination of the diluted moduli more prone to errors and the interpretations are to be taken with care. Nonetheless, the diluted modulus of the backbone strongly suggests to scale with a power law of 1, i.e. $G^0_{\mathrm{N,s}} \propto \phi^1_{\mathrm{bb}}$.

This scaling of the dilution exponent $\alpha_{\mathrm{bb}} = 0$ is very interesting and is to be highlighted in the bigger context anticipating results from the following Chapter 7 (see Section 7.3). When comb-linear blends of the PS290-N_{br}-44 series have been rheologically studied in the framework of the diluted modulus, the power law also resulted in an exponent of $\alpha_{\mathrm{bb}} = 0$ for backbone dilutions from $\phi_{\mathrm{bb}} = 0.1$ down to 0.01. Due to the core comb structure of the dendrigraft bob PS310 being similar to the comb PS290 series ($M_{\mathrm{lcb}} \approx M_{\mathrm{br}}$, and $60 < N_{\mathrm{lcb}} < 190$), a very similar dilution exponent for both, the dendrigraft PS and the comb-linear blends, indicates that the backbone is diluted by the same factor, independently if the inner branches are furthermore covalently bound to higher-generation branches or merely surrounded by unattached chains. This analogy of the dilution between attached and unattached chains might become more clear when considering that comb polymers have the same dilution exponent as linear polymers surrounded by loose chains of theta solvent-like oligomers or polymers.[9,262,298]

[50] In the case of backbone dilution: $\phi_{\mathrm{bb}} + \phi_{\mathrm{lcb}} + \phi_{\mathrm{scb}} = 1$. In the case of LCB dilution: $\phi_{\mathrm{lcb}} + \phi_{\mathrm{scb}} = 1$, with $\phi_{\mathrm{bb}} \to 0$ because the backbone is considered "static".

That would – cautiously – conclude that the dilution for each generation of grafting is different (from $\alpha = 1$–1.3 for combs to $\alpha = 0$ for branch-on-branch), however the tube dynamics have the same effect, independently whether the linear-linear or comb-linear precursors are furthermore grafted with the surrounding chains or not. In short, additional branches or their unattached, free analogues – in first approximation – dilute similarly. The molecular theories satisfactorily describe both cases. This seems to be confirmed on the basis of the here presented experimental data by comparing dendrigraft PS with comb-linear PS blends.

This section emphasizes that more research is needed to prove and further investigate what is here only scratched at the surface and to point out the contribution of dendrigrafts for understanding chain dynamics of multiply branched polymers.

6.2.1.4 Complex Modulus

In the previous Chapter 5, when the linear viscoelastic behavior of the comb PS290 series was discussed, the vanGurp-Palmen (vGP) plot was introduced as a tool to investigate the structure-property relationship in the framework of the complex modulus, $|G^*|$, see Section 5.3.1.5.
Consequently, the data of the dendrigraft bob PS310 series in **Figure 6.3d** is also investigated using the methods described earlier, which is at first the intersect of the complex moduli, $|G^*|$, with the phase angle, δ.

Phase Angle Intercept as Branching Criteria

In Figure 5.6, it was shown that the complex modulus at a phase angle of $\delta = 60°$, $|G^*|_{\delta=60°}$ (as a vertical line at the y-intercept of 60° crossing $|G^*|$ at low frequencies, graphically illustrated in Figure 5.5d), proved as useful criteria for the rheological quantification of branching. However, in contrast to the majority of combs with PS290 backbone, as well as the here presented combs[51] PS310-100-15 and PS310-100-40, this parameter ($|G^*|_{\delta=60°}$) was not applicable in the case of the synthesized dendrigraft PS, as the phase angle curve of only one bob PS310 (with $N_{scb} = 120$) did intersect with $\delta = 60°$ (dotted horizontal line), shown in **Figure 6.6a**. Thus, no scaling law can be postulated.

[51] The complex moduli, $|G^*|_{\delta=60°}$, of comb PS310-100-15 and PS310-100-40 were used as supplementary data in Fig. 5.6 fitting in the same power law function of the comb PS290 series, see Chapter 5, and specifically Section 5.3.1.6.

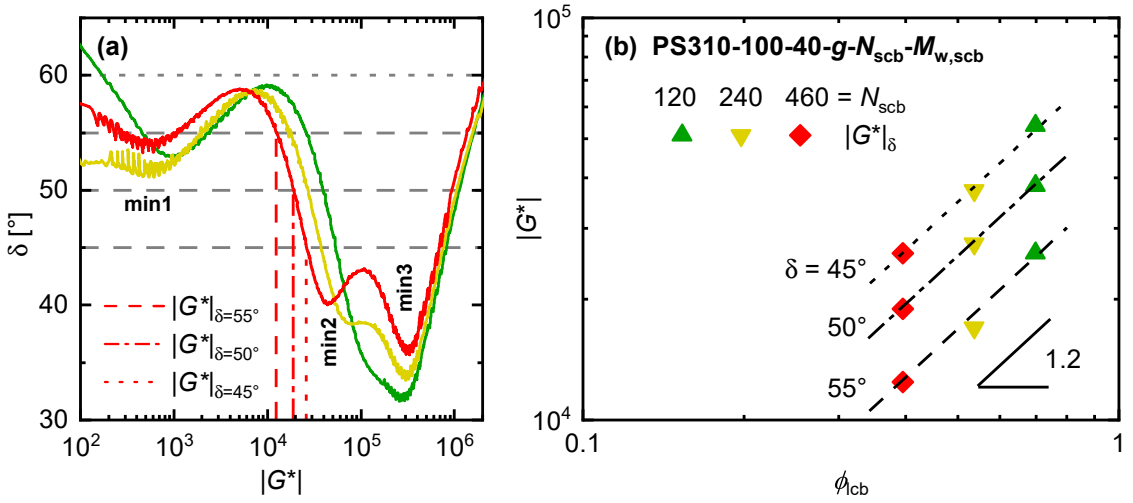

Figure 6.6: Investigation of the complex modulus, $|G^*|$, at different phase angles, δ. **(a)** Graphical illustration to obtain $|G^*|_\delta$ at the intersects of $\delta = 45°$, 50° and 55°; shown on the example of bob PS310 with $N_{scb} = 460$. **(b)** Complex modulus of at different phase angles, $|G^*|_\delta$ with $\delta = 45°$–55°, against the LCB volume fraction, ϕ_{lcb}, as a criteria for branching.

However, lowering the phase angle criteria to an intercept below $\delta \leq 60°$ promised to still be able to extract moduli data and evaluate the feasibility of those criteria with respect to possible dependencies and scaling/power laws correlating to structural parameters. It is needless to say that this "new" criteria does not account for the backbone dilution, for the simple reason that δ fails to cross the descending phase angles (going from low towards high $|G^*|$) towards the first minima (min1) correlated to backbone dynamics. However, the $\delta = 45°$–55° (dashed horizontal lines) cross the descending phase angles towards the second minima (min2) and therefore might be related to the LCB of bob PS.

Figure 6.6a graphically illustrates the extraction of $|G^*|_{\delta=45°}$, $|G^*|_{\delta=50°}$, and $|G^*|_{\delta=55°}$ at the respective phase angles, δ, on the example of bob PS with $N_{scb} = 460$ (cf. also Figure 5.5d). Those complex moduli parameters are then reported in **Figure 6.6b** as a function of the LCB volume fraction, ϕ_{lcb}.

As can be seen, independently of the particular angle, all $|G^*|$ nearly perfectly align in a power law of $|G^*|_\delta \sim \phi_{lcb}^{1.2}$. Due to the lack of a wide range of SCB branching series, this behavior could only be observed down to a volume fraction of $\phi_{lcb} \approx 0.4$ (as compared to comb PS with minimum $\phi_{bb} \approx 0.05$). Those results suggest that the complex moduli at a certain phase angle, e.g. $\delta = 50°$, might not only be a feasible criteria for branching in simple comb topologies, but furthermore might be used for branching in polymers with a dendritical build of sufficiently large chain segments. Most probably the applicability and the choice of the phase angle will depend on the specific structural parameters.

Phase Angle Minimum as Branching Criteria

In Section 5.3.1.4 and 6.2.1.3, the minima of the phase angle in the δ vs. ω plot were used to determine the diluted moduli, $G^0_{N,s} = G'|_{\delta=min}$, of comb and dendrigraft PS and investigate the power laws with respect to the backbone and branch volume fractions.

In a similar way, the complex modulus at the minima of the phase angle, $|G^*|_{\delta=min}$, is also

found to provide information about structure-properties and scaling laws.[299]
This criteria for branching will be more extensively addressed in the scope of Section 7.4.3, dedicated to give a broader overview of the investigation of $|G^*|$ using the synthesized comb PS290 series, as well as comb-linear and linear-linear blends prepared for Chapter 7. Therefore, in the following, $|G^*|_{\delta=\min}$ will be only briefly discussed, limited to its phenomenon in dendrigraft-type PS.

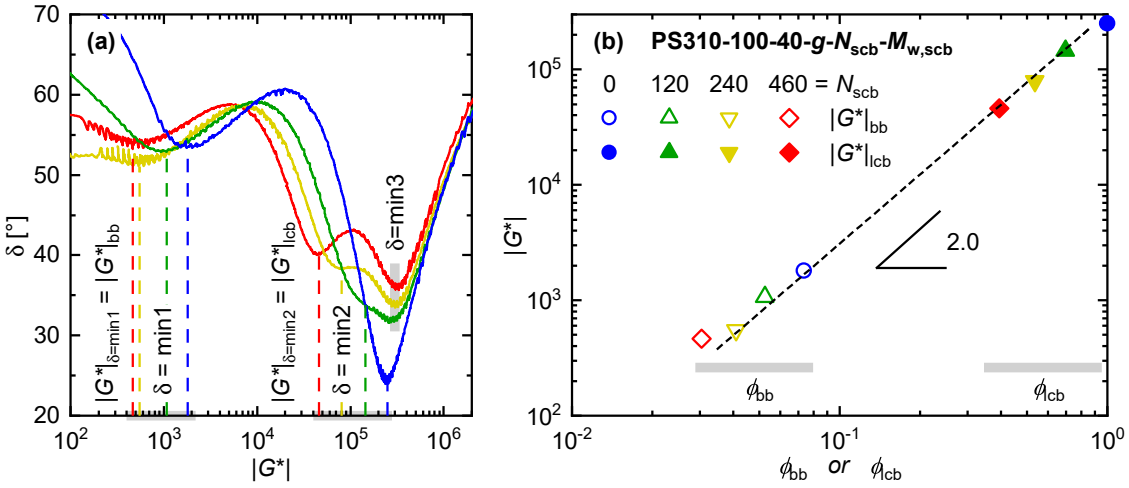

Figure 6.7: Investigation of the complex moduli data, $|G^*|$, of the bob PS310 series showing three distinct minima in the phase angle, δ, correlated to backbone (min1), LCB (min2) and SCB (min3) relaxation. **(a)** Graphical illustration to obtain $|G^*|_{\delta=\min}$ of the respective minima. **(b)** $|G^*|_\delta$ at the first (◇, etc.) and second (◆, etc.) minimum accounting for backbone and LCB dilution, plotted against their volume fraction, ϕ_{bb} and ϕ_{lcb}, respectively.

The three minima in the phase angle, δ vs. $|G^*|$, can be assigned to the backbone, inner LCB and outer SCB dynamics. **Figure 6.7a** graphically illustrates the extraction of the respective complex moduli, $|G^*|_{\delta=\min}$. In **Figure 6.7**, the obtained complex moduli of the first and second minima were plotted against their respective volume fractions, i.e. ϕ_{bb} and ϕ_{lcb}, see **Equations 6.4** and **6.5**, assuming backbone dilution through both, LCB and SCB (with the latter mediated by the former), whereas LCB dilution is only affected by the grafted SCB.[52]

$$|G^*|_{\delta=\mathrm{min1}} \equiv |G^*|_{\mathrm{bb}} \propto \phi_{\mathrm{bb}}^2 \tag{6.4}$$

$$|G^*|_{\delta=\mathrm{min2}} \equiv |G^*|_{\mathrm{lcb}} \propto \phi_{\mathrm{lcb}}^2 \tag{6.5}$$

Figure 6.7b reveals a power law of 2.0 (indicated by the dashed line) that strongly holds for the scaling of $|G^*|_{\mathrm{lcb}}$, but also seems to include the data group of the complex moduli of the backbone, $|G^*|_{\mathrm{bb}}$. However, this might only be coincidental without general physical meaning. Unfortunately, even though also suggesting a power law of 2.0, the scaling amongst the "backbone group" is diffcult to determine with confidence, because this data itself underlies a non-negligible uncertainty. On one hand, the minima occuring at such low frequencies or complex moduli are rather broad due to a wider spectrum of chain dynamics.

[52] For explanation the reader is referred to Section 6.2.1.3.

On the other hand, the accuracy suffers from insufficient instrument sensitivity in a sense that even though the TTS principle is used to extend the measurement window, the sample might show thermorheological complexity[53], and even more so found for structurally branched polymers.[300,301] Sample alterations (i.e. degradation) at elevated temperatures (to capture lower frequency regions) might also occur. On the other hand, especially for bob PS with the highest degree of functionalization of 460 LCB and a relatively high dispersity indicating coupling side reactions, the synthetically obtained structure deviates more drastically from the idealized topology of the sample series.

Nonetheless, these findings of a power law of $|G^*|_{\delta=\min} \sim \phi^2$ are quite unique considering that the here synthesized type of dendrigraft PS exhibits a branch-on-branch structure with chain parameters suitable for rheological characterization and correlation to its molecular structure.
At this point it is also interesting to point out that about the same slope in $|G^*|_{\delta=\min}$ was found for the dilution effect in pure comb PS, as well as comb-linear and linear-linear blends, matching approximately the same power law of $|G^*|_{\delta=\min} \sim \phi^2$ down to dilutions of $\phi > 0.2$, thus being widely independent of the structural parameters like molecular weights and branching number.

6.2.2 Nonlinear Viscoelastic Properties – Uniaxial Elongation

Uniaxial extensional measurements of the synthesized bob PS310 series, including its LCB comb PS310-100-40 precursor, as well as SCB comb PS310-100-15 and the linear reference PS310 were performed on the EVF geometry using the same measurement conditions ($T = 180\,°C$), operation procedure (from $\dot{\varepsilon}_H = 10\,s^{-1}$ down to slow rates at $0.001\,s^{-1}$) and data processing as previously reported for comb PS290 series, see Section 5.3.2.1. Furthermore, the data was analyzed with respect to the SHF, see also Section 5.3.2.2, p. 89.

6.2.2.1 Extensional Viscosity

The extensional data of the bob PS310 series in **Table 6.2** is shown in **Figure 6.8** in the frameworks of the tensile stress growth coefficient (extensional viscosity) vs. stretch time, η_E^+ vs. t, for different extensional rates, $\dot{\varepsilon}_H$, with the envelope of the LVE predicted by the relaxation modes of the multi-mode Maxwell fitting from the SAOS data (see Figure 6.3) via Equation 5.13.

As can be seen from **Figure 6.8a**, the extensional viscosity of the linear backbone PS310 matches the LVE prediction with little-to-no upturn deviation. Therefore, no strain hardening behavior was observed during the stretch time t, as also expected after elongational tests with linear PS290 with almost the same $M_w \approx 300\,kg/mol$ (cf. Figure 5.7a). In contrast to the linear chains, all branched topologies of comb (**Figure 6.8b–c**) and dendrigraft (**Figure 6.8d–f**) structures exhibited a significant upturn from the start-up LVE envelope, already referred to as strain hardening. The increase in elongational viscosity is quantified

[53] The first publication of van Gurp and Palmen[252] used the vGP plot to assess thermorheological complexity of blends of miscible and immiscible polymers, also explained in Section 7.4.

in the framework of the strain hardening factor (SHF) and further discussed in the following **Section 6.2.2.2**.

Nevertheless, several points are already noteworthy from the extensional viscosity data of branched PS specimen which should here be briefly addressed. Comb PS310-100-15 with just barely entangled SCB achieved a remarkably high strain hardening at fast extensional rates of $\dot{\varepsilon}_H \geq 1\,s^{-1}$, whereas slower elongation was increasingly unfavorable for extensional hardening. In contrast to that, LCB comb PS310-100-40 did also show pronounced strain hardening behavior, but in this case especially at lower rates of $\dot{\varepsilon}_H \leq 0.3\,s^{-1}$.

A more drastic change in the elongational behavior, however, can be observed if the LCB side chains of the comb PS underwent further grafting with SCB branches. All three bob PS with dendrigraft-type topology achieved pronounced strain hardening over a broad range of strain rates from fast rates, but even more at rates as low as $\dot{\varepsilon}_H = 10^{-3}\,s^{-1}$. Apart from that, at low rates the bob PS exhibited also good stretchability. All data displayed and the SHF calculated are presented up to a maximum Hencky strain of $\varepsilon_H = 4$, which is the suggested limit for reliable transient viscosity data due to instrumental restrictions in the design of the EVF geometry.[54]

The point when the stretching filament touches the sample ends and the strain becomes non-uniform can be seen as a sudden, unusual increase or upwards bump in the viscosity, or even more cleary as a jump in the force data.[184] Even though the measurement was recorded until filament rupture, those data have not been reported. However, as an example of the high stretchability, the viscosity data of bob PS with $N_{scb} = 120$ is shown over the full elongation time for the strain rate of $10^{-3}\,s^{-1}$, with the greyed out data as the beginning when the Hencky strain exceeds the experimental limit, see Figure 6.8d. Even though the steady state elongational viscosity is overstated, the strain hardening calculated up to $\varepsilon_H = 4$ is assumed to be underestimated.

Those complications in properly assessing the extensional behavior of very stretchable, branched polymer melts over an extended strain range might be overcome by using a filament stretch rheometer (FSR, see Section 3.4.3) with a maximum $\varepsilon_H = 6$,[185] or employing a modification of the EVF that prevents the sample ends of premature contact with the stretching filament.

[54] After one evolution, the filament will touch the sample end and starts winding up on top of itself. Owing to the sudden step increase and the change in effective drum diameter, the deformation becomes non-uniform and renders the viscosity data unusable. The maximum elongation depends on the sample thickness, which is $\varepsilon_H = 4.3$ for a sample thickness of $d \leq 0.7\,mm$.[183,184] This necessitates, however, that the sample has to be perfectly trimmed for the distance of 12.7 mm from drum-to-drum center, which is – to ensure good sticking and to avoid initial slippage – not always practical. Therefore, a slightly lower Hencky strain is more realistic.

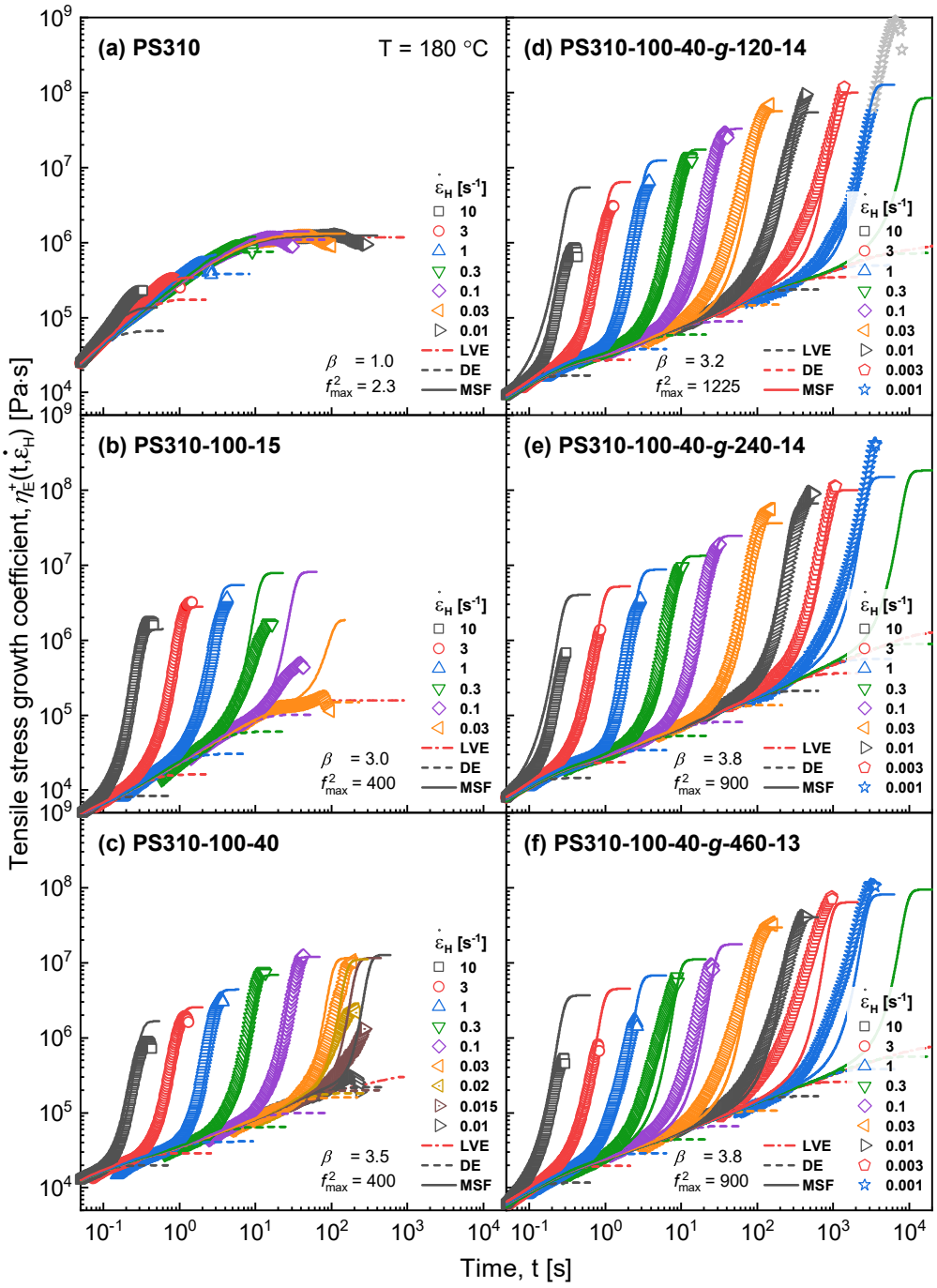

Figure 6.8: Tensile stress growth coefficient data, η_E^+ of **(a)** linear PS310, **(b)** comb PS310-100-15 with SCB, **(c)** comb PS310-100-40 precursor with LCB and **(d)**–**(e)** dendrigraft bob PS310-100-40-*g*-N_{scb}-$M_{w,scb}$ with N_{scb} = 120, 240 and 460 additional SCB. All data is reported up to a Hencky strain of $\varepsilon_H = \dot{\varepsilon}_H \cdot t \approx 4$, the experimental limit of the EVF geometry, considering a sample thickness of 0.5 to 0.8 mm. The Greyed out data in (d) at $\dot{\varepsilon}_H = 0.001\,s^{-1}$ exceeds the instrumental limit, but is shown to prove the high stretchability or potential to reach higher extensional viscosities than confirmed reliably with the EVF geometry.
Simulations and fittings of the DE model (dashed lines) and MSF model (straight lines) were performed by Dr. Masood Khabazian and Dr. Mahdi Abbasi.

6.2.2.2 Strain Hardening

Figure 6.9 summarizes the extensional viscosity data in the framework of the strain hardening factor, SHF $\equiv \eta^+_{\mathrm{E,max}}/\eta^+_{\mathrm{DE,max}}$, as a criteria of melt strength in elongational flow (cf. Section 5.3.2.2, Figure 5.8).

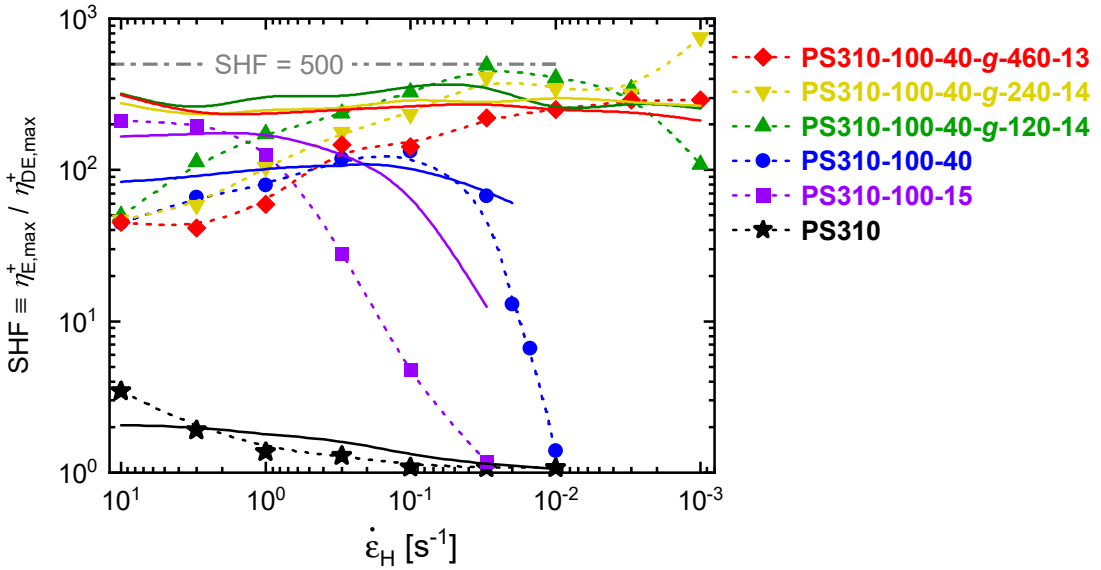

Figure 6.9: Strain hardening factor, SHF $\equiv \eta^+_{\mathrm{E,max}}/\eta^+_{\mathrm{DE,max}}$ as a function of extensional rate, $\dot{\varepsilon}_{\mathrm{H}}$, from short times (high strain rates) to long times (low strain rates), following the time order of the extensional data in Figure 6.8. Symbols are based on the maximum experimentally achieved stress growth coefficient $\eta^+_{\mathrm{E,max}}$ up to a Hencky strain of $\varepsilon_{\mathrm{H}} = 4$. Dashed lines show the general trend as guide to the eye. Solid lines are predictions of the MSF model.

The quantification and direct comparison of the strain hardening reveals, that comb PS310-100-15 with barely entangled side chains of $M_{\mathrm{w,scb}} = 15\,\mathrm{kg/mol}$ excels in SHF, especially in the high range of Hencky strain rates. For $\dot{\varepsilon}_{\mathrm{H}} = 10\,\mathrm{s}^{-1}$, the SCB comb reaches a SHF > 200 for Hencky strains below $\varepsilon_{\mathrm{H}} = 4$. This tremendous effect of branching has so far only been reported for comb PS with well-entangled side chains of 44 kg/mol, however at much lower strains of $0.1\,\mathrm{s}^{-1}$,[120] see also Section 5.3.2. Comparing those with the newly synthesized PS310-100-40 possessing similar topological features, the results are consistent as the LCB comb also shows its maximum SHF at the same rate of $0.1\,\mathrm{s}^{-1}$, although the SHF ≈ 130 is slightly lower but between that of combs PS290-60-44 (SHF = 100) and PS290-120-44 (SHF = 200), see Figure 5.8. On the other hand, the melt strength of PS310-100-40 drasically reduces at slower rates of $\dot{\varepsilon}_{\mathrm{H}}$. Assumingly, the slighter shortness (ca. 10 %) of the side chains might not irrelevantly contribute to this, as $M_{\mathrm{w,br}} = 44\,\mathrm{kg/mol} \mathrel{\widehat{=}} Z_{\mathrm{br}} = 3$ and comb PS with branches of 40 kg/mol possess less than below 3 entanglements.
The introduction of additional graft chains drastically changes the extensional properties, especially towards higher SHF at even lower rates. Whereas the SHF at high rates is barely affected by the presence of SCB, dendrigraft-type PS further exceed the combs strain hardening ability at $\dot{\varepsilon}_{\mathrm{H}} \leq 0.3\,\mathrm{s}^{-1}$. Lowest branch-dense bob PS310-100-40-*g*-120-14 achieves a major SHF ≈ 500 at $\dot{\varepsilon}_{\mathrm{H}} = 0.03\,\mathrm{s}^{-1}$ until it declines to SHF ≈ 100 at $10^{-3}\,\mathrm{s}^{-1}$.

As already discussed above, this value is most likely underestimated due to instrument limitations regarding the maximum Hencky strain $\varepsilon_H = 4$.

With PS310-100-240-*g*-240-14 having double the number of outer SCB, the lowest strain rate yielded an even higher SHF ≈ 700. However, lower strain rates did not result in superior melt strength over the former. Consequentially, this trend continued for the bob PS with the most dense SCB corona, $N_{scb} = 460$, only achieving SHF ≈ 300 and surpassing the strain hardening of the combs only by a relatively small margin.

Van Ruymbeke et al.[284] and Huang et al.[285] investigated the uniaxial extension of symmetric model Cayley-tree PMMA polymers using an SER and FSR instrumentation, respectively. Those dendritically branched topologies with 4- and 3-arm star core and a regular, dendrimer-like branching with a multiplicity of two, showed increased strain hardening with increasing number of graft generations (G). Whereas the extensional viscosity of a second-generation (G2) PMMA Cayley-tree only slightly increased above the LVE envelope, further generations (G3 and G4) achieved SHF in the order of 5–7 at low strain rates of about $\dot{\varepsilon}_H = 10^{-1}$–$10^{-3}\,s^{-1}$. It is important to mention that the branch segments of each generation were low in molecular weight, $M_s = 11\,kg/mol \mathrel{\widehat{=}} Z_s \approx 2.4$[55], giving a mere total of $M_w = 308\,kg/mol$ (G3) and $M_w = 660\,kg/mol$ (G4). Additionally, the dense branching from the core to the periphery and the resulting sphere-like geometry lowers the effective amounts of entanglements.

The here presented results highlight the tremendous effect of the presence of branching on the melt strength of a polymer, even when the additional branch feature barely exceeds one entanglement. The extensional properties are not only governed by the theoretical number of those entanglements, but moreover by their arrangement to effectively contribute to the constraints and friction of elongating polymers.

6.3 Foaming

The anionically synthesized, and rheologically characterized dendrigraft PS310, as well as their comb and linear precursor PS were foamed using supercritical CO_2 as blowing agent. The foaming experiments were conducted in two different types of autoclave systems: a benchtop mini reactor with a maximum pressure of 180 bar and a high pressure reactor for foaming at 500 bar.

6.3.1 Implementation

The sample preparation and implementation of the batch foaming procedure was the same for both reactors as already described in the previous Chapter (see Section 5.4.1). However, the foaming conditions were subject to the individual construction of the autoclave system, with a needle valve allowing depressurization in about 4 s and a ball (on-off) valve

[55] With $M_e(PMMA) = 5\,kg/mol$

supporting an immediate pressure drop in 1 s. The actual pressure profile during expansion could not be recorded.
The specific saturation and foaming conditions for each reactor are briefly summarized in **Table 6.3**.

Table 6.3: Summary of saturation and foaming conditions for each autoclave system for the foaming of polymers of the bob PS310 series.

Conditions	180 bar (Mini Reactor)[a]	500 bar (HPR)[a]
Saturation:		
Blowing agent source	$CO_{2,s}$ (dry ice)	$scCO_2$ (gas bottle)
p_{sat} [bar]	180	500
T_{sat} [°C]	125 / 135 / 145	145 / 155 / 165
t_{sat} [h]	4	4
Foaming:		
Δt_{foam} [s]	4	1

[a] Product name as given by the company. For details about the employed reactor types, the reader is referred to Appendix A.1.7.1 and A.3.

To ensure comparability with previous results of the foamed comb PS290-N_{br}-44 series, the foaming conditions in the 180 bar reactor were kept within the same temperature range, T_{sat} = 125–145 °C, see also Section 5.4.1, as they already proved optimal for the foaming of linear and branched PS in this setup.[234,235] The criteria for optimizing the foaming depends on the focus of interest, which in this case was the assessment of the volume expansion, as this is related to the here investigated melt strength.[56] Therefore, the foaming temperature needs to be sufficiently high over T_g, so that the melt viscosity is low enough to support bubble expansion. On the other hand, in the later stage of the foaming, the increasing melt viscosity needs to stabilize the bubbles early enough to prevent cell coalescence or re-melting if the autoclave does not cool down sufficiently before collecting the expanded samples.
Preliminary tests with the high pressure reactor at 500 bar found the optimum foaming window to be within T_{sat} = 145–165 °C in order to maximize the volume expansion ratios (VER) and make a significant difference on the foam densities among the samples. The high pressure difference and the rapid gas expansion lead to a significant Joule-Thomson thermodynamic effect, so that the temperature of the system dropped faster below the glass transiton temperature of the plasticized polymer as compared to the lower pressure autoclave with 180 bar. As a result, the foamed specimen from the 500 bar reactor were generally more dense with a lower volume expansion. In contrast, slow depressurization delays the solidification of the foam and therefore promotes expansion.[204]

[56] If maximizing the cell density by minimizing the cell size is in the focus of investigation, different foaming conditions might apply.

6.3.2 Foaming Results

Figure 6.10 exemplarily shows the closed cell morphologies for samples foamed at the same temperature, $T_{\text{foam}} = 145\,°\text{C}$, but different pressure conditions at 180 bar (**Figure 6.10a**–**h**) and 500 bar (**Figure 6.10i**–**p**). Each sample is shown in lower and higher magnification. For the purpose of direct comparison, SEM images of (**Figure 6.10e**–**h**) and (**Figure 6.10i**–**l**) represent the same set of samples at the same magnification (1000×) but different autoclaves. In general, the 180 bar autoclave produced larger cells in the range of about 20–60 µm, while at much higher pressures of 500 bar, diameters as low as 3–8 µm could be achieved.

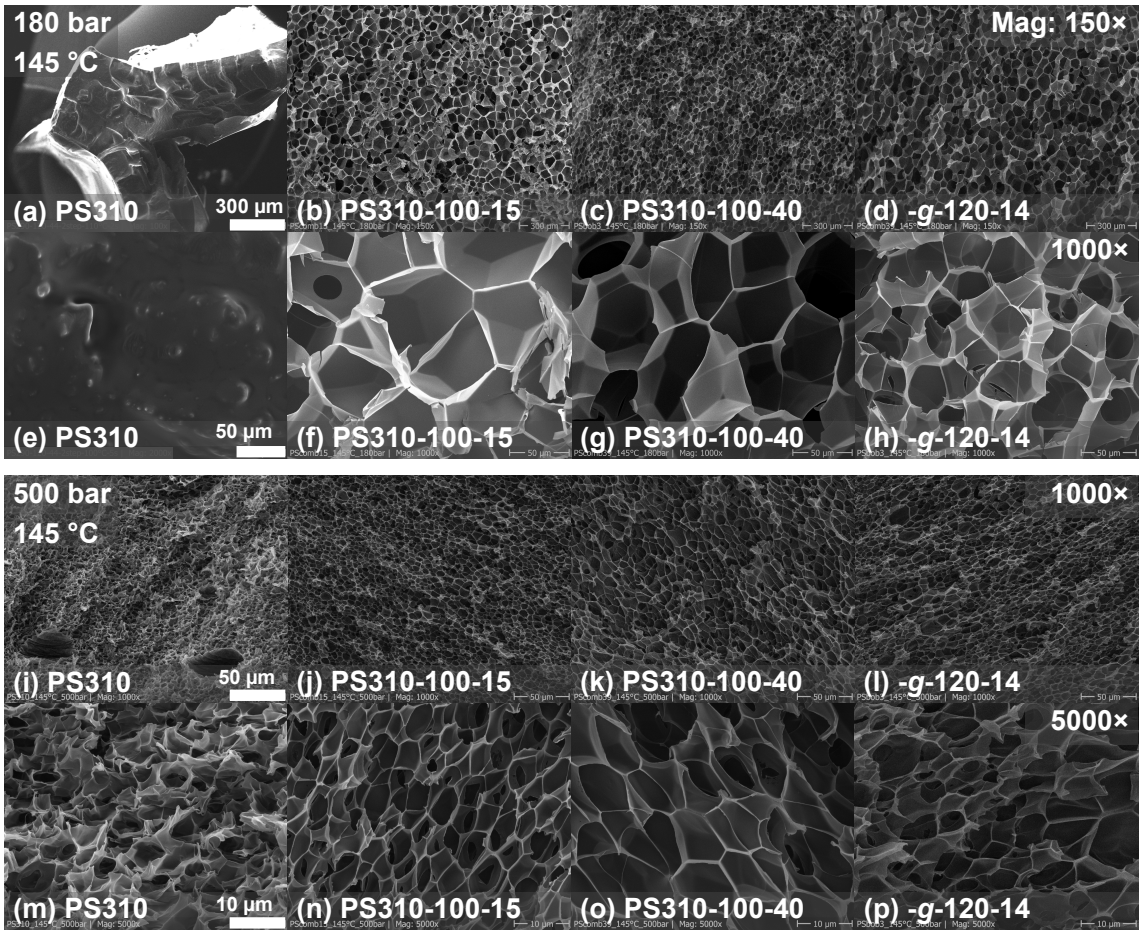

Figure 6.10: SEM images of the cellular structure of PS foams, expanded at the same temperature at $T_{\text{foam}} = 145°\text{C}$ in different pressure vessels. **(a)**–**(d)** 180 bar autoclave (Mini) at low magnification (150×), and **(e)**–**(h)** same at higher magnification (150×). **(i)**–**(l)** 500 bar autoclave (HPR) at low magnification (1000×), and **(m)**–**(p)** same at higher magnification (5000×).

It is noticed immediately that linear PS310 did not exhibit any foamability at 180 bar (Figure 6.10e). Also the cell morphology obtained at 500 bar (Figure 6.10m) is rated as rather poor (inhomogenous) in comparison with the SCB (Figure 6.10f and n) and LCB comb PS (Figure 6.10g and o), as well as the bob PS with $N_{\text{scb}} = 120$ representing the dendrigraft topologies (Figure 6.10h and p). All of those foams made of branched polymers show good foamability with rather evenly sized cells and relatively homogenous and thin cell walls.

Figure 6.11 shows the dependence of the cell size at different foaming temperatures from $T_{\text{foam}} = 125$–145°C for the 180 bar autoclave (**Figure 6.11a–f**), and $T_{\text{foam}} = 145$–165°C for the 500 bar autoclave (**Figure 6.11g–l**). Both temperatures are shown for the example of a comb and a dendrigraft PS, in particular PS310-100-15 and PS310-100-40-*g*-120-14), respectively.

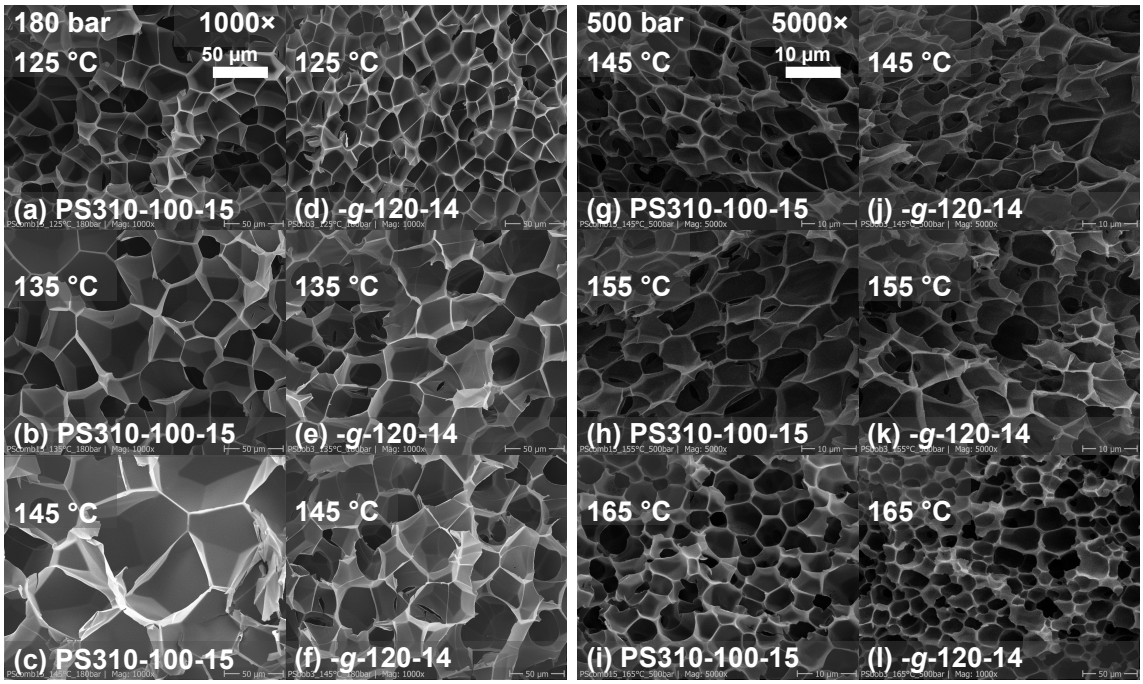

Figure 6.11: SEM images of the cellular structure of PS foams, expanded at increasing temperatures **(a)–(f)** from T_{foam} = 125–145 °C in the 180 bar autoclave; and **(g)–(l)** from T_{foam} = 145–165 °C in the 500 bar autoclave at the examples of SCB comb PS310-100-15 and bob PS310-100-40-*g*-120-14.

Expanded at the pressure of 180 bar, the cell size for both, comb and bob PS increased with increasing temperature. However, whereas the average cell diameter of the comb approximately triples (**Figure 6.11a–c**), from about 20 to 60 µm, the cell diameter of the bob PS only doubles to about 40 µm (**Figure 6.11d–f**). In comparison, the morphological changes at 500 bar were rather small within the temperature range of 20 °C, with only a slight decrease in cell size at 165 °C.

The foam properties were macroscopically assessed with respect to the foam density, ρ_{foam}, and volume expansion ratio, VER. Furthermore, the closed cell morphologies were analyzed in terms of their average cell size, d_{cell}, and cell density, N_{cell}.
The results of the foam analysis are summarized as a function of the foaming temperature in **Figure 6.12** for both batch reactor systems.

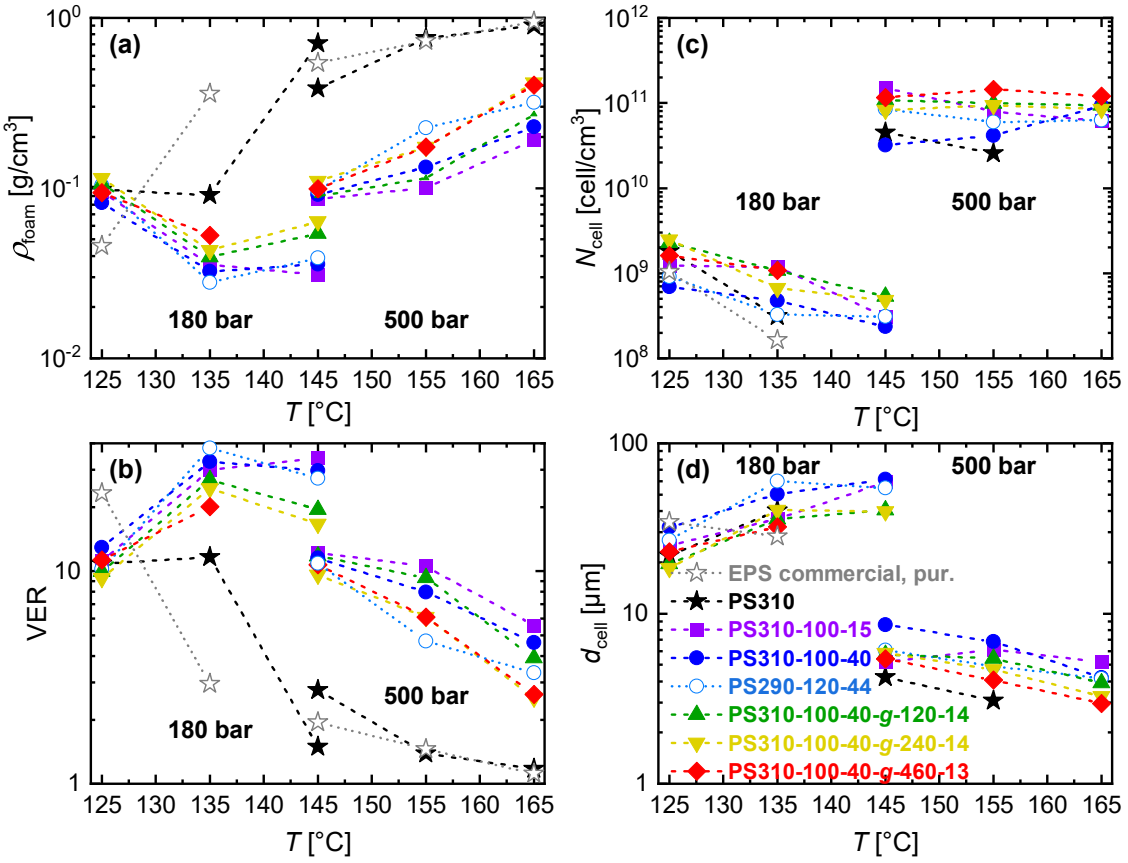

Figure 6.12: Effect of the temperature on the foaming properties of linear PS310, SCB comb PS310-100-15, LCB comb PS310-100-40 and the bob PS310 series with $N_{scb} = 120$, 240 and 460; expanded at 180 bar (125–145 °C) and 500 bar (145–165 °C). **(a)** Foam density, ρ_{foam}. **(b)** Volume expansion ratio, VER. **(c)** Cell density, N_{cell}. **(d)** Cell size, d_{cell}. Dashed lines are guide to the eye. For comparison, data of foams made of PS290-120-44 (○, see previous Chapter 5) and purified commercial EPS (☆) are added.

Foaming at 180 bar: At the lowest foaming temperature of 125 °C, all foams of the synthesized linear, comb and bob PS310 series had roughly the same density of $\rho_{foam} \approx 0.1$ g/cm^3, that decreased to about 0.03 g/cm^3 for comb and 0.05–0.08 g/cm^3 for dendrigraft topologies (**Figure 6.12a**). In contrast, the foamability – as a criteria to expand to high volumes – of commercial EPS and linear PS310 drastically decreased with increasing temperature. Both samples drastically lost foamability, and barely expanded at temperatures of 135 °C and even 145 °C, respectively (**Figure 6.12b**). Only the branched PS that also exhibited strain hardening in elongation were able to reach high volume expansions. It is interesting to note, that with a VER of 30–40, i.e. very efficiently using the dissolved gas for bubble growth (see also Section 5.5), the comb PS performed better than the bob PS, especially with a more significant difference at the maximum foaming temperature of 145 °C. It is remarkable that comb PS310-100-15 with only barely entangled side chains excelled at this high temperature, whereas PS310 was not even closely able to stabilize the cells during the bubble growth.

When it comes to microscopic proberties, the cell density in general showed for all samples a decreasing trend with increasing temperature, but with a more significant reduction for the linear ones, i.e. PS310 and EPS (**Figure 6.12c**). Conversely, the cell size was increasing,

with combs having slightly higher cell size than dendrigraft topologies (**Figure 6.12d**). Assumingly, this is a consequence of the lower expansion ratio of the latter.

Foaming at 500 bar: Conversely to the foaming with the 180 bar autoclave, the volume expansion of samples foamed in the high pressure reactor decreased with increasing temperature (Figure 6.12b). The volume expansions of the samples with branched topologies were remarkably similar about VER ≈ 10, with a maximum foaming efficiency of 20 % (as compared to 90 % in the 180 bar reactor), but neither of the linear ones reached a VER > 3. Alike observed at 180 bar, at higher foaming temperatures of $T = 165\,°C$, comb PS kept a better volume expansion as their more highly branched bob PS. Granted, the differences were less significant.
The cell densities in the range of 10^{11} cell/cm^3 were about 100 times higher with the high pressure reactor, while there was not much change within the experimental temperature range (Figure 6.12c). Consequently, the general (but not pronounced) decrease in cell size within 145 °C to 165 °C is more attributed to the lower volume expansion (Figure 6.12d). Since the linear samples, i.e. PS310 and EPS, did not even marginally expand at the highest temperature, no cell structure could be analyzed.

6.4 Conclusive Summary: Structure–Property Relationship

In both foaming reactors, operating at 180 bar and 500 bar, at the low temperature range of 125 °C and 145 °C, respectively, all synthesized polymers of branched topologies (i.e. comb and dendrigraft) achieved the same volume expansion ratio of about VER ≈ 10. This was also the case for linear PS in the Mini Reactor at low pressures, that however did show drastically reduced foamability in the high pressure reactor (HPR). Independently of the autoclave type, i.e. pressure conditions, differences in foamability between the samples became most obvious at the high ends of the operating temperatures.
At those thermal conditions, it is obvious, that the melt strength gained significant importance in stabilizing the foam and to prevent cell coalescence and cell wall rupture. Interestingly, comb-like structures that nearly achieved a maximum theoretical volume expansion (VER $\approx$ 30–40), overall performed better than dendrigraft topologies, even though their maximum achievable strain hardening in general was lower (SHF $\lesssim 200$) as compared to bob PS (SHF = 200–700). At this point it is evident, that further influential factors have to be considered for such a complex process like foaming.

First of all, the strain hardening factor highly depends on the strain rate, that is furthermore individual to the elongational process. The biaxial extensional flow during the bubble growth phase yields rather high strain rates of $\dot{\varepsilon}_H > 0.1\,s^{-1}$,[302,303] and can even reach fast stretch times in the dimension of $5\,s^{-1}$.[6] Since extensional tests have shown that comb PS310-100-15 excels in SHF ≈ 200 at strain rates above $1\,s^{-1}$ (see Figure 6.9), and also performed best in volume expansion at all conditions, the results suggest a strong correlation between foamability and strain hardening. It is assumed that the nonlinear field of deformation approximately matches both, the biaxial growth of the bubbles as well

as the strain rate measured in uniaxial deformation. That particular SCB comb PS with barely entangled side chains moreover obtained the lowest zero-shear viscosity (ZSV) of all investigated samples, with η_0 being nearly one decade lower than its linear PS310 precursor. Those findings match the conclusion made in the previous Chapter 5 (see Section 5.5), that a low η_0 is expected to be beneficial for achieving a high VER, but for sure it is not detrimental in case the polymer's structure is inherently strain hardening in the applied region of strain rate at processing conditions. Consequently, both structurally similar combs PS310-100-40 and PS290-120-44 also did show improved expandability, resulting in low dense foams. When it comes to the dendrigraft PS, the tremendous strain hardening of SHF > 500 at rates $\dot{\varepsilon}_H < 0.1\,s^{-1}$ did not translate into a higher VER as compared to the combs. Here again, two factors suggest to play a significant role: The strain rates in the batch foaming process did not represent the lower strain rates at which a maximum SHF was demonstrated in uniaxial elongational tests. Moreover, the zero-shear viscosities were much higher as compared to the comb topologies, but still less than the ZSV of the linear PS310.

It needs to be mentioned that – unlike the undoubted significance of the strain hardening for the melt strength in foaming – the influence of the viscosity here is less evident. For sure, the very low viscosity of SCB comb PS310-100-15 does not hinder its expandability and cell stabilizing property in foaming, because at the later stage the deformation field is within the nonlinear elongational regime, making use of the strain hardening (see also Section 5.5). But although a low η_0 is considered to expedite the bubble growth once a stable nuclei is formed, it has been found by Chen et al.[304] and Leung et al.[230] that this effect – if at all – is not pronounced.

Of course, the foaming outcome is also widely governed by homogenous and heterogenous bubble nucleation, an effect that has not been taken into consideration in the scope of this thesis. However, for amorphous homopolymer PS, equal conditions in the nucleation stage should be presumed and only homogenous nucleation is expected.

7 Model Comb-Linear Polystyrene Blends: Rheological Studies

This chapter's main focus is to study the rheological properties of model comb-linear PS blends. The previously synthesized LCB comb PS290 series with well-entangled side chains now have been diluted in different concentrations with additional linear chains (PS44) of 44 kg/mol. The melt behavior in the linear (SAOS) and nonlinear (extensional) flow is investigated and compared to their undiluted states. Additional rheological data is provided by SCB comb PS to give insights into the effects of the dynamic tube dilution and the interplay between branched and linear topologies. All polymer samples studied in this chapter were synthesized and characterized in Chapter 5 & 6.

7.1 Introduction

The rheological properties of a polymeric melt are profoundly influenced not only by the topological structure or the weight-average molecular weight, but also by its molecular weight distribution with each chain length contributing differently to the chain relaxation dynamics. Consequently, the presence of high or low molecular weight compounds can drastically alter the melt flow behavior. This can be intentionally used so that polydispersity is not a mere side effect of polymerization, but moreover a necessary prerequisite for improving the polymer's processing properties or performance in application.[305]

The binary blend of two linear, monodisperse homopolymers can be considered as the simplest case of a broad molecular weight distribution. Conversely to a monomodal polydisperse system, a bidisperse distribution allows the investigation of the individual contribution of each mode on the melt behavior. Its extent of impact can be analyzed by changing the concentrations. Overlay effects caused by gradually different chain lengths – as seen in polydisperse distributions – are circumvented and the interpretation of the rheological response is far more conclusive. Thus, linear-linear blends of various polymer compositions have been comprehensively studied as model systems on experimental and theoretical basis.[306–311]

However, polymer processing in elongational flow rather benefits from the presence of branching and the advantages of improved melt strength, as already emphasized in the course of this thesis. In that respect, blending also allows to enhance, to tune and optimize

the melt properties of linear polymers when a definded amount of LCB polymer is added or vice versa. Apart from that, the simultaneous presence of more or less branched and linear chains can also originate from the choice of the polymerization method, i.e. the involved reagents and catalyst system, but also might come from post-polymerization processing (e.g. via reactive extrusion with free radical initiators or via gamma radiation).
Even though blends of branched and linear polymers have been extensively studied, so far most of the known literature has demonstrated the benefits of branching on the basis of disperse and commercial grade samples. In that sense, the structure-property elucidation of topologically diverse systems is challenging.

As a consequence, model branched polymers are universally valuable in providing information on the melt properties of purely branched systems, and also but furthermore can serve as defined co-components to study the mutual influence of linear-branched chain interactions.
Therefore, in this chapter, previously synthesized model comb PS series (see **Chapters 5** & **6**) with similar backbone length $M_{w,bb}$ = 290–310 kg/mol, defined number of branching, N_{br}, and similar branch molecular weight, $M_{w,br}$ = 40–44 kg/mol are used. The rheology of their blends with unattached, linear chains of 44 kg/mol, named PS44, is investigated. The homopolymeric nature makes the lower molecular weight component a theta solvent in the melt.

Table 7.1 lists the comb PS samples and the respective concentration series with linear PS44 prepared for the experimental part of this chapter. The volume fraction of the backbone, ϕ_{bb}, refers to the volume fraction on the basis of the whole melt volume, consisting also of its branches, ϕ_{br}, and – if blended – the linear PS44 chains, ϕ_{lin} amongst which the backbone chain is embedded in. In short, the melt volume is defined by **Equation 7.1**.

$$\phi_{bb} + \phi_{br} + \phi_{lin} = \phi_{comb} + \phi_{lin} = 1 \tag{7.1}$$

The prepared comb-linear PS blends were characterized in oscillatory shear (SAOS) and elongational flow, analogously to the conditions presented in Sections 5.3.1 and 5.3.2. Furthermore, the data treatment and extraction of significant values was previously explained. The experimental data of the blends can be found in the **Appendix A.2**.

Table 7.1: Blend compositions of PS290-N_{br}-44 and PS44.

Sample name [a]	Sample [vol%]	PS44 [vol%]	ϕ_{comb}	ϕ_{bb}
PS290-190-44	100	–	1.00	0.034
	90	10	0.90	0.031
	75	25	0.75	0.026
	50	50	0.50	0.017
	25	75	0.25	0.0086
	10	90	0.10	0.0034
PS290-120-44	100	–	1.00	0.053
	65	35	0.65	0.034
	35	65	0.35	0.019
	20	80	0.20	0.011
PS310-100-40 [b]	100	–	1.00	0.074
	65	35	0.65	0.047
	35	65	0.35	0.026
	20	80	0.20	0.015
	10	90	0.35	0.0074
PS290-60-44	100	–	1.00	0.99
	65	35	0.65	0.064
	35	65	0.35	0.035
	20	80	0.20	0.021
PS290-30-44	100	–	1.00	0.18
	65	35	0.65	0.12
	35	65	0.35	0.063
	20	80	0.20	0.036
	10	90	0.10	0.018
PS290-29-44	100	–	1.00	0.17
PS290-14-44	100	–	1.00	0.32
PS290-10-44	100	–	1.00	0.40
PS290-5-44	100	–	1.00	0.57
PS290-3-44	100	–	1.00	0.68
PS290 [c]	100	–	1.00	1.00
	65	35	0.65	0.64
	35	65	0.35	0.34
	20	80	0.20	0.20
	10	90	0.10	0.097
PS310-100-15	100	–	1.00	0.172
PS290-90-6	100	–	1.00	0.48
PS290-50-6	100	–	1.00	0.34

[a] Nomenclature: PS[$M_{w,bb}$]-[N_{br}]-[$M_{w,br}$]. [b] PS310-100-40 with similar backbone and branch molecular weight is classified into the comb PS290-N_{br}-44 group for simplification of data presentation and ease of reading. Calculations are based on original structural parameters. [c] For simplicity and consistency, the volume fraction of PS290 also refers to ϕ_{comb} as a "comb" with $N_{br} = 0$.

7.2 Arm Relaxation

The side chains of a comb-shaped polymer molecule not only interact with the backbone chain that they are attached to or the branches of another molecule, but also – if branch points are close enough or flexibility of chain segments allows – with their neighboring side chains attached to the same parent backbone molecule. Therefore, this section considers in detail this interaction and how the presence of linear chains changes the chain dynamics of the branches, specifically the arm relaxation process.

7.2.1 Introduction

Revisiting the tube model from the rheology introduction (see Chapter 3.3, Figure 3.6 and 3.7a), the relaxation mechanisms of a linear chain is either by reptation of the whole molecule or contour length fluctuation (CLF) from the chain ends wrinkling inwards, retracting into the tube and re-expanding again while forming a new tube.
Although CLF is a fast relaxation mechanism for the chain ends, deep fluctuations down to more interior chain segments are entropically unfavored and become exponentially so improbable, that those inner parts of the chain most likely will already have relaxed by reptation.

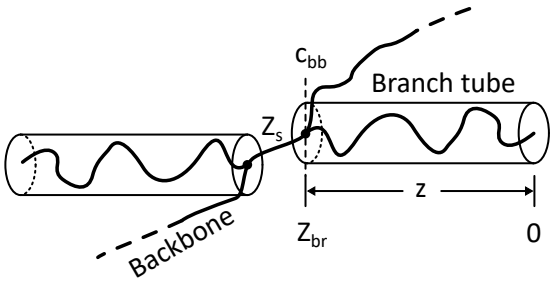

Figure 7.1: Schematic illustration of a backbone segment with side chains, showing the branch tube with coordinate z, from $z = 0$ for the fully extended arm and $z = Z_{\mathrm{br}}$ when the arm fully retracted to the backbone center, c_{bb}, via CLF relaxation mechanism.[9]

The dynamics of the exterior segments near the tube ends with relaxation time τ_{early}, accounted for "early-time chain end fluctuations", is controlled by fast Rouse motions (Rouse reorientation time[57], τ_{r}), for which Milner and McLeish[138] proposed a model using the tube (retraction) coordinate, z, equal to units of initial entanglement lengths, Z,[150] as illustrated in **Figure 7.1** at the example of a side chain tube. At the position $z = 0$ the chain is fully extended[58] and at $z = Z_{\mathrm{br}}$ the chain is retracted to the backbone center.[9,312] Using the relation between τ_{r} and the entanglement time, τ_{e}, i.e. $\tau_{\mathrm{r}} = Z^2\,\tau_{\mathrm{e}}$,[9] it can be derived that τ_{early} is simply expressed by **Equation 7.2**.

$$\tau_{\mathrm{early}} = \frac{9}{16}\,\pi^3\,\tau_{\mathrm{e}}\,z^4 \tag{7.2}$$

[57] The Rouse reorientation time, τ_{r}, is a useful quantity in entangled melts as a time scale for CLF, whereas the Rouse stress relaxation time, τ_{R}, is more relevant for unentangled melts and dilute solutions.[9]
[58] For a fully extending chain, $\tau_{\mathrm{early}} \to 0$ if $z \to 0$.

Considering a linear chain that is now highly immobilized at one chain end through a branch point, i.e. reptation relaxation is considerably retarded as found for star or comb polymers (neglecting DTD), the CLF is solely "responsible" to drag all the side arm chain segments towards the center of the tube. Those deep fluctuations necessary for the whole side arm to relax impose a probability function, $\exp(U(z))$, governed by the free energy, $U(z)$, which can be interpreted as an arm retraction potential;[312] an entropic barrier that takes effect at late times, τ_{late}, see **Equation 7.3**.[313] Simply, early time relaxation, τ_{early}, precedes late relaxation, τ_{late}.

$$\tau_{\text{late}}(z) = \tau_{\text{early}} \cdot \exp\left[U(z)\right] \qquad \text{with} \quad U(z) = \nu \, \frac{z^2}{Z_{\text{br}}} \tag{7.3}$$

The tube coordinate is $z = 0$ at the side arm end and goes to $Z_{\text{br}} = M_{\text{w,br}}/M_{\text{e}}$ at the branch point. Assuming a straight, impenetrable tube, the numerical constant has shown to be equal to $\nu = 3/2$.[9]

$$\tau_{\text{late}}(z) = \tau_{\text{early}} \cdot \exp\left(\nu \, \frac{z^2}{Z_{\text{br}}}\right) \tag{7.4}$$

Regarding comb polymers, dynamic tube dilution (DTD) still plays a significant role of relaxation, especially for backbone dynamics. The DTD is an effect of the branches towards the backbone, i.e. the backbone itself does not contribute to dilution, and therefore the proportion of the contribution depends on the volume fraction of branches, ϕ_{br}, vs. the fraction of backbone, ϕ_{bb}, with $\phi_{\text{bb}} + \phi_{\text{br}} = 1$. While the relaxation "late" time of a chain fixed at one end in the absence of dilution is expressed via **Equation 7.4**, in the specific case of branching, the longest arm relaxation time, τ_{a}, can be derived using molecular parameters, leading to **Equation 7.5**.[9]

$$\tau_{\text{a}} = \tau_{\text{early}} \cdot \exp\left[\nu \, Z_{\text{br}} \left(1 - \frac{2\phi_{\text{br}}}{3}\right)\right] \tag{7.5}$$

7.2.2 Results

Applying the extended DTD theory of Milner and McLeish[145] on the topology of comb PS290-N_{br}-44 series and with molecular parameters (i.e. Z_{br}, τ_{e}, and ϕ_{br})[59] known from their characterization, the effect of branch point spacing on the behavior of the longest arm relaxation time, τ_{a}, can be investigated. Due to the same branch length (i.e. entanglement number, Z_{br}), τ_{a} can be simply expressed via **Equation 7.6** (i.e. Equation 7.2 in Equation 7.5) as a function of the number of branches, N_{br}.

$$\tau_{\text{a}} \approx \frac{1}{2}\,\pi^3\,\tau_{\text{e}}\,Z_{\text{br}}^2 \cdot \exp\left[\nu \, Z_{\text{br}} \left(1 - \frac{2\,\phi_{\text{br}}}{3}\right)\right] \quad \text{with} \quad \phi_{\text{br}} = 1 - \frac{20}{20 + 3\,N_{\text{br}}} \tag{7.6}$$

[59] The entanglement number of the branches is $Z_{\text{br}} = M_{\text{w,br}}/M_{\text{e}} = 3$. The entanglement relaxation time is $\tau_{\text{e}} = 2 \cdot 10^{-4}$ s at $T_{\text{ref}} = 180\,°\text{C}$, as graphically illustrated in Figure 5.5a, page 79. Due to the same backbone and branch length, the branch volume fraction, ϕ_{br}, is a function of the number of branches, N_{br}, expressed via $\phi_{\text{br}} = 1 - \frac{20}{20 + 3\,N_{\text{br}}}$.

Figure 7.2 shows the exponential decrease of the dominant arm relaxation time, τ_a, with inreasing branch volume fraction, ϕ_{br} (equal to increasing N_{br} and decreasing backbone segment entanglement number, Z_s), as predicted by the DTD theory following Equation 7.6 (blue straight line).

The experimental arm relaxation times[60], τ_a, of branched combs and their linear blends are presented as data points in Figure 7.2, and can be obtained from the SAOS frequency data as the local maxima of the phase angle vs. the angular frequency, δ vs. ω. An example of this method is shown for comb PS290-190-44 in Figure 5.5c. The "arm relaxation frequency" at this maximum is simply converted into its time by the inverse: $\tau_a = 1/\omega|_{\delta=\text{loc.max}}$.[314]

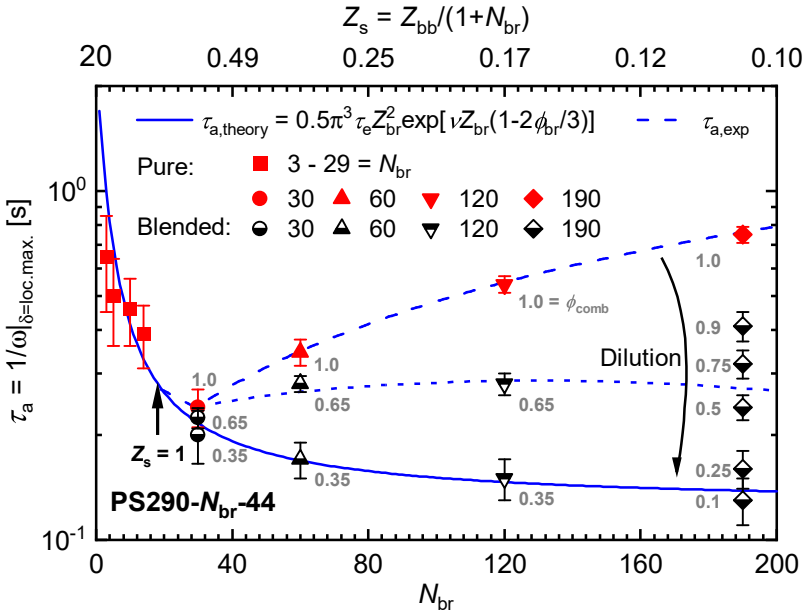

Figure 7.2: Arm relaxation times, τ_a (calculated from the inverse angular frequency as $\tau_a = 1/\omega|_{\delta=\text{loc.max.}}$, obtained from the local maxima in the δ vs. ω plot, see Figure 5.5c, page 79), as a function of the number of branches, N_{br}.
Full symbols (■, ●, etc.) are data of undiluted comb PS290-N_{br}-44 and the solid line (blue) their theoretical prediction, $\tau_{a,theory}$. The dashed line (blue) is guide to the eye to show the deviation of experimental arm relaxation times, $\tau_{a,exp}$, of combs with $Z_s < 1$. Half-filled symbols (◒, etc.) depict data of comb PS diluted with PS44 in comparison with their undiluted (●, etc.) parent sample. Respective dilutions of the comb, ϕ_{comb}, are indicated in grey. The dotted line (blue) serves as guide to the eye for a dilution of ca. 65 % comb PS. Reproduced and modified (blend data was added) with permission.[120] Copyright 2017, American Chemical Society.

7.2.2.1 Pure Comb PS

For pure combs of the PS290 series (Figure 7.2, filled symbols), the experimental data of those characteristic times were extracted from SAOS data presented in Fig. 5.5c as graphically illustrated there (τ_a signified by a red arrow). For increasingly branched combs from $N_{br} = 3$ to 30, this peak maximum shifts to higher frequencies and thus, shorter relaxation times which corresponds well with molecular theories that predict a significant contribution of the dynamic dilution effect. However, a further increase in branching number and a tighter branch point spacing along the backbone towards more

[60] Also called side arm retraction time.

densely grafted comb and bottlebrush-like structures reverses the shift of the relative maximum δ to lower frequencies. The arm relaxation gets retarded, contrary to theoretical expectations (blue line) of a steady decrease. The increase in τ_a for combs with $N_{br} > 30$ (visualized by a dashed blue line) indicates, that side chain crowding imposes an additional intermolecular interaction between adjacent branches and slows down relaxation. This takes effect especially when the branch point distance approaches and falls below entanglement dimensions, i.e. $Z_s < 1$.
Apparently, the dynamic dilution theory as presented by Equation 7.6 is insufficient to describe the arm relaxation when neighboring branches are close enough to mutually influence each other. The molecular theories seems to fail to describe this additional entropic barrier.

7.2.2.2 Comb-Linear PS blends

By blending the same comb PS with additional "free" side chains (Figure 7.2, half-filled symbols), not only the arm retraction times of the combs decrease, but with sufficient extent of dilution, the branch relaxation approaches the theoretical expectation of a steady decrease with increasing grafting density.
For loosely grafted bottlebrushes with $N_{br} = 190$, the dilution factor has to be as low as 10 %, i.e. diluted with 90 % linear PS44, to match the arm relaxation time predictions of Eq. 7.6 on the basis of pure combs. In contrast, densely grafted combs of $N_{br} = 120$ and 60 show good theoretical agreement at a dilution of just 35 %. Thus, the lower the grafting density, the less the influence of linear chains on the dominant arm relaxation time. Most obvious is this increasing insensitivity to dilution for comb PS with $N_{br} \geq 30$ branches when the segment number entanglement between two branch points gets close to or below $Z_s = 1$, and the arm relaxation remains unchanged.
This leads to the conclusion that neighboring branches of loosely grafted comb PS and densely grafted PS with medium $N_{br} \leq 60$ are too widely spaced and therefore barely interact or hinder each other with respect to their relaxation. Conversely, the intermolecular interaction of adjacent arms is inevitable when the branch points above $N_{br} \approx 30$ move closer together. Free linear chains disturb those relaxation restricting interactions as their highly dynamic presence replace the retarded motion of their molecular analogues that are onesidedly tied to a backbone. Assumingly, at some point, the branching becomes so dense that lowering the arm relaxation time necessitates a big excess of "solvent chains" to statistically counterbalance the neighboring branch proximity.

7.3 Diluted Modulus

This section is investigating the effect of dynamic tube dilution that results from the presence of relatively short chains. Those can be either covalently connected side chains or unconnected linear chains with low molecular weight. Both are affecting the longer backbone or blend component with otherwise impeded relaxation dynamics.
The diluted modulus describes the extent of interplay between those mechanisms. Specific scaling laws with the volume fraction of linear, long chain parent backbone component are found, depending on the bimodal composition of long and short chains: either pure combs, comb-linear or linear-linear blends.

7.3.1 Introduction

In Chapter 5.3.1.4 the linear rheology of synthesized comb PS series was discussed with specific focus on the dilution effect of the branches on the plateau modulus, G_N^0. Recalling Equation 5.12 as **Equation 7.7**, the solvating influence of low molecular weight components (e.g. covalently bonded branches, free oligomers or solvents) on an entangled, higher molecular weight component (e.g. linear polymer or backbone with volume fraction ϕ_{bb}) is described by:

$$G_{N,s}^0 = G_N^0 \, \phi_{bb}^{1+\alpha} \tag{7.7}$$

Evolving from the tube theory, the dynamic tube dilation concept was widely applied to investigate the dilution effect of relatively fast relaxing, solvent-like environment on entangled polymers.[262] A broad spectrum of polymer compositions and topologies were exposed to the diluting matrix of shorter-chain polymers, oligomers and solvent molecules, for example systems of star-like combs[315], bidisperse linear blends,[298,316] star-linear blends[262,317–319] and polymer dilutions with oligomers (i.e. $M_w \ll M_e$)[320,321] as well as solvent-size molecules (i.e. solvents and plasticizers)[321].
The self-dilution effect of side chains on the backbone tube of comb- and bottlebrush-like polymers in the melt state has been extensively studied.[322] However, dilution of those branched topologies in a matrix of lower molecular weight molecules acting as additional solvent has rarely been in focus of research and experimental data about their dilution exponent α is scarce. Therefore, the synthesized comb PS and their mixtures with side chain-size linear chains contribute to the experimental data and extend this field towards investigation of blended combs polymers.

7.3.2 Results

The diluted moduli, $G_{N,s}^0 = G'|_{\delta=\min 1}$, were determined using the G' value at the angular frequency, $\omega|_{\delta=\min 1}$, where the phase angle, δ, has a (local) first minimum (going from the low- towards the high-frequency regime). This method is graphically shown in **Figure 7.3** on the example of the blends of PS290-60-44 with PS44.

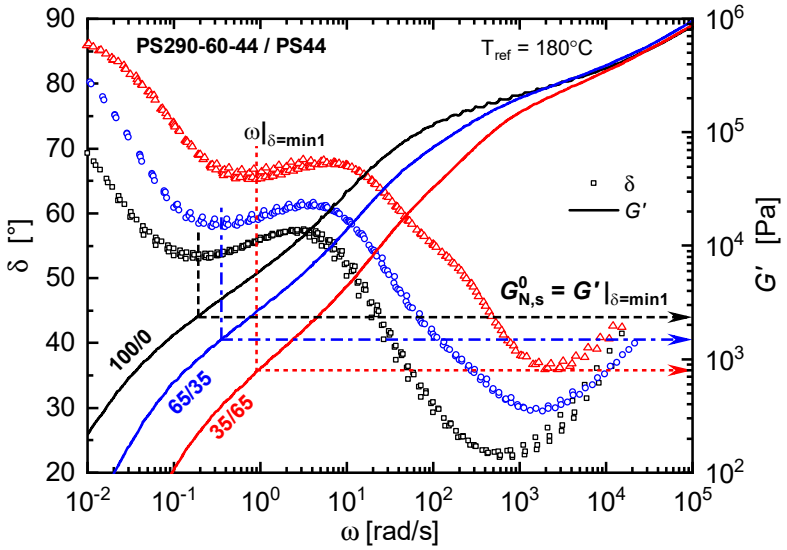

Figure 7.3: Graphical illustration of the extraction of the diluted modulus, $G^0_{\mathrm{N,s}}$, from the SAOS experimental data. The diluted modulus, $G^0_{\mathrm{N,s}} = G'|_{\delta=\mathrm{min1}}$, is the storage modulus, G', at the angular frequency, $\omega|_{\delta=\mathrm{min1}}$, where the phase angle, δ, shows a first (local) first minimum in the plot of δ vs. ω plot (cf. Figure 5.5). Shown on the example of comb-linear PS blends of PS290-60-44 with PS44.

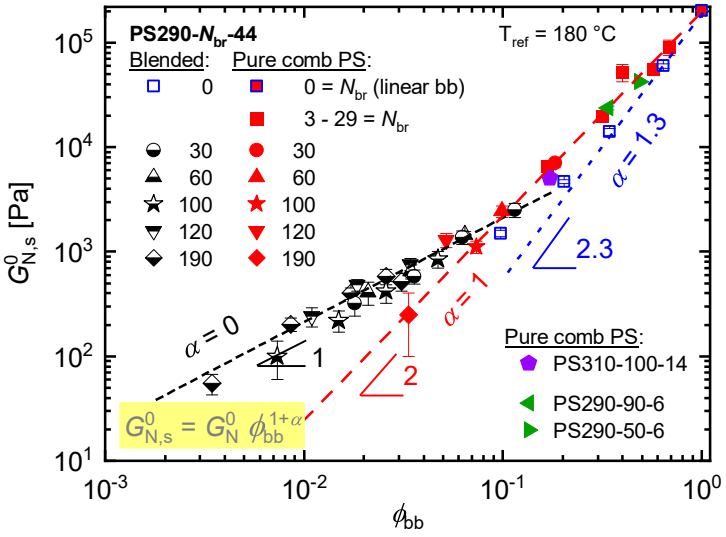

Figure 7.4: Diluted modulus, $G^0_{\mathrm{N,s}}$, extracted from SAOS experimental data as G' at the first minimum in the plot of δ vs. ω (see Figure 7.3), and plotted against the total volume fraction of the backbone, ϕ_{bb}. Full symbols (e.g. ■, ●, etc.) are data of pure LCB comb PS with respective number of branches, N_{br}; and half-filled symbols (e.g. ◒) represent comb PS290 series blended with PS44. Hollow squares (□) are blends of linear PS290 with PS44. Data of pure SCB comb PS with barely entangled (⬟) and unentangled (◀ and ▶) side chains is added. Dashed and dotted lines are guide to the eye with slopes indicating the power law of $1 + \alpha$.

The moduli of pure combs of the series PS290-N_{br}-44, PS290-N_{br}-6 and PS310-100-$M_{\mathrm{w,br}}$ were extracted from SAOS experimental data of Figure 5.5 (p. 79), Figure A.2.1 (p. 195), and Figure 6.3 (p. 112), respectively. The moduli of the mixtures of linear PS290 and comb PS290-N_{br}-44 series with well-entangled, linear chains PS44 of $M_{\mathrm{w}} = 44\,\mathrm{kg/mol}$ were extracted from SAOS experimental data presented in Appendix A.2.2 (p. 196).

Figure 7.4 summarizes $G^0_{N,s}$ as a function of the volume fraction of the backbone, ϕ_{bb}, with respective dashed and dotted lines as guide to the eye for the slopes, indicating the power laws.[61]

7.3.2.1 Pure Comb PS

From the scaling of the diluted modulus of pure comb PS with the molecular weight via $G^0_{N,s} \sim M_w^{-2}$ (already discussed in Section 5.3.1.4 and Figure 5.6), and the relationship $M_w \sim \phi_{bb}^{-1}$ (see Equation 3.21), the diluted modulus scales with the backbone volume fraction via $G^0_{N,s} \sim \phi^2_{bb}$, corresponding to a dynamic dilution exponent of $\alpha = 1$. Again, it should be emphasized that not only well-entangled LCB comb PS display a quadratic scaling law, but also comb PS with slightly entangled and even unentangled SCB of $M_{br} = 15$ and 6 kg/mol, respectively, exhibit the same dilution behavior for same (or similar) backbone molecular weight.
Kapnistos et al.[323] investigated the linear rheology of comb homopolymers with PS and PB chemistry which showed α to be between the two limiting predictions of 1 and 4/3 and thus ultimately insufficiently conclusive, whereas their model predictions fell closer to $\alpha = 4/3$. The relatively low molecular weight range of their samples of less then 1 decade might not have been irrelevantly contributed to this ambiguity in experimental data.

7.3.2.2 Linear-Linear PS Blends

In contrast to the quadratic scaling of the diluted modulus of comb PS, the linear PS44 side chains has a stronger diluting effect on the PS290 backbone precursor in the bidisperse, linear-linear model blends. The data suggests a scaling with a higher exponent, $G^0_{N,s} \sim \phi^{2.3}_{bb}$, and therefore $\alpha = 1.3$ for low concentrations of "solvent" PS44, i.e. $\phi_{bb} > 0.3$. However, the exponent seems to transition to a lower slope of $\alpha = 1$ with further dilution.

The dynamic tube dilution and proper value for α either being 1 or 4/3 has been widely discussed by rheologists. The inconsistency in choice for model predictions is still an unresolved issue for accurately fitting experimental SAOS data.[62] Hence, the experimental and "model-free" way of determining α via a concentration series of the polymer in a theta-like solvent (e.g. same chemical composition but lower M_w) and plotting the diluted plateau modulus against the volume fraction – like accomplished here – presents as promising approach to shine light on this ongoing discussion.

[61] From the comb PS290-N_{br}-44 series, only combs with $N_{br} \geq 30$ have been blended with PS44 in various concentrations (half-filled, black symbols). For direct comparison of those samples, the shape of the symbols of unblended comb PS (filled, red) were matched. Samples with $N_{br} \leq 29$ are not explicitly distinguished and represented as red squares.

[62] The dilution exponents in literature are mostly determined on theoretical approaches using α as a fitting parameter for relaxation data. Depending on the mathematical model, the observed polymer system and specific assumptions, values for $\alpha = 1$ or 4/3 can be obtained.[312] As prominent examples, the "Hierarchical model" of Park and Larson[324,325] gives the former for bidisperse linear blends, whereas the latter fits for star-linear blends. Other models are the "time-marching algorithm" (TMA)[321] and the "branch-on-branch (BoB)"[150] model. Even for the same polymer-solvent systems, the appropriate α can transition depending on the observed relaxation times. Van Ruymbeke et al.[298] compared experimental data with theoretical model predictions of viscoelastic relaxation functions (i.e. storage moduli) and reported a transition of the best fitting dilution exponents depending on the relaxation time. For example, at short times $\alpha = 1$, and at longer times $\alpha = 4/3$ were more appropriate.

Hall et al.[262] stated that the exponent difference of 0.33 is "hard to distinguish with confidence in such a plot". This can also be said for the ambiguity displayed in data of bidisperse, linear-linear PS dilutions. Especially within a limited range of concentrations, $G^0_{N,s}$ is considered as not very sensitive to the value of α.[261] For the linear-linear dilution series presented here, more data would provide more certainty about which of the exponents is more accurate.
On the other hand, experimental values of linear PS and PB solutions in their oligomers showed a quite clear scaling following a slope of 2.3 ($\alpha = 4/3$) when the normalized diluted modulus $G^0_{N,s}/G^0_N$ was plotted against the polymer concentration.[321]

7.3.2.3 Comb-Linear PS Blends

If free linear chains are added in increasing volume fraction, ϕ_{lin}, to the model LCB comb PS290-N_{br}-44 series, as expected, the backbone plateau moduli at low frequencies tend to further decrease due to those amplified, complementing dilutive effects of attached and unattached branches. With respect to the bare volume fraction of backbone, ϕ_{bb} (with $\phi_{bb} + \phi_{br} + \phi_{lin} = 1$), the dilution results in an exponent of 1 for $G^0_{N,s}$, corresponding to a dilution exponent value of $\alpha = 0$. As a consequence of the lack of experimental data of comb-linear polymer blends, this dilution exponent – to the best of my knowledge – has not been reported. In contrast to that, mixtures of other branched topologies with linear compounds, for example, blends of multiarm stars with linear chains[262,317], have "familiar" α of 1 or 4/3.
As a result of the drastic difference of the dilution exponent between the here presented undiluted comb PS ($\alpha = 1$) and a much less pronounced dilution of linear-comb PS mixtures ($\alpha = 0$), it can be concluded that the dynamic tube dilution (DTD) via grafting of chains is more efficiently acting on the backbone than compared with the solvent-like presence of unbound PS.

7.4 Complex Modulus

This section investigates the complex modulus in the framework of the van Gurp-Plamen (vGP) plot and is picking up the idea of a topological map. Whereas the complex modulus at a phase angle of 60° is used as a parameter for branching in comb- and bottlebrush-like topologies (see Section 5.3.1.5), the use of the vGP plot is now extended, further highlighting another criteria using the minimum of the phase angle. The scaling laws are observed, looking for differences or commonalities between linear and comb PS of different structural parameters, as well as their blend compositions.

7.4.1 Introduction

The van Gurp Palmen (vGP) plot (also see Section 5.3.1.5) is a rather novel way of studying the rheological data obtained under SAOS conditions. The temperature invariance of the

complex modulus against the phase angle, $|G^*|$ vs. δ, allows merging of the data obtained at different measurement temperatures into a single curve.[299] Since horizontal or vertical shift factors are not required, the vGP plot can be used to validate the time-temperature superposition (TTS) principle and also to confirm the reliability and reproducibility of dynamic oscillatory data. In addition, the vGP plot is also helpful to qualitatively assess the thermorheological complexity of a polymer or polymer system with respect to its composition or topological features.[300,301]

Van Gurp and Palmen[252] initially used this principle of the vGP plot to investigate the failure of the TTS by means of chemically heterogenous polymeric materials, in particular copolymer blends. These were characterized into 4 different groups: miscible and immiscible blends for which TTS holds or fails. They concluded that deviations amongst the isotherms (i.e. dynamic frequency sweeps at different temperatures) might be caused by thermal instability, physical changes (e.g. phase transitions) or should be related to specific (e.g. interfacial and temperature dependent) interactions amongst the different polymer compounds. In case of branched homopolymers they explained possible failure of the TTS (exhibiting inconsistencies and deviations in vGP overlay curves) with thermorheological complexity, considering them as blends of polymers with different degree of branching and inhomogeneous branch distribution.

7.4.2 $|G^*|$ at the Phase Angle of 60°

Trinkle and Friedrich[253] observed, that the vGP curve is stretched towards low modulus with increased broadening of the molecular weight distribution and found $|G^*|$ at a phase angle of $\delta = 60°$ as a criterion quantitatively related to the polymer's dispersity.
Between the terminal and the glassy regime, linear monomodal polymers exhibit only one minimum of δ where the "global" $|G^*|_{\delta=\min}$ is closely related to the plateau modulus[63], G^0_N.
In contrast, bimodality (i.e. blending of distinctively different molecular weight fractions, see Figure A.2.6d, p. 200) and branching (e.g. see Figure 5.5d, p. 79) makes a "local" second minimum appear at lower $|G^*|$[64].[299]
Trinkle et al.[254] further investigated the vGP to identify long chain branching and classified LCB polymers using this minimum in the low frequency region accounting for the dilution of the backbone media.[326]
In addition to quantify dispersity effects in the vGP plot, Bahreini et al.[14] proved $|G^*|_{\delta=60°}$ to be also a suitable criterion to quantify the LCB content in blends of industrial, polydisperse linear and branched PP which – owing to the dispersities – did not exhibit a local minimum at low frequencies.

[63] At the example of polystyrene: $|G^*|_{\delta=\min}(\mathrm{PS}) \approx G^0_N(\mathrm{PS}) = 2.0 \times 10^5$ Pa.

[64] The second, local minimum that appears is the *first* minimum when moving from the low to the high frequency region. Thus, for better discrimination and simplification of nomenclature it is here called 1st minimum, $|G^*|_{\delta=\min 1}$; and – in case of two minima – to distinguish from the 2nd minimum, $|G^*|_{\delta=\min 2}$. If the polymer system (e.g. linear monomodal) by nature exhibits only one minimum, of course: $|G^*|_{\delta=\min 1} = |G^*|_{\delta=\min 2}$., which is also consistent with $|G^*|_{\delta=\min 1} \to |G^*|_{\delta=\min 2}$ for branching degrees $N_{br} \to 0$.

In Chapter 5 (Figure 5.5d, p. 79), the feasibility of the criterion $|G^*|_{\delta=60^\circ}$ to characterize the degree of LCB was confirmed on the basis of the model LCB comb PS290-N_{br}-44 series with the same backbone and branch molecular weight.[120]
As the "medium" ($M_{\mathrm{w,br}} \approx M_{\mathrm{e}}$) and short chain branched ($M_{\mathrm{w,br}} \ll M_{\mathrm{e}}$) comb PS samples of the same backbone precursor fit the same power law of $|G^*|_{\delta=60^\circ} \sim M_{\mathrm{w}}^{-1}$ (Figure 5.6), the results strongly suggest a general dependency over a wide range of side chain lengths and branching degrees for the same $M_{\mathrm{w,bb}}$. However, this value could not be detected for PS290-190-44 with LB conformation as the phase angle does not cross the y-intercept at $\delta = 60^\circ$ in the terminal region.

When it comes to blends of comb PS with additional low-M_{w} linear PS (i.e. comb PS290-N_{br}-44 series blended with PS44; see SAOS data of diluted combs in Appendix A.2.2), the increasing backbone dilution shifts the local, first minimum above the y-intercept at $\delta = 60^\circ$. As this first minimum is related to the "strength" of backbone dilution caused by side chain relaxation, the missing intersection of $\delta = 60^\circ$ with the $|G^*|$ at the low-frequency range of this minimum therefore renders the $|G^*|_{\delta=60^\circ}$ criteria as not applicable for the quantification of LCB or the dilution effect in mixtures of comb PS with free linear chains.

7.4.3 $|G^*|$ at the 1st Minimum of the Phase Angle

The presence of a minimum in the phase angle, δ, in the vGP plot is caused by the different relaxation mechanisms contributing to the dilution effect of the backbone. Since the individual impact of each of those dynamics manifests in the shape of the curve, the locations of the minima hold structural information about the contributing chain segments. Trinkle et al.[254] explored the vGP plot in order to find characteristics or commonalities in the positioning of the minima. The positioning might be related to specific topological features of differently branched and blended systems, e.g. star-, comb- and H-type polymers. They suggested a topological map where the first minima of certain types of polymers or blends are predominantly related to certain regions in the δ vs. $|G^*|$ coordinate system[65], or, conversely, there might be a forbidden area for certain topologies. However, the data was rather scarce and areas of the map were not unambiguously exclusive to one polymer structure.
Building on that same concept, Liu et al.[327] simulated the rheological behavior of different polymer topologies using the "branch-on-branch" (BOB) theoretical model, analyzed the resulting reduced vGP (rvGP[66]) plot and compared their topological vGP map with sets of experimental data from various literature sources.

[65] To be more specific, Trinkle et al.[254] used the reduced vGP plot (rvGP) with $|G^*_{\mathrm{red}}| = |G^*|/G^0_{\mathrm{N}}$ in order to compare homopolymer topologies with different chemical compositions.
[66] $|G^*_{\mathrm{red}}| = |G^*|/G^0_{\mathrm{N}}$

Figure 7.5 illustrates the extraction of the minimum points in the phase angle vs. complex modulus, δ vs. $|G^*|$, from the vGP plot of the SAOS experimental data. The chosen example shows four sets of data of a backbone PS290 and three comb PS that have significantly different branch molecular weights, $M_{w,br}$. The first minimum, δ=min1, corresponds to the backbone dilution, whereas the second minimum, δ=min2, is related to the side chain dynamics. When branching is introduced to a linear PS, the first (backbone) minimum shifts towards lower $|G^*|$. Furthermore, a second minumum appears towards higher $|G^*|$. Since both minima evolve (in opposite directions) from the linear backbone, therefore the complex modulus at the phase angle minimum of the pure linear backbone should be here consequently defined as $|G^*|_{\delta=\text{min1}} = |G^*|_{\delta=\text{min2}}$ from which both minima originate.

In order to correlate the relaxation dynamics of branched and blended chains to structural trends, the data of the minima in Figure 7.5 can be conveniently replotted and complemented with futher rheological data to a topological map.

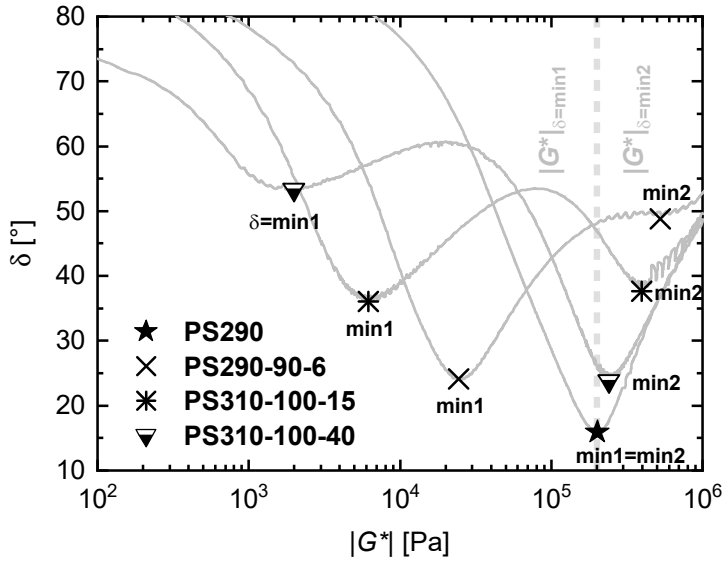

Figure 7.5: Graphical illustration of a rheological map by extracting the location of the first and second minimum of the phase angle, δ=min1 and δ=min2, respectively. The position of $|G^*|$ of the backbone is here defined as $|G^*|_{\delta=\text{min1}} = |G^*|_{\delta=\text{min2}}$ where both minima emerge. In the following Figure 7.6, the data is extended with further SAOS data of pure combs, as well as comb-linear and linear-linear PS blends.

Figure 7.6 summarizes the location of the first and second minima of all vGP curves of the here synthesized linear and comb PS, as well as their mixtures with linear PS44 and replots those characteristic points in a single vGP "map". For linear PS290, only one minimum appears in the vGP plot at $|G^*| \approx 2 \cdot 10^5$ Pa. With increasing backbone dilution (due to side chain branching or blending), the first minimum, $|G^*|_{\delta=\text{min1}}$, shifts to lower moduli, of which it can be distinguished in the map from the the second minimum, $|G^*|_{\delta=\text{min2}}$, that stays or (slightly) shifts towards higher moduli.

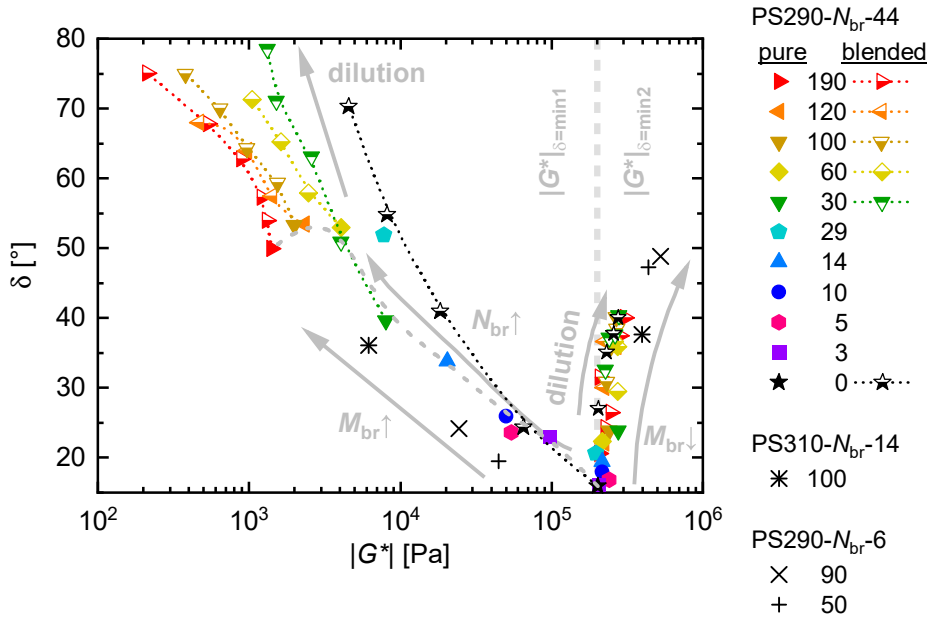

Figure 7.6: Topological map of the vGP plots displaying the locations of the 1st minimum, $|G^*|_{\delta=\text{min1}}$ (left side, $|G^*| \leq 2 \cdot 10^5$ Pa); and 2nd minimum, $|G^*|_{\delta=\text{min2}}$ (right side, $|G^*| \geq 2 \cdot 10^5$ Pa). Data were extracted from all vGP plots of linear PS290 ($N_{\text{br}} = 0$, ★) and its blends with PS44 (☆), as well as synthesized LCB comb PS290 (full symbols, e.g. ▶) and their blends with PS44 (half symbols, e.g. ⊳). The map is supplemented with data of comb PS with barely entangled ($M_{\text{w,br}} = 14$ kg/mol, ✳) and unentangled ($M_{\text{w,br}} = 6$ kg/mol, ✕ and +) SCB. Dotted lines are a guide to the eyes. Arrows (grey) show tendencies of the position of the 1st and 2nd maximum according to changes in N_{br} and $M_{\text{w,br}}$.
Data of undiluted linear and comb PS were extracted from the vGP plots in Figure 5.5d, Figure 6.3d and Figure A.2.1d; data of diluted linear and comb PS were exracted from Figure A.2.2d to A.2.6d.

From Figure 7.6 it can be seen that branching diagonally shifts the first minimum towards lower $|G^*|$ as wells as higher phase angles, with an increase in branching number and branch molecular weight having approximately the same effect, however to a different extent. For example, comparing comb PS with similar degree of branching of $N_{\text{br}} \approx 90$–100, unentangled side chains with $M_{\text{w,br}} = 6$ kg/mol exhibit only a relatively small impact on backbone dilution in contrast to barely ($M_{\text{w,br}} = 14$ kg/mol) or well-entangled ($M_{\text{w,br}} = 44$ kg/mol) branching structure. Conversely, the shift of the second minimum to higher $|G^*|$ is more pronounced for un- and barely entangled arms, with a very strong effect towards higher phase angles. As long as the branch molecular weight exceeds the critical molecular weight ($M_{\text{w,br}} \gtrsim M_{\text{c}} \approx 2$–$3\, M_{\text{e}}$), the phase angle of the second minimum at $|G^*|_{\delta=\text{min2}}$, is assumed to be rather invariant to changes in side chain length.

Blending the linear PS290 backbone or its combs with branch-size, linear PS44 results in a strong increase in backbone dilution displayed by a steep increase of the first minimum towards higher phase angles, which happens to a lesser extent also for the second minimum.

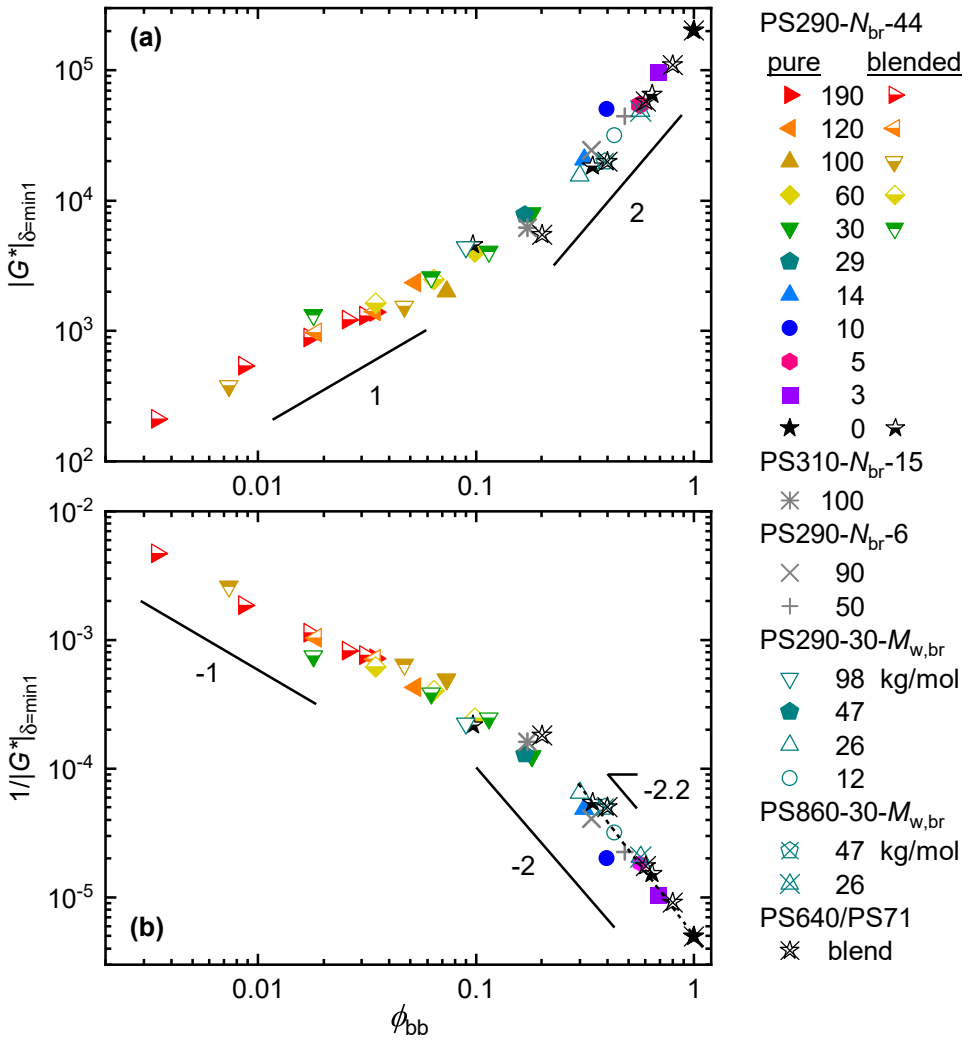

Figure 7.7: Analysis of the vGP plot. **(a)** Complex modulus at the 1st minimum in the low frequency region, $|G^*|_{\delta=min1}$, representing the backbone dilution. **(b)** Inverse of the complex modulus, $1/|G^*|_{\delta=min1}$, as a function of the volume fraction of the backbone, ϕ_{bb}. Experimental data is represented by unblended linear PS290 (★) and its blends with PS44 (☆), as well as and LCB comb PS290 (full symbols, e.g. ▶, etc.), and their blends with PS44 (half symbols, e.g. ◀, etc.); furthermore data of comb PS with barely entangled (✳) and unentangled (× and +) SCB is added.
Data of undiluted linear and comb PS were extracted from the vGP plots in Figure 5.5d, Figure 6.3d and Figure A.2.1d; data of diluted linear and comb PS were exracted from Figure A.2.2d–A.2.6d. For literature comparison, experimental data set from this work was supplemented by data from Kempf[105] (⬟), Qian[299], Trinkle[253] and Roovers[236,328], representing comb PS290 (▽, etc.) and PS860 (⊠, etc.) series with varying $M_{w,br}$ as indicated in [kg/mol], as well as a series of linear-linear blends (✳). Structural parameters ($M_{w,bb}$, N_{br} and $M_{w,br}$) were rounded if necessary to systemize the legend for simplicity and ease of reading; calculations of ϕ_{bb} are based on real, published structural information.

7.4.4 Inverse of the Complex Modulus

Recently, Qian and McKenna[299] further extended the use of the vGP plot in order to investigate the evolution of the local minimum (1st minimum from the terminal regime) and introduced the inverse of the complex modulus, $1/|G^*|_{\delta=min1}$, as a new parameter to provide new insights into the melt properties and compositions of polymers.

For linear polymer systems with only one minimum in the vGP[67], $1/|G^*|_{\delta=\min 1}$ increases with increasing M_w as $1/|G^*|_{\delta=\min 1} \sim M_w$, and becomes constant for high M_w when the chain is well-entangled, i.e. $M_w > M_c$.[68]
Another useful example of the vGP plot is the investigation of polymer ring system dynamics, which are known to lack sufficient entanglement, even at high molecular weights. When using the criteria $1/|G^*|_{\delta=\min 1}$, ring purity can be evaluated via rheology as the value decreases with decreasing linear chain contamination and reaches a plateau[69].[299]

Since (nearly) all synthesized comb PS series, as well as the binary blends of linear and comb PS with PS44 display a pronounced local, 1st minima at low $|G^*|$ as a common feature in the vGP plots (see Appendix A.1.6.1), they present as suitable model systems to examine the relations and scalings of $|G^*|_{\delta=\min 1}$ and its inverse, $1/|G^*|_{\delta=\min 1}$, with increasing dilution.

Figure 7.7 summarizes $|G^*|_{\delta=\min 1}$ and $1/|G^*|_{\delta=\min 1}$ from the vGP topological map of Figure 7.6 as a function of the volume fraction of the backbone, ϕ_{bb}. Both parameters appear to share common power law dependencies and suggest thermorheological independence from topological parameters and blend composition; which is further discussed in the following subsections.

7.4.4.1 Linear-Linear PS Blends

The phase angle of the pure PS290 backbone shows a single minimum at $|G^*| \approx 2 \cdot 10^5$ Pa, corresponding to the plateau modulus of well entangled PS. Aside from this permanent minimum that all binary blends of linear PS290 and PS44 approximately share, another distinct minimum arises that is gradually evolving towards lower $|G^*|$ as the dilution of PS290 progresses and relates to the DTD as a consequence of the solvating effect of relatively fast relaxing short chains.
Previously introduced and denoted as $|G^*|_{\delta=\min 1}$, this parameter extracted from the vGP plots corresponds to the volume fraction of undiluted (★, $\phi_{bb} = 1$) and diluted linear PS290 (✯), as shown in **Figure 7.7a**. Applying the inverse of this parameter, a power law of roughly $1/|G^*|_{\delta=\min 1} \sim \phi_{bb}^{-2}$ is observed, see **Figure 7.7b**. However, if the value at very low dilution of <10 % is not taken into consideration, the inverse of the complex modulus scales with a power law very closely to −2.2, thus quite accurately matching the power law $1/|G^*|_{\delta=\min 1} \sim \phi_{bb}^{-2.24}$ found by McKenna et al.[299] for linear, binary mixtures of PS (✵) with 644 and 71 kg/mol. From the perspective of this large structural difference of both binary blend systems, i.e. PS290/PS44 and PS644/PS71, it is strongly suggested that this power law should be valid over a broad spectrum of blend compositions. Note that their dilution series did also not undercut a concentration of 20 % of high-M_w compound, so this power law seems only to hold for $\phi_{bb} \geq 0.2$, matching my experimental data.

[67] where the 1st minimum equals the global or 2nd one, $|G^*|_{\delta=\min 1} = |G^*|_{\delta=\min 2}$
[68] For linear PS: $1/|G^*|_{\delta=\min 1} \to$ const. $\approx 1/G_N^0 \approx 1/2 \cdot 10^5$ when $M_w \to 60$ kg/mol.[299]
[69] For example, this plateau is observed for a 240 kg/mol ring PS at linear chain contaminations of < 1 %.

From the present data towards $\phi_{bb} < 0.2$, it is assumed that the power law of $1/|G^*|_{\delta=\min 1}$ generally is concentration dependent with two scaling regimes and transitioning from -2 into a slope of about -1 happens below a knee point of $\phi_{bb} \approx 0.2$.

7.4.4.2 Pure Comb PS

The tube dilution of long chains caused by the relaxation of short chains gives the vGP plot its characteristic curve shape with two minima. This DTD mechanism – which has already been extensively discussed from the beginning of this chapter – is not exclusively caused by free chains, but also by segments of chains which influence the relaxation of the larger structure via CLF. Therefore, the vGP plot is not only sensitive to polymer blend compositions but moreover an excellent accessory to rheology for investigating molecular structures.
Analogous to binary blends, the 1st minimum at lower $|G^*|$, i.e. $|G^*|_{\delta=\min 1}$, is sensitive to the individual molecular weights of the chain components that constitute that exact topology. In case of comb-like polymers, those are namely the long backbone and the relatively short branches with $M_{w,bb}$ and $M_{w,br}$, respectively. As a third important influential parameter, the actual weight or volume fraction of each component is then defined by the structural parameter of branching number[70], N_{br}.

With respect to the backbone dilution of comb PS, one remarkably interesting finding illustrated in Figure 7.7b is that $1/|G^*|_{\delta=\min}$ scales with ϕ_{bb}, independently whether the branches are disconnected (i.e. linear-linear blends) or covalently bound to the backbone. Similarly to the binary blends, the structural parameters of comb PS do not matter for the absolute value of the complex modulus as long as the backbone volume fraction is matched. This is supported by further samples found in the literature[299,328], covering a broader spectrum of topological features from long backbones of PS860 and shorter backbones of PS290, both with fixed number of branching of $N_{br} \approx 30$ but variation of the side chain lengths from $M_{w,br} = 12$ to 98 kg/mol.
High dilutions of the backbone with $\phi_{bb} \lesssim 0.2$, corresponding e.g. to combs of the synthesized PS290 series with $N_{br} > 30$, flatten the slope of $|G^*|_{\delta=\min 1}$, approaching a power law of $\sim \phi_{bb}^{-1}$ for the inverse parameter of the complex modulus. The change of the slope from -2 to -1 below such a critical point, $\phi_{bb} < 0.2$, was suggested from the present literature, but there was no further evidence up until now with the confirmation from dynamic-mechanical data of the here synthesized DC and LB PS topologies ranging from $\phi_{bb} \approx 0.2$ to 0.03 ($\widehat{=} N_{br} = 30$ to 190 LCB).

7.4.4.3 Comb-Linear PS Blends

With the investigation of comb-linear blends, the range showing a slope of -1 (with respect to $1/|G^*|_{\delta=\min 1}$, Figure 7.7b) extends to backbone concentrations of as low as 0.25 % ($\phi_{bb} \approx 0.0025$), if 10 % of PS290-190-44 is diluted with 90 % of PS44. From $|G^*|$ of the less diluted backbone of comb PS290-30-44 mixed with only 35 % of side chains, one

[70] since $\phi_{br} = \frac{N_{br}\, M_{w,br}}{M_w}$, and $\phi_{bb} = 1 - \frac{N_{br}\, M_{w,br}}{M_w}$

might expect that comb-linear blends will also obey to a power law of $1/|G^*|_{\delta=\min 1} \sim \phi_{\mathrm{bb}}^{-2}$ for $\phi_{\mathrm{bb}} \gtrsim 0.2$ and therefore be identical in scaling compared to purely linear blends and also unblended comb PS. However, from this point further rheological experiments with binary mixtures of sparsely branched combs and low volume fractions of linear PS will be needed to confirm the assumption.

7.5 Zero-Shear Viscosity

This section explores the melt properties of comb-linear bimodal blends in the framework of the zero-shear viscosity (ZSV), η_0. The dependency of the ZSV with increasing dilution of combs is explored and the scaling is used to try to propose a generalized function to qualitatively describe the η_0 as a function of branching number.

7.5.1 Introduction

Besides reptation, which is the dominant relaxation mechanism of a linear, entangled polymer chain along a tube created by surrounding chains, further chain dynamics like CLF (and under strong flow field also CCR) that contribute to the relaxation have to be considered to fully describe the dynamics of a polymer system in the melt.
Binary blends of linear polymers with distinctively different molecular weights provide simple, useful systems for investigating the effects of CLF on the polymer tube and its dilution.[325]

In Section 5.3.1, the linear viscoelastic properties of the synthesized comb PS290-N_{br}-44 have been investigated and the zero-shear viscosity, η_0, has been analyzed with respect to the total molecular weight of the comb polymer, M_{w}, as illustrated in Figure 5.6. Furthermore, the different scaling laws of η_0 with M_{w} of different conformational regimes were related to the entanglement number of the backbone segments between the branch points, Z_{s}. The change of scaling regimes were discussed with respect to the chain dynamics that retard or expedite the relaxation of comb- and bottlebrush-like topologies, see Section 5.3.1.6.

In this section, the dilution effect of unattached side chains of PS44 on the linear backbone precursor as well as several densely-grafted comb PS of $N_{\mathrm{br}} \geq 30$ is investigated.
Since the zero-shear viscosity is highly molecular weight dependent and scales with $\eta_0 \sim M_{\mathrm{w}}^{3.4}$ for entangled linear polymers, therefore, PS290 and PS44 exhibit distinctively different zero-shear rate viscosities of $\eta_0(\mathrm{PS290}) = 250 \cdot \eta_0(\mathrm{PS44})$. Even though well-entangled, PS44 with significantly lower molecular weight acts as an effective solvent for the former, see dynamic mechanical SAOS data in Figure A.2.6. Additionally, a strong dilution is furthermore found for comb PS blended with PS44, (see Figure A.2.2 to A.2.5).

7.5.2 Results

In order to find a dependency of the zero-shear viscosity value corresponding to the dilution of comb PS, η_0 was plotted against the volume fraction of the backbone, ϕ_{bb}, as seen in **Figure 7.8a**. In the semi-logarithmic plot, η_0 of the blended samples, i.e. linear-linear blends and comb-linear blends with comb PS of $N_{br} \geq 30$, follow an exponential function for η_0, that decreases for each comb sample from the undiluted η_0 value towards $\eta_0(\text{PS44}) = 380\,\text{Pa·s}$, measured at $T_{ref} = 180\,°\text{C}$. At this point it is important to mention that for comb PS with $N_{br} = 3$ to 29, there is no rheological data of blends with PS44. Therefore, it cannot be safely assumed that the (nearly) linear scaling (on the semi-log plot) of η_0 vs. ϕ_{bb} also holds for those. However, to explore the notion of a simple exponential relationship over the whole range of degree of branching and assuming consistency with combs of $N_{br} \geq 30$, that claim is boldly presumed here. It should be kept in mind that a deviation of this idealized dependency is probable, however to be expected within an acceptable margin of error as η_0 of the blends will need to gradually approach η_0(PS44) with increasing dilution, i.e. decreasing ϕ_{bb}. Those errors and their impact on the fittings will be briefly addressed later.

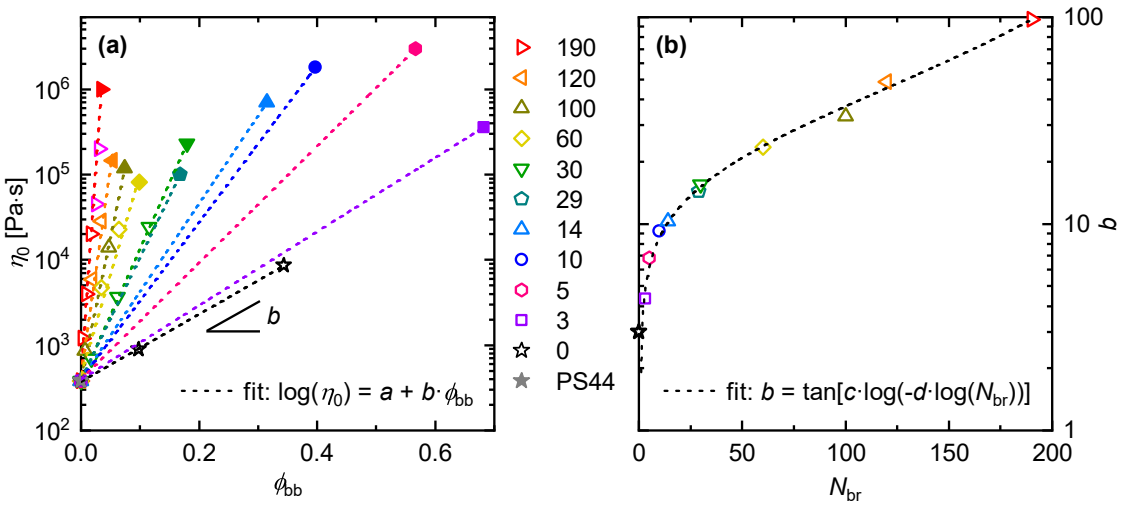

Figure 7.8: **(a)** Zero-shear viscosity, η_0, as a function of backbone volume fraction, ϕ_{bb}, of undiluted comb PS290-N_{br}-44 (filled symbols, ▶, etc.), as well as diluted comb PS with PS44 (half-filled, ▷, etc.). The apparent linear relationsship in the semi-log plot, represented by the proportionality factor b was fitted with an exponential function. **(b)** Proportionality factor, i.e. apparent slope b, as a function of the branching number, N_{br}, fitted with a Bradley-type function (explained in the text).

The numerical value of η_0 of each blend series were fitted with an exponential function, **Equation 7.8**, described by $a \approx 2.58$ as the y-intercept[71], and b as the proportionality factor for each concentration series of comb-linear blend that is shown as apparent slope in the semi-logarithmic graph of Figure 7.8a.

[71] Because $a = \log[\eta_0(\text{PS44})]$ for $\phi_{bb} = 0$; with $\eta_0(\text{PS44}) = 380\,\text{Pa·s}$.

$$\log(\eta_0) = a + b \cdot \phi_{\mathrm{bb}} \tag{7.8}$$

The monotonical increase of the apparent slope of b from linear PS290 to comb PS290 with 190 branches might be expressed furthermore as a function of the branching degree, N_{br}, as subsequently realized in **Figure 7.8b**.
In order to find a proper fit function for the experimental data, the "proportionality factor" b was converted into a "proportionality angle" using the arctangent trigonometric function, $\theta = \arctan(b)$. The shape of the resulting graph (θ vs. N_{br} plot; not shown here) resembled an exponential decay, for which – after testing several fit functions – the Bradley function (double logarithmic reciprocal function)[72], see **Equation 7.9**, deemed the best performing model function with the least number of only two fitting parameters, c and d.

$$y = c \cdot \ln\left(-d \cdot \ln\left(x\right)\right) \tag{7.9}$$

In order to make the Bradley function directly applicable to the fitting of b, **Equation 7.9** consequently was modified with the tangent, giving **Equation 7.10**.

$$b = \tan\{c \cdot \log\left[-d \cdot \log\left(N_{\mathrm{br}}\right)\right]\} \tag{7.10}$$

Figure 7.8b shows that the reciprocal double logarithmic fit function[73] of Bradley-type quite quantitatively describes the dependency of the slope b (that can be imagined as a dilution prefactor in Equation 7.8) with the number of branches.

There are several things to be addressed when using this method. First, the dependency, especially of b vs. N_{br}, is portrayed by a purely empirical fit. Secondly, as mentioned above, already the fit of η_0 vs. ϕ_{bb} must be taken with care, as b for comb-linear blends with $N_{\mathrm{br}} \geq 29$ might follow a different function than the assumed exponential function pretending linearity on the semi-log scale like observed for higher branched comb PS from 30 to 190 branches. Then, it is also possible that this simple exponential is only valid within a certain concentration range. On the other hand, if deviations of the slope from the "ideal apparent linearity" in the semi-log plot occured, they would be of little significance for the parameter fitting of the Bradley-type function in Figure 7.8b, simply because of its logarithmic nature of b (as can be seen from the logarithmic scale of the y-axis). That means, in lack of data of a concentration series, assuming "apparent linearity" for comb-linear blends with $N_{\mathrm{br}} \leq 29$ is a first good assumption as the deviations of b will not significantly affect the shape of the fitted curve. Therefore, the fitting in Figure 7.8b might resulted in similar fitting parameters c and d, even if the η_0 values had a higher deviation.

Interestingly, since the slopes b turn out to be describable with a modified Bradley function, the envelope shape of η_0 of pure comb PS in Figure 7.8a should be qualitatively reproducible.

[72] The Bradley function is found in some literature to empirically fit experimental data that describes an exponential decrease.[329,330]
[73] Fitting parameters applying Equation 7.10: $c = 0.295$, $d = -84840$; $R^2 = 0.9953$.

For fixed molecular weights of backbone and branches, $M_{w,bb}$ and $M_{w,br}$, respectively, the volume fraction of the backbone, ϕ_{bb}, can be expressed as a function of the number of branches, N_{br}, see **Equation 7.11**.

$$\phi_{bb} = \frac{M_{w,bb}}{M_{w,bb} + M_{w,br}\, N_{br}} \tag{7.11}$$

Consequently, if Equation 7.11 and Equation 7.10 is inserted into Equation 7.8, η_0 is then described as a function of the number of branches using the fit parameters c and d in **Equation 7.12**.

$$\log(\eta_0) = a + \tan\{c \cdot \log\left[-d \cdot \log\left(N_{br}\right)\right]\} \cdot \phi_{bb} \tag{7.12}$$

Figure 7.9 plots the ZSV as η_0 vs. N_{br} using Equation 7.12, and compares it with the experimental results of the ZSV (cf. also Figure 5.15). As can be seen, using the comb-linear PS blends to apply fitting functions and determine the respective fit parameters, resulted in finding a combined function that is able to qualitatively describe the envelope of η_0 of the comb PS290 series. It is noteworthy that calculating η_0 of the fit function necessitates to use the exact parameter values for a, c and d, as even a small deviation of e.g. 1 % in c and d drastically changes the shape of the curve, owing to the exponential nature of η_0.

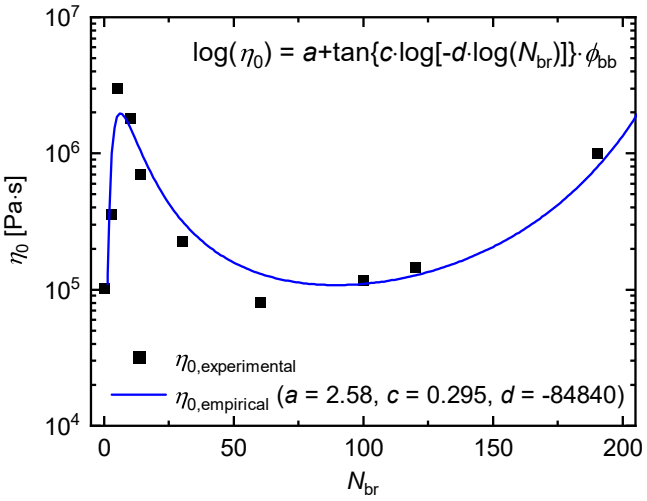

Figure 7.9: Derived Equation 7.12 qualitatively describing the experimental results of the ZSV, η_0, of comb PS290-N_{br}-44 series with respect to the branching number, N_{br}.

It is obvious, that Equation 7.12 only allows a qualitative description of the behavior of η_0, as it simply cannot account for different scaling regimes (see Figure 5.6), that are impossible to simulate with a constantly differentiable function, and based on two fitting parameters (considering $M_{w,bb}$ and $M_{w,br}$ as constant), the course of such a curve is inadequately represented. Moreover, the fit is more or less specific for comb PS290 series with the structural parameters of synthesized backbone and branches with a maximum branching number of 190. It must be expected that η_0 for different structures comprise different

scaling laws. Thus, using the same method with the slope b as determined from the dilutions like shown above, might result in a different dependency with respect to N_{br}. Ultimately, a different fit function other than the modified Bradley-type might then need to be employed.

In this section, the comb-linear PS blends were investigated with the goal of finding relationships of the zero-shear viscosity, η_0, between branching and blending as already shown in the first Figure 7.8a. Even though the following empirical fitting and the qualitative description of η_0 was rather a result of "curiously testing ideas" rather than based on a solid scientific foundation, it should be noted that up to this point experimental η_0 data of comb-linear blends with model structure – especially over such a broad range of braching and dilution – is scarce. However, the linear viscoelastic data already here presented in the framework of η_0 shows the untapped potential of looking closer into the dependencies between branching and blending, and suggests that more research would be needed into a topic for which little can be found in present literature.

It is obvious that both, blending and branching can be practically exploited – also in combination – to tune the melt flow behavior of polymers with respect to achieving certain properties and optimizing processing conditions. Those properties of the melt and their tuning capabilities are not merely limited to linear viscoelastic flow, but can furthermore used when it comes to elongational flow and the balance between viscosity and strain hardening. The latter is addressed now in the closing section of this chapter.

7.6 Uniaxial Extensional Rheology

Whereas the previous sections were focussed on highlighting the linear rheology of comb-linear PS blends in oscillatory shear, this section completes this chapter with the investigation of the melt properties in nonlinear transient elongational flow. Model PS blends of densely grafted combs and loose bottlebrushes with well-entangled, low molecular weight PS were measured with respect to their extensional viscosity. The potential processing performance was assessed in the framework of the strain hardening and compared to their original, unblended parent samples.

7.6.1 Introduction

Branching is known to improve the processing performance of polymers where elongational flows occur. Especially long chain branching has a positive impact on processess that benefit from enhanced melt strength. Strain hardening plays a crucial role in stabilizing thin polymeric film and filament structures in micrometer size dimensions and thus is of fundamental importance in extensional processes like film blowing, foaming,[234,235] or fiber spinning[106]. Commercial LCB polymers of LDPE and LCB-iPP exhibit improved strain hardening (typical values are in the range of SHF = 2–10) when compared with their linear analogues of LLDPE and L-iPP. The investigation of their branched-linear blend properties

is a reoccurring research topic due to their availability and economical importance. In industry, the application of linear or branched polymers and the balance between properties are often assessed based on the balance of performance and economical benefit. In general, high grades of LCB also show the highest melt strength which gradually decreases with blending towards the relatively poor elongational performance of purely linear polymer melt.[14,16,301,331]

However, those commercial LCB not only are highly undefined in structure and may distort the interpretation of rheological measurements due to cristallization effects in e.g. LDPE or iPP, but also even the higher branched grades of LCB polymers have a relatively low branching content, often in the range of 0.1 to 1 LCB per 1000 carbon atoms. Therefore, concluding that more branching will consequently lead to higher strain hardening might only be valid for those low levels of branching degree that do not allow to observe adverse effects when a critical point of too much branch crowding is not reached yet. As already shown in Chapter 5.5 at the example of synthesized model comb PS, at first, branching improved the strain hardening to a maximum of about SHF $\approx$ 200 for comb PS in the high range of densely-grafted comb (DC) conformation with 120 branches, but upon transitioning towards loose bottlebrush-like (LB) conformation around 190 branches, the extensional hardening did suffer significantly.[120,235]

Therefore, blending might be a suitable way to reduce the total branching content of the melt and improve the elongational performance of LCB samples, that otherwise – in their pure state – were negatively affected by the branch point crowding.

7.6.2 Extensional Viscosity of Comb-Linear Blends

Model comb PS290-N_{br}-44 with $N_{\mathrm{br}} = 190$, 120 and 60 LCB exhibited best melt performance in terms of strain hardening in extensional tests as well as low zero-shear viscosity, with their range of branching also enclosing the optimum when it comes to high expandability in batch foam processing (see Section 5.3.2.2). Consequently, those three parent comb PS were also considered the best candidates for a further investigation of model blends in uniaxial elongational flow.

The sample preparation and measurement procedure was kept analogous to the extensional experiments of the pure combs, as reported in Section 5.3.2. The linear viscoelastic properties were already presented in Appendix A.2.2.

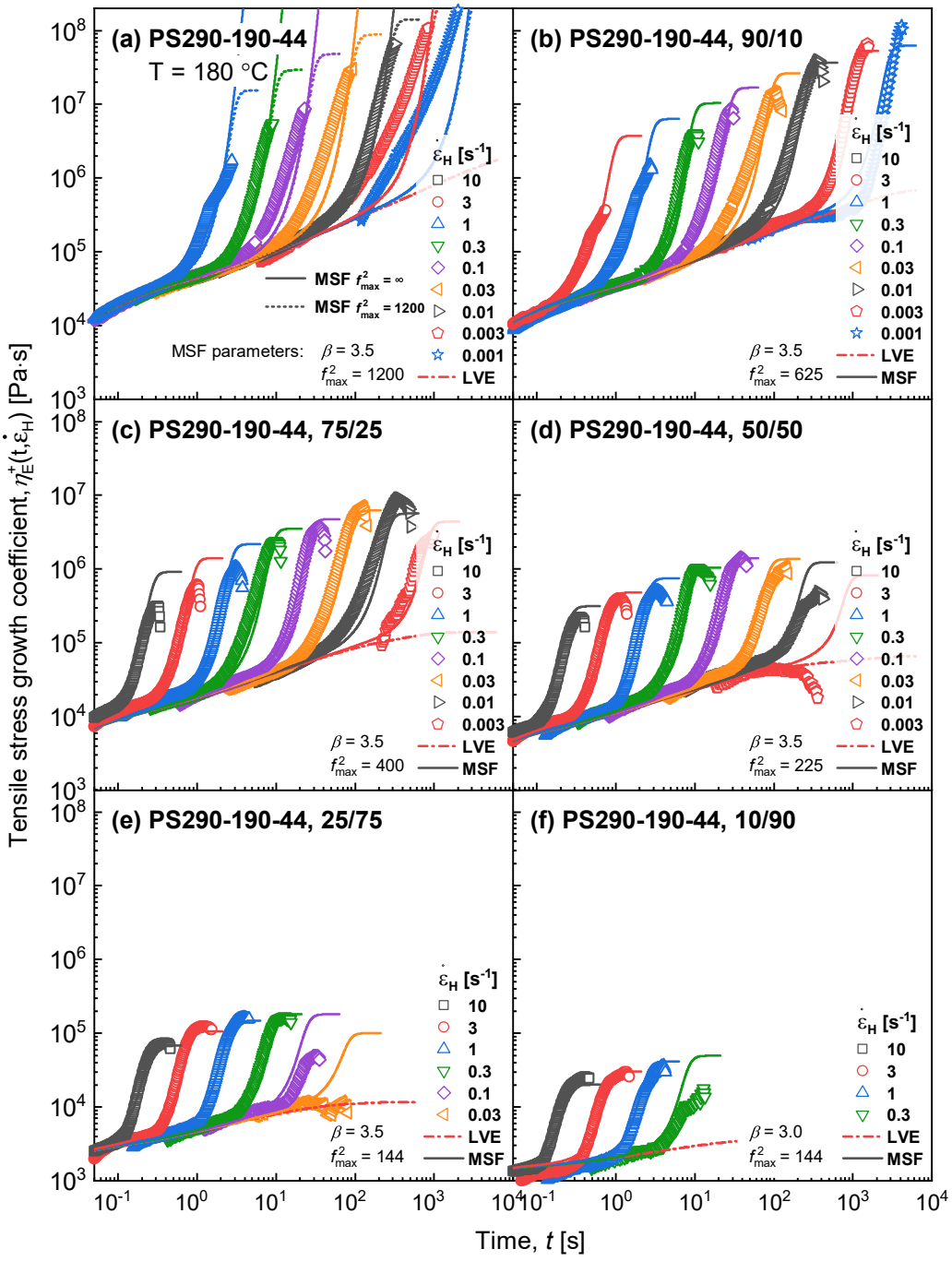

Figure 7.10: Tensile stress growth coefficient data. **(a)** Pure comb PS290-190-44 (cf. Fig. 5.7h). **(b)**–**(f)** Blends of 90 % comb PS mixed with 10 % PS44 (90/10), down to 10% comb PS diluted with 90 % PS44 side chains (10/90).

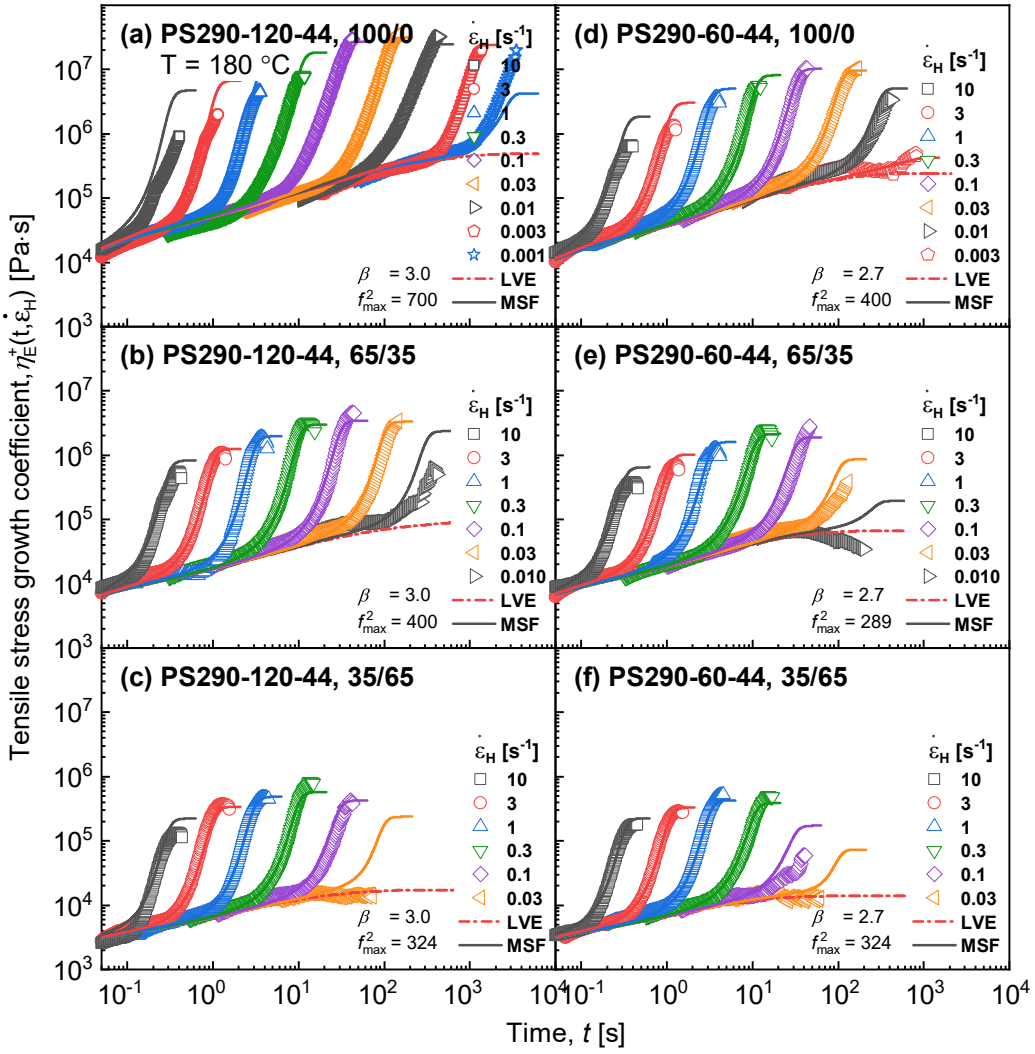

Figure 7.11: Tensile stress growth coefficient data. **(a)** Pure comb PS290-120-44 (cf. Figure 5.7g), and **(b)**–**(c)** blends of 65 % and 35 % mixed with 35 % (65/35) and 65 % (35/65) of PS44, respectively. **(d)** Same for pure comb PS290-60-44 (cf. Figure 5.7f), and **(e)**–**(f)** blends with PS44.

Figure 7.10 displays the extensional viscosity of LB PS290 with 190 branches of 44 kg/mol in the undiluted melt **(a)**, as well as its blends with free side chains of PS44 in declining concentrations from 90–10 % **(b)**–**(f)**. **Figure 7.11** displays the same for DC PS290 with 120 branches **(a)**–**(c)** and 60 branches **(d)**–**(f)**, however at dilutions of 65 and 35 %. A brief comparison of all three concentration series of different combs shows that the capability of achieving strain hardening at low strain rates, $\dot{\varepsilon}_H$, gradually suffers with increasing dilution, with lower branched combs showing even worse performance at long stretching times, t, i.e. low strain rates. The decrease in melt strength at high dilutions seems to be strongly correlated with the total branching amount in the comb-linear blends: the higher the number of branches, the less detrimental is the effect of blending for archieving strain hardening at slow stretch rates. For example, PS290-190-44 with only 25 % of comb fraction still shows strain hardening at extensional rates as low as 0.1 s^{-1}, whereas a blend with 35 % of PS290-60-44 is barely stretchable at the same rate.

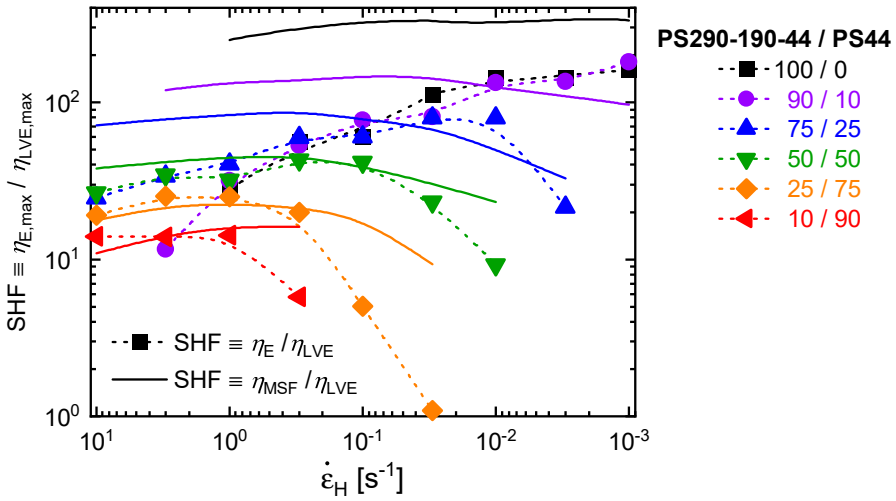

Figure 7.12: Strain hardening factor, SHF, of comb-linear blends of PS290-190-44 with PS44 as a function of extensional rate, $\dot{\varepsilon}_H$, from short times (high strain rates) to long times (low strain rates), following the time order of the extensional data, see Figure 7.10. Symbols are based on the maximum experimentally achieved stress growth coefficient and dashed lines show the general trend as guide to the eye. Solid lines are predictions of the MSF model.

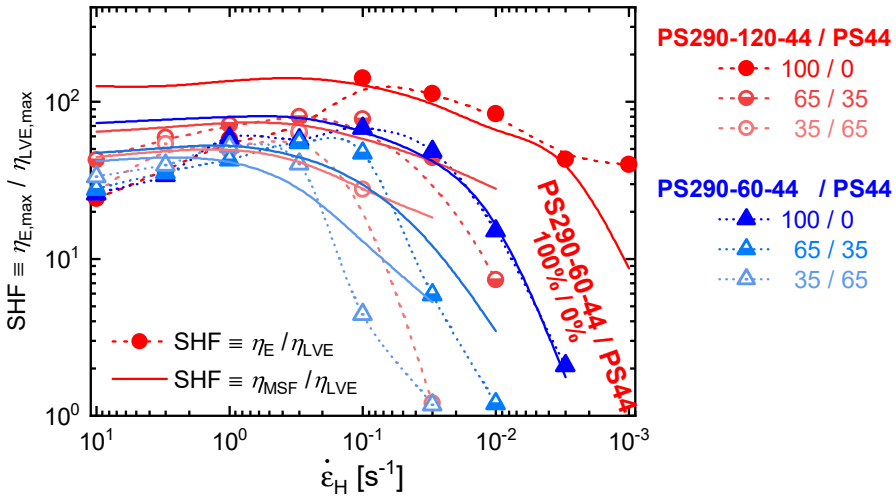

Figure 7.13: Strain hardening factor, SHF, of comb-linear blends of PS290-120-44 and PS290-60-44 with PS44 as a function of extensional rate, $\dot{\varepsilon}_H$, from short times (high strain rates) to long times (low strain rates), following the time order of the extensional data, see Figure 7.11. Symbols are based on the maximum experimentally achieved stress growth coefficient and dashed lines show the general trend as guide to the eye. Solid lines are predictions of the MSF model.

7.6.3 Strain Hardening

Figure 7.12 summarizes the maximum experimentally achieved extensional viscosity of comb-linear blends of PS290-190-44 with PS44 in the framework of the strain hardening factor (SHF). A closer analysis of the SHF reveals that the strain hardening towards higher rates is barely influenced by the plasticizing effect of lower molecular weight PS44. Generally, the SHF values of undiluted PS290-190-44 were also achieved when the branching concentration was lowered by blending. Moreover, diluted samples of 75 % and even only 50 % comb fraction performed better at short times, i.e. high Hencky rates of $\dot{\varepsilon}_H \geq 0.3\,s^{-1}$,

while melts of 100 and 90 % purity, ruptured at early times at the same rates and failed to reach a plateau in the stress growth coefficient data.
Similar behavior was observed for comb-linear blends of 120 and 60 branches with PS44, as further shown in **Figure 7.13**. Purified comb PS290-120-44 clearly outperformed its diluted melts below a strain rate of $\dot{\varepsilon}_H \leq 0.1\,s^{-1}$ with respect to the strain hardening which is well above SHF = 100. Conversely, at faster times, the increase in extensional viscosity relative to the linear viscoelastic envelope is significantly less pronounced owing to premature filament rupture before reaching a steady-state plateau.
In contrast to the combs with a higher branching number, pure PS290-60-44 quite consistently performs best over its blends within the whole range of experimental strain rates, only showing a rather insignificant drop in SHF at rates above $\dot{\varepsilon}_H = 3\,s^{-1}$.

Figure 7.14 replots the SHF data against the volume fraction of the comb, ϕ_{comb}, thus summarizing Figure 7.12 and 7.13. For clarity, only three Hencky strain rates are shown, that is $\dot{\varepsilon}_H = 1\,s^{-1}$, $0.1\,s^{-1}$ and $0.01\,s^{-1}$, serving as representative examples signifying here the transition from rather "higher" to "lower" rates. To compare the strain hardening performance of the pure combs and the blends at different comb concentrations, those rates we intentionally chosen, as the biaxial extensional flow in bubble growth yields strain rates in the range of $0.1–1\,s^{-1}$,[302,303] or even up to $5\,s^{-1}$ depending on the polymer and foaming conditions.[6]

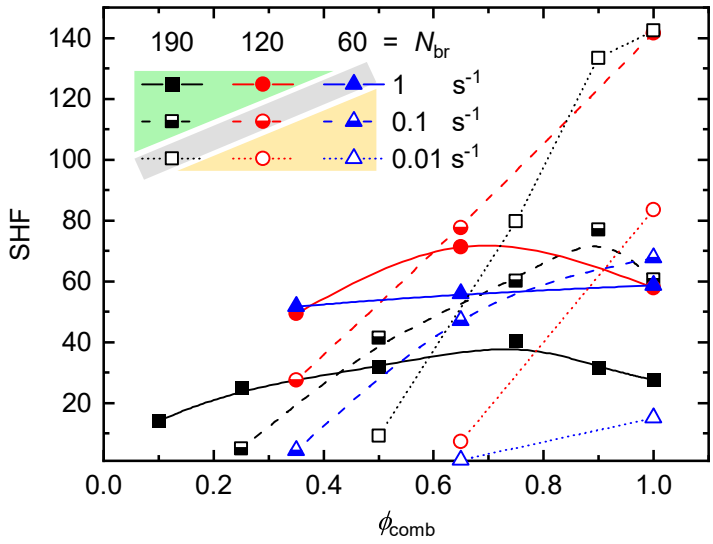

Figure 7.14: Strain hardening factor, SHF, as a function of the comb volume fraction, ϕ_{comb}, in the comb-linear blends of PS290-N_{br}-44 and PS44 for combs with N_{br} = 190, 120 and 60 branches. Full (■, etc.), half-filled (⬓, etc.) and hollow symbols (□, etc.) represent extensional rates of $\dot{\varepsilon}_H = 1\,s^{-1}$, $0.1\,s^{-1}$ and $0.01\,s^{-1}$ respectively. Lines serve as guide to the eye. The grey bar signifies the best performing combination of strain rate and respective branching number regarding undiluted sample, $\phi_{comb} = 1$. The grey bar moreover serves as a criteria: combinations in the left upper corner (green) gain SHF when blended; combinations in the right lower corner (yellow) loose SHF upon blending.

At high rates of $\dot{\varepsilon}_H = 1\,s^{-1}$, comb PS290-190-44 with bottlebrush-like branch density performs poorly compared to dense combs with 120 or 60 branches and can only achieve a maximum SHF around 40 when slightly diluted to a volume fraction of $\phi_{comb} = 0.75$. For a lower branching number of 120, the maximum achievable SHF at the same rate nearly doubles with an optimum SHF ≈ 70 around 2/3rd of comb PS290-120-44 volume vs. PS44 linear chains. At higher dilution, the SHF decreases again for comb PS having half the grafting density. In contrast, PS290-60-44 exhibits consistently high SHF of $55 - 60$ over the whole range of investigated blend composition from $\phi_{comb} = 1$ down to even 0.35.
Whereas moderate blending (ca. 65 %) was beneficial for reaching a maximum in the SHF (slight increase) of combs with the highest and second highest branching number of $N_{br} = 190$ and 120, respectively, at $\dot{\varepsilon}_H = 1\,s^{-1}$, at a lower rate of $0.1\,s^{-1}$ only PS290-190-44 gains a small initial increase in SHF when the concentration of comb PS in the blend is lowered. At this strain rate, both densely grafted combs with $N_{br} = 120$ and 60 already continuously loose melt strength upon dilution.
Conversely to the SHF at rates of $1\,s^{-1}$, at verly low rates of $0.01\,s^{-1}$ the melt strength performance is now reversed, being the highest for 190 branches showing SHF = 140, but below SHF = 20 for 60 branches. At this low strain rate, dilution with linear PS44 has in all cases of comb PS samples a detrimental effect on the SHF.

In the grand scheme, considering undiluted combs with $\phi_{comb} = 1$, at low strain rates (represented by $\varepsilon_H = 0.01\,s^{-1}$) a higher number of branches excels in SHF, but at much higher rates the trend inverts, with lower number of branching outperforming combs which are too densely branched. This is represented by the grey bar in the legend of Figure 7.14, that shows the "sweet spot" of which number of branches, N_{br}, performs best at which strain rate, $\dot{\varepsilon}_H$. Using this as criteria, the findings here can simply be summarized, that more branches and higher strain rates will – to some extent – benefit from blending when it comes to strain hardening. This is indicated by the left upper corner (green). For those combinations, i.e. high $\dot{\varepsilon}_H$ and also high N_{br}, a maximum SHF will only be reached when those comb PS are diluted with PS44.
On the other hand, the lower right corner (yellow) signifies branching and strain rate combinations that will suffer from blending. Low $\dot{\varepsilon}_H$ and also low N_{br} will in any case of dilution drastically have a negative effect on the SHF.
It is important to mention here, that this relation only applies for this comb PS290-N_{br}-44 series within a number of 60 to 190 branches, because reduction of side chains towards more loosely branched structures is accompanied with progressive loss in melt strength when N_{br} falls below this optimum range due to insufficient constrictions and frictional sites imposed by side chains, see also Section 5.3.2.2 and 5.5.
If combs are too highly branched and the melt ruptures before steady flow is observed at short elongational times, reaching the plateau in extensional viscosity might be improved by decreasing the total density of the branches in the melt via blending with lower branched, e.g. linear polymers. This might be a way to get a more pronounced maximum with the occurrence of steady flow for dendrigraft PS comb-like branch-on-branch structures, see Section 6.2.2.2.

It is noteworthy that the linear PS44 fraction in the blends consisted of loose, "unattached" side chains of relatively low molecular weight with only $M_{\mathrm{br}} \hat{=} Z_{\mathrm{br}} \approx 3$ entanglements, compared to the parent backbone PS290 with $Z_{\mathrm{bb}} = 20$. Hence, even though PS44 is considered as well-entangled above M_{c}, from a processing point of view it is by itself – especially in elongational flow – not of any interest due to insufficient melt strength.
That raises the question if blend dilutions of comb PS with even better entangled linear PS (e.g. of backbone-size) might change the situation and give a better improvement in SHF as compared to a non-insignificantly low molecular weight component like PS44. On the contrary, PS44 reduced the viscosity (LVE) in the dimension of one order of magnitude while the sample still shows strain hardening. This might be beneficial in some elongational processes.
The results show that blending provides as a feasible means of lowering the total branching content of the melt and reduces effects originating from side chain crowding that impair elongational properties, while still reaping the melt performance benefits of LCB. In that sense, it is expected, that also the foamability of too highly branched polymers can be improved by reducing the total branching content via blending with linear chains. Vice versa, the elongational properties of polymers with poor melt strength can be significantly enhanced by adding only a small amount of topologies with high branch density, that by themselves exhibit rather bad performance in elongation. Polymer recycling might be one potential field of application.

8 Conclusion and Outlook

Conclusion

Polymeric foams are an important class of materials, mainly serving to save energy and resources. Especially closed cell foams enable to combine insulating properties, as well as light-weight but structurally stable construction with low material input.
Foaming is a highly complex process of bubble nucleation, bubble growth, and finally foam stabilization, each of those influenced by the chemistry and molecular structure of the polymer. The foam morphology and the achievement of low densities, i.e. high volume expansions, is majorly governed in the later phases of bubble growth and cell stabilization. In those phases, the architecture of the polymer and its resulting rheological properties are decisive for the expandability of the foam. Especially long chain branching (LCB) is known to be beneficial for achieving microcellular, low dense foams with small cell sizes (see Chapter 1).
Understanding the polymer's topological influence on the melt properties in the stages of foaming – along with the processing conditions – opens the door to optimize the foam properties towards a certain outcome. However, up to date foaming is exclusively conducted on commercial polymers, that exhibit rather random branching architectures but also have high dispersities as a consequence of the nature of their polymerization methods. Hence, even though their degree of branching can be roughly quantified and compared, the foaming outcome cannot be correlated to specific structural features. When using semi-crystalline polymers, possible crystallization effects may further contribute to the complications in systematically studying the molecular origins of the foam structure.

In this thesis, two different types of model branched architectures with comb and dendrigraft topology were synthesized on the basis of polystyrene, combining anionic polymerization, post-polymerization functionalization and grafting-onto methods (see Chapter 2).
The linear and nonlinear viscoelastic properties in the melt state were analyzed using small amplitude oscillatory shear (SAOS) and uniaxial extensional measurements, respectively. Both techniques are known to be sensitive towards branching and the obtained results provide a deeper understanding of the molecular chain dynamics and relaxation mechanisms in linear, as well as multiply branched polymers (see Chapter 3).
Furthermore, the melt flow properties directly translate to the foaming, where – besides nucleation – shear and elongational flow governs the expandability and cellular morphology of the foam (see Chapter 4). The foaming behavior of the synthesized model branched PS

was investigated using supercritical carbon dioxide ($scCO_2$) as physical blowing agent in low (180 bar) and high pressure (500 bar) batch foaming autoclaves. The resulting foams were analyzed with respect to their macroscopic properties and microscopic cell structures.

On the basis of the systematic variation of the topological features, from loosely to densely grafted comb PS towards bottlebrush-like conformation (see Chapter 5), the final foam characteristics, especially the volume expansion ratio (VER), could be correlated to influential molecular parameters like the number of branches. Moreover, rheology in linear and nonlinear flow proved as powerful tool to understand the melt flow properties and enabled to propose a foaming mechanism that correlates the zero-shear viscosity (ZSV) and the strain hardening factor (SHF) to the expandability of the foam and the resulting foam quality.

Potential improvement in the strain hardening was explored by the synthesis of dendrigraft PS with a comb PS core and a corona of short chain branches (see Chapter 6). Foaming and comparison with the foaming results of LCB and SCB comb PS suggests, that the strain rate is a deciding factors whether the polymer can make use of its strain hardening properties in the bubble growth and cell stabilization phase (see Chapter 6).
In the further scope of the thesis was the rheological investigation of model comb-linear PS blends and the elucidation of the molecular interplay between branched and linear chain. Here, the focus of interest was on the side chain relaxation, the dynamic dilution and the influence of blending on the elongational properties (see Chapter 7).

Synthesis and Characterization

Living anionic polymerization was used to control the structural features like chain lengths and to ensure low dispersities. First, a linear backbone was synthesized and post-polymerization functionalized via Friedel-Crafts (FC) acetylation method. The degree of acetylation (0.5–12 mol%) determined the number of potential branch points. Successive grafting of seperately polymerized side chains onto the acetylated, linear precursor substrate yielded in a comb-like structure with a nearly consistent grafting efficiency of about 60 %.
The first set of model branched PS (named PS290) was a series of comb- and bottlebrush-like topologies having the same backbone ($M_{w,bb}$ = 290 kg/mol) and branch ($M_{w,br}$ = 44 kg/mol) molecular weight, but different number of well-entangled long chain branches (LCB), covering a range from loosely-grafted combs (LC) with only $N_{br} = 3$ side chains to loose bottlebrush (LB) conformation up to 190 side chains.
The second set of investigated structures (named PS310) had a dendrigraft topology and was achieved by another iteration of FC functionalization and grafting-onto. The structural parameters of the comb PS core were similar to the first series, with a backbone of $M_{w,bb}$ = 310 kg/mol and 100 well-entangled LCB of 40 kg/mol. Grafting resulted in a corona of barely entangled short chain branches of about 14 kg/mol. In total, three samples with 120, 240 and 460 second-layer branches were synthesized that are shortly referred to as branch-on-branch (bob) PS.
Additionally, a SCB comb PS was synthesized, resembling the LCB comb precursor, however with the difference that this comb had also only barely entangled side chains of 15 kg/mol.

The comb PS series was molecularly well-characterized using NMR, SEC trace and SEC-MALLS methods, whereas for the dendrigraft PS the gravimetric method was employed to determine the number of braches. All samples of the comb PS series had low dispersities of ($Đ < 1.1$), and also the dendrigraft-type bob PS were still monodisperse ($Đ \approx 1.3$). All samples were perfectly soluble in standard solvents for PS such as THF.

Several concentration series of comb-linear PS blends were made by mixing comb PS with high branch densities ($N_{\mathrm{br}} > 30$) with their ungrafted, linear precursor side chains of the same molecular weight (44 kg/mol).

Correlation of Rheology and Foaming of Model Branched PS

All model branched PS systems were rheologically characterized in SAOS and uniaxial extension. The shear and elongational properties were quantifies in the frameworks of the zero-shear viscosity (ZSV) and the strain hardening factor (SHF) as the main influential parameters on the melt performance in foaming.
Batch foaming of the first set of model branched topologies, i.e. the comb PS290 series, revealed, that a densely grafted comb with 120 LCB achieved a volume expansion ratio (VER) of 40, and therefore expanded to about 90 % close to a theoretical maximum considering the solubility of $scCO_2$ at the foaming conditions of 180 bar and a temperature range between 125–145 °C. Interestingly, the high volume expansion did not compromise in the microcellular structure with respect to the cell size ($\sim$30 µm) or cell density ($\sim 10^9$ cells/cm^3) when compared to comb PS of the same series with lower or higher degree of branching that even showed a lower expandability. Moreover, the positive effect of cell stabilization was closely correlated to the strain hardening behavior of the melt, that was seperately analyzed in uniaxial elongation. The LCB sample with the best foamability also reached a tremendous strain hardening of SHF > 200 at a strain rate of $\dot{\varepsilon}_{\mathrm{H}} = 0.1\,\mathrm{s}^{-1}$. The same sample had also the lowest ZSV. However, this did not turn out as detrimental for bubble growth, even though the ZSV suggests a poor melt strength. From those results it was concluded that in the later stages of foaming, the deformation field mainly is within the nonlinear viscoelastic regime and consequently governed by the strain hardening as the progressive bubble size stretches the cell walls biaxially. Thus, on a molecular level, the polymer gets elongated. In case of strain hardening properties of the melt, the influence of a low ZSV is negligible for the bubble stability as compared to the extensional hardening. The results furthermore suggest, that a minimum ZSV might even expedite the growth of cells from bubble nuclei and benefit the foaming in the early stages.

Further investigations on the correlation between molecular structure and foaming properties were conducted using the second set of synthesized model architectures, comprising LCB and SCB comb PS310 with branches of 40 kg/mol and 15 kg/mol, respectively, as well as the dendrigraft-type bob PS with LCB comb core and SCB corona of $\sim$14 kg/mol. Due to the results of the abovementioned comb PS290 series suggesting an optimum foamability for a branch point spacing of about $Z_{\mathrm{s}} = 0.2$ entanglements at similar chain lengths, this number, converted to approximately 100 branches, served now as a benchmark

for yielding high quality, low dense foams. The molecular parameters, i.e. backbone functionalization, were adjusted accordingly from the synthesis procedure.
At low foaming temperatures (125 °C at 180 bar), the densities of the foams did not differ significantly amongst the synthesized linear, comb or dendrigraft PS topologies, all resulting in a VER ≈ 10. However, in the higher temperature range (> 135 °C), the topology was found to have a rather substantial influence on the foaming result. Whereas linear PS310 did not foam, the volume expansion of all bob PS increased (VER ≈ 20), but was further exceeded by the LCB and even the SCB comb PS (VER = 30–40). The exceptional expandability of all comb PS310 matched the findings in nonlinear rheology, that show high extensional hardening for LCB comb PS310 with SHF = 130 and SCB comb PS310 with SHF = 210. Contrary to the expectations, even though bob PS310 achieved much higher SHF > 200, and even up to 700 at strain rates of $\varepsilon_H = 0.001\,s^{-1}$, the elongational melt strength did not translate to enhanced foamability as compared to the comb polymers. To understand those outcomes – which seem on the first glance to be controversial – the foaming process and its operating conditions have to be taken into consideration. The nucleation in the one-step batch foaming is induced via rapid depressurization and the expanding bubbles create strain rates of $\dot{\varepsilon}_H > 1\,s^{-1}$, stretching the cell walls biaxially. The strain imposed by the expanding gas of course depends on the foaming conditions. The higher the temperature, the lower the viscosity of the sample and therefore, the growing bubbles can grow faster, i.e. impose a higher strain rate on the cell walls.
As obvious from the results, the strain rate matters for making use of the SHF in processing. The SCB comb, even though its side chains are barely entangled, achieves its superior strain hardening (SHF > 200 at $\dot{\varepsilon}_H > 1\,s^{-1}$) at exactly those high rates and therefore is able to sustain cell wall stability. This is further supported by foaming in the high pressure reactor (500 bar) and at even shorter depressurization times ($\sim$1 s), at which the SCB comb consistently performed best at any temperature when it comes to foam expandability.
It should be kept in mind, that this comb also had the lowest zero-shear viscosity, η_0, of all investigated samples (one decade lower than the linear PS310). Obviously, a low η_0 is no exclusion criteria for good foamability, because the importance of extensional hardening outweighs in the nonlinear deformation fields at late bubble growth stages. The possible role of a low η_0 maybe being beneficial for on the foaming at earlier stages is still debatable.

Just as the volume expansion, the strain hardening of bottlebrush-like comb PS was found to be rather low as compared to a less densely grafted comb who showed optimized foamability. It could be shown that upon blending the extensional viscosity was able to reach a steady state plateau and the strain rate dependent strain hardening could be improved, even when only relatively short, side chain-size linear PS was added. In addition to that, combs with lower grafting densities did only benefit from blending when the strain rate was sufficiently high.

Chain Dynamics, Dynamic Dilution and Scaling Laws

Due to the choice of molecular parameters, i.e. distinctively different molecular weights of the backbone and branch components, as well their volume fractions, the relaxation

dynamics found via SAOS could be uniquely assigned to the relaxation of each component. The relaxation of the LCB depend on the SCB's relaxation, for which a scaling law with the dilution exponent being $\alpha = 2.3$ is found and therefore within the expectations that are based on the dynamic tube dilution concept. Further hierarchical relaxation towards the core backbone strongly suggests a scaling law of $\alpha \approx 1$, that interestingly was also found for the backbone dilution of model comb-linear PS blends.

Recent studies of the van Gurp Palmen (vGP) plot found the complex modulus at the phase angle of $\delta = 60°$, $|G^*|_{\delta=60°}$, to be a quantitative criteria of the polydispersity and also branching in polydisperse commercial, as well as monodisperse model systems. Even though this criteria was not applicable for the synthesized model dendrigraft PS in this thesis, the complex modulus at different phase angles, $\delta = 45$–$55°$, did also show a strong quantitative relationship with branching, however in this case correlated to the dilution of the inner LCB by outer SCB.

Apart from the central topic of stuying the structure-property relationship of model branched systems on the foaming, the synthesized set of model comb PS290 series with its broad range of degree of branching from loose comb to loose bottlebrush conformation proved also as a valuable source to highlight further aspects of rheology. Bidisperse comb-linear blends enabled to investigated the interplay between branches and free linear chains in the frameworks of the arm relaxation, the diluted modulus, the complex modulus, the zero-shear viscosity and the strain hardening.

Outlook

From this point, considering an infinite set of possible structural parameters (i.e. $M_{w,bb}$, $M_{w,br}$ and N_{br}), a general statement about the optimum degree of branching for strain hardening and foaming cannot be made. However, in this LCB comb PS series, the foaming efficiency already reached 90 % of the theoretical limit and a further improvement with respect to the volume expansion might not be of benefit, let alone practically feasible. In that sense, shifting the focus on the microscopic properties, i.e. cellular structure and increasing the cell density while decreasing the cell size will be more advantageous. For example, the transition from microcellular foams, characterized by a cell density of between 10^9–10^{12} cells/cm^3, towards nanocellular foams with $>10^{15}$ cells/cm^3 and corresponding cell sizes of <1 µm has a significant impact on the thermal and mechanical properties. At those cell dimensions around 1 µm, the mean free path of the gaseous blowing agent exceeds the diameter of the cell. As a consequence, the cell is barely occupied with gas molecules and the Knudsen effect comes into play, which shows as a sudden drop of the thermal conductivity since the main driver for heat transfer, i.e. the convection due to the gas collision, is significantly impeded, as explained in Section 4.3.2.
In order to reach these effects, the diffusion-controlled nucleation has to be maximized, either by utilizing polymers with substantial blowing agent affinity (e.g. acrylates and fluorinated polymers with CO_2) or the addition of nucleating agents.

Achieving those nanocellular foams but also without excessively compromising on volume expansion is a major challenge with the cell wall thickness and stability as a critical factor. Therefore, the benefits of high strain hardening and its rheological fingerprint on foamability, as shown in this work, will still be of great relevance.

With that respect, blending also comes in as a viable option. As the work here showed, mixing highly branched comb PS (or probably even dendrigraft PS) with even low molecular weight linear chains, offers the benefit to improve the elongational properties at strain rates that are relevant in the bubble growth and stabilization phase of the foaming process. Consequently, it stands to reason to modify the melt properties of such a highly branched polymer matrix with a linear copolymeric system of high blowing agent affinity with potentially gaining or at least not compromising melt strength.

Another topic that deserves attention is the experimental investigation of the rheology of multi-level branched topologies like dendrigrafts, of which still little is known. However, their defined branch-on-branch structure presents as suitable model systems to study the hierarchical relaxation. Also here, the synthesized examples only represent a tiny fraction of possible structural parameters and for sure the tendencies towards optimizing properties, e.g. in strain hardening, are not explored. For example, lowering the branch density of the first grafting layer and conversely increasing it in the second, might be another way for further maximizing the the melt strength in elongational flow. This is probably not restricted to foaming alone, but also other elongational processes – which may even benefit from melt strength at lower strain rates – should be considered as possible fields of application.

Acknowledgements

This PhD thesis, although written in countless nightshifts and in quarantine-like solitude by myself, would not have been possible without the support of people that contributed to and helped me in my scientific work during the daytimes. I want to emphasize that this support happened in the broadest meaning possible and comprises opportunities, scientific enrichment, companionship, financial and emotional support in an environment with people of integrity.

There are so many people for who I feel deep gratitude for reaching this milestone, and I want to specifically acknowledge the following:

Prof. Manfred Wilhelm as my Doktorvater and supervisor for his scientific support, the encouragements, his guidance and ideas, but also the freedom to test own ideas, upon probably one third of this thesis is based. I am thankful for giving me such a multifaceted, challenging topic and I always value his interest in my research, his knowledge, and the sincere and insightful discussions.

Prof. Chul B. Park who accepted me as a visiting Ph.D. student to work in his lab at the University of Toronto. Those months that went by too fast were a truly outstanding experience and surely left a lasting impression. Your group made me immediately feel welcome, so I could enjoy the entirety of my stay in such a pulsating city and in a country that I immediately took into my heard.
In that regard, also thanks to **Dr. Vahid Shaayegan** for your patient help and the time you spent supervising my work and making my stay comfortable. It was great work experience with you.
Special thanks also to the **Karlsruhe House of Young Scientists (KHYS)**, who financially supported my trip with a travel research grant and thus also contributed to an experience that shaped my personality.

Prof. Christopher Barner-Kowollik for borrowing me the 180 bar pressure reactor for so many years. Without it my thesis would only be half as thick. Still works like a charm. Thanks for the trust.

The DECHEMA on behalf of Dr. Mahdi Abbasi for the Max-Buchner research grant. The financial supporting enriched my work with a 600 bar high pressure reactor.

Dr. Mahdi Abbasi and **Dr. Kamran Riazi** who mentored me since this project came to life and started to shape the next years of my scientific endeavour already during my diploma thesis. You supported me in every aspect of my topic and had a major contribution

such as the theoretical model fittings, for which I also received help from **Dr. Masood Khabazian**. Also thanks to **Dr. Miriam Cziep** and **Dr. Michael Kempf** who were the first to introduce me to the anionic synthesis when I was a HiWi or just a greenhorn practical course student in the polymer lab. Thanks also for one or the other sample that enriched my set of data. Moreover, thanks to **Marie-Christin Röpert** for the help on the finish line.

Mrs. Sabine Weiland, **Mrs. Ingrid Zeller** and **Mr. Daniel Zimmermann**, the silent but busy angels who keep the business running for the good of the whole group. I always received immediate help and guidance in issues concerning bureaucracy or infrastructure. I cherish your support that I would miss if you were not here. I guess we too often take it for granted when things go smooth, but probably that's thanks to you.

Dr. Nico Dingenouts for his immensely knowledgeable presence and allround support. I never left a discussion without being smarter – but also at least two hours older.

The Workshop Team and especially **Mr. Jörg Finsterle**, the electrical technician. All of you inexhaustibly repaired and helped improving devices with your skills and expertise.

The whole **Group of Dr. Patrick Théato** for willingly accepting my samples and performing NMR measurements, as well as for further help as lab-neighbors. Special thanks to **Katharina Elies** who always quickly responded when I asked for help or support.

My HiWis, namely **Daniel Döpping**, **Jonas Küng**, **Martin Schäfer**, **Benjamin Schramm** and **Ralf Stüber** for your helping hands in the daily labwork.

Dr. Carlo Botha, **Christian Fengler**, **Dr. Valerian Hirschberg**, **Dr. Christopher Klein**, **Dr. Shouliang Nie** for the unforgettable business trips we did and the rooms or cars we shared while trying hard to not get caught up in unscientific adventure.
Good times. I will always rem amber.

Thanks also to **Dr. Carlo Botha**, **Nonkululeko Radebe** and **Markus Matz** for the unique South African-Palatine vibes in the best office one could imagine. Lovely.

The whole **WiDo Group** thanks for the pleasant and supporting atmosphere in any aspect of the work. All your countless contributions – big or small – added up over time, forming my work and bringing me closer to my goal.

Thanks to all the individuals who proofread and commented on this thesis or helped me with LaTeX, namely **Carlo**, **Christian**, **Christos**, **Jonas**, **Lea**, **Marie**, **Masood**, **Maxi**, **Noni**, **Vale**.

My parents, **my sisters and their families** for the unconditional love, the encouragement, the mental and financial support and for enriching my life.

Shoutout also to the **Walk-In** gym at the KIT and **myprotein** to support muscle protein synthesis after long days of anionic synthesis in the lab.

List of Figures

List of Tables

Bibliography

[1] D. Feldman, *Designed Monomers and Polymers* **2008**, *11*, 1–15.

[2] H. Staudinger, *Berichte der deutschen chemischen Gesellschaft A/B* **1920**, *53*, 1073–1085.

[3] G. Akoval, *Polymers in construction*, Rapra Technology Ltd, Shawbury, **2005**.

[4] *Polymeric foams: Technology and developments in regulation, process, and products*, (Eds.: S.-T. Lee, D. Scholz), CRC Press, Boca Raton, **2009**.

[5] N. J. Mills, *Polymer foams handbook: Engineering and biomechanics applications and design guide*, Butterworth Heinemann, Oxford, **2007**.

[6] *Foam extrusion: Principles and practice*, (Ed.: S.-T. Lee), Technomic Publishing, Lancaster, **2000**.

[7] D. Eaves, *Polymer foams: Trends in use and technology*, Rapra Technology Ltd, Shawbury, **2001**.

[8] R. Gendron, *Thermoplastic foam processing: Principles and development*, CRC Press, Boca Raton, **2005**.

[9] J. M. Dealy, D. J. Read, R. G. Larson, *Structure and Rheology of Molten Polymers: From Structure to Flow Behavior and Back Again*, Hanser Publications, Cincinnati, **2018**.

[10] J. M. Dealy, K. F. Wissbrun, *Melt Rheology and its Role in Plastics Processing: Theory and Applications*, Springer, Boston, **1990**.

[11] C. W. Macosko, *Rheology: Principles, measurements, and applications*, VCH, New York, **1994**.

[12] N. S. Ramesh, S.-T. Lee, *Polymeric foams: Mechanisms and materials*, CRC Press, Boca Raton, **2004**.

[13] P. Spitael, C. W. Macosko, *Polymer Engineering & Science* **2004**, *44*, 2090–2100.

[14] E. Bahreini, S. F. Aghamiri, M. Wilhelm, M. Abbasi, *Journal of Cellular Plastics* **2018**, *54*, 515–543.

[15] G. J. Nam, J. H. Yoo, J. W. Lee, *Journal of Applied Polymer Science* **2005**, *96*, 1793–1800.

[16] J. Stange, H. Münstedt, *Journal of Cellular Plastics* **2006**, *42*, 445–467.

[17] J. Stange, H. Münstedt, *Journal of Rheology* **2006**, *50*, 907–923.

[18] Y. Zhang, P. Tiwary, J. S. Parent, M. Kontopoulou, C. B. Park, *Polymer* **2013**, *54*, 4814–4819.

[19] P. Pötschke, B. Krause, J. Stange, H. Munstedt, *Macromolecular Symposia* **2007**, *254*, 400–408.

[20] A. D. Gotsis, B. L. F. Zeevenhoven, A. H. Hogt, *Polymer Engineering & Science* **2004**, *44*, 973–982.

[21] S. H. Tabatabaei, P. J. Carreau, A. Ajji, *Polymer Engineering & Science* **2010**, *50*, 191–199.

[22] H. E. Naguib, C. B. Park, S.-W. Song, *Industrial & Engineering Chemistry Research* **2005**, *44*, 6685–6691.

[23] L. Wang, D. Wan, J. Qiu, T. Tang, *Polymer* **2012**, *53*, 4737–4757.

[24] A. Wong, Y. Guo, C. B. Park, *The Journal of Supercritical Fluids* **2013**, *79*, 142–151.

[25] A. Rizvi, A. Tabatabaei, P. Vahedi, S. H. Mahmood, C. B. Park, *Polymer* **2018**, *135*, 185–192.

[26] N. Weingart, D. Raps, M. Lu, L. Endner, V. Altstädt, *Polymers* **2020**, *12*, 725.

[27] R. Liao, W. Yu, C. Zhou, *Polymer* **2010**, *51*, 568–580.

[28] R. B. Grubbs, R. H. Grubbs, *Macromolecules* **2017**, *50*, 6979–6997.

[29] K. Ziegler, *Angewandte Chemie* **1936**, *49*, 499–502.

[30] M. Szwarc, M. Levy, R. Milkovich, *Journal of the American Chemical Society* **1956**, *78*, 2656–2657.

[31] M. Szwarc, *Nature* **1956**, *178*, 1168–1169.

[32] R. Quirk in *Handbook of Polymer Synthesis, Characterization, and Processing*, (Eds.: E. Saldívar-Guerra, E. Vivaldo-Lima), John Wiley & Sons, Hoboken, **2013**, pp. 127–162.

[33] PlasticsEurope, Plastics - the Facts 2019, (online; accessed 23. May 2021), `https://rb.gy/dt1sc9`.

[34] H. Frey, T. Ishizone, *Macromolecular Chemistry and Physics* **2017**, *218*, 1700217.

[35] *Applications of Anionic Polymerization Research*, (Ed.: R. P. Quirk), American Chemical Society, Washington, **1998**.

[36] N. Hadjichristidis, A. Hirao in *Anionic Polymerization*, (Eds.: N. Hadjichristidis, A. Hirao), Springer, Tokyo, **2015**.

[37] H. L. Hsieh, R. P. Quirk, *Anionic Polymerization: Principles and Practical Applications*, Chapman and Hall/CRC, Boca Raton, **1996**.

[38] R. J. Young, P. A. Lovell, *Introduction to Polymers, Third Edition*, CRC Press, Hoboken, **2011**.

[39] B. Tieke, *Makromolekulare Chemie: Eine Einführung*, Wiley-VCH, Weinheim, **2014**.

[40] H.-G. Elias, *Makromoleküle: Chemische Struktur und Synthesen*, Wiley-VCH, Hoboken, **2009**.

[41] G. Odian, *Principles of Polymerization*, Wiley-Interscience, New Jersey, **2004**.

[42] Y. Gnanou, M. Fontanille, *Organic and physical chemistry of polymers*, Wiley-Interscience, Hoboken, **2008**.

[43] B. Vollmert, J. X. Huang, *Die Makromolekulare Chemie Rapid Communications* **1981**, *2*, 467–472.

[44] S. Koltzenburg, M. Maskos, O. Nuyken, *Polymer Chemistry*, Springer, Berlin, **2017**.

[45] J. Cowie, V. Arrighi, *Polymers: Chemistry and Physics of Modern Materials*, CRC Press, Hoboken, **2007**.

[46] A. Pagliarulo, L. R. Hutchings, *Macromol. Chem. Phys.* **2018**, *219*, 1700386.

[47] R. P. Quirk, W.-C. Chen, *Die Makromolekulare Chemie* **1982**, *183*, 2071–2076.

[48] R. P. Quirk, W.-C. Chen, *Journal of Polymer Science: Polymer Chemistry Edition* **1984**, *22*, 2993–3000.

[49] M. D. Lechner, K. Gehrke, E. H. Nordmeier, *Makromolekulare Chemie*, Birkhäuser, Basel, **2010**.

[50] W. Lee, H. Lee, J. Cha, T. Chang, K. J. Hanley, T. P. Lodge, *Macromolecules* **2000**, *33*, 5111–5115.

[51] N. Hadjichristidis, *Complex macromolecular architectures: Synthesis, characterization, and self-assembly*, Wiley Interscience, Hoboken, **2011**.

[52] H. Iatrou, J. W. Mays, N. Hadjichristidis, *Macromolecules* **1998**, *31*, 6697–6701.

[53] F. L. Beyer, S. P. Gido, C. Büschl, H. Iatrou, D. Uhrig, J. W. Mays, M. Y. Chang, B. A. Garetz, N. P. Balsara, N. B. Tan, N. Hadjichristidis, *Macromolecules* **2000**, *33*, 2039–2048.

[54] S. Paraskeva, N. Hadjichristidis, *Journal of Polymer Science Part A: Polymer Chemistry* **2000**, *38*, 931–935.

[55] D. Uhrig, J. W. Mays, *Macromolecules* **2002**, *35*, 7182–7190.

[56] J. W. Mays, D. Uhrig, S. Gido, Y. Zhu, R. Weidisch, H. Iatrou, N. Hadjichristidis, K. Hong, F. Beyer, R. Lach, M. Buschnakowski, *Macromolecular Symposia* **2004**, *215*, 111–126.

[57] N. Hadjichristidis, H. Iatrou, M. Pitsikalis, J. Mays, *Progress in Polymer Science* **2006**, *31*, 1068–1132.

[58] A. Hirao, T. Watanabe, R. Kurokawa, *Macromolecules* **2009**, *42*, 3973–3981.

[59] A. Hirao, K. Murano, R. Kurokawa, T. Watanabe, K. Sugiyama, *Macromolecules* **2009**, *42*, 7820–7827.

[60] A. Hirao, K. Murao, A. Abouelmagd, M. Uematsu, S. Ito, R. Goseki, T. Ishizone, *Macromolecules* **2011**, *44*, 3302–3311.

[61] A. Hirao, M. Uematsu, R. Kurokawa, T. Ishizone, K. Sugiyama, *Macromolecules* **2011**, *44*, 5638–5649.

[62] D. Uhrig, J. Mays, *Polymer Chemistry* **2011**, *2*, 69–76.

[63] K. Ratkanthwar, N. Hadjichristidis, S. Lee, T. Chang, Z. Pudukulathan, D. Vlassopoulos, *Polymer Chemistry* **2013**, *4*, 5645.

[64] S. Ito, S. Senda, T. Ishizone, A. Hirao, *Polymer Chemistry* **2016**, *7*, 2078–2086.

[65] S. Ito, R. Goseki, T. Ishizone, A. Hirao, *Polymer Chemistry* **2014**, *5*, 5523.

[66] K. Hong, D. Uhrig, J. W. Mays, *Current Opinion in Solid State and Materials Science* **1999**, *4*, 531–538.

[67] P. J. Lutz, F. Peruch in *Polymer Science: A Comprehensive Reference*, Elsevier, **2012**, pp. 511–542.

[68] J. C. Falk, R. J. Schlott, *Journal of Macromolecular Science: Part A - Chemistry* **1973**, *7*, 1663–1668.

[69] N. Hadjichristidis, J. Roovers, *Journal of Polymer Science: Polymer Physics Edition* **1978**, *16*, 851–858.

[70] K. Adachi, R. Uemura, H. Nishimura, D. Kubota, Y. Tsukahara, *Chemistry Letters* **2017**, *46*, 1027–1029.

[71] P. Jannasch, B. Wesslén, *Journal of Polymer Science Part A: Polymer Chemistry* **1995**, *33*, 1465–1474.

[72] H. Drand, P. Jannasch, B. Wessln, *Journal of Polymer Science Part A: Polymer Chemistry* **1998**, *36*, 803–811.

[73] J. Zhao, G. Mountrichas, G. Zhang, S. Pispas, *Macromolecules* **2009**, *42*, 8661–8668.

[74] T. Altares, D. P. Wyman, V. R. Allen, K. Meyersen, *Journal of Polymer Science Part A: General Papers* **1965**, *3*, 4131–4151.

[75] M. Camps, M. Chatzopoulos, J.-M. Camps, J.-P. Montheard, *Journal of Macromolecular Science Part C: Polymer Reviews* **1987**, *27*, 505–557.

[76] S. Itsuno, K. Uchikoshi, K. Ito, *Journal of the American Chemical Society* **1990**, *112*, 8187–8188.

[77] M. Gauthier, M. Moeller, *Macromolecules* **1991**, *24*, 4548–4553.

[78] M. Gauthier, L. Tichagwa, J. S. Downey, S. Gao, *Macromolecules* **1996**, *29*, 519–527.

[79] R. A. Kee, M. Gauthier, *Macromolecules* **2002**, *35*, 6526–6532.

[80] M. Kempf, V. C. Barroso, M. Wilhelm, *Macromolecular rapid communications* **2010**, *31*, 2140–2145.

[81] J. Li, M. Gauthier, *Macromolecules* **2001**, *34*, 8918–8924.

[82] J. Li, M. Gauthier, S. J. Teertstra, H. Xu, S. S. Sheiko, *Macromolecules* **2004**, *37*, 795–802.

[83] A. Munam, M. Gauthier, *Journal of Polymer Science Part A: Polymer Chemistry* **2008**, *46*, 5742–5751.

[84] M. Gauthier, T. Aridi, *Journal of Polymer Science Part A: Polymer Chemistry* **2019**, *57*, 1730–1740.

[85] D. Rahlwes, J. E. L. Roovers, S. Bywater, *Macromolecules* **1977**, *10*, 604–609.

[86] G. G. Cameron, M. Y. Qureshi, *Die Makromolekulare Chemie Rapid Communications* **1981**, *2*, 287–291.

[87] M. A. Hempenius, W. Michelberger, M. Möller, *Macromolecules* **1997**, *30*, 5602–5605.

[88] X. Guo, R. Farwaha, G. L. Rempel, *Macromolecules* **1990**, *23*, 5047–5054.

[89] A. Iraqi, S. Seth, C. A. Vincent, D. J. Cole-Hamilton, M. D. Watkinson, I. M. Graham, D. Jeffrey, *Journal of Materials Chemistry* **1992**, *2*, 1057.

[90] Q. Sheng, H. D. H. Stöver, *Macromolecules* **1997**, *30*, 6712–6714.

[91] M. Xenidou, N. Hadjichristidis, *Macromolecules* **1998**, *31*, 5690–5694.

[92] R. B. Grubbs, M. E. Broz, J. M. Dean, F. S. Bates, *Macromolecules* **2000**, *33*, 2308–2310.

[93] Z. Yuan, M. Gauthier, *Macromolecules* **2005**, *38*, 4124–4132.

[94] H. Zhang, Y. Li, C. Zhang, Z. Li, X. Li, Y. Wang, *Macromolecules* **2009**, *42*, 5073–5079.

[95] D. A. Tomalia, J. M. J. Fréchet, *Journal of Polymer Science Part A: Polymer Chemistry* **2002**, *40*, 2719–2728.

[96] H. Frey, *Angewandte Chemie International Edition* **1998**, *37*, 2193–2197.

[97] A.-D. Schlüter, C. J. Hawker, J. Sakamoto, *Synthesis of polymers: New structures and methods*, Wiley-VCH, Weinheim, Germany, **2012**.

[98] D. Yan, C. Gao, H. Frey, *Hyperbranched polymers: Synthesis, properties, and applications*, Wiley, Hoboken, N.J, **2011**.

[99] S. J. Teertstra, M. Gauthier, *Progress in Polymer Science* **2004**, *29*, 277–327.

[100] M. Gauthier, *Journal of Polymer Science Part A: Polymer Chemistry* **2007**, *45*, 3803–3810.

[101] J. He, J. Li, S. Yang in *Anionic Polymerization*, (Eds.: N. Hadjichristidis, A. Hirao), Springer, Tokyo, **2015**, pp. 719–752.

[102] B. I. Voit, A. Lederer, *Chemical reviews* **2009**, *109*, 5924–5973.

[103] A. Lederer, W. Burchard, *Hyperbranched Polymers*, Royal Society of Chemistry, Cambridge, **2015**.

[104] D. A. Tomalia, D. M. Hedstrand, M. S. Ferritto, *Macromolecules* **1991**, *24*, 1435–1438.

[105] M. Kempf, D. Ahirwal, M. Cziep, M. Wilhelm, *Macromolecules* **2013**, *46*, 4978–4994.

[106] K. Riazi, J. Kübel, M. Abbasi, K. Bachtin, S. Indris, H. Ehrenberg, R. Kádár, M. Wilhelm, *Polymer* **2016**, *104*, 240–250.

[107] D. M. Knauss, H. A. Al-Muallem, T. Huang, D. T. Wu, *Macromolecules* **2000**, *33*, 3557–3568.

[108] T. A. Osswald, N. Rudolph, *Polymer rheology: Fundamentals and applications*, Hanser Publications, Cincinnati, **2015**.

[109] J. W. Goodwin, R. W. Hughes, *Rheology for Chemists: An Introduction*, 2nd ed., Royal Society of Chemistry, Cambridge, **2008**.

[110] T. Mezger, *The rheology handbook: For users of rotational and oscillatory rheometers*, Vincentz, Hannover, **2020**.

[111] A. Casale, *Polymer Stress Reactions*, Elsevier Science, Oxford, **1978**.

[112] A. J. Malkin, A. I. Isayev, *Rheology: Concepts, methods, & applications*, ChemTec Publishing, Toronto, **2006**.

[113] F. Mainardi, G. Spada, *The European Physical Journal Special Topics* **2011**, *193*, 133–160.

[114] W. P. Cox, E. H. Merz, *Journal of Polymer Science* **1958**, *28*, 619–622.

[115] N. Orbey, J. M. Dealy, *Journal of Rheology* **1991**, *35*, 1035–1049.

[116] M. L. Williams, R. F. Landel, J. D. Ferry, *Journal of the American Chemical Society* **1955**, *77*, 3701–3707.

[117] P. E. Rouse, *The Journal of Chemical Physics* **1953**, *21*, 1272–1280.

[118] F. Bueche, *The Journal of Chemical Physics* **1952**, *20*, 1959–1964.

[119] *Deformation and Flow of Polymeric Materials*, (Eds.: H. Münstedt, F. R. Schwarzl), Springer, Berlin, **2014**.

[120] M. Abbasi, L. Faust, K. Riazi, M. Wilhelm, *Macromolecules* **2017**, *50*, 5964–5977.

[121] H. Y. Song, L. Faust, J. Son, M. Kim, S. J. Park, S.-K. Ahn, M. Wilhelm, K. Hyun, *Polymers* **2020**, *12*, 365.

[122] Z. Dobkowski, *Rheologica Acta* **1995**, *34*, 578–585.

[123] J. F. Vega, S. Rastogi, G. W. M. Peters, H. E. H. Meijer, *Journal of Rheology* **2004**, *48*, 663–678.

[124] H. J. Unidad, M. A. Goad, A. R. Bras, M. Zamponi, R. Faust, J. Allgaier, W. Pyckhout-Hintzen, A. Wischnewski, D. Richter, L. J. Fetters, *Macromolecules* **2015**, *48*, 6638–6645.

[125] L. J. Fetters, D. J. Lohse, D. Richter, T. A. Witten, A. Zirkel, *Macromolecules* **1994**, *27*, 4639–4647.

[126] H. Münstedt, *Elastic behavior of polymer melts: Rheology and Processing*, Hanser Publications, Cincinnati, **2019**.

[127] A. Eckstein, J. Suhm, C. Friedrich, R.-D. Maier, J. Sassmannshausen, M. Bochmann, R. Mülhaupt, *Macromolecules* **1998**, *31*, 1335–1340.

[128] H. Münstedt, F. R. Schwarzl in *Deformation and Flow of Polymeric Materials*, (Eds.: H. Münstedt, F. R. Schwarzl), Springer, Berlin, **2014**, pp. 387–418.

[129] S. F. Edwards, *Proceedings of the Physical Society* **1967**, *92*, 9–16.

[130] P. G. de Gennes, *The Journal of Chemical Physics* **1971**, *55*, 572–579.

[131] M. Doi, S. F. Edwards, *Journal of the Chemical Society Faraday Transactions 2* **1978**, *74*, 1789–1801.

[132] M. Doi, S. F. Edwards, *Journal of the Chemical Society Faraday Transactions 2* **1978**, *74*, 1802–1817.

[133] R. G. Larson, T. Sridhar, L. G. Leal, G. H. McKinley, A. E. Likhtman, T. C. B. McLeish, *Journal of Rheology* **2003**, *47*, 809–818.

[134] T. A. Kavassalis, J. Noolandi, *Macromolecules* **1988**, *21*, 2869–2879.

[135] T. Ge, S. Panyukov, M. Rubinstein, *Macromolecules* **2016**, *49*, 708–722.

[136] T. A. Kavassalis, J. Noolandi, *Macromolecules* **1989**, *22*, 2709–2720.

[137] K. Kremer, G. S. Grest, *The Journal of Chemical Physics* **1990**, *92*, 5057–5086.

[138] S. T. Milner, T. C. B. McLeish, *Physical Review Letters* **1998**, *81*, 725–728.

[139] G. Ianniruberto, G. Marrucci, *Journal of Non-Newtonian Fluid Mechanics* **1996**, *65*, 241–246.

[140] J. Des Cloizeaux, *Europhysics Letters* **1988**, *5*, 437–442.

[141] R. C. Ball, T. C. B. McLeish, *Macromolecules* **1989**, *22*, 1911–1913.

[142] G. Marrucci, *Journal of Polymer Science: Polymer Physics Edition* **1985**, *23*, 159–177.

[143] J. D. Ferry, *Viscoelastic properties of polymers*, John Wiley & Sons, New York, **1980**.

[144] H. Watanabe, *Progress in Polymer Science* **1999**, *24*, 1253–1403.

[145] S. T. Milner, T. C. B. McLeish, *Macromolecules* **1997**, *30*, 2159–2166.

[146] D. R. Daniels, T. C. B. McLeish, B. J. Crosby, R. N. Young, C. M. Fernyhough, *Macromolecules* **2001**, *34*, 7025–7033.

[147] R. G. Larson, *Macromolecules* **2001**, *34*, 4556–4571.

[148] S. J. Park, S. Shanbhag, R. G. Larson, *Rheologica Acta* **2005**, *44*, 319–330.

[149] T. C. B. McLeish, *Advances in Physics* **2002**, *51*, 1379–1527.

[150] C. Das, N. J. Inkson, D. J. Read, M. A. Kelmanson, T. C. B. McLeish, *Journal of Rheology* **2006**, *50*, 207–234.

[151] R. Tanner, E. Tanner, *Rheologica Acta* **2003**, *42*, 93–101.

[152] F. T. Trouton, *Proceedings of the Royal Society of London. Series A Containing Papers of a Mathematical and Physical Character* **1906**, *77*, 426–440.

[153] G. Liu, H. Sun, S. Rangou, K. Ntetsikas, A. Avgeropoulos, S.-Q. Wang, *Journal of Rheology* **2013**, *57*, 89–104.

[154] J. M. Dealy, *Rheology Bulletin* **2010**, *79*, 14–18.

[155] S. Kheirandish, M. Stadlbauer, *Journal of Thermal Analysis and Calorimetry* **2009**, *98*, 629–637.

[156] N. J. Inkson, T. C. B. McLeish, O. G. Harlen, D. J. Groves, *Journal of Rheology* **1999**, *43*, 873–896.

[157] M. H. Wagner, H. Bastian, P. Hachmann, J. Meissner, S. Kurzbeck, H. Münstedt, F. Langouche, *Rheologica Acta* **2000**, *39*, 97–109.

[158] J. Hepperle, H. Münstedt, *Rheologica Acta* **2006**, *45*, 717–727.

[159] C. R. López-Barrón, M. E. Shivokhin, J. R. Hagadorn, *Journal of Rheology* **2019**, *63*, 917–926.

[160] M. H. Wagner, P. Rubio, H. Bastian, *Journal of Rheology* **2001**, *45*, 1387–1412.

[161] M. H. Wagner, M. Yamaguchi, M. Takahashi, *Journal of Rheology* **2003**, *47*, 779–793.

[162] M. H. Wagner, J. Hepperle, H. Münstedt, *Journal of Rheology* **2004**, *48*, 489–503.

[163] M. H. Wagner, J. Schaeffer, *Rheologica Acta* **1992**, *31*, 22–31.

[164] M. Abbasi, N. Golshan Ebrahimi, M. Wilhelm, *Journal of Rheology* **2013**, *57*, 1693–1714.

[165] M. A. Cziep, M. Abbasi, M. Heck, L. Arens, M. Wilhelm, *Macromolecules* **2016**, *49*, 3566–3579.

[166] C. Tropea, J. F. Foss, A. L. Yarin, *Handbook of Experimental fluid mechanics*, Springer, Berlin, **2007**.

[167] P. K. Currie, *Journal of Non-Newtonian Fluid Mechanics* **1982**, *11*, 53–68.

[168] M. Abbasi, N. G. Ebrahimi, M. Nadali, M. K. Esfahani, *Rheologica Acta* **2012**, *51*, 163–177.

[169] V. H. Rolón-Garrido, *Rheologica Acta* **2014**, *53*, 663–700.

[170] M. H. Wagner, S. Kheirandish, O. Hassager, *Journal of Rheology* **2005**, *49*, 1317–1327.

[171] M. H. Wagner, V. H. Rolón-Garrido, J. K. Nielsen, H. K. Rasmussen, O. Hassager, *Journal of Rheology* **2008**, *52*, 67–86.

[172] M. H. Wagner, S. Kheirandish, K. Koyama, A. Nishioka, A. Minegishi, T. Takahashi, *Rheologica Acta* **2005**, *44*, 235–243.

[173] V. H. Rolón-Garrido, M. H. Wagner, *Rheologica Acta* **2007**, *46*, 583–593.

[174] M. H. Wagner, S. Kheirandish, J. Stange, H. Münstedt, *Rheologica Acta* **2006**, *46*, 211–221.

[175] M. H. Wagner, V. H. Rolón-Garrido, *Journal of Rheology* **2008**, *52*, 1049–1068.

[176] H. K. Rasmussen, A. L. Skov, J. K. Nielsen, P. Laillé, *Journal of Rheology* **2009**, *53*, 401–415.

[177] E. Narimissa, M. H. Wagner, *Journal of Rheology* **2016**, *60*, 625–636.

[178] F. N. Cogswell, *Plastics and Polymers* **1968**, *36*, 109–111.

[179] H. Münstedt, *Journal of Rheology* **1979**, *23*, 421–436.

[180] J. Meissner, J. Hostettler, *Rheologica Acta* **1994**, *33*, 1–21.

[181] M. L. Sentmanat, *Rheologica Acta* **2004**, *43*, 657–669.

[182] M. Sentmanat, B. N. Wang, G. H. McKinley, *Journal of Rheology* **2005**, *49*, 585–606.

[183] A. Franck, The ARES-EVF: Option for Measuring Extensional Viscosity of Polymer Melts (PN002), Application Note, TA Instruments, (online; accessed 18. Mar. 2021), `https://rb.gy/to0y9l`.

[184] P. Hodder, A. Franck, *Annual Transactions of the Nordic Rheology Society* **2005**, *13*, 227–232.

[185] A. Bach, H. K. Rasmussen, O. Hassager, *Journal of Rheology* **2003**, *47*, 429–441.

[186] B. Li, W. Yu, X. Cao, Q. Chen, *Journal of Rheology* **2020**, *64*, 177–190.

[187] Markets and Markets, Polymer Foam Market, (online; accessed 18. May 2021), `https://rb.gy/k5dk7n`.

[188] Grand View Research, Polymer Foam Market Size, (online; accessed 18. May 2021), `https://rb.gy/swkvgd`.

[189] Global Market Insights, Metal Foam Market Size, (online; accessed 18. May 2021), `https://rb.gy/8ai4e8`.

[190] D. Eaves, *Handbook of polymer foams*, Rapra Technology, Shawbury, **2004**.

[191] R. Mülhaupt, *Angewandte Chemie International Edition* **2004**, *43*, 1054–1063.

[192] Wikipedia, IG Farben, (online; accessed 04. June 2021), `https://rb.gy/mzn4rb`.

[193] C. G. Munters, J. G. Tandberg, Patent US0020223204, (online; accessed 10. Mai 2021), `https://rb.gy/g4a0wd`.

[194] W. Wang, N. J. Themelis, K. Sun, A. C. Bourtsalas, Q. Huang, Y. Zhang, Z. Wu, *Waste Disposal & Sustainable Energy* **2019**, *1*, 67–78.

[195] GlobeNewswire, Global Polystyrene Industry, (online; accessed 20. May 2021), `https://rb.gy/jq0syz`.

[196] Grand View Research, Expanded Polystyrene Market Size, (online; accessed 18. May 2021), `https://rb.gy/2iicz9`.

[197] D. Weaire, R. Phelan, *Philosophical Magazine Letters* **1994**, *69*, 107–110.

[198] W. Thomson, *Philosophical Magazine* **1887**, *24*, 503–514.

[199] T. Aste, D. L. Weaire, *The pursuit of perfect packing*, Institute of Physics Pub, Bristol, **2000**.

[200] B. Notario, J. Pinto, E. Solorzano, J. A. de Saja, M. Dumon, M. A. Rodríguez-Pérez, *Polymer* **2015**, *56*, 57–67.

[201] G. Wang, J. Zhao, L. H. Mark, G. Wang, K. Yu, C. Wang, C. B. Park, G. Zhao, *Chemical Engineering Journal* **2017**, *325*, 632–646.

[202] C. Forest, P. Chaumont, P. Cassagnau, B. Swoboda, P. Sonntag, *Polymer* **2015**, *77*, 1–9.

[203] J. Martín-de León, V. Bernardo, M. Á. Rodríguez-Pérez, *Materials* **2019**, *12*, 797.

[204] S. Costeux, *Journal of Applied Polymer Science* **2014**, *131*, 41293.

[205] B. P. Jelle, A. Gustavsen, R. Baetens, *Journal of Building Physics* **2010**, *34*, 99–123.

[206] S. Liu, J. Duvigneau, G. J. Vancso, *European Polymer Journal* **2015**, *65*, 33–45.

[207] S. Costeux, L. Zhu, *Polymer* **2013**, *54*, 2785–2795.

[208] S. Costeux, S. P. Bunker, H. K. Jeon, *Journal of Materials Research* **2013**, *28*, 2351–2365.

[209] S. Costeux, I. Khan, S. P. Bunker, H. K. Jeon, *Journal of Cellular Plastics* **2015**, *51*, 197–221.

[210] *Handbook of plastic foams: Types, properties, manufacture and applications*, (Ed.: A. H. Landrock), Noyes Publications, Park Ridge, **1995**.

[211] United Nations., Montreal Protocol on Substances that Deplete the Ozone Layer, (online; accessed 18. Mar. 2021), `https://rb.gy/vbaq50`.

[212] C. Fan, C. Wan, F. Gao, C. Huang, Z. Xi, Z. Xu, L. Zhao, T. Liu, *Journal of Cellular Plastics* **2016**, *52*, 277–298.

[213] S. Yao, T. Guo, T. Liu, Z. Xi, Z. Xu, L. Zhao, *Journal of Applied Polymer Science* **2020**, *137*, 49268.

[214] C. Okolieocha, D. Raps, K. Subramaniam, V. Altstädt, *European Polymer Journal* **2015**, *73*, 500–519.

[215] M. Altan in *Recent Research in Polymerization*, (Ed.: N. Cankaya), InTech, **2018**.

[216] A. N. Spörrer, V. Altstädt, *Journal of Cellular Plastics* **2007**, *43*, 313–330.

[217] A. N. Spoerrer, D. S. Bangarusampath, V. Altstaedt, *Cellular Polymers* **2008**, *27*, 101–121.

[218] S. Ries, A. Spoerrer, V. Altstaedt, *AIP Conference Proceedings of PPS-29* **2014**, 401–410.

[219] M. Rohleder, F. Jakob in *Specialized Injection Molding Techniques*, Elsevier, **2016**, pp. 53–106.

[220] Z. Zhou, J. D. Schultze, J. Springer, *Journal of Applied Polymer Science* **1993**, *47*, 13–20.

[221] F. Esposito, M. A. Del Nobile, G. Mensitieri, G. Astarita, *Industrial & Engineering Chemistry Research* **1996**, *35*, 2939–2945.

[222] J. D. Schultze, Z. Zhou, J. Springer, *Angewandte Makromolekulare Chemie* **1991**, *185*, 265–274.

[223] Y. Sato, M. Yurugi, K. Fujiwara, S. Takishima, H. Masuoka, *Fluid Phase Equilibria* **1996**, *125*, 129–138.

[224] U. A. Handge, V. Altstädt, *Journal of Rheology* **2012**, *56*, 743–766.

[225] T. S. Chow, *Macromolecules* **1980**, *13*, 362–364.

[226] J. S. Colton, N. P. Suh, *Polymer Engineering & Science* **1987**, *27*, 485–492.

[227] J. S. Colton, N. P. Suh, *Polymer Engineering & Science* **1987**, *27*, 493–499.

[228] H.-J. Butt, K. Graf, M. Kappl, *Physics and chemistry of interfaces*, Wiley-VCH, Weinheim, **2003**.

[229] M. Amon, C. D. Denson, *Polymer Engineering & Science* **1984**, *24*, 1026–1034.

[230] S. N. Leung, C. B. Park, D. Xu, H. Li, R. G. Fenton, *Industrial & Engineering Chemistry Research* **2006**, *45*, 7823–7831.

[231] M. Ataei, V. Shaayegan, C. Wang, F. Costa, S. Han, C. B. Park, M. Bussmann, *Journal of Rheology* **2019**, *63*, 895–903.

[232] S. K. Goel, E. J. Beckman, *AIChE Journal* **1995**, *41*, 357–367.

[233] M. Abbasi, L. Faust, M. Wilhelm, *Advanced materials* **2019**, *31*, e1806484.

[234] M. Abbasi, L. Faust, M. Wilhelm, *Polymer* **2020**, *193*, 122351.

[235] M. Abbasi, L. Faust, M. Wilhelm, *Polymer* **2020**, *193*, 122354.

[236] J. Roovers, *Polymer* **1979**, *20*, 843–849.

[237] P. Chambon, C. M. Fernyhough, K. Im, T. Chang, C. Das, J. Embery, T. C. B. McLeish, D. J. Read, *Macromolecules* **2008**, *41*, 5869–5875.

[238] M. Takaki, R. Asami, Y. Kuwata, *Macromolecules* **1979**, *12*, 378–382.

[239] M. Janata, B. Masař, L. Toman, P. Vlček, P. Polická, J. Brus, P. Holler, *Reactive and Functional Polymers* **2002**, *50*, 67–75.

[240] J. Clayden, N. Greeves, S. G. Warren, *Organic chemistry*, Second edition, Oxford University Press, Oxford, **2012**.

[241] B. Hird, A. Eisenberg, *Journal of Polymer Science Part A: Polymer Chemistry* **1993**, *31*, 1377–1381.

[242] Y. Gao, H.-M. Li, *Polymer International* **2004**, *53*, 1436–1441.

[243] M. E. Coustet, M. S. Cortizo, *Polymer Journal* **2011**, *43*, 265–271.

[244] F. Francuskiewicz, *Polymer Fractionation*, Springer, Berlin, **1994**.

[245] B. H. Zimm, *The Journal of Chemical Physics* **1948**, *16*, 1093–1099.

[246] B. H. Zimm, *The Journal of Chemical Physics* **1948**, *16*, 1099–1116.

[247] J. Paturej, S. S. Sheiko, S. Panyukov, M. Rubinstein, *Science advances* **2016**, *2*, 1601478.

[248] W. F. M. Daniel, J. Burdyńska, M. Vatankhah-Varnoosfaderani, K. Matyjaszewski, J. Paturej, M. Rubinstein, A. V. Dobrynin, S. S. Sheiko, *Nature materials* **2016**, *15*, 183–189.

[249] H. Liang, Z. Cao, Z. Wang, S. S. Sheiko, A. V. Dobrynin, *Macromolecules* **2017**, *50*, 3430–3437.

[250] L. Szántó, R. Vogt, J. Meier, D. Auhl, E. van Ruymbeke, C. Friedrich, *Journal of Rheology* **2017**, *61*, 1023–1033.

[251] C. Bailly, V. Stephenne, Z. Muchtar, M. Schappacher, A. Deffieux, *Journal of Rheology* **2003**, *47*, 821–827.

[252] M. van Gurp, J. Palmen, *Rheology Bulletin* **1998**, 5–8.

[253] S. Trinkle, C. Friedrich, *Rheologica Acta* **2001**, *40*, 322–328.

[254] S. Trinkle, P. Walter, C. Friedrich, *Rheologica Acta* **2002**, *41*, 103–113.

[255] J. Hepperle, H. Münstedt, P. K. Haug, C. D. Eisenbach, *Rheologica Acta* **2005**, *45*, 151–163.

[256] N. J. Inkson, R. S. Graham, T. C. B. McLeish, D. J. Groves, C. M. Fernyhough, *Macromolecules* **2006**, *39*, 4217–4227.

[257] M. Ahmadi, S. Pioge, C.-A. Fustin, J.-F. Gohy, E. van Ruymbeke, *Soft matter* **2017**, *13*, 1063–1073.

[258] P. G. Santangelo, C. M. Roland, *Journal of Non-Crystalline Solids* **1998**, *235-237*, 709–716.

[259] C. A. Bero, C. M. Roland, *Macromolecules* **1996**, *29*, 1562–1568.

[260] M. H. Wagner, *Rheologica Acta* **2014**, *53*, 765–777.

[261] Q. Huang, O. Mednova, H. K. Rasmussen, N. J. Alvarez, A. L. Skov, K. Almdal, O. Hassager, *Macromolecules* **2013**, *46*, 5026–5035.

[262] R. Hall, B.-G. Kang, S. Lee, T. Chang, D. C. Venerus, N. Hadjichristidis, J. Mays, R. G. Larson, *Macromolecules* **2019**, *52*, 1757–1771.

[263] V. Hirschberg, M. Wilhelm, D. Rodrigue, *Polymer Testing* **2017**, *60*, 343–350.

[264] V. Hirschberg, L. Schwab, M. Cziep, M. Wilhelm, D. Rodrigue, *Polymer* **2018**, *138*, 1–7.

[265] V. Hirschberg, F. Lacroix, M. Wilhelm, D. Rodrigue, *Mechanics of Materials* **2019**, *137*, 103100.

[266] V. Hirschberg, L. Faust, D. Rodrigue, M. Wilhelm, *Macromolecules* **2020**, *53*, 5572–5587.

[267] R. Verduzco, X. Li, S. L. Pesek, G. E. Stein, *Chemical Society reviews* **2015**, *44*, 2405–2420.

[268] K. A. Arora, A. J. Lesser, T. J. McCarthy, *Macromolecules* **1998**, *31*, 4614–4620.

[269] C. M. Stafford, T. P. Russell, T. J. McCarthy, *Macromolecules* **1999**, *32*, 7610–7616.

[270] H. Janani, M. Famili, *Polymer Engineering & Science* **2010**, *50*, 1558–1570.

[271] T. Otsuka, K. Taki, M. Ohshima, *Macromolecular Materials and Engineering* **2008**, *293*, 78–82.

[272] J. A. Reglero, P. Viot, M. Dumon, *Journal of Cellular Plastics* **2011**, *47*, 535–548.

[273] Y. P. Handa, Z. Zhang, B. Wong, *Macromolecules* **1997**, *30*, 8499–8504.

[274] Y. P. Handa, Z. Zhang, V. Nawaby, J. Tan, *Cellular Polymers* **2001**, *20*, 241–254.

[275] P. Linstrom, NIST Chemistry WebBook, NIST Standard Reference Database 69, **1997**.

[276] W.-C. V. Wang, E. J. Kramer, W. H. Sachse, *Journal of Polymer Science: Polymer Physics Edition* **1982**, *20*, 1371–1384.

[277] A. Kasturirangan, C. A. Koh, A. S. Teja, *Industrial & Engineering Chemistry Research* **2011**, *50*, 158–162.

[278] E. Reverchon, S. Cardea, *The Journal of Supercritical Fluids* **2007**, *40*, 144–152.

[279] R. Li, D. Zeng, Q. Liu, Z. Jiang, T. Fang, *Polymer-Plastics Technology and Engineering* **2015**, *54*, 119–127.

[280] Y. Li, Z. Yao, Z.-h. Chen, K. Cao, S.-l. Qiu, F.-j. Zhu, C. Zeng, Z.-m. Huang, *Chemical Engineering Science* **2011**, *66*, 3656–3665.

[281] M. A. Hempenius, W. F. Zoetelief, M. Gauthier, M. Möller, *Macromolecules* **1998**, *31*, 2299–2304.

[282] E. van Ruymbeke, K. Orfanou, M. Kapnistos, H. Iatrou, M. Pitsikalis, N. Hadjichristidis, D. J. Lohse, D. Vlassopoulos, *Macromolecules* **2007**, *40*, 5941–5952.

[283] J. H. Lee, K. Orfanou, P. Driva, H. Iatrou, N. Hadjichristidis, D. J. Lohse, *Macromolecules* **2008**, *41*, 9165–9178.

[284] E. van Ruymbeke, E. B. Muliawan, S. G. Hatzikiriakos, T. Watanabe, A. Hirao, D. Vlassopoulos, *Journal of Rheology* **2010**, *54*, 643–662.

[285] Q. Huang, S. Costanzo, C. Das, D. Vlassopoulos, *Journal of Rheology* **2017**, *61*, 35–47.

[286] Z. Muchtar, M. Schappacher, A. Deffieux, *Macromolecules* **2001**, *34*, 7595–7600.

[287] M. Schappacher, J. Bernard, A. Deffieux, *Macromolecular Chemistry and Physics* **2003**, *204*, 762–769.

[288] R. A. Kee, M. Gauthier, *Macromolecules* **1999**, *32*, 6478–6484.

[289] M. Gauthier, J. Li, J. Dockendorff, *Macromolecules* **2003**, *36*, 2642–2648.

[290] J. F. Rabek, J. Lucki, *Journal of Polymer Science Part A: Polymer Chemistry* **1988**, *26*, 2537–2551.

[291] J. A. Blanchette, J. D. Cotman, *The Journal of Organic Chemistry* **1958**, *23*, 1117–1122.

[292] W. O. Kenyon, G. P. Waugh, *Journal of Polymer Science* **1958**, *32*, 83–88.

[293] J. Li, C. A. Wilkie, *Polymer Degradation and Stability* **1997**, *57*, 293–299.

[294] A. P. Deshmukh, K. J. Padiya, M. M. Salunkhe, *Journal of Chemical Research* **1999**, 568–569.

[295] H. C. Zhao, J. L. Guo, A. J. Sun, L. L. Gao, *Key Engineering Materials* **2010**, *428-429*, 102–105.

[296] B. Gao, L. Wang, R. Du, *Journal of Macromolecular Science Part A* **2010**, *47*, 927–934.

[297] M. Gauthier, M. Möller, W. Burchard, *Macromolecular Symposia* **1994**, *77*, 43–49.

[298] E. van Ruymbeke, Y. Masubuchi, H. Watanabe, *Macromolecules* **2012**, *45*, 2085–2098.

[299] Z. Qian, G. B. McKenna, *Polymer* **2018**, *155*, 208–217.

[300] F. J. Stadler, J. Kaschta, H. Münstedt, *Macromolecules* **2008**, *41*, 1328–1333.

[301] H. Münstedt, *Polymers* **2021**, *13*, 1123.

[302] Z. Xu, Z. Zhang, Y. Guan, D. Wei, A. Zheng, *Journal of Cellular Plastics* **2013**, *49*, 317–334.

[303] K. Taki, K. Tabata, S.-i. Kihara, M. Ohshima, *Polymer Engineering & Science* **2006**, *46*, 680–690.

[304] X. Chen, J. J. Feng, C. A. Bertelo, *Polymer Engineering & Science* **2006**, *46*, 97–107.

[305] R. Whitfield, N. P. Truong, D. Messmer, K. Parkatzidis, M. Rolland, A. Anastasaki, *Chemical science* **2019**, *10*, 8724–8734.

[306] H. Watanabe, T. Sakamoto, T. Kotaka, *Macromolecules* **1985**, *18*, 1008–1015.

[307] M. J. Struglinski, W. W. Graessley, *Macromolecules* **1985**, *18*, 2630–2643.

[308] W. W. Graessley, M. J. Struglinski, *Macromolecules* **1986**, *19*, 1754–1760.

[309] M. Rubinstein, R. H. Colby, *The Journal of Chemical Physics* **1988**, *89*, 5291–5306.

[310] Juliani, L. A. Archer, *Journal of Rheology* **2001**, *45*, 691–708.

[311] X. Ye, T. Sridhar, *Macromolecules* **2005**, *38*, 3442–3449.

[312] Z. Wang, X. Chen, R. G. Larson, *Journal of Rheology* **2010**, *54*, 223–260.

[313] M. Doi, S. F. Edwards, *The theory of polymer dynamics*, Clarendon Press, Oxford, **2007**.

[314] H. Lentzakis, C. Das, D. Vlassopoulos, D. J. Read, *Journal of Rheology* **2014**, *58*, 1855–1875.

[315] M. Kapnistos, G. Koutalas, N. Hadjichristidis, J. Roovers, D. J. Lohse, D. Vlassopoulos, *Rheologica Acta* **2006**, *46*, 273–286.

[316] H. Watanabe, S. Ishida, Y. Matsumiya, T. Inoue, *Macromolecules* **2004**, *37*, 1937–1951.

[317] A. Miros, D. Vlassopoulos, A. E. Likhtman, J. Roovers, *Journal of Rheology* **2003**, *47*, 163–176.

[318] M. E. Shivokhin, E. van Ruymbeke, C. Bailly, D. Kouloumasis, N. Hadjichristidis, A. E. Likhtman, *Macromolecules* **2014**, *47*, 2451–2463.

[319] P. S. Desai, B.-G. Kang, M. Katzarova, R. Hall, Q. Huang, S. Lee, M. Shivokhin, T. Chang, D. C. Venerus, J. Mays, J. D. Schieber, R. G. Larson, *Macromolecules* **2016**, *49*, 4964–4977.

[320] Q. Huang, L. Hengeller, N. J. Alvarez, O. Hassager, *Macromolecules* **2015**, *48*, 4158–4163.

[321] T. Shahid, Q. Huang, F. Oosterlinck, C. Clasen, E. van Ruymbeke, *Soft matter* **2016**, *13*, 269–282.

[322] H. Liang, B. J. Morgan, G. Xie, M. R. Martinez, E. B. Zhulina, K. Matyjaszewski, S. S. Sheiko, A. V. Dobrynin, *Macromolecules* **2018**, *51*, 10028–10039.

[323] M. Kapnistos, D. Vlassopoulos, J. Roovers, L. G. Leal, *Macromolecules* **2005**, *38*, 7852–7862.

[324] S. J. Park, R. G. Larson, *Journal of Rheology* **2003**, *47*, 199–211.

[325] S. J. Park, R. G. Larson, *Macromolecules* **2004**, *37*, 597–604.

[326] S. G. Hatzikiriakos, *Polymer Engineering & Science* **2000**, *40*, 2279–2287.

[327] J. Liu, W. Yu, C. Zhou, *Journal of Rheology* **2011**, *55*, 545–570.

[328] J. Roovers, W. W. Graessley, *Macromolecules* **1981**, *14*, 766–773.

[329] C. Hui, Z. Xiaoye, L. Ya, *International Journal of Metallurgy and Metal Physics* **2020**, *5*, 58.

[330] J. J. Thevarajah, M. P. van Leeuwen, H. Cottet, P. Castignolles, M. Gaborieau, *International journal of biological macromolecules* **2017**, *95*, 40–48.

[331] D. Ahirwal, S. Filipe, I. Neuhaus, M. Busch, G. Schlatter, M. Wilhelm, *Journal of Rheology* **2014**, *58*, 635–658.

[332] G. Wypych, *Handbook of foaming and blowing agents*, ChemTec Publishing, Toronto, **2017**.

Appendix

A.1 Materials and Methods

A.1.1 Monomer and Solvent Purification

All operations, i.e. polymerization, grafting-onto and Friedel-Crafts acetylation reaction, were carried out under argon protection using standard Schlenk techniques.[36]

A.1.1.1 Monomers

Prior to purification all monomers were degassed by three freezing-evacuation-thawing cycles.

Styrene (Acros, 99 %) was purified by first stirring over calcium hydride (CaH_2, Acros, 93 %), distilled at reduced pressure, and then distilled from di-*n*-butylmagnesium (di-*n*-BuMg; Sigma-Aldrich, 1 M in heptane) into Schlenk-type ampoules. The purified monomer was stored under Argon protection in the refigerator at −18 °C until needed.

A.1.1.2 Solvents

Toluene (Acros, 99.5 %) was refluxed over CaH_2 and then distilled prior to use.

Chloroform ($CHCl_3$; Sigma-Aldrich, 99 %) was dried and stored over molecular sieve (3 Å).

Tetrahydrofuran (THF; Acros, 99 %) was stirred over CaH_2 overnight. After distillation it was refluxed over sodium in the presence of benzophenone as an indicator until a purple color was observed. The required amount of solvent was distilled as needed.

Methanol was degassed prior to terminate living anionic polymerization. It was obtained by three cycles of freezing-evacuation-thawing and afterward kept in a Schlenk-type flask at the high vacuum line until needed.

A.1.2 Synthesis of Monodisperse Comb Polystyrene (Comb PS)

A.1.2.1 Backbone and Side Chain Polymerization

Backbone and side chains of the comb PS series were synthesized separately using anionic polymerization methods. Dried toluene (ca. 600 mL) was distilled into a 1 L Schlenk flask with two stopcocks. Then the flask was directly mounted to the vacuum line and the ampoule containing the purified styrene was mounted onto the second ground joint. After

adding the styrene (10 vol%) to the toluene (90 vol%), the polymerization was initiated by adding *s*-butyllithium (*s*-BuLi, Sigma-Aldrich, 1.4 M in cyclohexane) at room temperature via a syringe. For the PS backbone, after complete conversion of the monomer, the living anions were terminated using degassed methanol and the polymer was then precipitated in excess methanol and dried under vacuum at 70 °C. For the PS side chains, the procedure was similar to that of the backbone polymerization, except that the living anion side chains were kept "alive" for the subsequent grafting reaction onto the carbonyl groups of the functionalized backbone (see next section). However, a small sample of the PS side chains was removed from the flask under argon counterflow using a syringe and then terminated with degassed methanol for the characterization of the molecular weight and dispersity.

A.1.2.2 Acetylation of the Polystyrene Backbone

Carbonyl groups as branching points were introduced to the PS backbone via Friedel-Crafts acetylation of the aromatic rings. Linear PS backbone was acetylated with different degrees of carbonyl groups ranging from 0.1 to 13.0 mol%. Acetyl chloride was used as the acetylation agent. In the following, a typical acetylation reaction is described at the example of 100 branching points on the backbone. PS (5 g, $M_w = 290$ kg/mol) was dissolved in 50 ml of dry chloroform, and then a solution of AcCl (1.14 ml, 1.14 mmol) in 50 ml of chloroform was added. The mixture was stirred at room temperature for 5 h. Afterwards the polymer was precipitated in acidified methanol (500 ml, 7 ml of HCl, 6 M). Residual reaction products were removed by redissolving the polymer in THF and reprecipitating it in methanol. Finally, the functionalized backbone was dried under vacuum at 70 °C. ^{1}H-NMR ($CDCl_3$) was used to quantify the number of acetylated backbone phenyl groups.

A.1.2.3 Grafting-onto Reaction

A 2 l two-neck round-bottomed flask was connected to the vacuum line and charged with the pre-dried, partially acetylated backbone (ca. 5 g) and dry LiCl (5 eq. compared to acetyl groups). After 1 l of dried THF was added and the reagents were dissolved completely, the solution was cooled to approximately −78 °C with an acetone/liquid nitrogen cooling bath. Then, an excess of 1.5 times living PS side chains per acetyl group was slowly added. The temperature was maintained at approximately −78 °C for 30 min. Afterwards the cooling bath was removed and the reaction mixture was allowed to reach room temperature. The reaction was stirred overnight and the residual side chains were terminated with degassed methanol.

A.1.2.4 Precipitation Fractionation

The comb PS were separated from the unreacted side chains by precipitation fractionation in a THF/methanol mixture. Samples were taken from the supernatant and precipitate phases and analyzed via SEC to track the separation quality and progress of the purification. The supernatant phase, containing lower molecular weight side chains, was decanted, and the precipitate phase underwent further precipitation/fractionation steps until SEC confirmed

successful removal of the side chains. The purified comb PS was then dried under vacuum overnight at 70 °C.

A.1.3 Synthesis of Dendrigraft Branch-on-branch Polystyrene (bob PS)

The synthesis of the bob PS series was analogous to the synthetic route of the comb PS series as described in Appendix A.1.2, except that a comb-PS was used as a precursor instead of a linear PS backbone. Another cycle of Friedel-Crafts acetylation and grafting-onto reaction with a second generation of branches was repeated, and the product was precipitation fractionated. The resulting bob PS was dried under vacuum overnight at 70 °C.

A.1.4 Preparation of Comb-Linear PS Blends

Homogenous mixtures of comb and linear PS were prepared by solution blending in THF. Then, the polymer solution was left for several days at room temperature until the majority of the solvent evaporated. The residue was then dried in the vacuum oven by gradually increasing the temperature of the oven well above the T_g of PS (ca. 140 °C), for several days.

A.1.5 Molecular Characterization

A.1.5.1 SEC-MALLS

Comb PS The molecular weights of the backbone, side chains and combs were determined using size exclusion chromatography (SEC; Agilent 1200 series) equipped with multi angle laser light scattering (MALLS; PSS SLD7000/BI-MwA, Brookhaven Instruments) from Polymer Standards Service (PSS, Mainz, Germany). The measurements were conducted phase at 25 °C at flow rate of 1 ml/min using THF as mobile phase. The SEC columns (SDV-Lux-1000 Å and 10^5 Å, 5 µm) were calibrated using linear PS standards ranging from 476 to $2.5 \cdot 10^6$ g/mol. Typically 100 µl of a sample solution with a concentration between 0.7 and 3 mg/mL was injected onto the columns. The absolute weight-averaged molecular weight, M_w, was determined by the MALLS detector. The refractive index increment, dn/dc, was determined in THF using a DnDc2010 (PSS, Mainz, Germany) instrument.

A.1.5.2 ^{1}H-NMR

Proton NMR spectra were used to analyze the degree of functionalization after the FC acetylation and grafting-onto. The ^{1}H-NMR spectra (typically 1024 scans) were measured in deuterated chloroform ($CDCl_3$, Sigma Aldrich) at 25 °C using a 400 MHz Bruker Avance III Microbay specrometer and a 600 MHz Bruker Avance III spectrometer with a cryogenically helium cooled CP TCI probehead.
The peak integrals at $\delta = 2.5$ ppm (s, 3H, CO-CH_3), $\delta = 7.4$–7.7 ppm (m, 2H, benzyl protons *ortho* to acetyl group), and $\delta = 6.2$–7.3 ppm (m, 5H, benzyl protons in nonacetylated aromatic ring and 2H, benzyl protons *meta* to acetyl group) were analyzed to calculate

the average number of carbonyl groups (acetylated aromatic rings) per backbone, using Equation 5.7 from the ratio of the peak integrals as shown in Figure 5.3a.
Furthermore, the number of branches per comb molecule was determined via NMR, analyzing the relevant peak integrals after the grafting (Figure 5.3b) as well as before the grafting (described above, Figure 5.3a) and using Equation 5.9.

A.1.5.3 Scaling Analysis

Table A1: General criteria to categorize structural characteristics of comb and bottlebrush polymers according to grafting density, z_g, or number of entanglements per backbone segment, Z_s. Conformational regimes were summarized using the scaling analysis by Sheiko et al.[247–249]

Conformational regime	Grafting density [a]	Segment entanglement number [b]
Loose comb (LC)	$z_g < \frac{1}{n_{br}}$	$Z_{br} < Z_s$
Dense comb (DC)	$\frac{1}{n_{br}} < z_g < \frac{(b\,l)^{3/2}}{\nu\, n_{br}^{1/2}}$	$\frac{(Z_{br}/n_e)^{1/2}\,\nu}{(b\,l)^{3/2}} < Z_s < Z_{br}$
Loose bottlebrush (LB)	$\frac{(b\,l)^{3/2}}{\nu\, n_{br}^{1/2}} < z_g < \frac{b\,l^2}{\nu}$	$\frac{\nu}{n_e\, b\, l^2} < Z_s < \frac{(Z_{br}/n_e)^{1/2}\nu}{(b\,l)^{3/2}}$
Dense bottlebrush (DB)	$\frac{b\,l^2}{\nu} < z_g$	$\frac{1}{n_e} < Z_s < \frac{\nu}{n_e\, b\, l^2}$ [b]

[a] Number of branches per backbone monomer: $z_g = N_{br}/n_{bb}$.
[b] Number of entanglements between two branch points: $Z_s = Z_{bb}/(N_{br}+1)$.
[c] For PS: density $\rho = 0.909\,\mathrm{g/cm^3}$, $M_0 = 104.15\,\mathrm{g/mol}$, $M_e = 14.5\,\mathrm{kg/mol}$, excluded volume $\nu = 0.19\,\mathrm{nm^3}$, Kuhn length $b = 1.8\,\mathrm{nm}$, persistence length $C_\infty = 9.5$ and $l = b/C_\infty = 0.19\,\mathrm{nm}$.

Table A2: Specific criteria to categorize comb PS290-N_{br}-44 series, applying scaling analysis from **Table A1**.

Loose comb PS LC-PS	Dense comb PS DC-PS	Loose bottlebrush PS LB-PS	Dense bottlebrush PS DB-PS
$Z_s > 3$	$3 \geq Z_s \geq 0.14$	$0.14 \geq Z_s \geq 0.021$	$0.021 \geq Z_s \geq 0.007$
$N_{br} < 6$	$6 \leq N_{br} \leq 142$	$142 < N_{br} < 951$	$951 < N_{br} < 2783$
$1 \geq \phi_{bb} > 0.14$	$0.14 \geq \phi_{bb} \geq 0.045$	$0.045 \geq \phi_{bb} < 0.007$	$0.007 < \phi_{bb} < 0.0024$

[a] Number of branches per backbone monomer: $z_g = N_{br}/n_{bb}$.
[b] Number of entanglements between two branch points: $Z_s = Z_{bb}/(N_{br}+1)$.

A.1.6 Rheological Characterization

Rheological measurements were performed on an ARES-G2 rheometer from TA Instruments. The disk-shaped samples for SAOS measurements (1 mm thickness) as well as rectangular-shaped films ($17 \times 10\,\mathrm{mm^2}$ and 0.5–0.8 mm thickness) for extensional experiments were press-molded in a hot press (Weber, PW 20) under vacuum at 180 °C for 15 min.

A.1.6.1 Small Amplitude Oscillatory Shear (SAOS)

Small amplitude oscillatory shear measurements were conducted between 130 °C to 240 °C under nitrogen flow using a parallel plate geometries with diameters of $d = 8$, 13 and 25 mm, and a gap of $h \approx 1$ mm. The strain amplitude ranged from $\gamma_0 = 0.01$ to 0.25 and the angular frequency ranged from $\omega = 0.01$ to 100 rad/s. The master curves were obtained by time-temperature superposition (TTS) using 180 °C as the reference temperature.

A.1.6.2 Uniaxial Extension

Uniaxial extensional experiments were conducted under nitrogen flow using an extensional viscosity fixture (EVF, TA Instruments) at extensional rates between $\dot{\varepsilon} = 10^{-3}$ and $10\,\mathrm{s}^{-1}$. A rectangular sample was quickly attached to the preheated drums of the EVF in the nitrogen gas purged convection oven at 180 °C. Prestretch of the sample was applied if needed to correct minor sagging effects, especially at short rates and for low viscosity samples. Each experiment was repeated if a discrepancy was observed between the stress growth coefficient at early stage of stretching (Hencky strain $\varepsilon_\mathrm{H} < 1$) and the linear viscoelastic predictions from the Maxwell model fitted to the SAOS data (G' and G'') using relaxation spectra g_i and τ_i, with $\eta_\mathrm{E}^+(t) = 3\,\Sigma_{i=1}^{N}\, g_i\tau_i(1 - \exp(-t/\tau_i))$.

A.1.7 Foaming Experiments

A.1.7.1 Foaming Experiments

Disk-shaped test specimen for foaming ($\varnothing = 10$ mm, $d = 2$ mm) were hot-pressed under vacuum. First, the sample-filled mold was heated up to 150 °C for 10 min and then to 180 °C for another 10 min until a force of 5 kN was applied and subsequently the mold was slowly cooled down to room temperature.
Batch foaming experiments were performed under supercritical condition with CO_2 as the foaming agent, using 2 different types of autoclave systems as described in the following. Pictures of the hardware can be found in Appendix A.3.

180 bar Pressure Reactor Foaming experiments at a saturation pressure of 180 bar were conducted in a standardized stirred mini benchtop reactor (Parr Instrument, Type 4560 with $V = 300$ mL and $p_\mathrm{max} = 200$ bar, SOLO 4848 temperature controller), see Figure A.3.1. For the experiments the stirring rod was dismounted. The CO_2 was supplied by dry ice. In order to do so, samples were perforated and hooked onto a wire inside the pressure vessel. Then the reactor was filled with crushed dry ice and the lid was tightly closed. The reactor was heated up until the desired saturation temperature (125 to 145 °C) was reached, while the pressure was manually controlled by a needle valve. After a saturation time of 4 h the needle valves were rapidly opened and the CO_2 released with an average depressurization rate of about 40 bar/s.

500 bar Pressure Reactor Foaming experiments at a saturation pressure of 500 bar were performed in a standardized, custom-modified high pressure reactor (HPR-Series with

$V = 100\,\text{mL}$ and $p_{max} = 690\,\text{bar}$, Supercritical Fluid Technologies) with an on-off ball valve for fast pressure release. The reactor was connected to a supercritical fluid pump (SFT-10, Supercritical Fluid Technologies) that was supplied by a $scCO_2$ gas cylinder with a standpipe (Air Liquide, 99.7 vol%), see Figure A.3.2. The samples were placed into small aluminium cups which were stacked inside the reactor cylinder. After closing the lid, the reactor was filled with CO_2 at a flow rate of 10 mL/min. After a saturation time of 4 h the ball valve was opened and within about 2 s immediately depressurized to induce foaming nucleation.

A.1.7.2 Foam Analysis

Foam Density The densities of the foams were measured by the principle of buoyancy using a density kit (YDK 01-0D, Sartorius) on the balance with the weight of the foam in air, m_f, the apparent weight of the foam immersed in water, m_{f,H_2O}, and the density of the water, ρ_{H_2O}:

$$\rho_f = \frac{m_f \cdot \rho_{H_2O}}{m_f - m_{f,H_2O}} \tag{A.1}$$

Volume Expansion Ratio (VER) The volume expansion ratio of the foam, i.e. the factor of the increase in volume compared to the unfoamed specimen, is calculated by the ratio of the unfoamed (ρ_p) to the foamed (ρ_f) sample density:

$$\text{VER} = \frac{\rho_p}{\rho_f} \tag{A.2}$$

Cell Morphology To reveal the inner cell structure of the foamed specimen, samples were immersed in liquid nitrogen for 10 min and then fractured. Characterization of the foams was done by scanning electron miscroscopy (SEM, S5-70 with hard- and software update for digital imaging, Hitachi) after sputtering (SCD040, Bulzers Union) with gold (ca. 5 nm).
The SEM micrographs were analyzed manually using an image processing program (ImageJ).

Cell Density The number of cells n_{cell} per image area A was counted from an image with appropriate magnification (usually $200 - 800$ cells/image). The cell density, N_{cell}, as number of cells per unit volume of $1\,\text{cm}^3$ with respect to the unfoamed neat polymer, was calculated using the following equation:

$$N_{cell} = \left(\frac{n_{cell}}{A}\right)^{3/2} \cdot \text{VER} \tag{A.3}$$

Cell Size The average cell diameter (size), D [µm], can be calculated from:

$$d_{cell} = 10^4 \left(\frac{6 \cdot (\text{VER} - 1)}{\pi N_{cell}}\right)^{1/3} \tag{A.4}$$

Alternatively, the diameters d over a sample size of $n \approx 50$–100 cells were measured and the average cell size d_{cell} was calculated by the arithmetic mean:

$$d_{\text{cell}} = \frac{\sum_{i=1}^{n} d_i}{n} \tag{A.5}$$

Cell Wall Thickness The average cell wall thickness, δ_{wall} can be calculated from the following equation:[332]

$$\delta_{\text{wall}} = d_{\text{cell}} \times \left(\frac{1}{\sqrt{1 - \rho_{\text{f}}/\rho_{\text{p}}}} - 1 \right) \tag{A.6}$$

where d_{cell} is the average cell size and $\rho_{\text{f}}/\rho_{\text{p}}$ the inverse of the VER (see Equation A.2).

A.2 Additional Experimental Data

In the following section, the rheological data of comb PS and comb-linear PS blends in small amplitude oscillatory shear (SAOS) is presented.

For a further description of the graphical methods with which the investigated rheological parameters (arm relaxation time, τ_a; diluted modulus, $G^0_{N,s}$; complex modulus, $|G^*|$) were extracted, the reader is referred to Figure 5.5.

A.2.1 Comb PS290-N_{br}-6 Series

Comb PS290-N_{br}-6 (see Table 5.1) provided additional rheological data of the dilution effect of unentangled SCB (Fig. A.2.1).

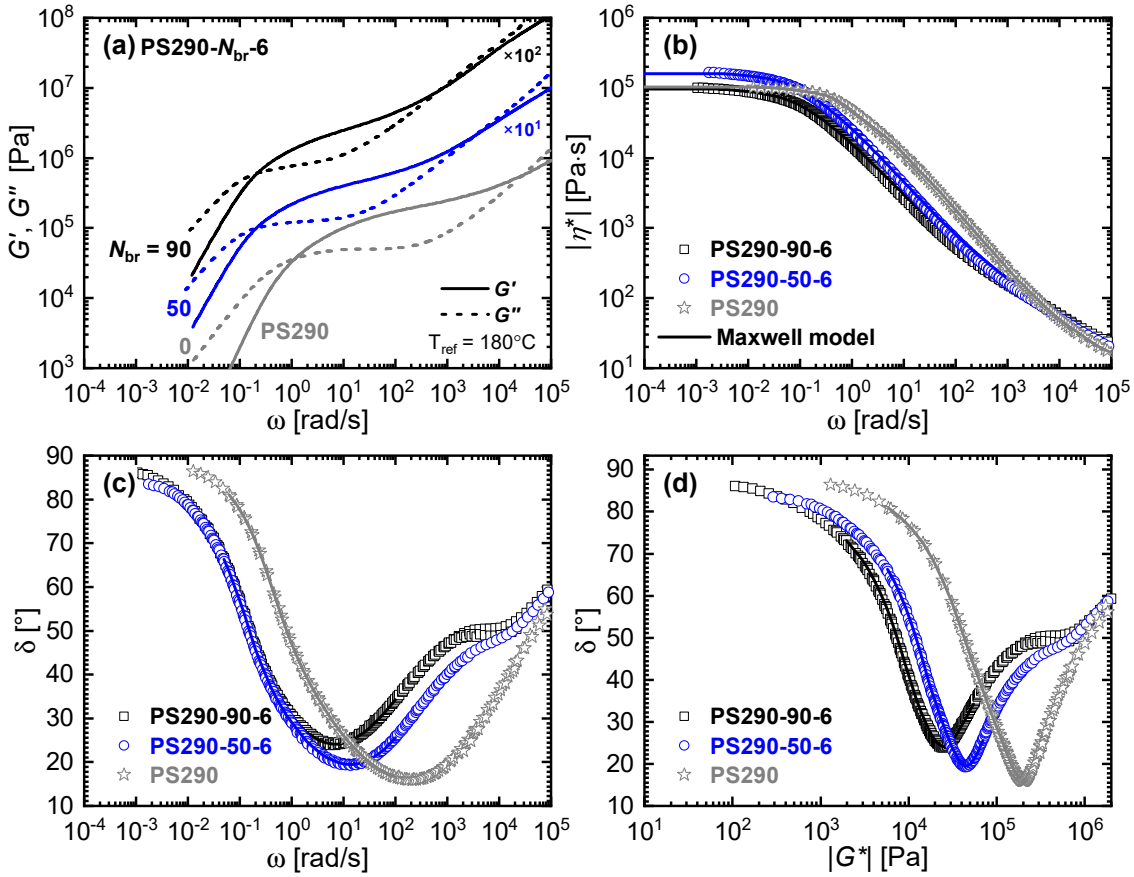

Figure A.2.1: LVE mastercurves from SAOS data of comb PS290-N_{br}-6 series with $N_{br} = 90$ and 50 SCB of $M_w = 6$ kg/mol, as well as the linear backbone precursor PS290. **(a)** Storage, G', and loss modulus, G''. **(b)** Complex viscosity, $|\eta^*|$, with Maxwell model fitting (solid lines) to obtain the zero shear viscosity, η_0 at $|\eta^*|_{\omega\to 0}$. **(c)** Phase angle, δ, vs. angular frequency, ω. **(d)** vGP plot, i.e. δ vs. complex modulus, $|G^*|$, with solid lines being DFS data directly obtained at $T_{ref} = 180\,°C$.

A.2.2 Comb PS290-N_{br}-44 Series

Comb PS290-N_{br}-44 with N_{br} = 190, 120, 60, 30 and 0 (i.e. linear backbone PS290) were blended with PS44 in various concentrations (Figure A.2.2 to A.2.6).

A.2.2.1 Comb-Linear Blends of PS290-190-44 and PS44

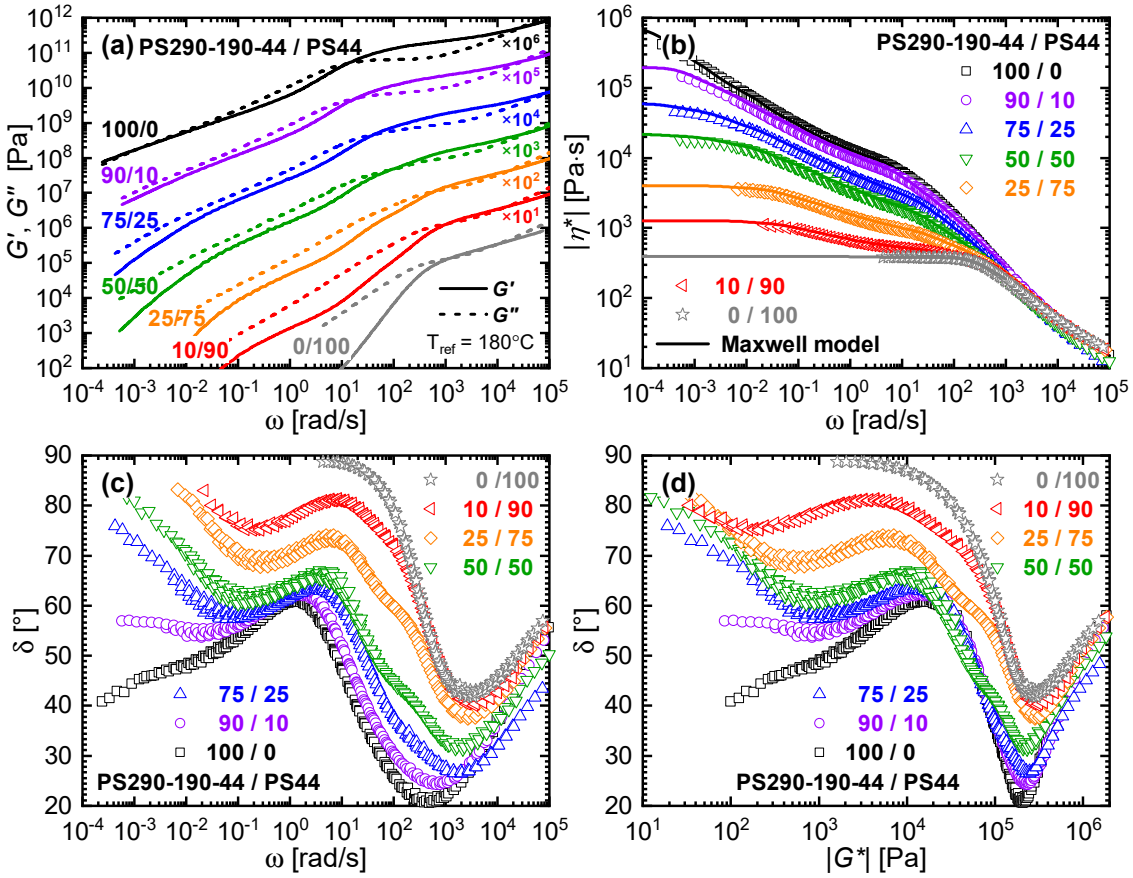

Figure A.2.2: LVE mastercurves from SAOS data of comb PS290-190-44 blended with PS44. The indicated blend composition is in percentage [%]. **(a)** Storage G' and loss modulus G''. **(a)** Storage, G', and loss modulus, G''. **(b)** Complex viscosity, $|\eta^*|$, with Maxwell model fitting (solid lines) to obtain the zero shear viscosity, η_0 at $|\eta^*|_{\omega\to 0}$. **(c)** Phase angle, δ, vs. angular frequency, ω. **(d)** vGP plot, i.e. δ vs. complex modulus, $|G^*|$, with solid lines being DFS data directly obtained at T_{ref} = 180 °C.

A.2.2.2 Comb-Linear Blends of PS290-120-44 and PS44

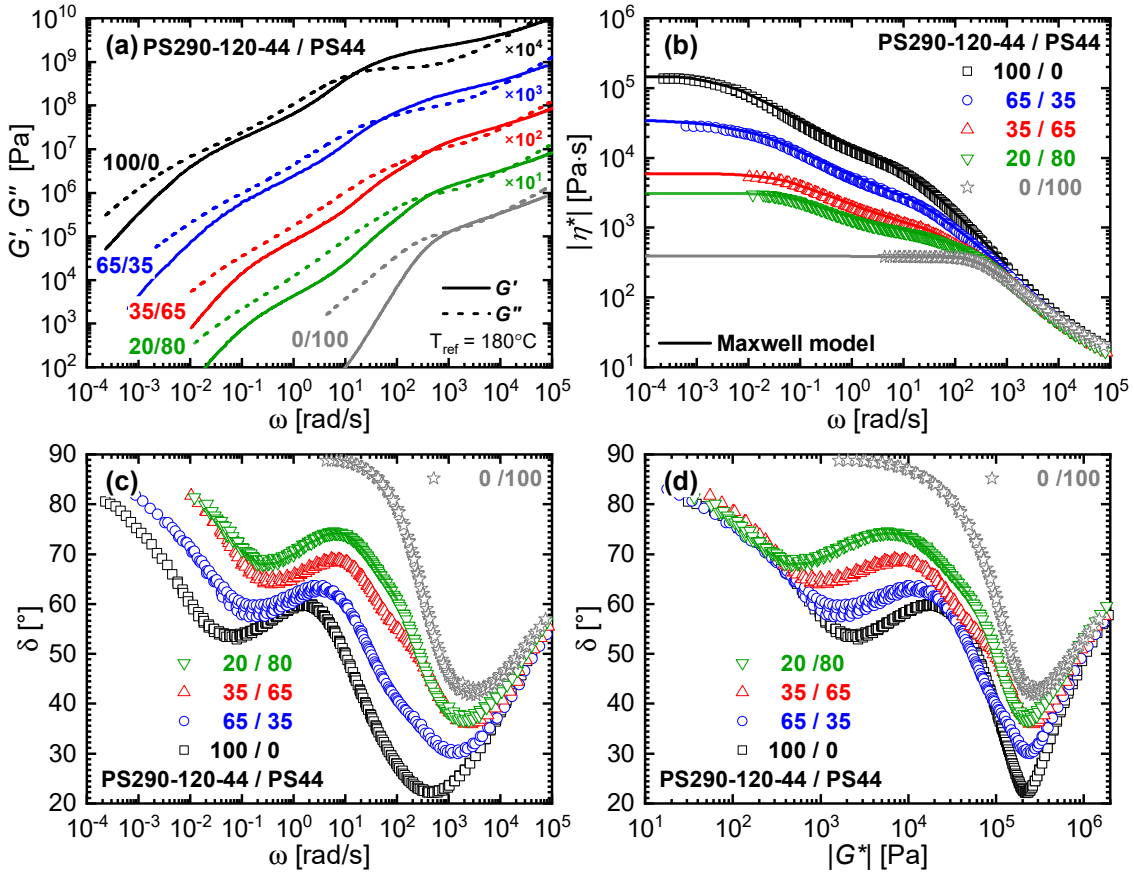

Figure A.2.3: LVE mastercurves from SAOS data of comb PS290-120-44 blended with PS44. The indicated blend composition is in percentage [%]. **(a)** Storage, G', and loss modulus, G''. **(b)** Complex viscosity, $|\eta^*|$, with Maxwell model fitting (solid lines) to obtain the zero shear viscosity, η_0 at $|\eta^*|_{\omega\to 0}$. **(c)** Phase angle, δ, vs. angular frequency, ω. **(d)** vGP plot, i.e. δ vs. complex modulus, $|G^*|$, with solid lines being DFS data directly obtained at $T_{\mathrm{ref}} = 180\,^{\circ}\mathrm{C}$.

A.2.2.3 Comb-Linear Blends of PS290-60-44 and PS44

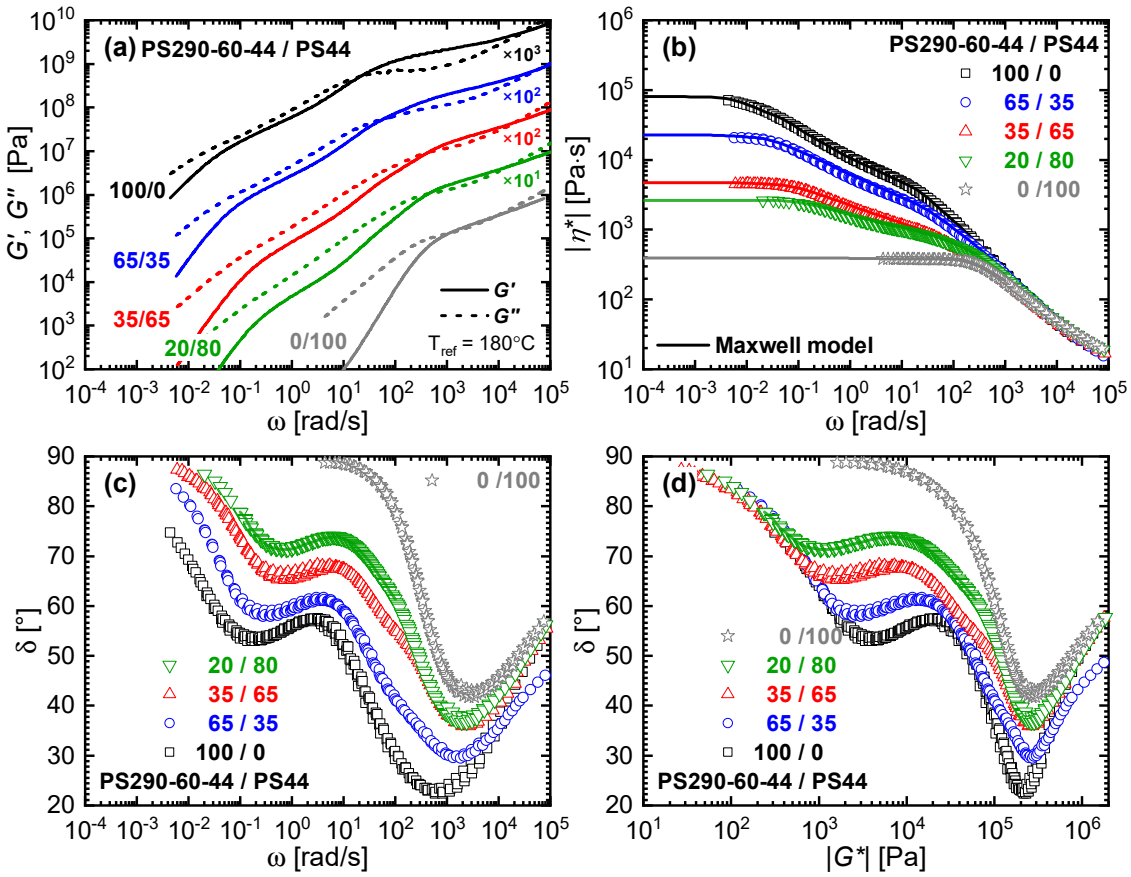

Figure A.2.4: LVE mastercurves from SAOS data of comb PS290-60-44 blended with PS44. The indicated blend composition is in percentage [%]. **(a)** Storage, G', and loss modulus, G''. **(b)** Complex viscosity, $|\eta^*|$, with Maxwell model fitting (solid lines) to obtain the zero shear viscosity, η_0 at $|\eta^*|_{\omega\to 0}$. **(c)** Phase angle, δ, vs. angular frequency, ω. **(d)** vGP plot, i.e. δ vs. complex modulus, $|G^*|$, with solid lines being DFS data directly obtained at $T_{\mathrm{ref}} = 180\,°\mathrm{C}$.

A.2.2.4 Comb-Linear Blends of PS290-30-44 and PS44

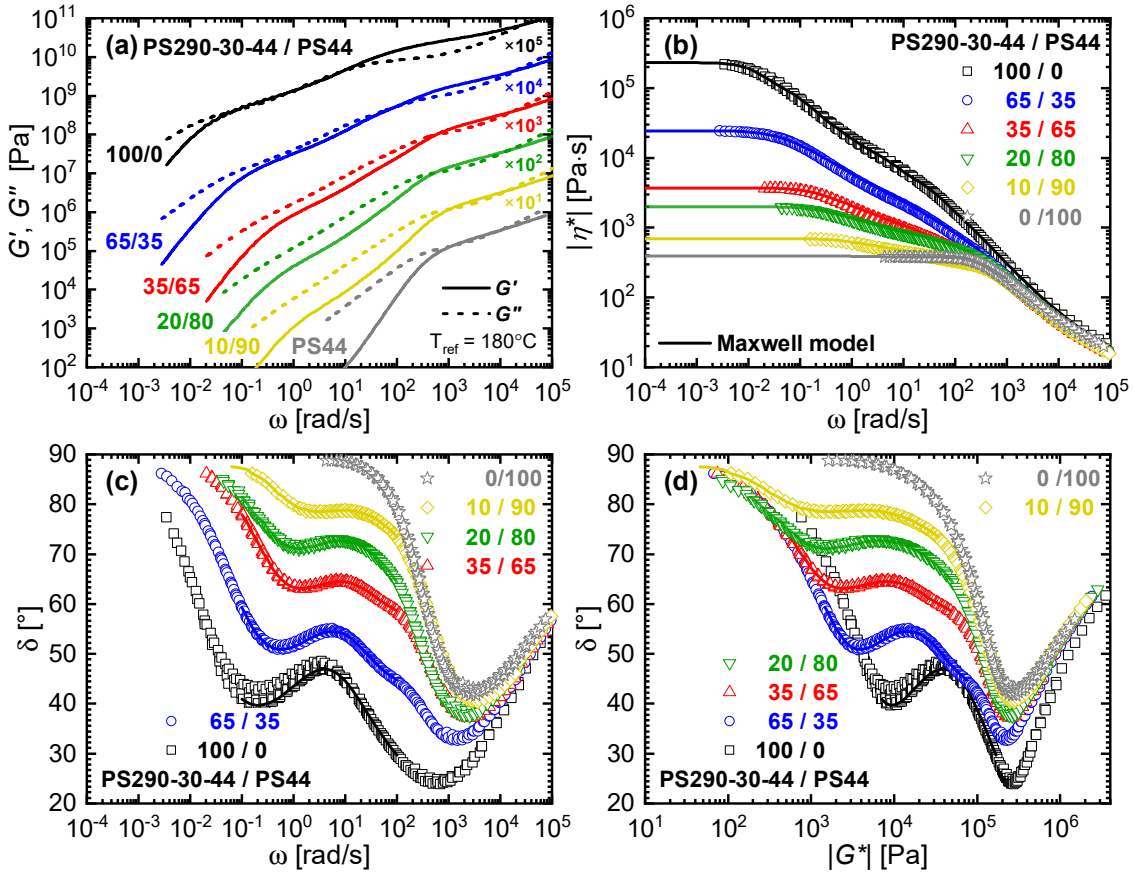

Figure A.2.5: LVE mastercurves from SAOS data of comb PS290-30-44 blended with PS44. The indicated blend composition is in percentage [%]. **(a)** Storage, G', and loss modulus, G''. **(b)** Complex viscosity, $|\eta^*|$, with Maxwell model fitting (solid lines) to obtain the zero shear viscosity, η_0 at $|\eta^*|_{\omega\to 0}$. **(c)** Phase angle, δ, vs. angular frequency, ω. **(d)** vGP plot, i.e. δ vs. complex modulus, $|G^*|$, with solid lines being DFS data directly obtained at $T_{\mathrm{ref}} = 180\,^{\circ}\mathrm{C}$.

A.2.2.5 Linear-Linear Blends of PS290 and PS44

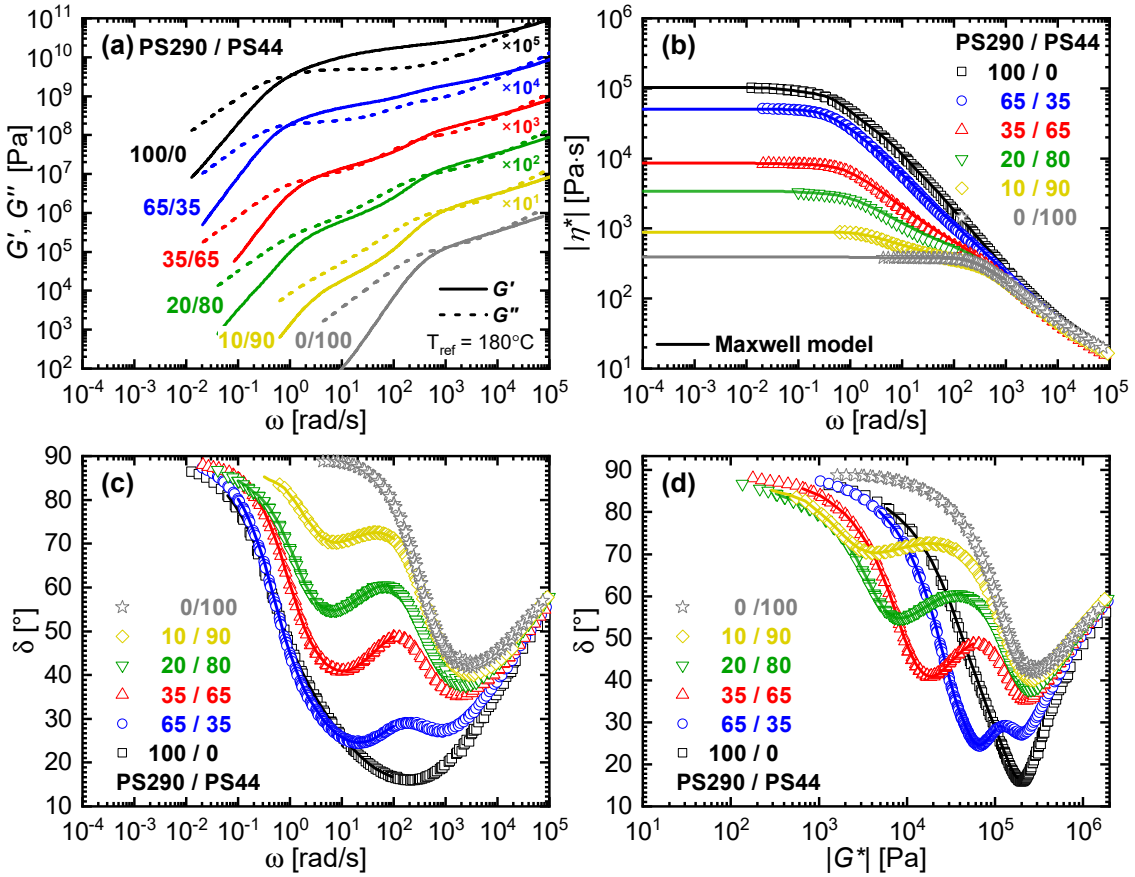

Figure A.2.6: LVE mastercurves from SAOS data of linear backbone precursor PS290 blended with PS44. The indicated blend composition is in percentage [%]. **(a)** Storage, G', and loss modulus, G''. **(b)** Complex viscosity, $|\eta^*|$, with Maxwell model fitting (solid lines) to obtain the zero shear viscosity, η_0 at $|\eta^*|_{\omega\to 0}$. **(c)** Phase angle, δ, vs. angular frequency, ω. **(d)** vGP plot, i.e. δ vs. complex modulus, $|G^*|$, with solid lines being DFS data directly obtained at $T_{\mathrm{ref}} = 180\,^{\circ}\mathrm{C}$.

A.2.2.6 Comb-Linear Blends of PS310-100-40 and PS44

Comb PS310-100-40, synthesized in Chapter 6 was blended in various concentrations with PS44 (Figure A.2.7).

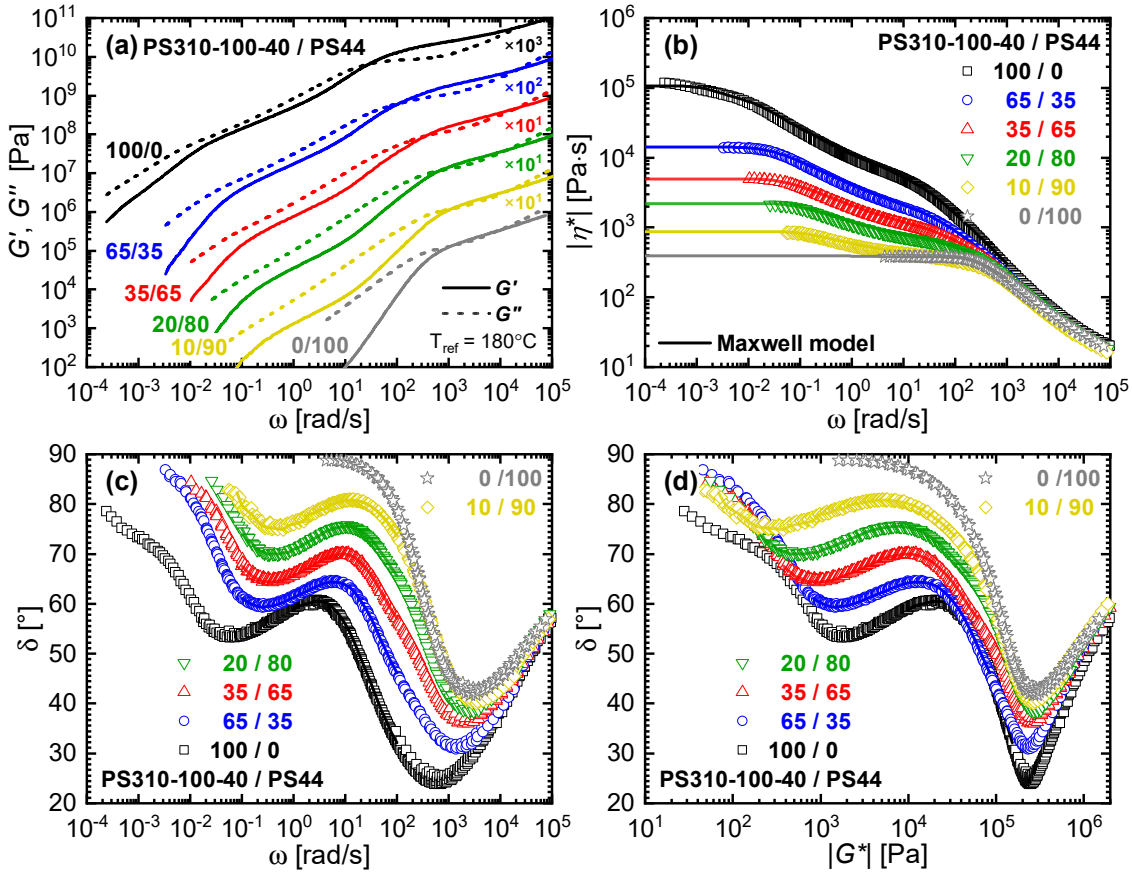

Figure A.2.7: LVE mastercurves from SAOS data of comb PS310-100-40 blended with PS44. The indicated blend composition is in percentage [%]. **(a)** Storage, G', and loss modulus, G''. **(b)** Complex viscosity, $|\eta^*|$, with Maxwell model fitting (solid lines) to obtain the zero shear viscosity, η_0 at $|\eta^*|_{\omega\to 0}$. **(c)** Phase angle, δ, vs. angular frequency, ω. **(d)** vGP plot, i.e. δ vs. complex modulus, $|G^*|$, with solid lines being DFS data directly obtained at $T_{\mathrm{ref}} = 180\,°\mathrm{C}$.

A.3 Hardware Photos

A.3.1 180 bar Mini Reactor

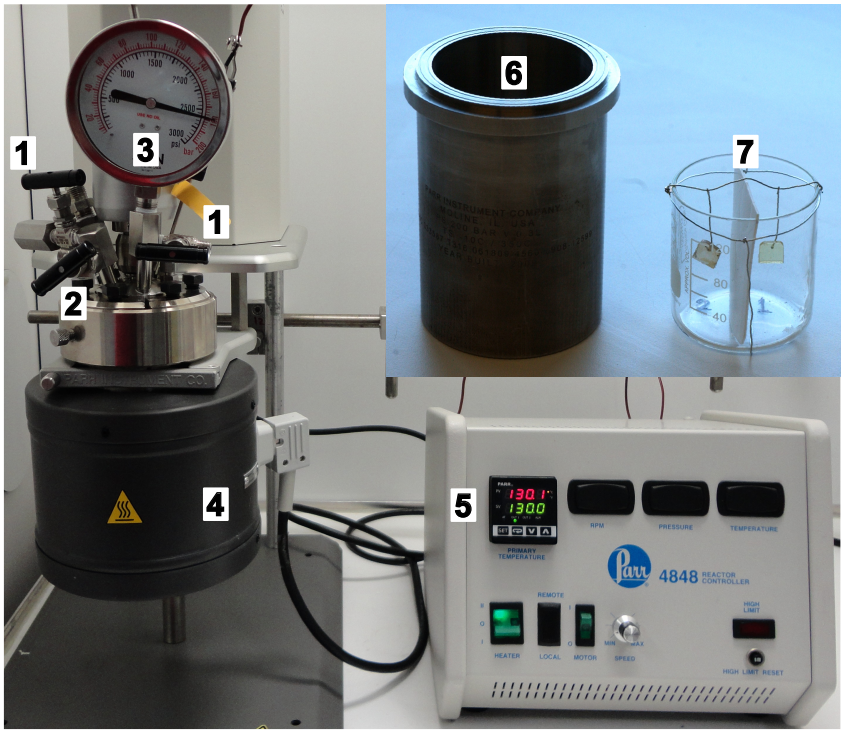

Figure A.3.1: Experimental setup of the 180 bar mini reactor. (1) Depressurization valves (2×). (2) Pressure control valve to regulate the pressure while heating up. (3) Manometer with pressure safety disc. (4) Heating jacket. (5) Temperature controller. (6) Reactor vessel. (7) Sample holder. The pressed samples are perforated and hooked to the wires of the sample holder. After placing the sample holder in the reactor vessel, the vessel is filled with dry ice ($CO_{2,s}$) and attached to the reactor lid with the manometer and pressure valves. The heating jacket is then moved up to surround the vessel.

A.3.2 500 bar High Pressure Reactor

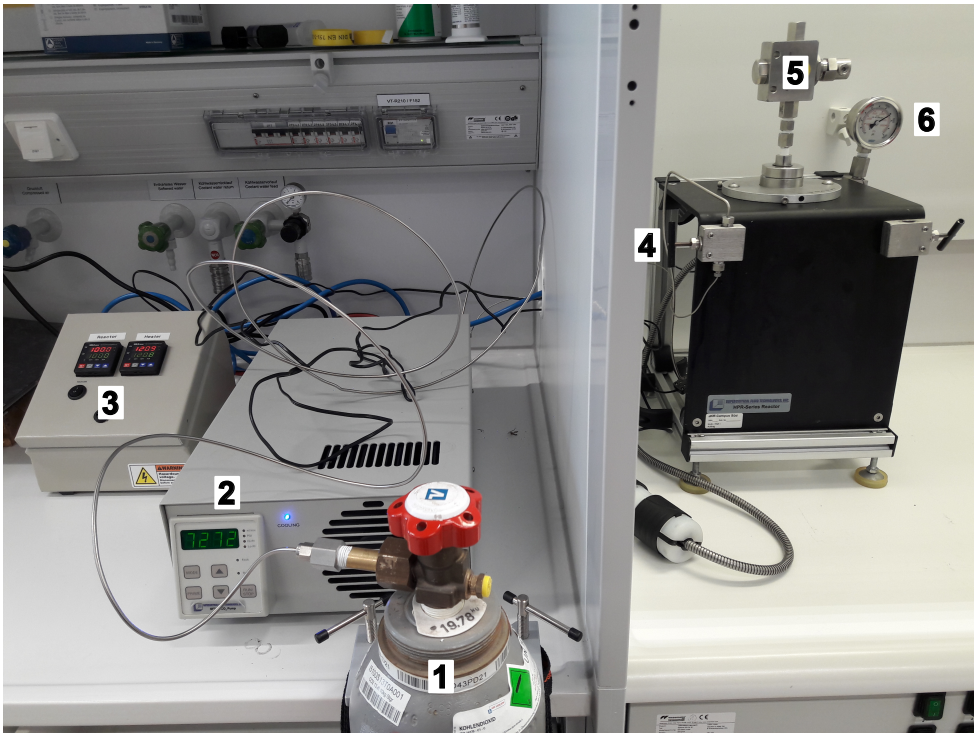

(a) Total setup of the pressure reactor.

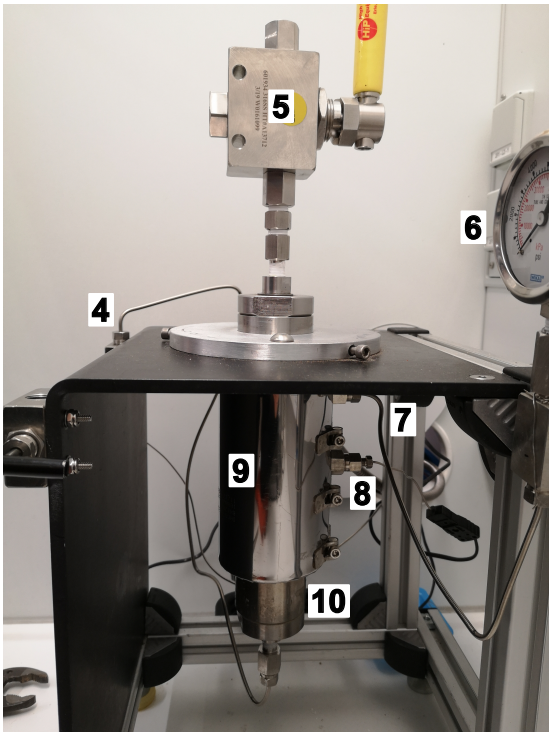

(b) Close-up of the high pressure vessel.

Figure A.3.2: Experimental setup of the 500 bar high pressure reactor (HPR). **(a)** Total setup. (1) Gas bottle with supercritical CO_2 ($scCO_2$). (2) Supercritical fluid pump. (3) Temperature controller. (4) Gas inlet valve. (5) Ball valve (on/off) for rapid depressurization. (6) Manometer with pressure safety disc. **(b)** Close-up of the HPR body. (7) Pressure line to the manometer. (8) Temperature sensor. (9) Heating jacket. (10) Pressure vessel.

Publications and Conference Contributions

Publications

O. Kreye, D. Kugele, L. Faust, M. A. R. Meier, Divergent Dendrimer Synthesis via the Passerini Three-Component Reaction and Olefin Cross-Metathesis *Macromol. Rapid Commun.* **2013**, *35*, 317–322.

M. Abbasi, L. Faust, K. Riazi, M. Wilhelm, Linear and Extensional Rheology of Model Branched Polystyrenes: From Loosely Grafted Combs to Bottlebrushes *Macromolecules* **2017**, *50* 5964–5977.

M. Abbasi, L. Faust, M. Wilhelm, Comb and Bottlebrush Polymers with Superior Rheological and Mechanical Properties *Advanced Materials* **2019**, *31* 1806484.

H. Y. Song, L. Faust, J. Son, M. Kim, S. J. Park, S.-K. Ahn, M. Wilhelm, K. Hyun, Small and Medium Amplitude Oscillatory Shear Rheology of Model Branched Polystyrene (PS) Melts *Polymers* **2020**, *12* 1806484.

M. Abbasi, L. Faust, M. Wilhelm, Molecular origin of the foam structure in model linear and comb polystyrenes: I. Cell density *Polymer* **2020**, *193* 122351.

M. Abbasi, L. Faust, M. Wilhelm, Molecular origin of the foam structure in model linear and comb polystyrenes: II. Volume expansion ratio *Polymer* **2020**, *193* 122354.

V. Hirschberg, L. Faust, D. Rodrigue, M. Wilhelm, Effect of Topology and Molecular Properties on the Rheology and Fatigue Behavior of Solid Polystyrene/Polyisoprene Di- and Triblock Copolymers *Macromolecules* **2020**, *53* 5572–5587.

V. Hirschberg, L. Faust, M. Wilhelm, D. Rodrigue, Universal Strain-Life Curves for Thermoplastics and Elastomers under Tension-Tension and Torsion *Macromol. Mater. Eng.* **2021**, 2100165.

Conference Contributions

GDCh 2018 L. Faust, M. Abbasi, M. Wilhelm, *Model Comb Polystyrenes: Synthesis, Rheology and Foaming Properties*, Biennial Meeting of the GDCh-Division of Macromolecular Chemistry together with SFB 1176 "Molecular Structuring of Soft Matter" (2018), Karlsruhe, Germany. – **Poster**

AERC 2019 L. Faust, M. Abbasi, M. Wilhelm, *Model Comb Polystyrenes: From Synthesis to Rheology and Correlated Foaming Properties*, Annual European Rheology Conference (2019), Portorož, Slovenia. – **Poster**

FIPS 2019 L. Faust, M. Abbasi, M. Wilhelm, *Model Comb Polystyrenes: From Synthesis to Rheology and Correlated Foaming Properties*, 6th International Symposium – Frontiers in Polymer Science (2019), Budapest, Hungary. – **Poster**

EPF 2019 L. Faust, M. Abbasi, M. Wilhelm, *Model Comb Polystyrenes: from synthesis to rheology and correlated foaming properties* European Polymer Congress (2019), Crete, Greece. – **Poster**

CellMAT 2020 L. Faust, M. Abbasi, M.-C. Röpert, M. Wilhelm, *Model Comb Polystyrenes: From Synthesis to Rheology and Correlated Foaming Properties*, 6th Cellular Materials (2019), online webinar. – **Oral**